MICROMAGNETIC AND STRUCTURAL STUDIES OF COPTCR LONGITUDINAL RECORDING MEDIA

by Richard John Neville

Submitted for the degree of Ph.D at the University of Glasgow

September 1996

ProQuest LLC.
789 East Eisenhower Parkway
P.O. Box 1346
Ann Arbor, MI 48106 – 1346

CONTENTS

ACKNOWLEDGMENTS

DECLARATION

SUMMARY

ACKNOWLEDGMENTS

Throughout the course of this thesis many people have helped it's completion. Foremost I wish to thank Prof. Robert Ferrier for his supervision of the whole project and for his continual support and guidance throughout. I am indebted to Dr. Tom Arnoldussen who supplied the media and for his discussions regarding both the MDPC images and the reconstruction technique. I would also like to thank Prof. John Chapman for his encouragement and for the provision of the electron microscope facilities in the Solid State Physics Group at the University of Glasgow. I am also deeply indebted to Dr. Stephen McVitie for his discussions on the subject and his assistance in the understanding and implementation of MDPC.

I would like to thank Dr. Pat Nicholson for his help in the use of the HB5 and for his knowledge regarding EDX analysis. I am also grateful to Dr. Laura Heyderman for the time she spent teaching me to operate the CM20 microscope. A special mention should be given to Dr. Colin Scott for his invaluable advice on specimen preparation.

I am extremely grateful to those at IBM who produced the media without which this project could not have occurred. In particular I wish to thank Dr. Dan Parker for recording on the media and Dr. Tom Chang for his MFM skills.

The following people must not go unmentioned for their backing over the course of this thesis. Mr Alan Howie for his microscope maintenance, computer talents and his gaudy tee shirts. For the up keep of the JOEL microscope suite I would like to thank Mr. Steven Connor, Mr. Colin How , the late Mr. Jim Simms and the late Miss Margaret Low.

I am also grateful for the financial assistance given by the EPSRC and IBM (UK) who funded the project.

Finally I wish to thank my family and friends for putting up with me over the course of this work; a non-trivial task. Special thanks should be given to Dr. Murray Gillies, Dr. Alan 'SPEK' Johnston and to Richard Henderson Ltd. for use of their PC facilities.

DECLARATION

This thesis is a record of the work carried out by myself in the department of Physics and Astronomy at the University of Glasgow during 1992-1995. The work described herein is my own, apart from the production of the hard disk samples which were supplied by Dr. Tom Arnoldussen of IBM. Some of the work given in this thesis can be found in the following paper.

Micromagnetic studies of Co-Pt-Cr Longitudinal Recording Media,
R. J. Neville and R. P. Ferrier, IEEE Trans. Mag. Vol. MAG. 31, No 6, 1995.

SUMMARY

The work presented in this thesis is a study of the micromagnetic structure of inductive and magnetoresistive playback CoPtCr longitudinal recording media. Through the use of Lorentz electron microscopy the magnetic structure of the recorded bits can be viewed directly.

An introduction to the theory and properties of ferromagnetic materials and their applicability to digital magnetic recording is presented in chapter 1. An overview of magnetic recording and the properties required for a good recording media are discussed.

Electron microscopy and in particular the Lorentz modes used to view the magnetic structure of the media are discussed in chapter 2. Image formation in an electron microscope and the Lorentz modes of Fresnel, Foucault and MDPC are introduced and explained.

An essential part of electron microscopy is the fabrication of electron transparent samples. Chapter 3 describes techniques of fabricating both planar and cross-sectional specimens from hard disks. To allow the verification that the integrity of the composition of the media has been maintained throughout the preparation an EDX analysis method is provided.

In chapter 4 the macroscopic properties of the media types are investigated. The film thickness and the magnetic layer composition are verified using the EDX techniques outlined in chapter 3. In addition to this, the value of the saturation induction in the DC bands in each medium is also verified using the technique of LAD.

The Lorentz microscopy results obtained from both media types are presented in chapter 5. A tilting method of reducing scratch contrast is introduced and discussed. Preliminary magnetic investigations are performed using the Fresnel and Foucault modes and images are presented from both media types. Magnetic features such as the bit transitions and the side write are examined, discussed and comparisons between the media types are drawn. The remainder of the chapter concentrates on the MDPC imaging of the media. A technique is presented which verifies the mapping directions using the alternate DC banding on the media. A set of characteristic MDPC images are established and MDPC images are presented from tracks written over a range of

frequencies. In particular the MDPC technique is applied to imaging the bit transitions at high magnifications to determine the magnetic structure in that area. The MDPC images also suggest the existence of a slight anisotropy in these media which is seen when the head writes off axis or is skewed with respect to the write direction. MFM images are also presented to verify some of the result seen in the MDPC images.

Two methods of MDPC image simulation are presented in chapter 6. The results are shown from each technique and are compared with the experimental MDPC images.

Chapter 7 outlines and shows the result from a reconstruction technique which use the curl and divergence of MDPC image sets to produce one possible magnetisation map which could produce such a set of MDPC images.

Finally chapter 8 discusses the main conclusions obtained from the previous chapters and includes data which is the grounding for future work in this area.

CHAPTER 1

FERROMAGNETISM OF THIN FILMS AND THEIR APPLICATION TO DIGITAL MAGNETIC RECORDING

1.1 INTRODUCTION

The topic of magnetism and the study of magnetic materials has shown an increase in activity in recent years. One part of this increase has been driven by the need for high density data storage applications. For this reason, ferromagnetic materials are of current interest in the computing industry as these materials can be used to create high capacity data storage media and transducers. The following text aims to introduce ferromagnetism and show how it can be used for data storage in digital magnetic recording applications.

1.2 THE BASICS OF FERROMAGNETISM

A ferromagnet is defined to be a material that exhibits a spontaneous bulk magnetisation, a magnetic moment per unit volume, in the absence of an applied magnetic field. An explanation of this bulk magnetisation put forward by Weiss known as the 'Weiss Molecular Field Theory' suggests that an internal field forces parallel alignment of the atomic spins resulting in a net magnetisation [Weiss 1907]. Heisenberg addressed the theory quantum mechanically with the introduction of an exchange between spins [Heisenberg 1928]. The atomic spins can be thought of as interacting cooperatively forcing mutual alignment between neighbouring atomic spins. For the transition series metals, the atomic spin in a ferromagnet can be associated with an unfilled 3d electron shell.

As the temperature of a ferromagnetic material is increased the spin alignment becomes energetically less favourable as thermal agitation of the lattice attempts to destroy it. At the Curie temperature T_c thermal agitation has exceeded the energy barrier

producing zero spontaneous magnetisation.

1.3 MICROMAGNETIC THEORY AND ENERGY CONSIDERATIONS

The micromagnetic theory assumes that the magnetic structure of the sample can be described by a vector field. At each point unit vectors $\mathbf{m}_i$ represent the orientation and the strength of the magnetisation [Cohen 1970]. The magnitude of each dipole is the saturation magnetisation, M_s and $m_x^2+m_y^2+m_z^2=1$. The total magnetisation $\mathbf{M}$ is the vector sum of all the contributions from the dipoles.

$$\mathbf{M} = M_s \sum_i \mathbf{m}_i \tag{1.1}$$

The micromagnetics are defined by the direction and distribution of the vectors on the scale of the smallest magnetic particle. The smallest magnetic particle in the thin film media of the type being considered in this thesis consist of strongly coupled grains acting as single units called clusters. Clusters sizes are typically an order of magnitude larger than the grain size of the film.

The micromagnetic theory attempts to determine the direction and distribution of the $\mathbf{m}_i$ by minimising the local energy contributions. These energy contributions arise from three main sources and are the subject of the following sections.

1.3.1 Exchange Energy

The exchange force is fundamental to ferromagnetic theory. The energy between two atoms having spins $\mathbf{S}_i$ and $\mathbf{S}_j$ can be expressed as

$$E_E = -2J \sum_{i,j;i\neq j} \mathbf{S}_i \cdot \mathbf{S}_j \tag{1.2}$$

where J is the exchange integral. This theory results from a quantum mechanical treatment of two electrons with overlapping wavefunctions [Jiles 1989, Chikazumi 1964]. As a consequence of the Pauli exclusion principle no two electrons can have the

same set of quantum numbers. Thus for a ferromagnet the wave function must be antisymmetric to allow parallel alignment i.e. J>0 such that the moments can have the same orientation; for an antiferromagnet J<0.

E_E is at a minimum when the spins are in parallel alignment. Any variation from alignment of the magnetisation will produce a change in the divergent component of the magnetisation, $\nabla \mathbf{M}$ in either of the x, y or z directions. Thus a second form for the exchange energy is:

$$E_E = A\int\left[\left|\nabla M_x\right|^2 + \left|\nabla M_y\right|^2 + \left|\nabla M_z\right|^2\right] \quad dV \qquad (1.3)$$

where A is known as the exchange constant. Thus introducing departure from parallel alignment of the magnetisation will be at the expense of exchange energy and minimum energy is attained when the magnetisation direction in the sample avoids abrupt changes.

1.3.2 Magnetostatic Energy

The second energy contribution to be considered is that due to the magnetostatic energy produced by the sample. This energy arises from the stray and internal fields produced by the Coulomb interaction of the free poles at discontinuities or divergences in the magnetisation, see Fig.1.1a. The magnetic field forms in the direction opposing the magnetisation producing it, hence it is denoted as a demagnetising field. This field arises from two sources. The volume charge density $\sigma = \mathbf{M}\cdot\mathbf{n}$, where $\mathbf{n}$ is the normal to the surface and the surface charge density, $\rho = -\nabla\cdot\mathbf{M}$. This demagnetising field, $\mathbf{H_M}$ can be expressed in integral form as:

$$\mathbf{H_M} = \frac{1}{4\pi}\int_V \frac{-(\nabla\cdot\mathbf{M})}{\mathbf{r}^2}\, dV + \frac{1}{4\pi}\int_S \frac{-(\mathbf{M}\cdot\mathbf{n})}{\mathbf{r}^2}\, dS \qquad (1.4)$$

where V and S are the volume and surface area of the sample and $\mathbf{r}$ is the vector

between the source and the field points. The magnetostatic energy associated with such a field is thus given by:

$$E_M = \frac{\mu_o}{2} \int \mathbf{H}_M \cdot \mathbf{M} \quad dV \tag{1.5}$$

Where μ_o is the permeability of free space. Magnetostatic energy is of particular importance in magnetic recording where free poles can exist at discontinuities in the magnetisation as will be discussed in section 1.6.2 in this chapter.

1.3.3 Crystalline Anisotropy Energy

A further influence on the minimum energy state of the magnetisation is due to the coupling of the atomic spins with the electrostatic charge distribution from the surrounding atoms. A minimum energy state occurs when the magnetisation is orientated along certain preferred directions, known as the easy axes. As the materials considered here form periodic lattice structures, these easy axes continue throughout the specimen. This phenomenon is termed crystalline anisotropy where preferred magnetisation directions exist which are defined by the crystallographic axes. Similarly, magnetisation directions exist which form states of maximum energy known as the hard axes which are orthogonal to the easy axes.

The uniaxial anisotropy energy in a particular direction in the sample may be written as:

$$E_A = K\sin^2\theta \tag{1.6}$$

where θ is the angle made between the magnetisation direction and the axis and K is the anisotropy constant for the axis. Easy axes are then given by a value of $\theta = 0$ (or π) and the hard axes by $\theta = \pi/2$. This effect is a strong function of the lattice structure. In the case where the crystalline field has no preferential orientation axes the sample is termed as isotropic where all orientations of the magnetisation form a minimum energy state.

1.4 ENERGY MINIMISATION, DOMAINS AND DOMAIN WALLS

The total energy of the system in zero applied field is the sum of all the contributions from the aforementioned sections.

$$E_{total} = E_E + E_M + E_A \tag{1.7}$$

The energy is a function of the direction of the magnetisation at each point. Ferromagnetic specimens form a stable minimum energy state governed by the balance between the energy processes available.

Energy reduction is achieved in zero applied field in several ways. The first is the formation of domains in the sample. Consider a uniformly magnetised rectangular block of magnetic material, as in Fig. 1.1.a. Due to the non vanishing components of $\nabla \cdot \mathbf{M}$ at the sample edges, free poles are induced. This results in the demagnetising field described in section 1.3.2. As a result of this field, areas of uniform magnetisation form known as domains in an attempt to reduce the free pole density. In the creation of these domains as in Fig.1b and c

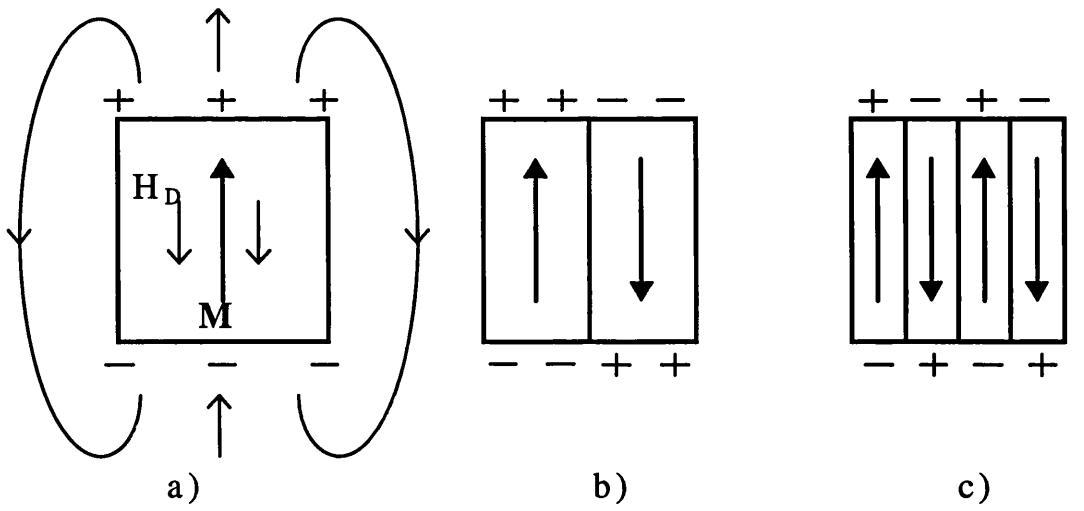

Fig. 1.1 Possible domain stages in energy minimisation of a block with uniaxial in-plane anisotropy. a) uniformly magnetised single domain b) and c)

introduction of domain walls producing reduced magnetostatic energy.

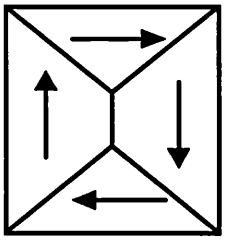

Fig. 1.2 Closure domain configuration of block with in-plane biaxial anisotropy.

boundaries or domains walls form where the magnetisation direction changes between oppositely magnetised domains. These domains walls form at the expense of exchange energy and domain splitting occurs in the sample until the decrease in magnetostatic energy is less than the energy necessary to create a domain wall. The magnetisation across a domain wall rotates over a finite distance determined by the exchange and anisotropy energies. An increase in domain wall thickness causes an increase in the anisotropy energy and a decrease in the exchange energy. The equilibrium wall width is that width that makes the two energies equal [Cohen 1970]. The energy density in a wall can be expressed for a bulk sample as:

$$\sigma_w = \sigma_e + \sigma_a \tag{1.8}$$

In the example shown in Fig.1.2 of a sample with biaxial in-plane anisotropy, closed type domain structures can also be formed. This closure occurs if the comparisons of the wall and anisotropy energy densities, σ_w and σ_a, are such that $\sigma_w/\sigma_a \ll 1$ [Prutton 1964]. In the above discussion is generally applicable to bulk specimens, no mention has been made of the film thickness and its role in energy minimisation. The film thickness is a very important parameter and as the subject of this thesis is to consider thin ferromagnetic films must be included. Examples from this point on are all assumed to be of the thin film type unless otherwise stated.

As already mentioned the magnetisation in a domain wall must rotate between the adjacent domains in order to maintain a stable energy minimum. In the example of a one dimensional model material with in-plane uniaxial anisotropy, the rotation of the

magnetisation between two antiparallel domains occurs in one of two ways.

1) Bloch walls

A Bloch wall forms when the magnetisation rotates out of the plane of the sample and produces a component of **M** normal to the film's plane, as in Fig.1.3a. This produces a magnetostatic contribution to the wall energy density due to the production of free poles at the surface of the film which increases with decreasing film thickness.

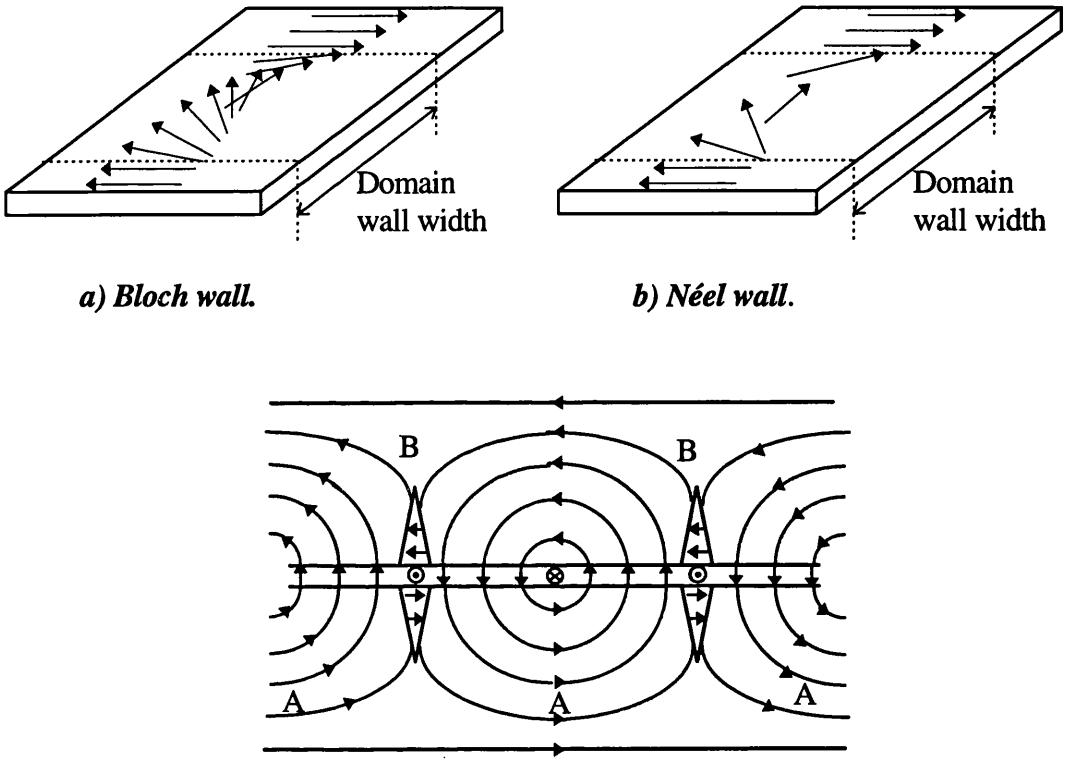

a) Bloch wall. *b) Néel wall.*

c) Planar view of Crosstie wall.

Fig. 1.3 ***Possible 180° wall structures in a sample with in-plane uniaxial anisotropy .a) Bloch wall : the magnetisation rotates out of the plane of the film and b) Néel wall : the magnetisation rotates in the plane of the film. c) planar view of the magnetic structure of a crosstie wall***

2) Néel walls

Néel walls minimise the magnetostatic energy contribution to the wall by rotation

of the magnetisation in the plane, as in Fig.1.3b. Hence volume poles as opposed to surface poles are produced.

The energy densities of both Bloch and Néel walls are thickness dependent as shown in Fig.1.4 for a typical ferromagnetic film. In thin samples, $\delta < 200$Å, the wall energy density favours Néel walls, whereas for thick or bulk samples, $\delta > 850$Å, the wall energy density favours Bloch walls, where δ is the film thickness. At intermediate film thicknesses between Bloch and Néel type walls, cross tie walls can form, as in Fig.1.3c. Crosstie walls arise from the fact that the magnetisation across a Néel wall can rotate in one of two directions. In one direction the closure in the sample is in the same sense as the magnetisation, as in the vicinity of the Bloch lines denoted as A in Fig.1.3c. But for the opposite direction of rotation for a Néel wall the closure is in the wrong sense to the magnetisation producing the crosstie regions denoted as B in Fig.1.3c.

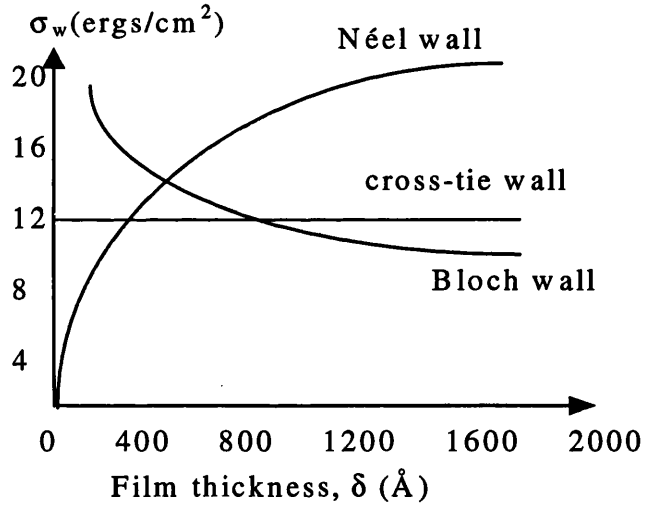

Fig. 1.4 ***Schematic plot of the energy density of each wall type as a function of magnetic layer thickness for a NiFe film [Prutton 1964].***

1.5 HYSTERESIS

A characteristic property of a ferromagnetic material is the response of the magnetisation to an externally applied magnetic field which can be non-linear and irreversible. Fig.1.5 shows a plot of the response of the magnetisation M, to an applied

field H of a typical ferromagnetic sample with uniaxial anisotropy. At A the sample is demagnetised due to the formation of domains within the sample giving a net component of zero magnetisation. As the field, H is increased M also increases as favourably aligned domains grow at the expense of those unfavourably aligned. The domains grow initially by domain wall motion and then by magnetisation rotation within favourably aligned domains. This increase in M is initially performed reversibly but at higher values of H the response becomes an irreversible process as the domain walls overcome energy barriers offered by the sample e.g. inclusions. At B the sample is now a single domain state where all the magnetisation in the sample is oriented along the axis of H. This is the saturated state where M reaches its maximum value, the saturation magnetisation, M_s. Any further increase in H following magnetisation saturation produces no further change in M.

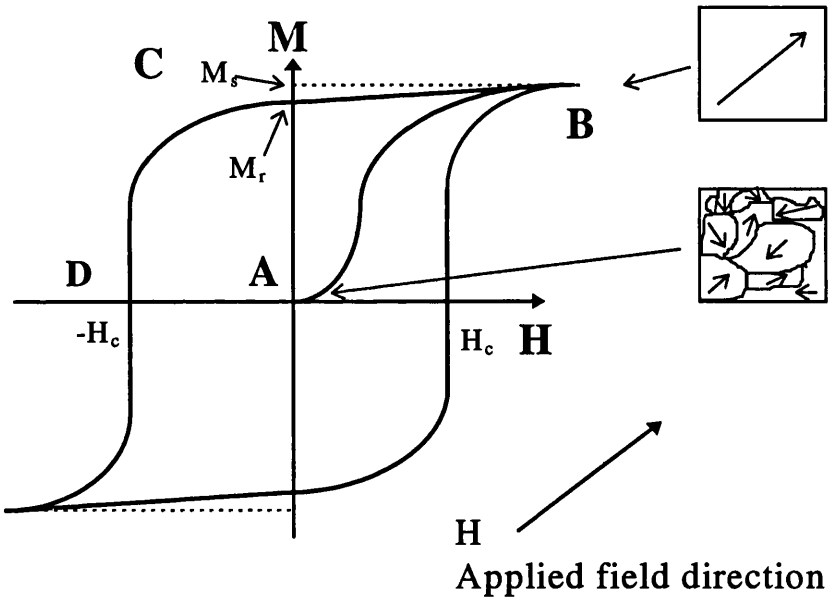

Fig.1.5 ***The hysteretic response of the magnetisation of a uniaxial ferromagnetic sample M, to an applied field H.***

As H is reduced to zero the magnetisation does not follow the initial magnetising path to A. Instead a separate curve is followed which allows the sample to retain a remanent component of magnetisation, M_r in zero applied field. The magnetisation, M is only reduced to zero on the application of the coercive field $-H_c$ at position D. If M_s is not

reached by the field the sample forms an intermediate magnetisation configuration. On application of a reversed field the magnetisation will again return to zero but at a lower value than H_c and a minor hysteresis loop will have been followed. Thus the path of magnetising a ferromagnet is dependent on the previous magnetic history of the sample.

Following the removal of the applied field the ferromagnet can retain a component of remanent magnetisation which is M_r if the sample has been fully saturated. The sample remains magnetised until a field of the order of H_c is applied or the sample is brought above it's Curie temperature.

A material with a high value of H_c is defined as a hard material. Alternatively, a material with a relatively low value of H_c is known as a soft material. Hard disks are made from hard materials as large hysteresis loops and large coercive fields are required to prevent accidental erasure, generally with H_c in the order of 1000 to 2000 Oe. Reading and writing heads covered in section 1.6, are soft materials as they require to be saturated by relatively low fields a few tens of Oe.

1.6 DIGITAL MAGNETIC RECORDING

The remaining sections of this chapter aim to show how the properties of ferromagnetic materials lead to their application for high density data storage.

Magnetic recording is the writing, storage and reproduction of information utilising the non-linear response of a ferromagnetic material to an applied field. There are currently a large variety of recording systems but the most common is longitudinal magnetic recording.

1.6.1 Fundamentals of Magnetic Recording

The basic constituents for magnetic recording are a head system to write the signal, a magnetic medium to store and a playback system to detect and reproduce the recorded signal [C. D. Mee and E. D. Daniel 1987] [Jorgensen 1980]. Fig.1.6 shows such a

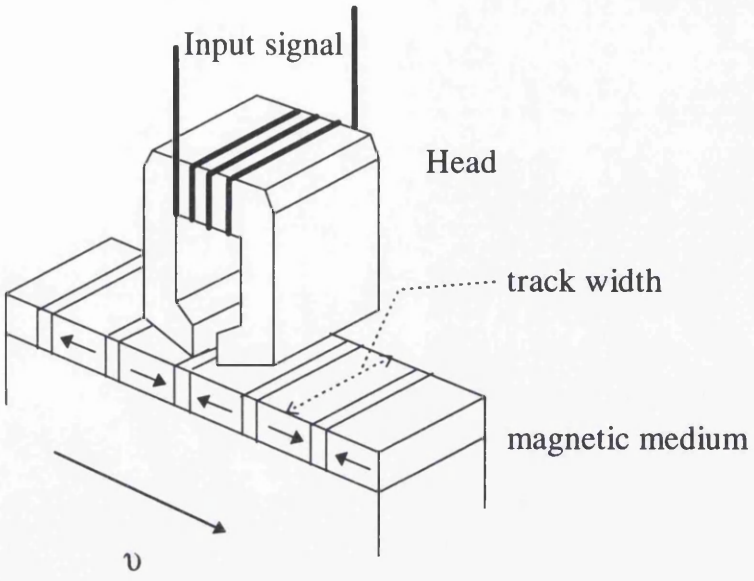

Fig.1.6 Basic longitudinal magnetic recording system

longitudinal recording system. In this case the head consists of a coil of wire wound around a ring of soft magnetic material with a gap at the surface facing the medium. The head acts as a transducer such that as current is fed to the coil, magnetic flux is induced through the ring of magnetic material. A fringing field emanates from the gap, g in the head, as in Fig.1.7. Written bits are recorded by passing a magnetically hard medium under the head at a velocity υ and at a separation less than or comparable with the extent of the fringing field. The gap fringing field can then enter and magnetise the medium from zero to saturation magnetisation or the maximum induced magnetisation due to the

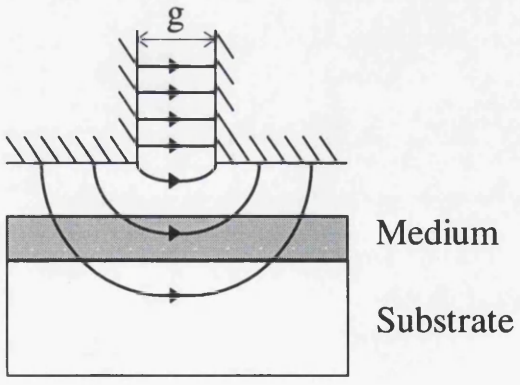

Fig.1.7 Fringing field emanating from the gap and into the medium

fringing field. As the head moves away the applied field reduces to zero and the medium retains a component of remanent magnetisation as in section 1.4.

Fig.1.8 shows a schematic of the conversion of data from the source to the head starting from either an analogue or digital signal. The digital signal is a series of zeroes and ones which is sent to the head via an amplifier. The alternating current sequence is then transferred to the media when a voltage is induced in the head coils corresponding to the timing of the input current. A one is recorded when a voltage reversal occurs and a zero otherwise.

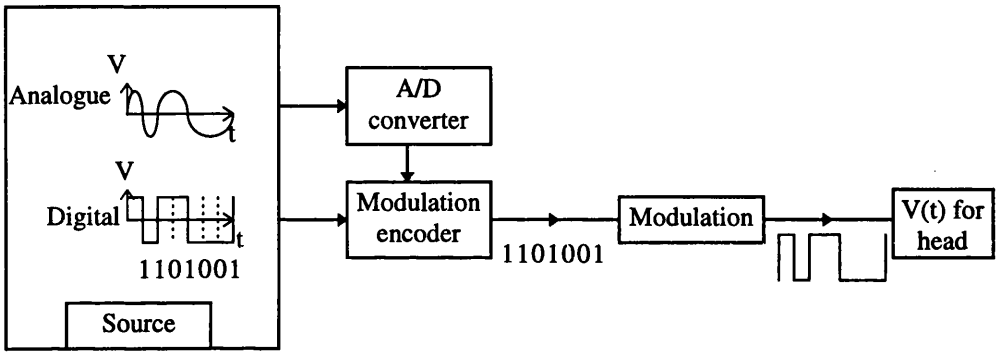

Fig. 1.8 Schematic of binary data conversion in digital applications

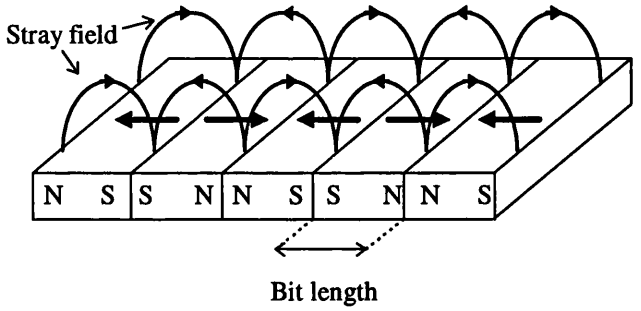

Fig.1.9 Written bit structure showing stray field due to free poles induced at head on transitions. (Only the stray field above the bits is shown for clarity)

The written bit structure resembles a line of bar magnets placed end to end, Fig.1.9. These alternating domains represent the digital recording of the original binary signal. At the boundaries where the magnetisation meets head on, free magnetic poles

are induced, producing stray field above and below each written bit. For reproduction of the original recorded data the medium is passed under a head, which can be the write head, at a velocity υ allowing the stray field to induce current in the head detecting the written bits. This head responds to the rate of change in flux through the ring.

$$\varepsilon = -N \, d\phi/dt \qquad (1.9)$$

Where ε is the induced voltage, N is the number of turns in the head coil and ϕ is the flux change through the head due to the stray field. As the stray field enters the ring the magnetisation rotates and flux closure occurs round the ring inducing a current in the coils.

1.6.2 Longitudinal Hard Disk Recording

The above sections outline the simplest recording system and an ideal magnetic recording model but some important problems leading to variations in the real recording system have been overlooked. The bit transition is the region between two written and

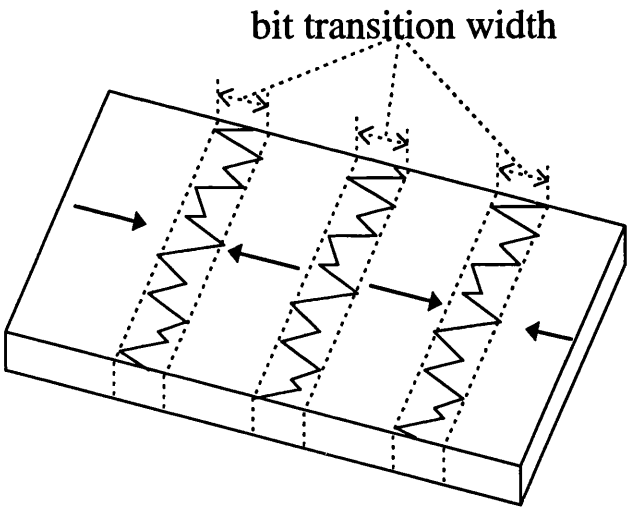

Fig.1.10 ***Schematic of zig zag structure at bit transitions in a highly anisotropic medium.***

oppositely magnetised bits. The magnetisation across the bit transition is ideally discontinuous resulting in a high density of free magnetic poles distributed across the wall. This discontinuity and the resultant high free magnetic pole density are energetically unfavourable. The energy mechanisms in the media attempt to form a stable bit transition reducing the large free magnetic pole density and hence the magnetostatic energy component associated with the discontinuity. One possible magnetisation configuration at the bit transition forms a zig zag or saw tooth structure increasing the wall length, as in Fig.1.10 [R. P. Ferrier et al 1983] [T. C. Arnoldussen and L. L. Nunnelly 1992]. The result of this increase in wall length is to reduce the free pole density along the bit transition. This occurs at the expense of increasing the wall energy component to E_{tot} and again a process of energy minimisation determines the final bit transition width and the extent of the zig zag structure. Other energy minimising structures can form at the bit transition such as vortex type structures or combinations of zig zag and vortex structures which also help to reduce the free magnetic pole density. The investigation and characterisation of bit transitions in actual materials are part of the subject of this thesis and will be investigated further in chapters 5. Regardless of the actual structure of the bit transition, energy minimisation has the effect of thickening the bit transition and introducing uncertainty in the position of the bit boundaries. This introduces an error in playback of the bits.

To increase storage densities, track widths and bit lengths need to be reduced implying narrowing of the writing head dimensions and increasing the write frequency. Inductive heads of the type shown in Fig.1.6, consist of a sensing coil wound around the magnetic core which can produce inconsistency and unacceptable tolerances in manufacture as the head parameters become more critical with reduction. This prompted the move to thin film heads giving gaps and track widths of the order of a few microns [White 1984].

Thin film heads are fabricated using thin film deposition and lithographic techniques developed for VLSI manufacture [White 1984]. Reducing the bit lengths and track widths also reduces the stray field emanating from the medium. This decline in stray field diminishes the signal that can be reproduced by the inductive head. Compensation can be made for this by increasing the head to medium velocity or the

number of turns in the inductive head coil or by decreasing the head to medium spacing. These options become less practical as the areal densities become very high and hence a new type of head has been developed.

This new type of head uses the anisotropic magnetoresistive (AMR) effect to sense the magnetic flux from the media. The AMR effect is the anisotropic change in resistivity as the magnetisation of a saturated ferromagnetic specimen is rotated with respect to an applied current [H. N. Bertram 1994]. The magnetisation direction can be

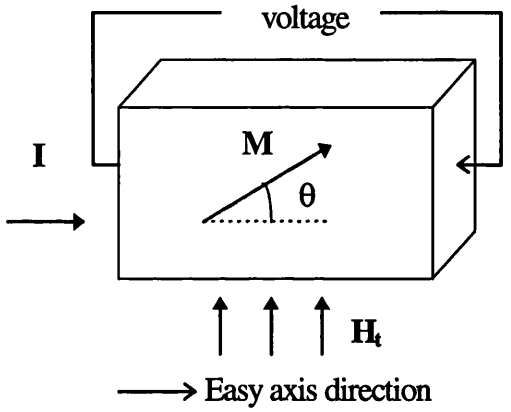

Fig.1.11 Schematic diagram of an MRE sensing a transverse field H_t.

altered by fluctuations in the temperature or the applied field in the magnetoresistive element (MRE). The AMR head uses an MRE to sense the magnetic flux from the sample by allowing stray field from the written bits to rotate the magnetisation and thus change the resistivity of the MRE, see Fig.1.11. [Hunt 1971] [McGuire and Potter 1975]. The magnetic flux through the MRE is measured by passing a sensing current along the easy axis of the MRE, the resulting change in resistivity due to the flux is then detected by the change in voltage across the MRE. The magnetic flux sensing can be characterised by the resistivities parallel and perpendicular to the magnetisation direction, $\rho_{\parallel}$ and $\rho_{\perp}$ respectively. The resistivity of the MRE can be expressed as

$$\rho = \rho_{\perp} + \Delta\rho\cos^2\theta \qquad (1.10)$$

where $\Delta\rho = \rho_{\parallel} - \rho_{\perp}$ is the difference between the parallel and perpendicular resistivities

and θ is the magnetisation rotation angle with respect to the easy axis. The sensed voltage is dependent on the angle of magnetisation which is in turn proportional to the magnetic flux entering the MRE. Thus the output of an AMR head is proportional to the magnetic flux through the head and not the rate of change of flux as in an inductive head

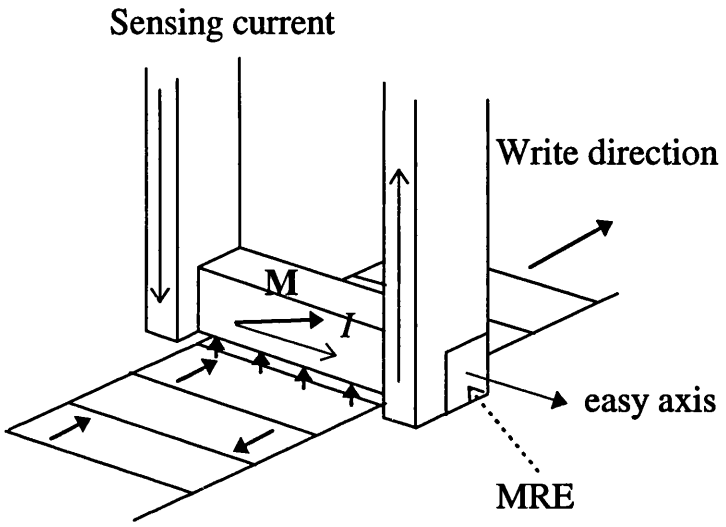

Fig.1.12 ***Diagram of an AMR head with MRE sensing stray field from bit transitions.***

which follows equation 1.9. The quantity $\Delta\rho/\rho_o = \Delta R/R_o$ is the normalised, anisotropic magnetoresistivity ratio and this denotes a measure of the performance of the MR element. Typical values of the anisotropic magnetoresistivity ratio fall in the range 2.5 - 3.5 % for NiFe alloys. A schematic of an MRE type head is shown in Fig.1.12. This is an AMR head with the easy axis of the MRE perpendicular to the write direction. Real MR heads are field biased both in the field sensing direction and along the easy axis of the element. For further details on MR head development the reader is referred to the following texts [C. D. Mee and E. D. Daniel 1987] [H. N. Bertram 1994]. Current developments in MR head design are leading to the use of the giant magnetoresistive effect (GMR) in spin valve and dual magnetoresistive (DMR) heads [B. Dieny 1994].

1.6.3 Magnetic Recording Formats

Magnetic recording has many varied forms; the above sections outlined the most common form namely longitudinal recording as in Fig.1.13a. Longitudinal recording writes the magnetisation of the bits parallel or anti parallel to the write direction as in Figs.1.6 and 1.8. The medium has an in-plane anisotropy effectively forcing the

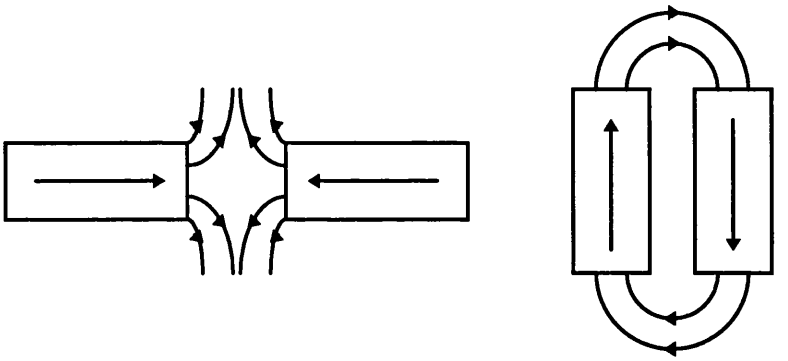

a) longitudinal recording *b) perpendicular recording*

Fig.1.13 ***Schematic cross section of media showing a) longitudinal and b) perpendicular recording written bit, self demagnetising effects using bar magnet analogy.***

magnetisation to remain in-plane. By using different head configurations and a medium with anisotropy perpendicular to the surface of the medium, perpendicular recording can be performed, as in Fig.1.13b. The expectation with perpendicular recording is that there would be an increased self demagnetising effect when compared to longitudinal recording due to the free poles being closer together, Fig.1.13. At the high areal densities of today's media the demagnetising effects of both perpendicular and longitudinal recording are little different [Mallinson and Bertram 1994]. Work is still continuing in the field of perpendicular recording and commercial drives using perpendicular recording are available. The decision as to which method is superior for digital recording is still controversial and as yet undecided. Currently the longitudinal configuration is still the most widely used.

A further variation on the magnetic recording system is magneto-optic recording

in which the medium used has perpendicular anisotropy and a Curie temperature not too far above room temperature. Prior to recording, the entire medium on the disk is uniformly magnetised out of the plane and along the direction of the easy axis. A laser is used to locally heat an area of the medium above it's Curie temperature. A field is then applied to the heated area in the opposite sense to that of the initial uniformly magnetised state. The laser is removed and the temperature of the heated area brought below it's Curie temperature once more. Information is then read from the disk using the magneto-optic Kerr effect detecting the change in the polarisation angle introduced to the incident laser beam by the orientation of the magnetisation in the written bits.

1.6.4 High Areal Density Hard Disk Recording

To attain high areal density, factors limiting the performance must be addressed. As the subject of this thesis is recording media I shall concentrate on the factors affecting media performance.

In high density digital recording thin film media the desire is to record the maximum number of bits per unit area of media with an acceptable level of readback noise. The reduction of both the bitlength and track width of the recorded bits will increase the areal density of the media. The main media limitation in longitudinal magnetic recording is noise due to bit transitions [Ferrier et al 1988]. Section 1.6.2 introduced the idea that bit transitions have a finite thickness due to energy minimisation. The nature of the bit transition and its effect on the written bits as the areal density increases is part of the subject of this thesis and will be covered in greater detail in later chapters. Reduction of the bit transition width allows smaller bitlengths to be recorded.

The ultimate limit for recorded bits results from superparamagnetism due to thermal demagnetisation [E Grochowski 1994] [CD Mee and E. D. Daniel 1987]. Each written bit consists of an array of magnetic particles. The mean number of particles per bit has to remain above a certain statistical limit to avoid the granularity of the particles affecting the bit transition width. The grain size must be reduced to maintain the same average number of particles in each bit as the bit area is reduced and hence the ultimate

recording limit is determined by a minimum grain size. The minimum grain size is determined by the ratio of the anisotropy energy KV, to the thermal energy kT for each grain, where K is the anisotropy constant, V is the mean volume of a grain, k is Boltzman's constant and T is the sample temperature, known as the aftereffect. Whereas the super paramagnetic limit occurs at a ratio of <25, in current thin film media the ratio is ~ 1000 [P. L. Lu 1994]. The critical volume V_p, below which superparamagnetism exists is given by

$$V_p = \ln(2tf_o)\frac{2kT}{\mu_o M_s H_c} \qquad (1.11)$$

where t is the time of observation, $f_o = 10^9 s^{-1}$ is the Larmor frequency. Hence increases in either or both of H_c or M_s decreases V_p [Murdock et al 1992]. For 10 Gbit/in^2 approximately 1000 grains are needed per bit with a grain diameter of ~8-10 nm and a film thickness of ~10 nm [Murdock et al 1992] [Yogi et al 1993]. The storage life of the recorded bit is reduced by a factor of approximately 10^{16} for a factor of two reduction in particle diameter all other parameters being the same, the storage life being the statistically determined time over which the particle magnetisation remains stable.

Present advances in magnetic recording have recently produced a demonstration of 3 Gbit/in^2 density [G Gorman 1995]. Further demonstrations of bit densities of 5 Gbit/in^2 are expected without significant problems in the near future [E Grochowski et al 1994] with the use of spin valve type heads and near contact recording.

CHAPTER 1
REFERENCES

T. C. Arnoldussen and L. L. Nunnelly, "Noise in Digital Magnetic Recording", 1992.

H. N. Bertram, "Theory of Magnetic Recording", Cambridge University press, 1994.

S. Chikazumi, "Physics of Magnetism", Wiley, 1964.

M. Cohen, "Handbook of Thin Film Technology", Editors L. I. Maissel and R Glang, Chapter 17, McGraw Hill, 1970.

B. Dieny, "Giant Magnetoresistance in Spin-Valve Multilayers", ***J. Magn. Magn.***

Mater., 136, pp. 335-359, 1994.

R. P. Ferrier, H. C. Tong, K. Parker and R. H. Geiss, "Lorentz Microscopy of a Thin Film High Density Magnetic Recording Medium", ***Inst. of Physics Conf. Ser.,*** Vol. 68, pp. 193, 1983.

R. P. Ferrier, F. J. Martin, T. C. Arnoldussen and L. L. Nunnelly, "Lorentz Image-Derived Film Media Noise", ***IEEE Trans. Magn.,*** Vol. MAG 24, pp. 2709, 1988.

W. Heisenberg, ***Z. Physik***, No. 49, p. 619, 1928.

G. Gorman, private communication, IBM Corp. Almaden Research, 1995.

E. Grochowski and D. A. Thompson, "Outlook for Maintaining Areal Density Growth in Magnetic Recording", ***IEEE Trans. Magn.,*** Vol. MAG 30, No. 6, pp. 3797-3800, 1994.

R. P. Hunt, ***IEEE Trans. Magn.,*** Vol. MAG 7, pp. 150, 1971.

D. Jiles, "Introduction to Magnetism and Magnetic Materials", Chapman and Hall, 1991.

F. Jorgensen, "The Complete Handbook of Magnetic Recording", TAB books Inc., 1980.

P. L. Lu and S. H. Charap, "Thermal Stability at 10 Gbit/in^2 Magnetic Recording", ***IEEE Trans. Magn.***, Vol. MAG 30, No. 6, pp. 4230-4232, 1994.

J. C. Mallinson and H. N Bertram, "Theoretical and Experimental Comparison of the Longitudinal and Vertical Modes of Magnetic Recording", ***IEEE Trans. Magn.,*** Vol. MAG 20, pp. 461, 1994.

C. D. Mee and E. D Daniel, "Magnetic Recording Volume I: Technology", McGraw Hill, 1987.

T. R. McGuire and R. I. Potter, "Anisotropic Magnetoresistance in Ferromagnet 3d Alloys", ***IEEE Trans. Magn.,*** Vol. MAG 11, No 4, pp. 1018-1038, 1975.

E. S. Murdock, R. F. Simmons and R. Davidson, "Roadmap for 10 Gbit/in^2 Media", ***IEEE Trans. Magn.,*** Vol. MAG 28, No. 5, pp. 3078-3083, 1992.

M. Prutton, "Thin Ferromagnetic Films", Butterworths, 1964

P. Weiss, ***J. Phys.***, No. 6, pp. 661, 1907.

R. M. White, "Introduction to Magnetic Recording", ***IEEE press***, 1984

T. Yogi and T. Nguyen, "Ultra High Density Media: Gigabit and Beyond", ***IEEE***

Trans. Magn., Vol. MAG 29, No. 1, pp. 307-315, 1993.

CHAPTER 2

ELECTRON MICROSCOPY OF THIN FILMS

2.1 INTRODUCTION

This chapter aims to outline the techniques used in this thesis to characterise the magnetic microstructure of hard disk specimens. Modes of electron microscopy allowing the physical, chemical and magnetic microstructures to be investigated will be included in this chapter together with descriptions of the specific experimental set-up and instruments necessary for each technique.

Microscopy is the main tool used to view structures whose size is smaller than can be resolved with the naked eye. Optical microscopy was the first branch of microscopy to investigate such structures. The resolution of a typical optical system is given by equation 2.1.

$$\text{Resolving power} = \frac{0.61\lambda}{n_o \sin\alpha} \qquad (2.1)$$

where λ is the wavelength of the incident light, n_o is the refractive index in object space and α is the semi-angle subtended by the object at the lens. For an optical microscope using yellow light with λ = 550 nm, the resolving power is ~ 0.2μm. In a standard optical microscope the images are formed due to the variance in the absorption of light in the specimen. Information on the magnetic structure can be obtained by placing a colloidal suspension of ferromagnetic particles on the surface of the specimen. The particles then delineate the domain walls in the specimen [Bitter 1931]. The main drawbacks with this technique are that the structure seen is highly dependent on the surface roughness and the results give no indication of the sense of the magnetisation in the domains delineated as the particles are attracted to field gradients of both signs. To attain higher resolution equation 2.1 implies either the wavelength of the radiation used

must be decreased or the numerical aperture ($n_o \sin\alpha$) must be increased. Different types of radiation sources can be used to reduce the wavelength the most important is the use of high energy electrons.

Electrons acquire momentum in an electron microscope when they are accelerated through a potential difference, V gaining energy equal to eV where e is the electronic charge (1.6×10^{-19}C). A wavelength λ, postulated by de Broglie can be associated with the electrons when they are subjected to a potential V. With relativistic corrections the de Broglie wavelength is given by

$$\lambda = \frac{h}{(2meV_r)^{1/2}} \qquad (2.2)$$

where

$$V_r = V\left(1+\frac{eV}{2m_oc^2}\right) \qquad (2.3)$$

where h is Planck's constant (6.626×10^{-34}), m_o is the rest electron mass (1.9×10^{-31}kg) and c is the speed of light in a vacuum (3×10^{8}ms^{-1}). Table 2.1 shows the variation of wavelength with accelerating potential. The wavelength range in typical electron microscopy is of the order of picometres a factor of 10^5 smaller than in optical microscopy implying increased resolution, although this is not the only contributing factor to the resolution.

V(kV)	λ(pm)
20	8.588
50	5.355
100	3.702
200	2.508
500	1.421
1000	0.872

***Table 2.1** Table of electron wavelength λ, dependence on accelerating voltage V. (Grundy and Jones 1976).*

2.2 THE ELECTRON MICROSCOPE

The subject of this section is to outline the typical elements that form a transmission electron microscope (TEM). A typical TEM is made up of a number of characteristic components. These are:

- An electron source or gun
- The probe forming or condenser lenses
- The objective lens
- The post specimen lenses
- A detection system

The majority of the magnetic imaging presented in this thesis was performed on a highly modified Philips CM20 field emission gun (FEG) electron microscope; each of the following sections apply to this microscope unless otherwise stated. A JEOL 2000FX was also used in parts of this work and reference will be made to this in the appropriate sections. This electron microscope is equipped with an objective lens with specially designed polepieces which permits the specimen to be located in an area where there is a very small magnetic field. The three main areas of interest are the gun, the column and the detection system. Since the detection systems used are highly mode dependent, discussion of this will be postponed until later in this chapter following the discussion of each mode of operation.

2.2.1 The Electron Gun

The electron gun is the first component in any EM system and consists of a source called the filament, from which the electrons are to be emitted, an accelerator system and an electrostatic lens, shown in Fig.2.1. In the case of the FEG source of the Philips CM20, the heated filament is subjected to a strong electric field at its tip area, this lowers the work function

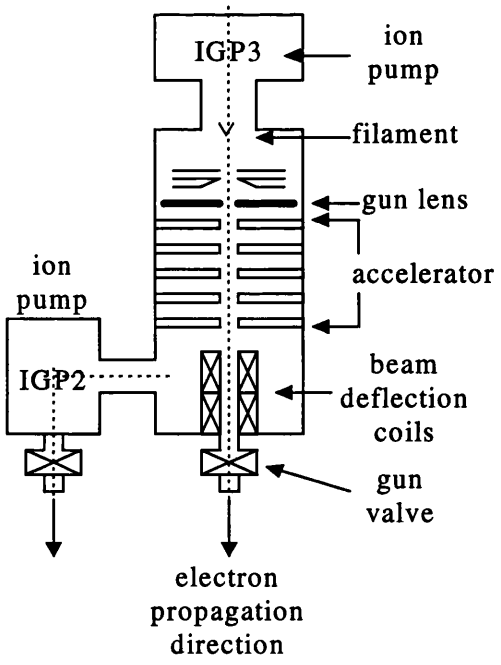

Fig.2.1 Schematic diagram of CM20 Field Emission Gun showing vacuum system

allowing electrons to be drawn off from within the metal. Tungsten is a typical material for a field emission filament. For a Schottky field emission gun (SFEG) of the type in our system, the filament is coated in a layer of zirconia (ZrO_2) which has the effect of decreasing the work function of the filament in comparison to the tungsten [P. M. Mul 1990]. The resulting source size in our SFEG is larger in comparison to a standard FEG source, 20nm as opposed to 3nm but there is an increase in the maximum attainable current for a SFEG, 300nA in comparison to 30nA. With the filament held at a fixed negative potential, 200kV, the resulting electrons then pass through an anode, an electrostatic lens known as the gun lens and an accelerator arrangement. Finally the beam passes through beam alignment deflection coils. The disadvantage of using an FEG type system is that an ultra high vacuum is required in the tip region.

The source in the JEOL 2000FX EM is a tungsten hairpin or LaB_6 filament which produces a beam of electrons by thermionic emission. Here the source of the electron optics is a beam cross over some distance below the tip. The disadvantage in using this system is the considerable increase in source size as a consequence of the low bias voltages necessary to reduce the overall energy spread from the tip. Any increase in

energy spread in the electron beam contributes aberrations to the system, see section 2.4.4. This lowered bias increases the curved area of the filament contributing to the emission and hence the effective size of the tip.

2.2.2 The Column

The column of an EM is the system of lenses, deflection coils and stigmators that the electron beam travels through, as shown in Fig.2.2. The interior of the column is held at a high vacuum to decrease the perturbing effects of collisions of the electrons in the beam with air molecules in the column and also to increase the filament lifetime. The series of lenses and stigmators produce the final in-focus image at the imaging plane. The column can be divided into three main areas; pre-specimen, specimen (or objective) and post-specimen areas, as shown in Fig.2.2.

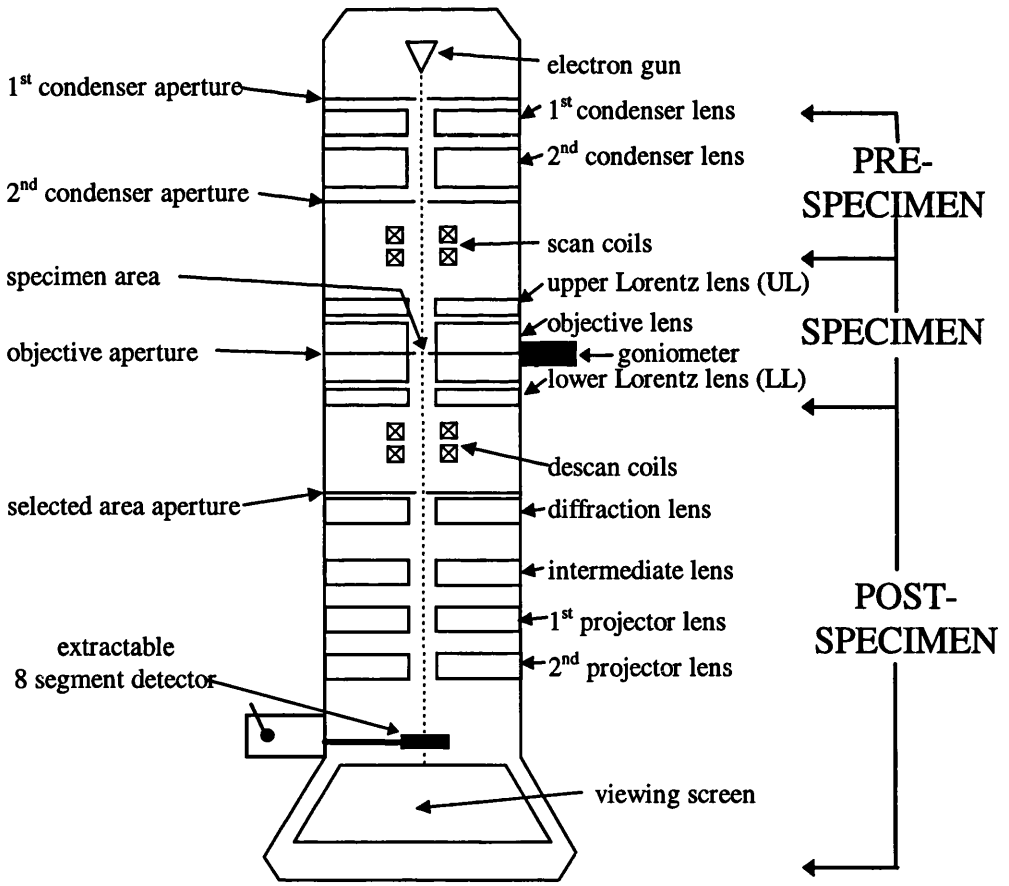

Fig.2.2 Schematic diagram of the CM20 FEG column.

The pre-specimen lenses are the probe forming lenses which condense and project the electron illumination probe on to the specimen. In our system this comprises two condenser lenses and apertures and the Upper Lorentz lens which combine to determine the effective size of the illumination spot and its angular convergence at the specimen plane.

The objective lens is used to focus the electron beam producing a diffraction pattern of the specimen in the Fourier plane which would normally be close to the back focal plane of the lens. This lens produces high magnetic fields in the specimen area. As the subject of this thesis is the consideration of the magnetic structure of recording media, such a lens would bulk erase a sample with written tracks (chapter 1 section 6). Previous magnetic investigations overcame this problem by using the EM with the objective lens switched off and using a lens below the objective for standard imaging or the condenser lenses to focus and form the probe on the specimen for STEM operation e.g. [D. Rogers 1990] [D. Donnet 1992]. To overcome this the Philips CM20 FEG is equipped with two non immersion mini lenses above and below the specimen area. Focusing on the specimen with the objective in an unexcited state is then performed by the mini lenses reducing the magnetic field at the specimen area to levels low enough to prevent the erasure of even soft materials. This is the mode that will be used when magnetic imaging is being considered in all later sections and the lenses will be referred to as the Upper and Lower Lorentz lenses (UL and LL respectively).

The final image is transferred to the viewing screen by the post objective lenses which determine the magnification of the image on the viewing screen. The settings of these lenses become of critical importance in image formation in the scanning mode of EM as they also determine the size of the probe on the viewing screen. Images can be recorded on photographic film or by an electronic detection system.

2.2.3 Electron Specimen Interactions

In EM the incident electrons can interact with the specimen in a number of different ways. The electrons can be undeviated, transmitted, reflected or absorbed by the specimen. Only those electrons which are transmitted are of interest in conventional

transmission electron microscopy (CTEM) as this is the dominant electron specimen interaction in this system. The transmitted electrons have undergone interaction with the specimen in three ways; elastic scattering, inelastic scattering and deflection due to the Lorentz force. In a crystalline specimen the electron interacts elastically with the screened Coulomb potentials of the atoms producing Bragg scattering from the planes of atoms. Typical Bragg deflections are angles of the order of ~10mrads. Inelastic scattering occurs when the electron transfers some or all of its energy to atoms in the specimen. This can result in the production of X-rays a topic covered in section 2.6.

The principal interaction of interest here is that due to the magnetic induction of the sample. The electron beam interacts with the magnetic induction of the sample in a way that classically can be described by means of the Lorentz force and modes utilising this effect fall under the heading of Lorentz electron microscopy. Fig.2.3 shows the path of the electrons incident on the specimen along the z axis, passing through a thin film specimen. The specimen contains two domains which are oppositely magnetised along the y axis.

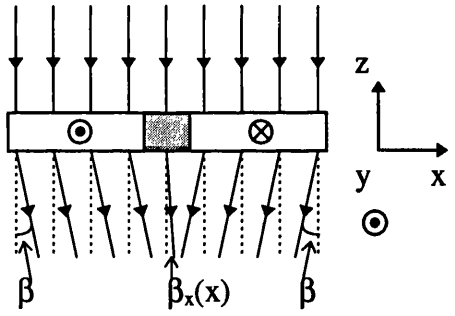

Fig.2.3 The Lorentz deflection of an incident electron beam passing through a thin film specimen containing two oppositely magnetised domains and a 180° wall.

Classically, an electron beam incident on the specimen along the z axis is deflected in the x axis direction by the y component of magnetic induction in the sample [Chapman 1984]. The direction and magnitude of the deflection are determined by the direction and strength of the magnetic induction in the sample respectively. Magnetisation along the y axis results in a deflection, β_L in the x axis direction. Correspondingly the

deflection due to magnetisation along the negative y axis results in a deflection, $-\beta_L$ in the x axis direction. The magnitude of this Lorentz deflection is given by the deflection angle:

$$\beta_L = eB_y\lambda\delta/h \qquad (2.4)$$

where B_y is y component of the saturation magnetic induction in the sample, λ is the wavelength of the electron, δ is the specimen thickness in the z direction and h is Planck's constant. Equation 2.4 assumes that the magnetic induction is contained in the sample and is uniform throughout the thickness of the specimen. The specimens of interest in this thesis have stray fields emanating out of the plane of the specimen and hence the appropriately modified form of equation 2.4 is:

$$\beta_L(x) = e\lambda/h \int_{-\infty}^{\infty} B_y(x,z)dz \qquad (2.5)$$

where $\beta_L(x)$ is the local Lorentz angle deflection and $B_y(x,z)$ is the local value of the y component of magnetic induction.

The above analysis of Lorentz electron microscopy follows a classical approach to the electron magnetic induction interactions. The system was approached quantum mechanically by Aharonov and Bohm 1959 producing the following results. They suggested that the effect of the magnetic induction of the sample was to introduce a phase shift between two electron rays which originate from the same source point but travel through different paths in the sample. When the paths of the rays rejoin they enclose a magnetic flux N resulting in a phase shift between the two rays, φ given by:

$$\varphi = \frac{2\pi N}{h} \qquad (2.6)$$

The Aharonov-Bohm effect was extended to include the incidence of a plane electron wave propagating along the negative z axis as in Fig.2.3. The phase shift experienced by

an electron wave between any two points on the x axis with coordinates x_1 and x_2 is given by:

$$\varphi = \frac{2\pi e\delta}{h} \int_{x_1}^{x_2} B_y(x)\ dx \qquad (2.7)$$

Thus a ferromagnetic specimen can be viewed as a pure phase object and hence Lorentz microscopy is a branch of phase contrast microscopy.

Electron microscopy has been shown to be a tool not only to view specimen structure in the nanometer range but also to view directly the magnetic induction of the sample. The various modes of Lorentz electron microscopy available for such characterisation will now be discussed.

2.3 LORENTZ MICROSCOPY I : CTEM

The conventional transmission electron microscope (CTEM) mode is highly flexible and is described in the following three sections. The first deals with a general description of image formation in the CTEM mode and the remainder deal exclusively with the CTEM magnetic imaging modes. It should be noted that the magnetic imaging modes used for work in this thesis can be denoted as branches of Lorentz microscopy as they utilise the Lorentz force-magnetic specimen interaction.

2.3.1 Bright Field imaging

As described in section 2.2.2, image formation in CTEM mode uses the objective lens (or the UL and LL lenses if in field-free mode) to focus the transmitted intensity in the back focal plane of the objective lens producing the diffraction pattern associated with elastic Bragg scattering from the crystal planes [Hawkes 1972]. If a sample consists of perfect single crystals the diffraction pattern will resemble a regular array of spots, whereas in a polycrystalline sample, concentric rings are formed. In wave optical terms the diffraction pattern is the Fourier transform of the wave transmitted by the specimen.

The specimen and viewing screen are conjugate planes as the final image is the Fourier transform of the diffraction pattern in the back focal plane of the objective lens.

2.3.2 Fresnel Mode

As outlined in section 2.2.3, the electron beam can interact with the magnetic induction of the sample. Fig.2.3 showed that a plane wave of electrons incident on a

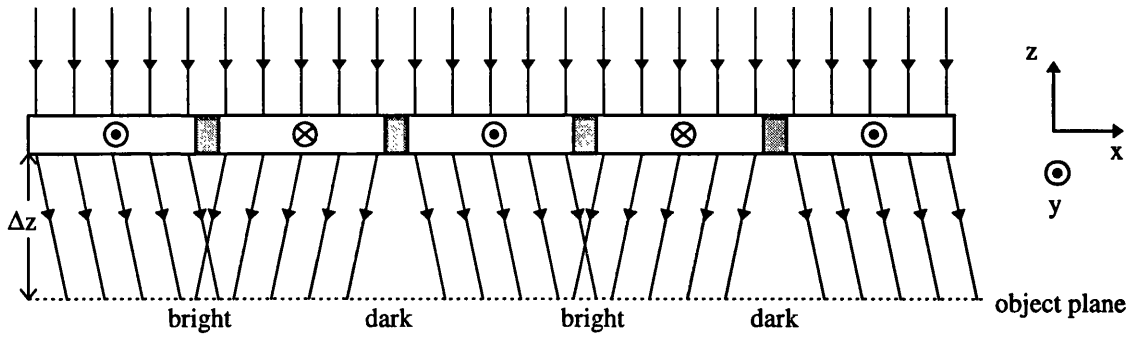

Fig.2.4 Ray diagram of Fresnel mode of a magnetic specimen.

magnetic specimen converges and diverges at domain walls due to the interaction of the incident beam with the magnetic induction from the sample through the Lorentz force. The Fresnel mode of Lorentz microscopy uses this effect to produce images containing wall contrast. The objective lens (or LL lens) is defocused by an amount Δz making the object plane lie at this distance from the specimen, as in Fig.2.4. The beam convergence or divergence is dependent on the directions of the magnetic induction in the domains on either side of the wall. The domain walls show up as bright or dark bands in the images for convergent and divergent beam deflections respectively. This allows a qualitative evaluation of the magnetic induction of the sample. The Fresnel mode shows wall contrast as in Fig.2.5.

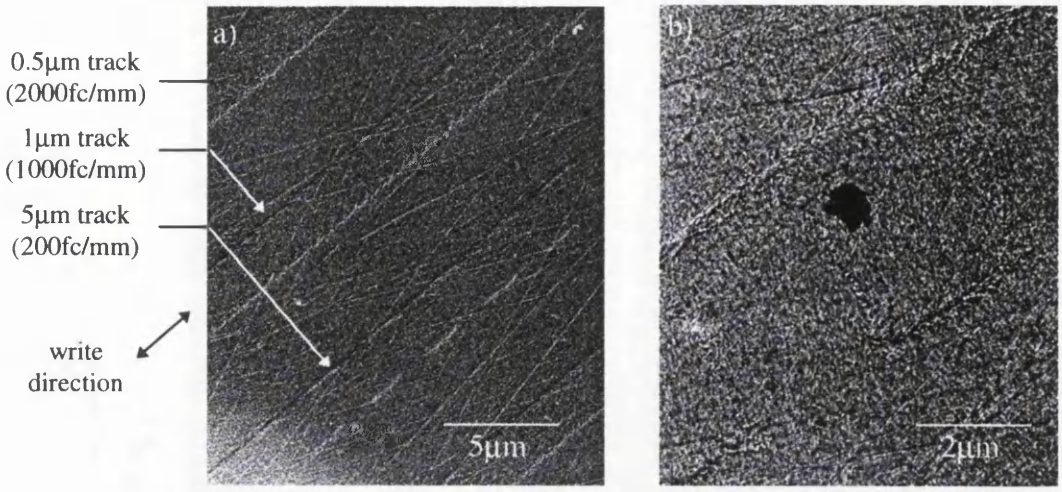

Fig.2.5 ***a) low magnification Fresnel image of all tracks.***
b) high magnification Fresnel image of 5µm track.

2.3.3 Foucault Mode

The Foucault mode of Lorentz microscopy uses the observation as in Fig.2.3 that the deflection from a domain in a specimen is uniform across that domain assuming the magnetisation vector is constant across the domain. The domain deflections are focused to single spots in the objective back focal plane for each direction of magnetic induction in the sample. As these magnetic deflection angles are considerably smaller than the Bragg deflection angles (µrads compared to mrads), the centre diffraction spot is split into several magnetic spots corresponding to each magnetic induction direction. Domain contrast is obtained by carefully positioning the objective aperture, in the back focal plane of the objective lens, to obscure one of the magnetic spots corresponding to a particular magnetic induction direction, as in Fig.2.6a. The deflections due to domains with a particular direction of magnetic induction are removed from the image and these domains show up as dark contrast in the image. The other spots are transmitted allowing the remaining oppositely magnetised domains to show up as bright contrast in the image, as in Fig.2.6b. An example of a Foucault image of written tracks is shown in Fig.2.7 respectively.

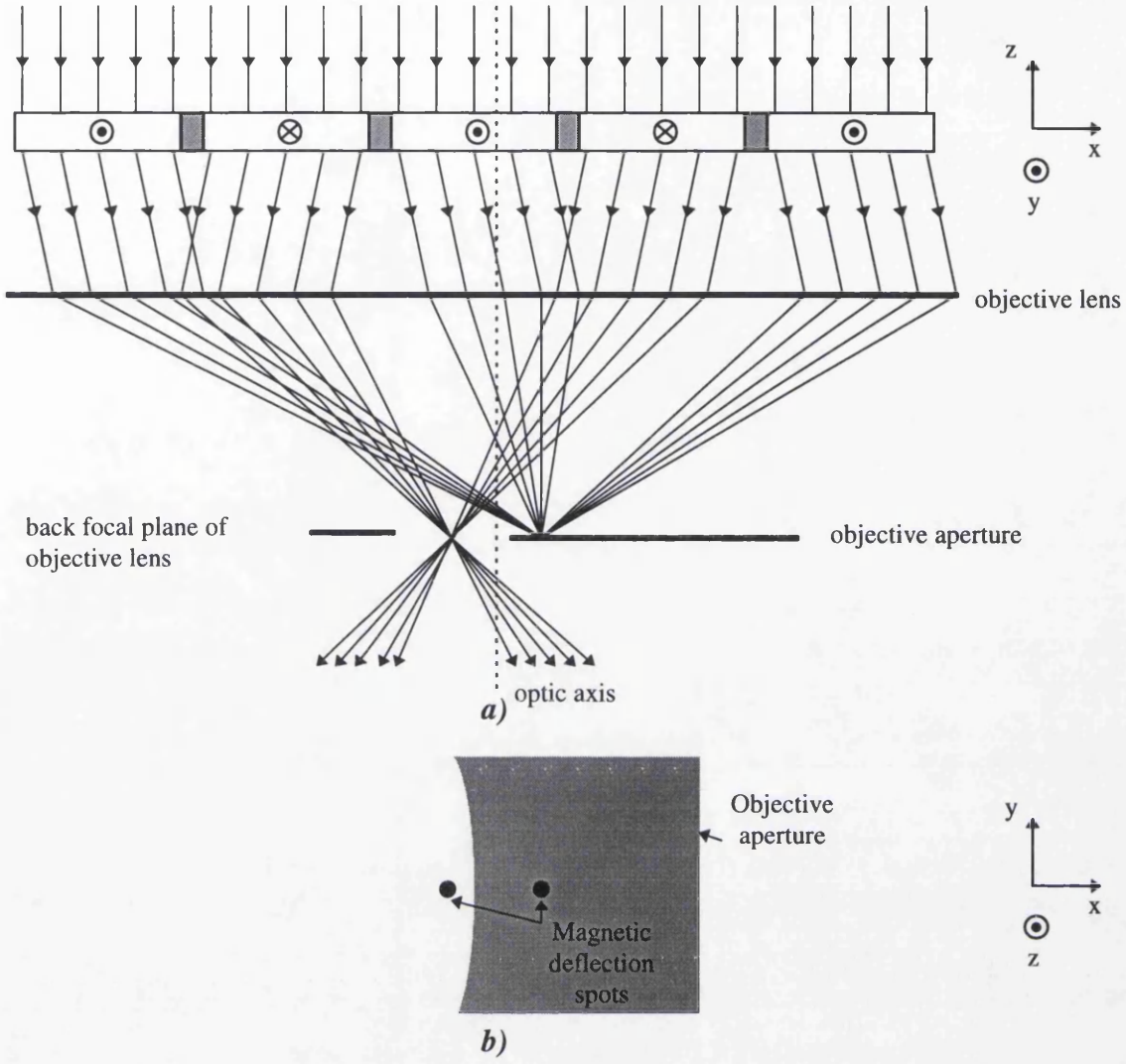

Fig.2.6 ***a)Ray diagram of Foucault mode of a magnetic specimen.***
b)Plan view of objective aperture and magnetic spot configuration.

Fig.2.7 ***Foucault micrograph.***

2.4 LORENTZ MICROSCOPY II : STEM

Modes of fixed beam CTEM Lorentz microscopy have been outlined above but Lorentz microscopy can also be implemented in scanning transmission electron microscopy (STEM). In STEM, the electron beam is focused to a probe which is scanned in a raster fashion across the specimen. The scanned probe interacts with the

specimen and is transmitted as outlined in section 2.2.3 [D. Rogers 1990]. The Philips CM20 FEG as in Fig.2.2 can be used in STEM mode using the pre-specimen lenses and scan coils to deflect the beam.

2.4.1 Differential Phase Contrast

A powerful mode of Lorentz microscopy which can be implemented in a STEM arrangement is called the differential phase contrast (DPC) mode. This mode was outlined by Dekkers and de Lang 1974 and 1977 and applied to magnetic thin films by Chapman et al 1979. The system uses a quadrant detector placed in the far field to produce image contrast related directly to the magnetic structure of the specimen.

The DPC mode of Lorentz microscopy is shown schematically in Fig.2.8. The classical interpretation is as follows. A beam of electrons is focused to a probe onto the specimen. A quadrant detector in the far field senses the deflection of the bright field cone by taking combinations of difference signals from the four quadrants. In the absence of a magnetic specimen, the post-specimen descan coils are set such that the bright field cone falls equally on all four quadrants producing zero difference signals. When a magnetic specimen is scanned, the bright field cone is deflected by the in-plane components of magnetic induction integrated along the electron trajectory, resulting in a Lorentz deflection, β_L. In this case the difference signals from the detector are proportional to β_L. The deflection is then displayed on a grey scale where white and black represent the maximum positive and negative signals respectively and hence grey is equivalent to zero signal. The image is then a pixel map of the integrated in-plane induction of the specimen shown on a grey scale.

The signals from each quadrant are acquired in parallel, allowing any mixing of the signals to occur with perfect registration. Generally three signals are acquired, two orthogonally mapped difference signals giving the magnetic image e.g. A-C, D-B, and

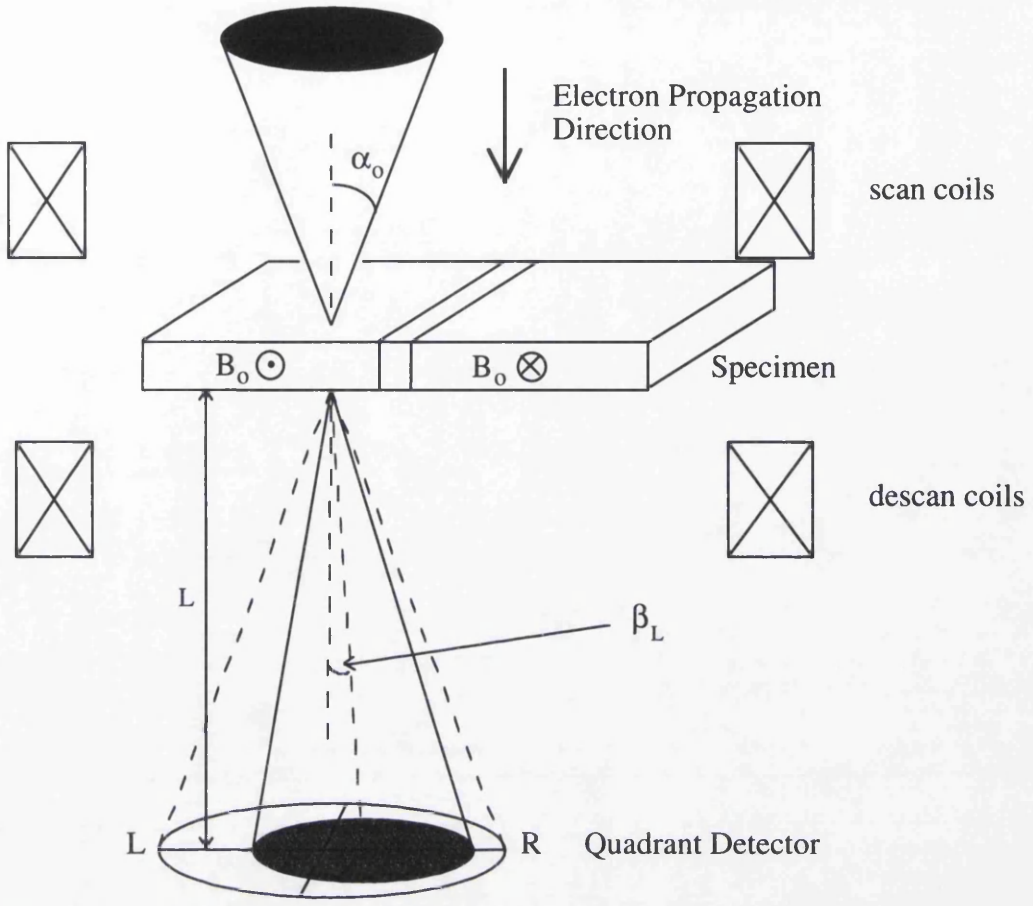

Fig.2.8 Schematic of DPC arrangement.

the sum signal A+B+C+D which forms an incoherent bright field signal showing the crystallite structure of the specimen.

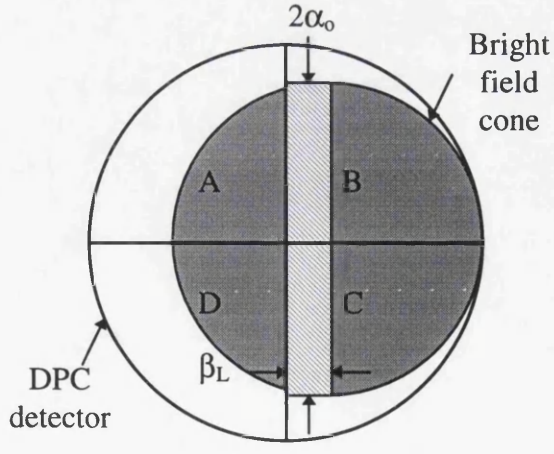

Fig.2.9 Schematic of DPC detector.

Fig.2.9 shows a schematic of the DPC detector depicting the Lorentz deflection of the bright field cone. The current falling on each segment is proportional to the area of the bright field disk incident on that segment. The shaded region represents the change in the difference signal between the two detector halves ({A+B}-{C+D}) due to the introduction of a magnetic specimen. The area of the shaded region is proportional to $2\alpha_o\beta_L$ and hence the difference signal is proportional to $4\alpha_o\beta_L$.

2.4.2 Image Formation in STEM

The previous explanation of Lorentz image formation followed a classical approach; here an outline of the quantum mechanical interpretation of STEM image formation with particular reference to DPC imaging will be given.

Consider a plane electron wave to be incident on a magnetic specimen, as in Fig.2.3. Following the theory of Aharanov and Bohm, a magnetic specimen resembles a pure phase object to the incident electron beam as outlined in section 2.3.3. When a plane electron wave ψ_i, is incident and transmitted through a magnetic specimen, the phase of the transmitted wave will be modulated by the specimen. Thus the resulting transmitted electron wave at the specimen exit plane is given by:

$$\psi_t(\mathbf{r}) = \psi_i(\mathbf{r})p(\mathbf{r}) \qquad (2.8)$$

where p is the phase imparted to the beam by the specimen such that:

$$p(\mathbf{r}) = \exp(-i\phi(\mathbf{r})) \qquad (2.9)$$

where $\mathbf{r}$ is a vector from the optic axis in the specimen plane. The transmitted electron wave ψ_t now contains information related to the phase imparted by the specimen, which is related to the in-plane component of magnetic induction of the specimen. As the beam is scanned across the specimen this must also be included in equation 2.9, but for convenience the standard procedure is to view the position of the beam as though the specimen were moving with respect to the optic axis. Equation 2.9 is modified such that

the position of the scanned beam with respect to the optic axis is $\mathbf{r}_o$ Hence the transmitted beam is given by:

$$\psi_t(\mathbf{r},\mathbf{r}_o) = \psi_i(\mathbf{r})p(\mathbf{r}-\mathbf{r}_o) \qquad (2.10)$$

The DPC system extracts this phase and hence magnetic information from the modified beam. After passing through the post-specimen lenses the transmitted wave is then incident on the detector plane. The post-specimen lenses magnify the spot arriving at the detector plane by an amount defined by a distance L, known as the camera length. The wave arriving at the detector plane is the Fourier transform of the transmitted wave. This is expressed as:

$$\psi_d(\mathbf{k},\mathbf{r}_o) = F\{\psi_t(\mathbf{r},\mathbf{r}_o)\} = F\{\psi_i(\mathbf{r})p(\mathbf{r}-\mathbf{r}_o)\} \qquad (2.11)$$

where F{quantity} denotes the Fourier transform of that quantity. At this point it is the detector response that will produce the phase information from the beam. The detector has a response function $D_{symm}(\mathbf{k})$ for a symmetric detector. A full discussion of detector response functions is given in Morrison [1981] and McFadyen [1986]. Dekkers and de Lang [1974] and [1977], proposed the use of a split detector which has an anti symmetric response function. This is expressed as:

$$D_{anti}(\mathbf{k}) = D_{symm}(\mathbf{k})H(\mathbf{k}) \qquad (2.12)$$

such that:

$$H(\mathbf{k}) = \begin{cases} +1 \text{ for } k > 0 \\ -1 \text{ for } k < 0 \end{cases} \qquad (2.13)$$

The DPC image intensity is a convolution of the wave incident on the detector and the detector response function. The Fourier transform of the detector response is given by:

$$i d_{anti}(\mathbf{r}_o) = d_{symm}(\mathbf{r}_o) * (i\pi \mathbf{r}_o)^{-1} \qquad (2.14)$$

where * denotes the convolution. Reducing this to one dimension, the detector response contribution in the DPC image is proportional to x^{-1}. This convolution with x^{-1} is approximately equivalent to differentiation with respect to x. Hence the intensity of a pixel in a DPC image is proportional to d/dx of the phase of the beam incident on the detector. This phase is proportional to the in-plane integrated component of magnetic induction due to the specimen, as in equation (2.7). Hence the intensity in the DPC image using a detector with an anti symmetric response function is given by:

$$\nabla_x \varphi(x,y) = \frac{2\pi e}{h} \int_{-\infty}^{\infty} B_y(x,y,z)\ dz \qquad (2.15a)$$

$$\nabla_y \varphi(x,y) = \frac{2\pi e}{h} \int_{-\infty}^{\infty} B_x(x,y,z)\ dz \qquad (2.15b)$$

where B_x and B_y are the components of magnetic induction in the x and y directions. For these conditions to be realised in practice the probe semi-angle at the specimen, $\alpha >>$ the Lorentz angle β.

2.4.3 Modified Differential Phase Contrast : MDPC.

DPC images inherently contain non-magnetic contrast such as scattering from an electrostatic potential V in the sample. This is due to the crystallites in the sample and primarily has the effect of changing the intensity of the bright field cone rather than shifting its position. Non-magnetic contrast can be included in the above theoretical DPC treatment by the addition of:

$$\nabla_x \varphi(x,y) = \frac{\pi e}{\lambda E_o} \nabla_x \left(t(x,y), V(x,y) \right) \qquad (2.16)$$

to equation 2.15a) and a similar form for equation 2.15b) as outlined by Plöβl [1992] and Chapman et al [1992]. This non-magnetic crystallite contrast tends to obscure the magnetic information in the images and hence a method to remove this contrast is required. It was noticed that the crystallite spatial frequencies are considerably higher than the magnetic information of interest. If a method of suppressing these higher spatial frequencies can be found while passing low frequencies in the bright field cone then the crystallite noise will be suppressed relative to the magnetic signal.

The solution found by simulation and by experiment is to use an eight segment detector in place of the quadrant detector of standard DPC [Chapman et al 1990] [I. R. McFadyen 1992]. Images are then formed by taking difference signals as before but only using the outer quadrants of the detector as the shaded area of fig. 2.10b.

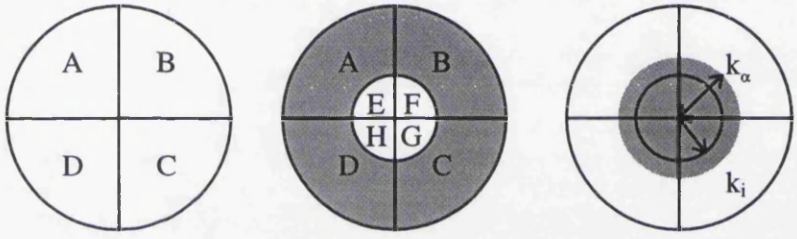

Fig.2.10 ***Schematic of***
a) quadrant DPC detector.
b) eight segment MDPC detector.
c) spatial frequency vectors for optimised MDPC.

The camera length must be set such that the resulting spot on the detector is only just larger than the inner quadrant, as in Fig.2.10c. This provide a non zero signal on all four outer quadrants. Justification for the high frequency suppression from this configuration can be outlined by consideration of the detector transfer function [Chapman et al 1990]. This can be expressed as a function of the single parameter κ given by:

$$\kappa = \frac{k_i}{k_\alpha} \qquad (2.15)$$

where k_i is the largest spatial frequency that can fall on the inner detector and k_α is the maximum spatial frequency of the bright field disk incident on the detector, determined by the size of the inner detector and the camera length respectively. Fig.2.11 shows the variation of the phase gradient signal to noise ratio with the reduced spatial frequency component defined as:

$$k_r = \frac{k_x}{k_\alpha} \qquad (2.16)$$

In a purely qualitative sense, this works by reducing the signal level which contains the crystallite contrast, for the magnetic signal we are only interested in the difference between the signals and not the signals themselves. The signal from the centre of the detector in D C does not add to the signal and only contributes to the noise.

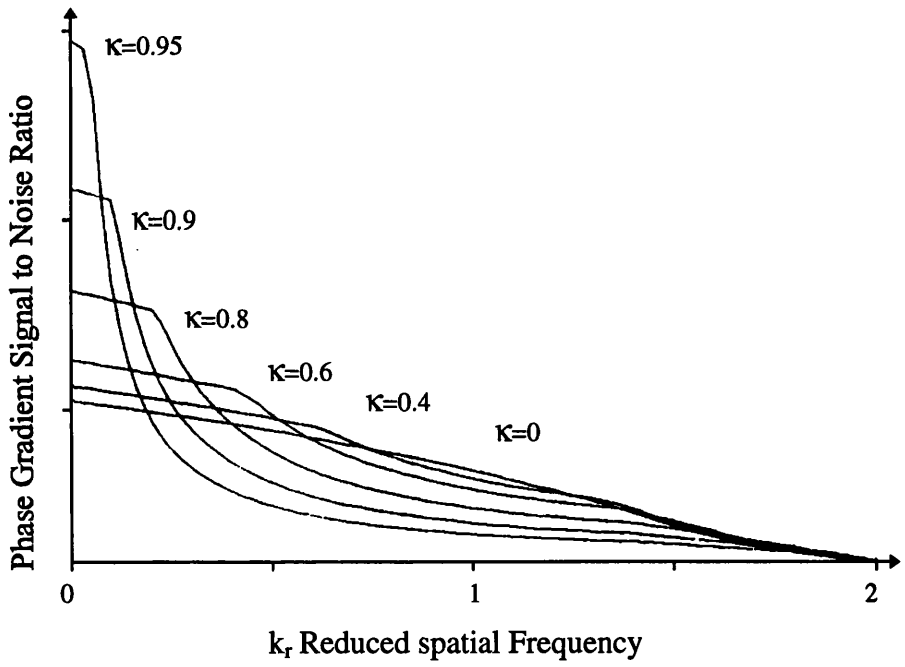

Fig.2.11 ***Variation of phase gradient signal to noise ratio with reduced spatial frequency for different values of κ. κ=0 no hole ie using all eight segments of the MDPC detector [Chapman et al 1990].***

Fig.2.11 shows that as κ is increased, the high frequency contribution to the transfer function is suppressed and the signal to noise ratio is enhanced at values of κ close to

one. A value of κ=1 denotes that the bright field cone is equal in size to the inner quadrant. The optimum value was found to be at $\kappa > 0.8$ [Chapman et al 1991].

2.4.4 Resolution in MDPC.

In all electron microscopes there are limitations imposed on the resolution due to imperfections in the electron optics. The source in the gun has a finite size and is not point like as has been assumed, the lenses in the system suffer from spherical and chromatic aberrations, diffraction and astigmatism; all of which contribute to the final image characteristics. The imaging imperfections cause the scanned probe incident on both the specimen to be broadened in size and to vary in current density across the probe.

The beam from the gun is forced to cross over by the gun lens which demagnifies the source leaving the gun. In the absence of lens aberrations a circular area of approximately uniform current density and diameter d_0 can be defined. The current density is uniform over its cross sectional area which is of diameter d_o. This is then expanded into a circle of least confusion following a path through the electron optics of the EM . The main contributors to the imperfections arise from spherical and chromatic aberrations, diffraction and astigmatism which are discussed below.

1) Spherical Aberration

Spherical aberration is an effect which shortens the focal length of the lens for off axis beams as the outer regions of the lens have a stronger focusing effect. This can be expressed as:

$$d_s = \tfrac{1}{2} C_s \alpha^3 \qquad (2.17)$$

where d_s is the diameter of least confusion due to spherical aberration, C_s is the spherical aberration coefficient and α is the probe semi angle defined by the radius of the probe forming aperture and the focal length of the probe forming lens.

2) Chromatic Aberration

Chromatic aberration results from the spread in initial energies of the electrons leaving the gun. There is a variation in the focal length of the lens with the variation in electron energy. This is expressed as:

$$d_c = C_c \alpha \frac{\delta E}{E} \qquad (2.19)$$

where d_c is the diameter of least confusion due to chromatic aberration, C_c is the chromatic aberration coefficient, E is the mean energy of the incident electrons and δE is the energy spread in electron energies. All other quantities are as previously defined.

3) Diffraction

Further beam broadening can occur due to diffraction of the electron beam by the finite size of the probe forming aperture. This is expressed as:

$$d_d = \frac{0.61\lambda}{\alpha} \qquad (2.20)$$

where d_d is the diameter of least confusion due to diffraction and λ is the de Broglie wavelength of the electron beam.

4) Astigamtism

Astigmatism in an electron lens can result from an absence of perfect symmetry about the optic axis and from inhomogeneties in the magnetic materials used resulting in a variation of the lens strength. The effect can be corrected using a quadrupole arrangement to counteract this difference in focusing and thus remove the astigmatism in the image. In a real system a large amount of the astigmatism can be removed.

The values can be used to estimate the final diameter of the disc of least confusion by summing in quadrature:

$$d^2 = d_o^2 + d_s^2 + d_c^2 + d_d^2 \qquad (2.21)$$

The MDPC system using the Lorentz lens system as the probe forming lens is expected to give a resolution better than 5nm [Chapman 1993].

2.5 ENERGY DISPERSIVE X-RAY ANALYSIS

X-rays are produced when the electrons in the beam are inelastically scattered when passing through the specimen. X-rays are produced by two main interactions, Bremsstrahlung or by inner-shell ionisation processes giving continuous and discrete X-ray spectra respectively. The inner shell ionisation processes produce sharply defined peaks in the X-ray spectra corresponding to the differences between various energy levels in the atoms of the specimen. Each element has a characteristic set of energy levels and through identification and comparisons of the relative sizes of each peak present, estimates can be made of the composition of the sample. Further more in-depth analysis of X-ray data will be given in section 3.4 of chapter 3 .

Here a JEOL 1200 CTEM and a VG HB5 STEM were used; essentially both systems use the same detection system. A Link Analytical SiLi detector was used in both systems.

CHAPTER 2 REFERENCES

Y. Aharonov and D. Bohm, ***Phys. Rev.***, Vol. 115, pp. 485-491, 1959.

F. Bitter, ***Phys. Rev.***, vol. 38, pp. 1903, 1931.

J. N. Chapman, E. M. Waddell, P. E. Batson and R. P. Ferrier, ***Ultramicroscopy*** **4**, pp. 283, 1979.

J. N. Chapman, "The Investigation of Magnetic Domain Structures in Thin Foils by Electron Microscopy", ***J. Phys. D: Appl. Phys.,*** vol. 17, pp. 623-647, 1984

J. N. Chapman, S. McVitie and S. J. Hefferman, ***J. Appl. Phys.,*** vol. 69, pp. 6078, 1991.

J. N. Chapman, I. R. McFadyen and S. McVitie, "Modified Differential Phase Contrast Lorentz Microscopy for Improved Imaging of Magnetic Structures", ***IEEE Trans. Mag.,*** Vol. MAG 26, No.5, 1990.

J. N. Chapman, R. P. Ferrier and B. Bormans, "Microscopy of Magnetic Materials using an Optimised FEG CTEM/STEM Instrument", ***Proc. AMMSA***, vol.51, pp. 1030-1031, 1993.

N. H. Dekkers and H. de Lang, ***Optik***, Vol. 41, pp. 452-456, 1974.

N. H. Dekkers and H. de Lang, "A Detection Method for Producing Phase and Amplitude Images Simultaneously in a Scanning Transmission Electron Microscope", ***Philips Technical Review***, Vol. 37, no.1, 1977.

D. M. Donnet, PhD thesis, University of Glasgow, 1992.

J. I. Goldstein et al, "Scanning Electron Microscopy and Xray Microanalysis", ***Plenum Press***, Second Edition 1992.

P. J. Grundy and G. A. Jones, "Electron Microscopy in the Study of Materials", ***Edward Arnold Press***, 1976.

P. W. Hawkes, "Electron Optics and Electron Microscopy", ***Taylor and Francis Press Ltd***, 1972

P. B. Hirsch, A. Howie, R. B. Nicholson, D. W. Pashley and M. J. Whelan, "Electron Microscopy of Thin Crystals", ***Butterworths***, revised edition, 1967.

I. R. McFadyen, PhD thesis, University of Glasgow, 1986.

I. R. McFadyen and J. N. Chapman, "Electron Microscopy of Magnetic Materials", ***EMSA Bulletin***, 22:2, May 1992

G. Morrison, PhD thesis, University of Glasgow, 1981.

P. M. Mul, B. J. M. Bormans and L. Schaap, "Design of a Field Emission Gun for the Philips CM20/STEM Microscope", ***Proc. Inter. Cong. for EM***, pp. 100-101, 1990.

C. W. Oatley, "The Scanning Electron Microscope", part 1; The Instrument, ***Cambridge University Press***, 1972.

R. Plöβl, PhD thesis, University of Regensberg and University of Glasgow, 1993.

D. Rogers, PhD thesis, University of Glasgow, 1990.

CHAPTER 3

SPECIMEN PREPARATION AND COMPOSITIONAL ANALYSIS

3.1 INTRODUCTION

The subject of this chapter is the fabrication of hard disk media and the processes involved in creating TEM specimens. Magnetic analysis is performed using planar specimens, compositional and structural analysis is obtained using both planar and cross-sectional specimens. Separate preparation techniques for planar and cross sectional samples are outlined in this chapter. An X-ray analysis technique is also discussed using cross-sectional specimens to allow the determination of the 'as deposited' magnetic layer composition of the samples. With this verification of the magnetic layer composition it is then possible to use this information to monitor the composition of the planar samples during the various processing stages to specimen completion.

3.2 FABRICATION OF A HARD DISK

A magnetic recording hard disk is typically composed of four layers deposited onto a non magnetic substrate as in Fig.3.1. Each layer has an important role to play in the overall performance of the hard disk and will be discussed individually in order of deposition.

The substrates used in this thesis are 950μm thick and 3″ in diameter, the bulk of which consists of a non-magnetic alloy providing a rigid platform for the magnetic and non-magnetic layers. The substrate is generally made of an aluminium manganese (4-5% Mn) alloy which is used for its rigidity, low density and low cost. The surface of the disk has to be extremely smooth as any defects in the substrate surface will be replicated throughout the upper layers and can produce missing or extra readback pulses. For this reason the surface of the AlMg disk is uniformly diamond polished and textured to

minimise topographic defects. The only drawback with the AlMg alloy is that it is too soft to withstand even moderate head to media impact [Arnoldussen 1987]. To increase the substrate hardness the surface of the disk is electroless-plated with a layer of Nickel Phosphor (NiP). This amorphous NiP layer is typically 10-25μm thick and is made non-magnetic

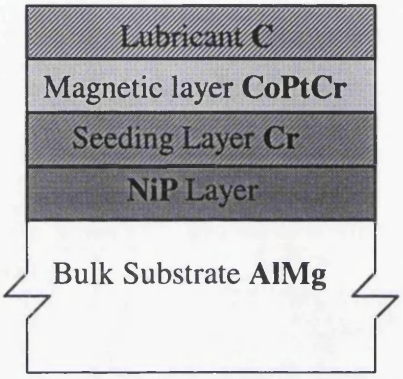

Fig.3.1 Schematic of Multilayered hard disk deposition structure.

through careful choice of phosphor composition, generally in the range 8-12 at %. This layer can be made extremely hard and can be used to smooth out any topographic defects in the surface of the AlMg disk. Abrasive polishing and texturing of the NiP layer produces a finished surface of 50-100Å RMS across ridges [K. E. Johnson 1992]. The texturing is used to prevent head stiction during recording or playback as this will result in media damage. In anisotropic media circumferential texturing is also used to provide the desired circumferential easy axis. In the isotropic media considered here the texturing is random to reduce or remove this effect. The lower fly heights less than 100nm demanded by near contact recording tend towards the use of smooth substrates. In this case during spin up and spin down of the disk the head is positioned above a small area at the inner radius which is deliberately textured to prevent stiction.

A Cr seed underlayer is deposited on the AlMg/NiP textured disk. This underlayer promotes the columnar growth of the next successive layer with the preference that the c axis of the underlayer lies in the plane of the film for longitudinal media. The seed layer has a considerable effect on the properties of the magnetic layer such as the coercivity which has been observed to increase with increasing Cr thickness [Davel and Randet

1970]. The Cr seed layer also influences the size and uniformity of the grains of the magnetic layer, parameters which are of considerable importance in the noise performance of the media [P. I. Mayo et al 1991].

The magnetic layer is a continuous thin film layer that is sputter deposited on the Cr seed layer; the magnetic information will be encoded in the magnetic layer. In all the media considered here the magnetic layer is composed of a ternary Co alloy, CoPtCr. This layer is predominately the ferromagnetic element Co accounting for ~70-80 at %. The other components in the alloy enhance the desired magnetic properties and the stability of the magnetic layer. The Pt is added substitutionally and has the effect of increasing the coercivity by introducing stress into the lattice of the thin film [K. E. Johnson 1992]. Pure Co has an H_c ~10Oe [Chikazumi 1964] whereas with Pt added, H_c can reach values up to ~2000Oe. The Cr in the magnetic layer composition is used to prevent corrosion of the magnetic layer thus increasing its long-term stability.

3.3 SPECIMEN PREPARATION: PLANAR SAMPLES

To allow any (S)TEM study, the specimens must be electron transparent and this places a maximum thickness on suitable specimens. This upper limit on thickness varies with specimen density but generally ~100nm is the maximum allowed thickness for a 200kV (S)TEM and for a material of ~8kgm^{-3}. As the hard disks to be investigated here are of the order of 950μm thick, various processing stages must be performed to produce (S)TEM samples. Planar samples have been fabricated from hard disk media deposited on standard AlMg and silicon substrates, using separate but similar techniques. These preparation methods are the subject of the next two sections.

3.3.1 AlMg Substrates

Planar samples are primarily desired for magnetic imaging and for this reason throughout the preparation technique it is of prime importance to ensure that the integrity of the magnetic layer has been maintained [F. J. Martin 1992]. The preparation technique aims to remove the bulk layers below the magnetic layer as in Fig.3.1.

The first stage in preparation is to remove the AlMg substrate. The disk is fixed to a textured aluminium mounting disk using thermal setting glue with the recording surface in contact with the mounting disk. This allows the hard disk substrate to be turned on a lathed down to a more manageable thickness. Care must be taken not to overheat the disk as the glue can degrade resulting in mechanical damage of the disk surface. The disk is turned to a thickness of approximately 400-500μm and removed from the mounting disk. To remove completely the remaining AlMg substrate the disk is floated on a boiling solution of dilute (50%) HCl taking approximately 5 minutes to etch fully. Adhesive tape is placed on top of the magnetic surface for protection as the acid solution can leech into the magnetic layer. The adhesive tape can be dissolved in a solution of chloroform leaving the magnetic layer clean and intact. The next stage is to remove the NiP layer. This layer is removed by floatation on a solution of concentrated Nitric acid at room temperature. The etch is complete when the dull NiP surface changes to 'silver' when viewed from below; this takes between 4 to 6 hours. The sample is then floated on a dilute solution of NaOH to neutralise any remaining acid and finally floated on water. The sample is then mounted on a folding gold microscope specimen grid.

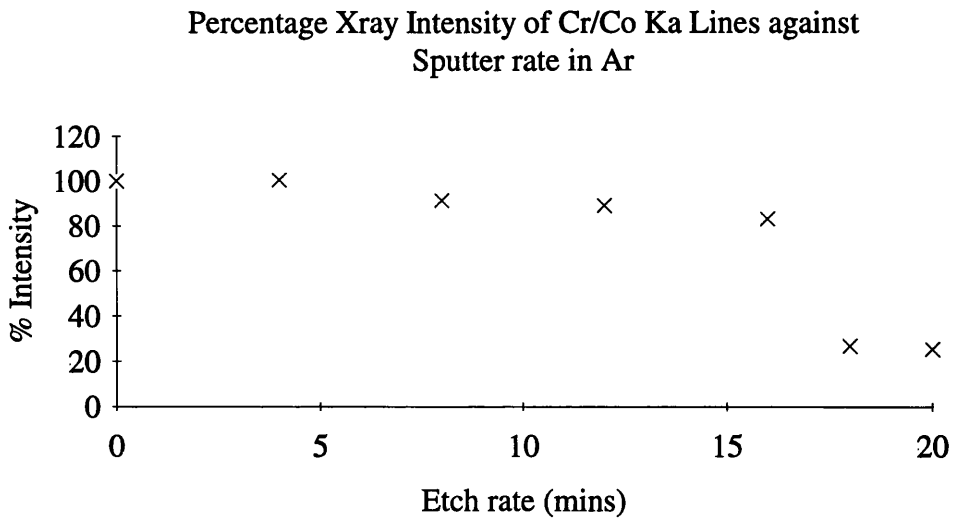

Fig.3.2 Graph of sputter etch rate in Ar.

At this stage the samples are electron transparent being just below the nominal maximum thickness of 100nm at 200kV. At this thickness the magnetic information is still masked by non-magnetic scattering arising principally from the Cr substrate. For

this reason a method of removing the now redundant Cr seed layer was sought to reduce the overall sample thickness. As Cr is used in photolithography masks, methods of wet Cr etch do exist. Cr masks are etched in a solution of ammonium cerric nitrate, glacial acetic acid and [find out what this means] R.O. water. When floated on this solution the hard disk samples do etch but the rate is extremely rapid and totally uncontrollable. The magnetic layer in the samples is completely leeched out following the etch leaving no tracks. A Freon-12 plasma etch had been reported by B. Spangenberg et al [1986] and a similar C_2F_6 plasma etch was observed to etch Cr masks. Again this method was too uncontrollable for the sample thickness being considered here. Sputtering in argon proved to be the most controllable method of seed layer removal. Fig.3.2 shows a graph of etch rate in argon. The previous etches are believed to have all been impeded by the formation of an oxide layer of the order of 5nm in thickness. This is removed after 16 minutes corresponding to the large change in the graph in Fig.3.2. Table 3.1 shows the entire preparation process. The final specimens now consist of the magnetic layer and the carbon lubricant and are approximately 30-50nm thick.

method of removal	layer removed	duration
1. lathe	500μm of AlMg	30 minutes
2. boiling HCl	remaining 450μm of AlMg	5 minutes
3. room temperature Nitric acid	10μm NiP	4-6 hours
4. Ar sputtering	Cr seed layer	15-20 minutes (see Fig.3.2)

Table 3.1 Table of stages of specimen preparation, layer removed and expected duration.

3.3.2 Silicon Substrates

As an alternative approach, recording media were deposited on 950μm thick silicon wafers with a ~400Å layer of Si_3N_4 deposited prior to media sputtering. The disk

structure shown in Fig.3.1 is similar to that of the silicon substrate samples the difference being the replacement of the NiP layer with the Si_3N_4 layer and the addition of a protective Si_3N_4 layer on the carbon surface. All other layers were deposited under the same conditions as for the AlMg substrate samples by the IBM corporation. Techniques exist for the use of self supporting $200\times200\mu m^2$ Si_3N_4 membranes made using conventional silicon processing techniques as TEM samples [J. W. M. Jacobs 1986] [M. W. Cole 1991]. The fabrication of specimens involves the use of photolithographic techniques with several complex processing and deposition stages finishing with a concentrated NaOH total immersion wet etch. Etching continues until the Si_3N_4 layer under the magnetic layer has been reached and the etch terminates. This should eliminate leeching of the magnetic layer as found in some AlMg samples. This method proved time consuming and unreliable due to pinholing in the Si_3N_4 protective layers allowing etching through to the magnetic layer surface. The etch is also extremely vigorous and this can damage the samples during the etch. A considerably simpler and more efficient processing method was to isolate $2\times2mm^2$ samples by scribing and then breaking the substrate. The individual samples are then float etched on concentrated NaOH heated to 70°C. Electron transparency is achieved when the sample glows red when lit from below. The samples are then placed on grids as before. These samples are particularly fragile and over-etching into the magnetic layers through any pinholes is still possible, thus careful observation of the minimum etch period is necessary.

3.4.3 SPECIMEN PREPARATION: CROSS-SECTIONAL SAMPLES

Details of the permitted tolerances in magnetic layer compositions and the thicknesses of all the layers deposited were supplied with the disks. In the preparation technique described above it is essential to be able to monitor the magnetic layer composition and compare with the information provided.

Compositional analysis can be performed using EDX analysis as mentioned in section 2.6. To determine the 'as deposited' magnetic layer composition a cross sectional sample must be used as both the magnetic and the seed layers contain Cr making determination of the Cr composition in the magnetic layer alone very difficult with a

planar sample. Using a cross-sectional specimen also allows the thicknesses of the deposited layers to be determined using high resolution TEM imaging. The preparation technique follows closely the method of cross-section fabrication developed by C. Scott [1993] for TiN/Ti multilayers deposited on silicon substrates.

A sample of hard disk ~2.5mm wide and ~25mm long is cut using a Buehler "Isomet" low speed circular saw. Cutting is performed without any cutting weight on the saw as the hard disk is soft and will easily bend when cut to this thickness. The strip is then cut into two parts ~12.5mm in length and attached with heated beeswax to a glass slide with the magnetic layer side down. The layers are thinned using a hand grinder to a thickness of ~250μm. This is the required total thickness of the two strips which are to be sandwiched in a ~440μm slot in a molybdenum rod as discussed later. The sections are required to be of the same length and width to ensure a tight fit in the slot and to allow the sections cut to be normal to the deposited layers. A stainless steel jig as in Fig. 3.3, is

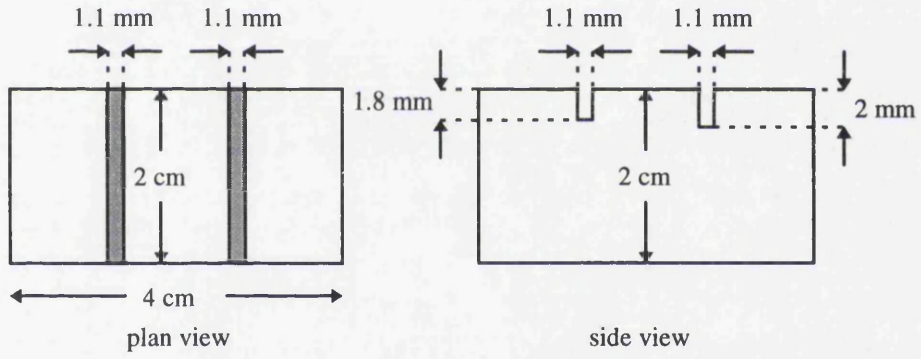

Fig.3.3 Diagram of stainless steel grinding jig.

used in conjunction with a handgrinder to shape the samples. The sections are placed face to face in the deeper of the two slots in the jig held with beeswax leaving part of the sample protruding from the top surface of the jig. Care is taken to ensure the sections are normal to the jig surface. The samples are then ground until the surface of the jig is met. The samples are then removed and replaced in the second slot with the untouched edge facing up and are ground as before. The ends of the sections are squared off by placing the sample allowing one end at a time to protrude over the edge of the jig and grind as before. The two samples are now the same shape of ~1.8mm by ~12mm and the ends

are square. Following this the samples are removed and cleaned using a reflux condenser with "Inhibisol" as the degreasant. The samples are to be sandwiched in a slot cut in a molybdenum rod. The slot is cut using a 375μm (0.015″) thick diamond blade. The sections are then fixed in the slot in the rod using "5minute Epoxy" resin. The whole sandwich is then pushed and glued into a brass rod with an inner diameter comparable to the molybdenum rod and an outer diameter of 3mm as in Fig.3.4. The brass rod provides an amount of compression forcing the two magnetic layers into the close contact required in later processing stages. The sample is then left to cure overnight. The disk shaped samples ~300μm thick are then cut from the rod using a 300μm diamond blade. The cut samples are then fixed using beeswax to a glass slide and are thinned to a thickness of ~150-200μm and polished on both sides using 3μm diamond paste on a felt lapping cloth rotating at

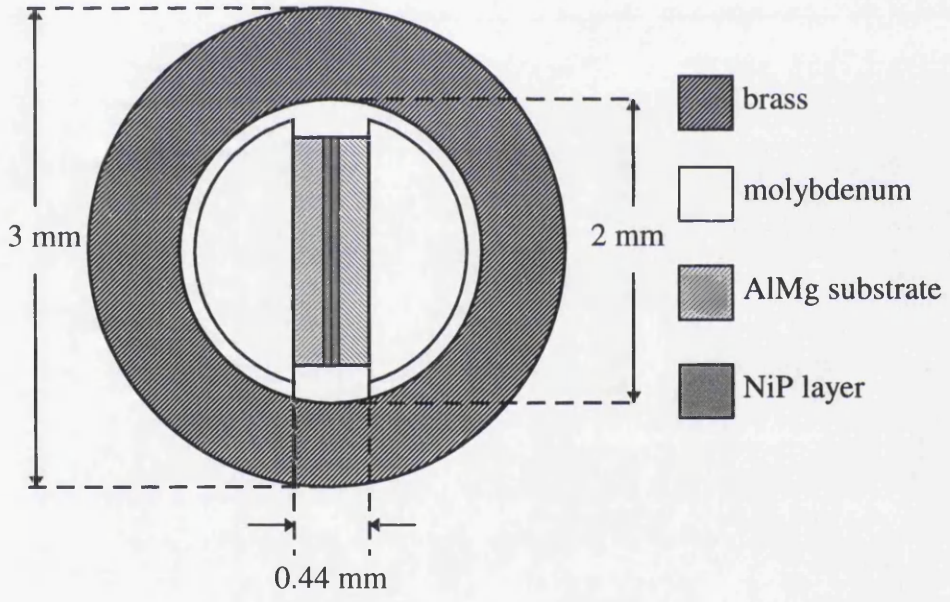

Fig.3.4 Diagram of disk cut from molybdenum/brass rod.

500rpm. A smooth sample then is selected from those cut and fixed to a stub using a small amount of beeswax. This is now mounted in a Gatan dimple grinder, a phosphor - bronze spherical section grinding wheel with coarse paste is used to dimple the centre of the sample. Normally 3μm diamond paste is used but the AlMg substrate is considerably softer than the grinding wheel and as a result using diamond paste tends to grind the

wheel instead of the specimen. Cubic boron nitride paste was found to be a suitable alternative and prevented wheel damage. Initially one side is dimpled to ~100μm depth. The sample is then removed from the stub, refitted dimpled side down and dimpled to a depth of ~40-90μm which is now from the opposite side leaving the central region of the sample <10μm thick. Further thinning can be performed but due to the vibration during dimpling this can ruin the sample.

The next stage in cross section preparation is to ion mill the sample from both sides until the sample is electron transparent. A Gatan 600 series duomill is used for this purpose. The optimum thinning conditions were found to be 0.5mA and 4kV per gun and ion incidence angle of 12-15°. To ensure that the majority of thinning time is spent perpendicular to the magnetic layer interface the sample is rotated at 2rpm over two 80° sectors aligned at right angles to the section and 10rpm everywhere else. A laser is used to terminate thinning at the point where a hole has just begun to form. This occurs after approximately 8 hours. Due to preferential etching this is not the point at which the sample is electron transparent in the region of interest. Fig.3.5 shows a diagram of a sample stopped at this stage. Due to the NiP layer being considerably harder than the AlMg layer the NiP layer remains relatively thick after this length of time whereas the AlMg has formed a large hole. Thinning should continue in 30-40minute stages checking the sample in a TEM after each stage until the NiP layer is sufficiently thin.

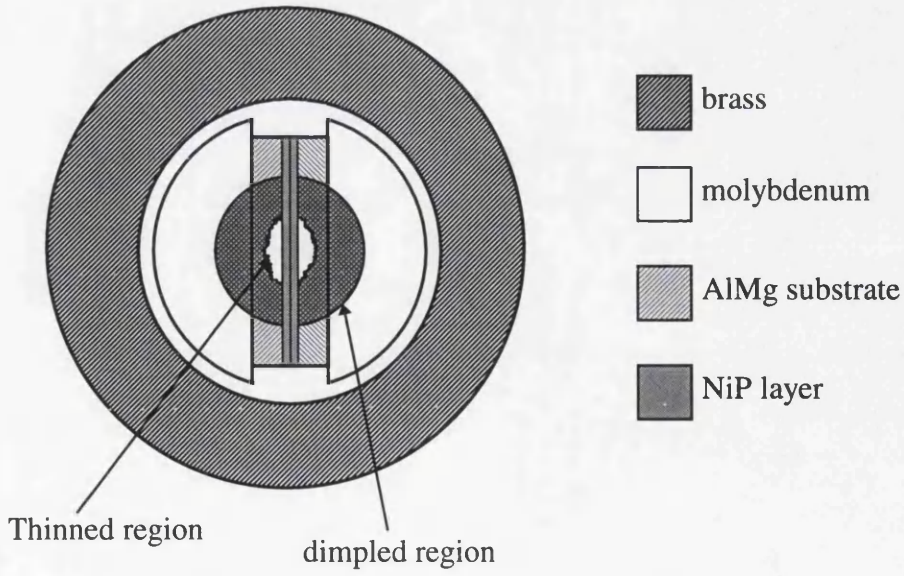

Fig.3.5 ***Diagram showing preferential thinning of disk after completion of ion beam thinning.***

3.5 EDX COMPOSITIONAL ANALYSIS

A valuable tool available in (S)TEM is energy dispersive X-ray analysis (EDX) allowing the relative composition of the sample to be investigated. X-ray production mechanisms in (S)TEM fall into two separate categories when electrons are incident on a specimen. These are Bremsstrahlung continuum X-ray processes and inner-shell ionisation processes giving rise to characteristic X-rays.

3.5.1 Continuum X-ray Production

When an electron beam passes through a specimen it can be decelerated by interaction with the Coulombic field produced by the atoms in the material. This deceleration causes the electrons to bend away from their original path. The energy of the exiting electrons is reduced by the bending and electromagnetic radiation is emitted. An incident electron can lose any amount of energy from zero to the maximum kinetic energy of the electron. Thus the energy of the electromagnetic radiation can take values across the full range of energies available. The maximum energy attained in this electromagnetic spectrum is an exact measure of the incident electron energy. This continuum produces a background component of X-ray Bremsstrahlung radiation over the whole region of interest (3-20keV). For our studies the continuum is an unwanted component of the spectrum and a method will be outlined in section 3.5.4 to remove its effect.

3.5.2 Inner Shell Ionisation X-ray Production

The inner shell ionisation process has the greatest importance in EDX analysis since this results in the generation of characteristic X-ray lines identifiable with specific elements. An incident electron can interact and eject a tightly bound inner shell electron which leaves the atom in an excited state. The atom can relax to its ground state through

allowed transitions from outer shells to fill the inner shell vacancy. The relaxation releases energy and generates a photon of a distinct energy due to the sharply defined energy levels in the atom. Two processes can occur before the photon leaves the atom. The Auger process transmits the energy from the inner shell photon to an outer shell electron which is then ejected from the atom and is known as an Auger electron. In the characteristic X-ray process the energy difference is emitted as an X-ray photon of defined energy which then leaves the atom without further interaction. The balance between Auger electron and X-ray generation is governed by the Auger and the fluorescence yields a and ω respectively. Such that:

$$\omega + a = 1 \qquad (3.1)$$

Typically low atomic numbers favour the Auger process e.g. $\omega_{carbon} \sim 0.005$ whereas for high atomic numbers X-ray process is favoured e.g. $\omega_{germanium} \sim 0.5$.

For our EDX analysis we are interested only in the characteristic X-ray production process as this can produce compositional information through characteristic X-rays which are unique to each element. Fig.3.6 shows an energy level diagram for a general atom depicting some of the possible relaxation routes which result in X-ray production. As a result of the Pauli Exclusion Principle, each shell contains a spread of energies; except for n = 1. This has been neglected from Fig.3.6 as the energy spread is narrow in comparison with the energies of the shells. If a K shell electron is removed the vacancy can be filled by an electron relaxing from the L shell resulting in the K_α line. Alternatively, an electron from the M shell can fill the K shell vacancy resulting in the K_β line. Generally the next higher energy shell has the greatest probability of filling the vacancy and hence it would be expected that K_α line would be the most intense. Similarly for an L shell vacancy.

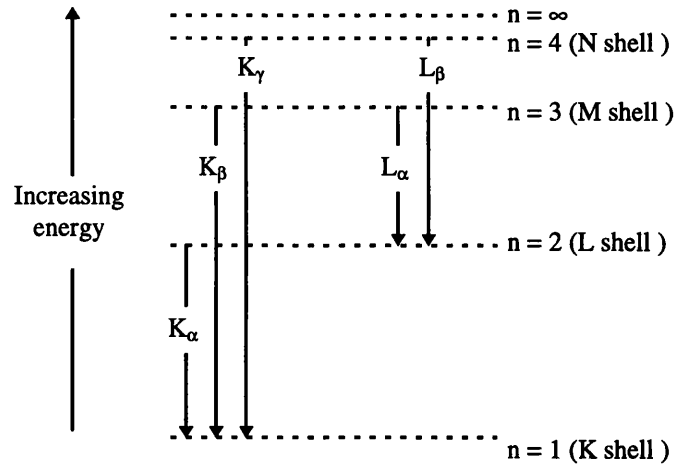

Fig.3.6 ***Energy level diagram showing the main transitions in the de-excitation of an atom.***

The X-ray intensity resulting from an atom of a particular element is discussed in the next section.

3.5.3 A Method of Compositional Determination

Elemental composition can be determined by EDX analysis using the ratio technique developed by Cliff and Lorimer [1975] for thin samples. A thin sample is defined to be of a thickness such that electrons can pass through without loosing an appreciable amount of energy and that a single electron is most likely to excite only one photon in its passage through the sample. The basis for the technique is that the concentration ratio of two elements in a sample is related to the ratio of the number of counts in the characteristic X-ray lines of each element. Through comparison of the respective characteristic X-ray peaks for each element a relative composition for the specimen can be made. The Cliff-Lorimer equation for the atomic ratio of two elements x and y in a specimen is given by:

$$\frac{P_x}{P_y} = \frac{C_x \varepsilon(h\nu)_x s_x \omega_x \sigma_{ix}}{C_y \varepsilon(h\nu)_y s_y \omega_y \sigma_{iy}} = \frac{C_x}{C_y} k_{xy} \qquad (3.2)$$

Where P_x is the number of characteristic X-rays under the peak, C_x is the concentration of the element in atomic percent, ε is the detector efficiency taken as 100% in the range of energies to be used here, s_x is the partition function, ω_x is the fluorescence yield and σ_{ix} is the ionisation cross-section in barns (1barn $\equiv 10^{-24}cm^2$) for the characteristic line of element x. The partition function, the fluorescence yield and the ionisation cross-section combine to give the probability of exciting a specific transition in an element. The partition function determines the relative intensities of the lines in a sub-shell and the fluorescence yield determines the balance between Auger and X-ray processes as described above. The ionisation cross-section initially derived by Bethe (1930) can be stated as [Nicholson 1994]:

$$\sigma_{ij} = 2N_j\pi e^4 b_j \ln\left(\frac{c_j T_o}{I_{ij}}\right)\Big/ T_o I_{ij} \qquad (3.3)$$

Where N_j is the sub-shell electron occupancy, T_o is the electron energy taken as eV where V is the accelerating voltage, I_{ij} is the ionisation energy for sub-shell j of the i^{th} shell and b_j and c_j are called the Bethe parameters. These parameters are determined by fitting equation 3.3 to experimental data measured over a range of overvoltage U_{ij} defined as T_o/T_{ij}. There is significant discussion upon the values of the Bethe parameters [C. J. Powell 1990] the values used here are given in table 3.2 are taken from the analysis given by J. H Paterson et al 1989. The analysis here will be a comparison between the characteristic lines of Co, Cr and Pt. The K shell ionisation energies fall within the detector limits of~3-20keV for Cr and Co with ionisation cross-sections of

Shell (4<U<25)	b_j	c_j
K	0.62	0.9
L	0.89	0.5

Table 3.2 Values of non-relativistic Bethe parameters for K and L shells [from J. H. Paterson et al 1989 and J. I. Goldstein et al 1992]

370 and 261 barns respectively. For Pt the critical ionisation energy at 78.39keV lies outwith the detector range. However the PtL ionisation energies lie within the range and hence the total L production characteristic lines will be used in the analysis. Equation (3.3) applies to both the K and L shells but in the L shell an effective fluorescence yield, ν is used in place of ω as there is the possibility of radiationless Coster-Kronig transitions between the three sub-shells in the L-shell. The effective fluorescence yields are given by:

$$\nu_1 = \omega_{L1} + \omega_{L2}f_{12} + \omega_{L3}(f_{13} + f_{12}f_{23}) \qquad (3.4a)$$

$$\nu_2 = \omega_{L2} + \omega_{L3}f_{23} \qquad (3.4b)$$

$$\nu_3 = \omega_{L3} \qquad (3.4c)$$

and hence the L_{ij} production cross-section is given by:

$$\sigma_{cLi} = \sigma_{Li}\nu_i \qquad (3.5)$$

where σ_{cLi} is the characteristic cross-section, σ_{Li} is the ionisation cross-section and ν_I is the effective fluorescence yield. Platinum emits a large number of characteristic X-ray lines but only three are sufficiently intense to be of interest for this analysis. The three lines are Lα1, Lβ1 and Lβ2.

characteristic line	transition	ionisation cross-section
Lα1	$M_5 \rightarrow L_3$	σ_{L3}
Lβ1	$M_4 \rightarrow L_2$	σ_{L2}
Lβ2	$N_5 \rightarrow L_3$	σ_{L3}

Table 3.3 Platinum L lines and their transitions.

The values of the ionisation cross-sections $\sigma(Pt)_{L2}$ and $\sigma(Pt)_{L3}$ are 117 and 298 barns before correction for radiationless transitions. Using equations 3.4b and 3.4c with

values from Krause [1979] giving final corrected values for $\sigma(Pt)_{L2}$ and $\sigma(Pt)_{L3}$ 42 and 91 bans respectively. It should be noted that the L shell ionisation cross sections are difficult to measure and hence these results may vary from other authors. The total L shell production cross-section $\sigma(Pt)_L$ is equal to 224 barns. Thus from equation (3.2):

$$\frac{C_{Cr}}{C_{Co}} = 0.95\frac{P_{Cr}}{P_{Co}} \qquad (3.6a)$$

$$\frac{C_{Pt}}{C_{Co}} = 0.58\frac{P_{Pt}}{P_{Co}} \qquad (3.6b)$$

where the parameters are defined above. Equations 3.6a and 3.6b allow the composition in atomic percent of the CoPtCr samples to be calculated.

3.5.4 Background Subtraction

A simple method has been used throughout this analysis for subtracting the background continuum X-rays present in all spectra. The subtraction method estimates the background component under the peak of interest by taking windows in the spectra either side of the peak. The average background under the peak can then be calculated using:

$$b_{peak} = \frac{bg_1/w_1 + bg_2/w_2}{2} \times w_{peak} \qquad (3.7)$$

Where bg_1 and bg_2 are the number of counts in the background channels, w_1, w_2 and w_{peak} are the widths of the background windows and the width of the peak as defined in Fig.3.7.

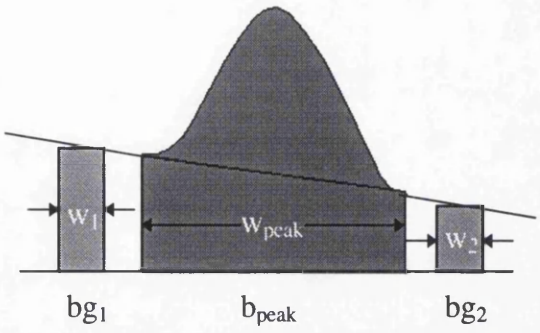

Fig.3.7 Schematic X-ray diagram of background subtraction technique.

3.6 CONCLUSION

The above sections have established methods of planar and cross-sectional (S)TEM specimen preparation from standard hard disks that will be used throughout this thesis. Also a technique has been outlined that allows the composition of the specimens to be analysed. The only drawback with this analysis technique is that the objective lens has to be used to form the probe on the specimen. This means that samples cannot be used for magnetic imaging following EDX characterisation.

CHAPTER 3 REFERENCES

T.C.Arnoldussen and E. Köster, Chapter 3, "Magnetic Recording Volume I: Technology",editors C. D. Mee and E. D Daniel, ***McGraw Hill press,*** pp. 174-241, 1987.

H. Bethe, ***Ann. Phys.,*** Vol. 5, pp. 325, 1930.

S. Chikazumi, "Physics of Magnetism", ***John Wiley and Sons Inc.***, 1964.

M. W. Cole and E. S. Zakar, "Rapid Plan View TEM Sample Preparation For Semiconductor Grain Size Analysis", ***J. Electron Microscopy Technique,*** Vol. 19, pp. 129-129, 1991.

J. Davel and D. Randet, "Electron Microscopy on High Coercive Force CoCr Composite Films", ***IEEE Trans. Magn.,*** MAG 6, pp. 768, 1970.

J. I Goldstein, D. E. Newbury, P. Echlin, D. C. Joy, A. D. Romig, Jr., C. E. Lyman, C. Fiori and E. Lifshin, "Scanning Electron Microscopy and X-ray Microanalysis", 2nd edition, ***Plenum Press***, 1992.

J. W. M. Jacobs and J. F. C. M. Verhoeven, "Specimen Preparation Techniques for High Resolution Transmission Electron Microscopy Studies on Model Supported Metal Catalysts", ***J. Microscopy***,Vol. 143, pp. 103-116, 1986.

K. E. Johnson, Chapter1, "Noise in Digital Magnetic Recording", Editors T. C. Arnoldussen and L. L. Nunnelley, ***World Scientific Press,*** pp. 7-64, 1992.

M. O. Krause, "Atomic Radiative and Radiationless Yields for K and L Shells", ***J. Phys. Chem. Ref. Data***, Vol. 8, No. 2, pp. 307-327, 1979.

F. J. Martin, PhD thesis, University of Glasgow, 1992.

P. I. Mayo, K. O'Grady, R.W. Chantrell, J. A. Cambridge, I. L. Sanders, T. Yogi and J. K. Howard, "Magnetic Measurement of Interaction Effects in CoNiCr and CoPtCr Thin Film Media", ***J. Magn. Magn. Mat.,*** vol. 95, pp. 109-117, 1991.

W. A. P. Nicholson, "Standardless Quantitiation of Thin Film Specimens", ***Mikrochimica Acta***, 114/115, pp. 53-70, 1994.

J. H. Paterson, J. N. Chapman, W. A. P. Nicholson and J. M. Titchmarsh, "Characteristic X-ray Production Cross-Section for Standardless Elemental Analysis in EDX", ***J. Microscopy***, Vol. 154, pp. 1-17, 1989.

C. J. Powell, "Inner Shell Ionisation Cross-Sections", ***Microbeam Analysis***, pp. 13-20, 1990

C. Scott, "TEM Cross-Section Preparation for Arc-Evaporated Films on Silicon Substrates", private communication, University of Glasgow, 1993.

B. Spangenberg, V. Orlinov, G. Danev, E. Spasova and J. Malinovski, "Reactive Ion Etching of Chromium Films using a Two-Layer Resist System of Ploymide and Evaporated Sliver Halide", ***Thin Solid Films***, Vol. 138, pp. 297-304, 1986.

CHAPTER 4

THE PHYSICAL AND BULK MAGNETIC PROPERTIES OF CoPtCr RECORDING MEDIA

4.1 INTRODUCTION

The measurement and analysis of the physical and magnetic microstructures of two types of hard disk media are the subject of the proceeding chapter. The media can be categorised by the method of playback which in this case is either inductive or magnetoresistive as outlined in section 1.6. Throughout this and subsequent chapters **inductive** media will be denoted as being of **type 1** and **magnetoresistive** media will be denoted as being of **type 2**. The study of these media is divided into two chapters. This chapter considers the bulk physical and magnetic characteristics for both types of media. The second chapter examines the magnetic microstructure of both types of media using the Lorentz imaging techniques outlined in chapter 2.

4.2 PHYSICAL CHARACTERISTICS

There are several TEM techniques which allow the investigation of the physical parameters of the media. The following sections cover the as deposited thin film thickness, the chemical composition and the grain size of media of both types.

4.2.1 Film thickness Verification

The thin film production process of sputter deposition produces variation in the layer thicknesses on the surface of the hard disk. High resolution TEM modes are used to accurately determine the as-deposited film thicknesses and the tolerances in that thickness. To allow such a study cross sectional samples are used of both media types manufactured using the technique described in section 3.4.3. This preparation method

ensures that the thin film layers are close to perpendicular to the electron beam when placed in the electron microscope allowing accurate thickness values to be obtained.

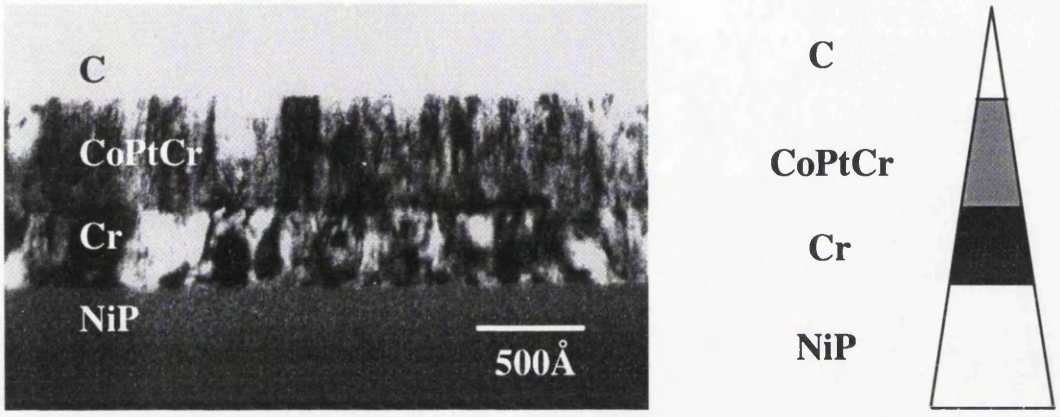

Fig.4.1 ***A high resolution TEM micrograph of type 1 media with a diagram of the side view of the cross section showing an approximate side view of the sample and the direction of ion etching.***

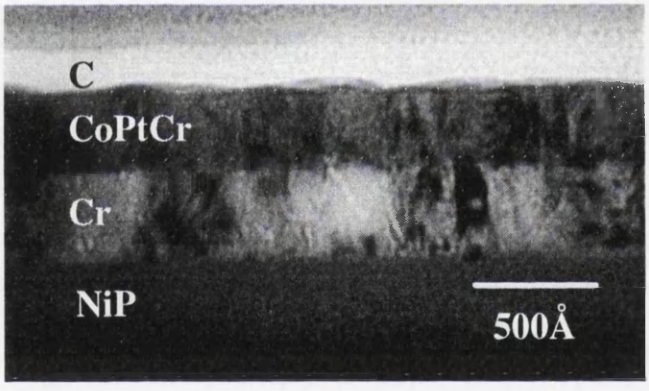

Fig.4.2 ***A high resolution TEM micrograph of type 2 media.***

Using cross sectional specimens created from both media, high resolution micrographs as in Figs.4.1 and 4.2 were produced. All the individual layers can be distinguished with the exception of the carbon overcoat which due to weak scattering and preferential etching shows up only in Fig.4.2. Fig.4.1 shows the approximate shape of the sample which tends to be thinned from the carbon edge. Several images are taken tilting the sample until the interface is clearly defined between layers to ensure the

correct sample orientation to the beam. The magnification was calibrated using a the structure of a cross grating; at these high magnifications the gratings are too large at ~0.46μm and internal features of the grating are used. The results for both media are given in table 4.1, the carbon thicknesses were determined from other images taken over shorter exposure intervals. Comparison with the actual values is not easy as only the range of possible thicknesses were given. The carbon overcoat has a range of 250-300Å and the Cr layer has a range of 200-800Å. No values for the magnetic layers were supplied. The carbon overcoat values determined from the micrographs are lower than the range quoted. This is as expected as the cross section preparation process tends to thin the samples from the carbon side gradually removing the layer. The measured value of the seed layer falls within these tolerances and with errors on the thicknesses of approximately 5% for both media types. The magnetic layer thicknesses are consistent with the values of remnant magnetisation×thickness product discussed in section 4.3.1. There is a very clear indication in both Figs. 4.1 and 4.2 of the columnar growth due to the Cr seed layer. Particularly in Fig.4.1 where the structure can be seen to continue from the seed layer through the magnetic layer as expected.

Media type	C	CoPtCr	Cr
1	125	550±5%	350±6%
2	85	255±5%	255±5%

Table 4.1 Thin film layer thicknesses in Å as determined from Figs. 4.1 and 4.2.

4.2.2 Chemical Composition

The chemical composition of the magnetic layer has a considerable effect on the properties of the hard disk. For this reason it is desirable to establish the as-deposited chemical composition. EDX analysis and the Cliff Lorimer ratio technique outlined in section 3.5.3 of chapter 3 form the basis for a method of compositional determination.

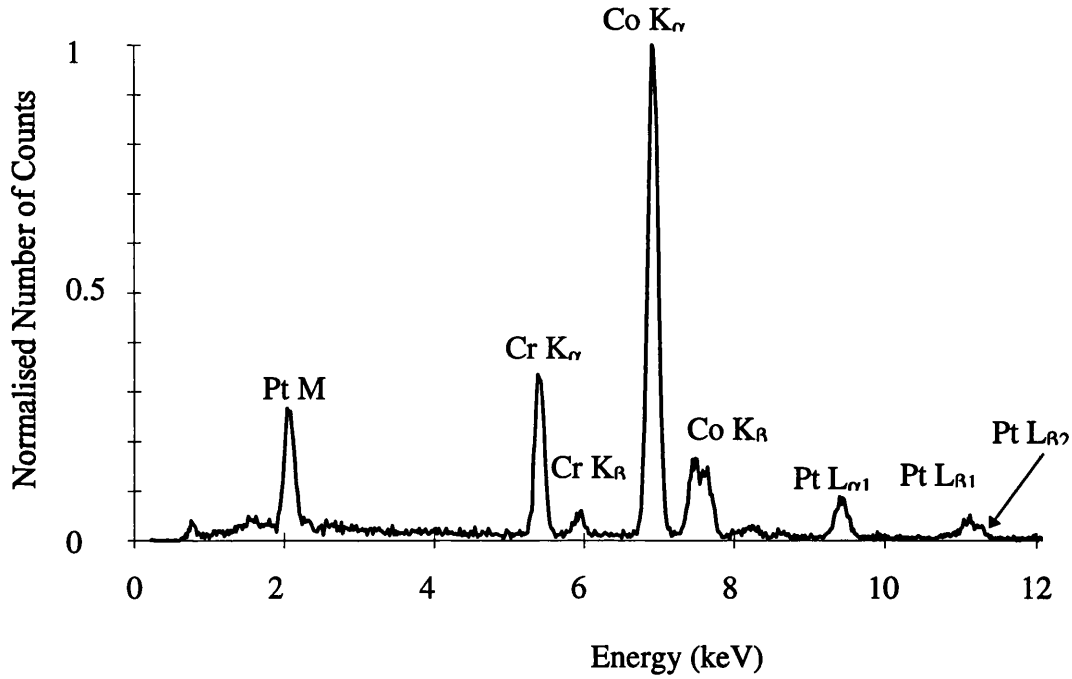

Fig.4.3 ***An example X-ray spectrum taken of the magnetic layer of a type 1 sample.***

The magnetic layer is a ternary alloy of Co, Pt and Cr. Here we are interested in the relative ratio of these elements in the magnetic layer of the media. Again cross-sectional samples are used here in attempt to remove the effect of the Cr seed layer on the EDX results as both this layer and the magnetic layer contain Cr. Fig.4.3 shows an example X-ray spectrum taken of the magnetic layer of a type 1 sample. The spectrum contains the K_α and K_β peaks of both Cr and Co in the centre of the detector range between 5 and 8KeV. The magnetic layer also includes Pt which has no K peaks in the detector range which can be used in the Cliff-Lorimer analysis. The spectrum does contain Pt L shell peaks in the detector range. As these L peaks are weak in comparison to the K_α and K_β peaks of Cr and Co the total L shell production is used in the method. This has two advantages the first being that this reduces the error determining the number of counts in in the L shell peak which is taken as the square root of the total number of characteristic X-rays under the peak which decreases with the increase in the amount of data collected. Secondly this eliminates the need to separate the two Pt L_β peaks simplifying the processing.

The results of the analysis are given in Table 4.2. The compositions quoted are all in atomic percent. In both cases there is an increased Cr composition in the Cliff-Lorimer result in comparison to the quoted values. This increase could be due to the beam spreading in the sample into the Cr seed layer adding to the overall Cr composition.

Type 1 media			
element	Co	Pt	Cr
target composition	75	12	13
sample	72.7±1.0	10.4±0.4	18.0±0.9
Type 2 media			
element	Co	Pt	Cr
target composition	73	7	20
sample	71.6±1.3	6.1±0.7	22.3±1.3

Table 4.2 ***Results of X-ray compositional analysis technique from type 1 and type 2 media.***

The largest drawback of this analysis technique is that due to the large beam convergence needed to form a probe to investigate the desired features, the electron microscope has to be used with an excited objective lens. Thus any magnetic information will be partially or totally erased from the samples after the analysis.

4.2.3 Grain Size

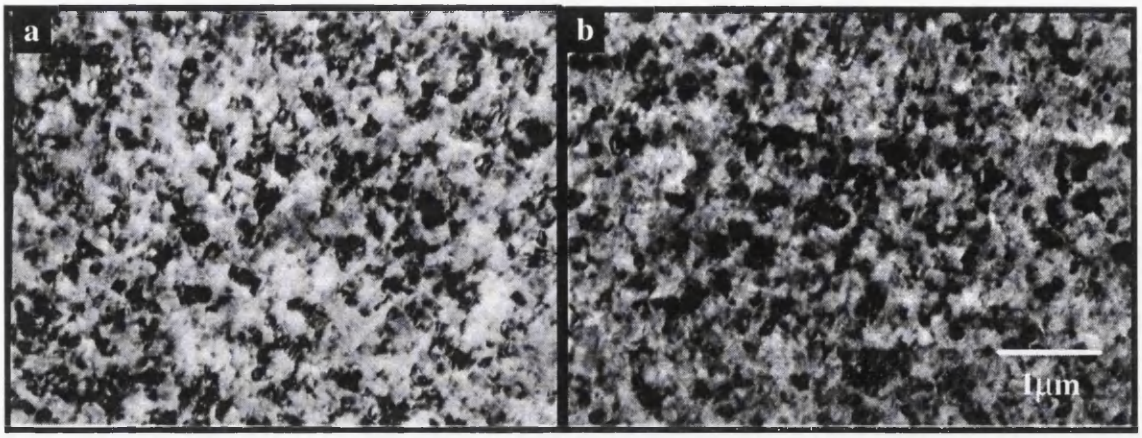

Fig.4.4 High magnification bright field images showing the crystallite structure of a) medium 1 and b) medium 2.

The thin film media being considered here consist of randomly oriented grains. Grains are assemblies of molecules acting as one physical unit. The magnetisation in a grain is assumed to be uniform throughout that grain. High magnification micrographs of media of type 1 and type 2 are shown in Figs.4.4a and b. The physical size of the grains of type 1 and type 2 media are very similar despite their different compositions. The average crystallite size of type 1 media is 17nm and the average crystallite size of type 2 media is 17 nm with standard deviations of 7.4 nm and 7.8 nm respectively. This granularity will effect the minimum magnetic particle size.

4.3 BULK MAGNETIC CHARACTERISTICS

Some of the bulk magnetic properties of the media can be determined by methods available to us. A TEM method known as low angle diffraction (LAD) is used to provide values of the remnant thickness product $M_r\delta$ where δ is the magnetic layer thickness.

For completeness it should be noted that the coercivities the media are 1800 and 1650 0e for medium 1 and medium2.

4.3.1 Low Angle Diffraction

As outlined in section 2.3.3 of chapter 2 the electron beam can also be deflected by the Lorentz interaction with the magnetic induction of the sample. This Lorentz deflection is of the order of only a few μrads which is a factor of 1000 smaller than that of the diffraction rings shown in Fig.4.6. The magnetic deflection spots are contained in the central diffraction spot and thus the camera length in Fig.4.6 is too short and the magnetic deflections become part of the central spot. In order to view the Lorentz deflections a considerably larger camera length has to be used such that splitting of the central spot can be observed. This Lorentz deflection is directly related to the integrated magnetic induction due to the sample through equation (4.1) where β is the Lorentz deflection angle, B is the magnetic induction due to the sample, h is Planck's constant taken as 6.626×10^{-34} Js and all other quantities are as previously defined.

$$\beta = \frac{eB\delta\lambda}{h} \quad (4.1)$$

Both sample types have values of $M_r\delta$ quoted of 2.5×10^{-3} and 1.1×10^{-3} in emu/cm^2. Using the values of δ determined in section 4.2.1 this gives the maximum magnetic induction B_{max} as 0.565T and 0.541T for media 1 and media 2 respectively. The resultant maximum deflections for these media are 18.8μrads and 8.3μrads for media 1 and media 2 respectively the difference being due to the variation in δ.

A LAD diffraction pattern of type 1 media is shown in Fig.4.7a and type two in Fig.4.17b at camera lengths of 475 and 949m respectively. A diffraction grating was used to calibrate the camera lengths in each case.

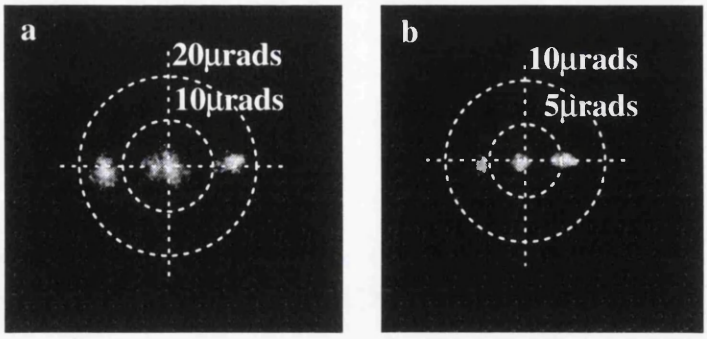

Fig.4.7 Low angle diffraction patterns of a) type1 and b) type 2 media.

Measurements taken from the LAD diffraction patterns of Fig.4.17 give 17.8μrads for the Lorentz deflection angle for type 1 and 5.87μrads for type 2. This is in close agreement with the predicted values using the TEM determined values of magnetic layer thicknesses of section 4.2.1.

4.4 CONCLUSIONS

In section one analysis has been made of both the physical and the bulk magnetic properties of media 1 and media 2. The thin film thicknesses measured were found to be within the tolerance limits of fabrication. The Cliff-Lorimer ratio technique was applied successfully using the total L production for the platinum lines due to the energies of the characteristic lines detectable. The technique produced compositional values well within those expected despite this there are variances due to the beam spreading into the Cr seed layer which tends to increase the effective Cr composition in both media. The grain size of both media was calculated and found to be 17.6 and 17.8 for media 1 and 2 respectively. There is a large amount of uniformity in the grain size throughout both media, this is an advantage in the production of low noise media.

CHAPTER 4 REFERENCES

J. N. Chapman, " The Investigation of Magnetci Domain Structures in Thin Foils by Electron Microscopy", ***J. Phys.D: Appl Phys***., vol. 17, pp. 623-647, 1984.

CHAPTER 5

LORENTZ MICROSCOPY OF CoPtCr THIN FILM RECORDING MEDIA

5.1 Introduction

In chapter 4 the bulk magnetic and structural properties of both media types were discussed. This chapter adds to the information of the previous through an examination of the micromagnetic behaviour of the media and in particular the written bit structures. The examinations in this chapter are performed using the techniques available through Lorentz electron microscopy. Due to the non-immersion Lorentz lenses used in the Philips CM20 and the 'field free' objective pole piece of the JEOL 2000 FX electron microscopes, the modes used in this study allow the fine detail of the media to be explored while retaining the magnetic written bit patterns. Both the modes and the instruments they are implemented on are described in chapter 2.

The study can be divided into two subsections of Lorentz electron microscopy the first deals with TEM modes and the second with the MDPC mode of STEM. In both sections the desire is to extract from the resulting images as much information as possible regarding the written magnetic structure.

5.2 Track Map

Sets of tracks were recorded on disks of each media type by colleagues at IBM SSD; the details of the recorded pattern are as follows.

The first step in the recording process is to DC erase the whole disk with the write head prior to recording the tracks. This is performed by feeding a constant DC excitation to the write head as it flies over the disk. Following this a set of tracks, is written over the DC erased region of each disk. This set of tracks is repeated at regular intervals across the disk. The set of tracks or track map is shown in binary form in Fig.5.1. A

head with a trailing pole width of ~6μm was used for all recording with a linear head to medium velocity of ~10ms^{-1} on a standard linear writing setup [White]. The initial track map written on the first samples consisted of three frequencies producing 5, 1 and 0.5 μm bit lengths or 200, 1000 and 2000 flux changes per mm (fc/mm). This was then refined with the addition of a higher frequency track producing bit lengths of 0.33μm or

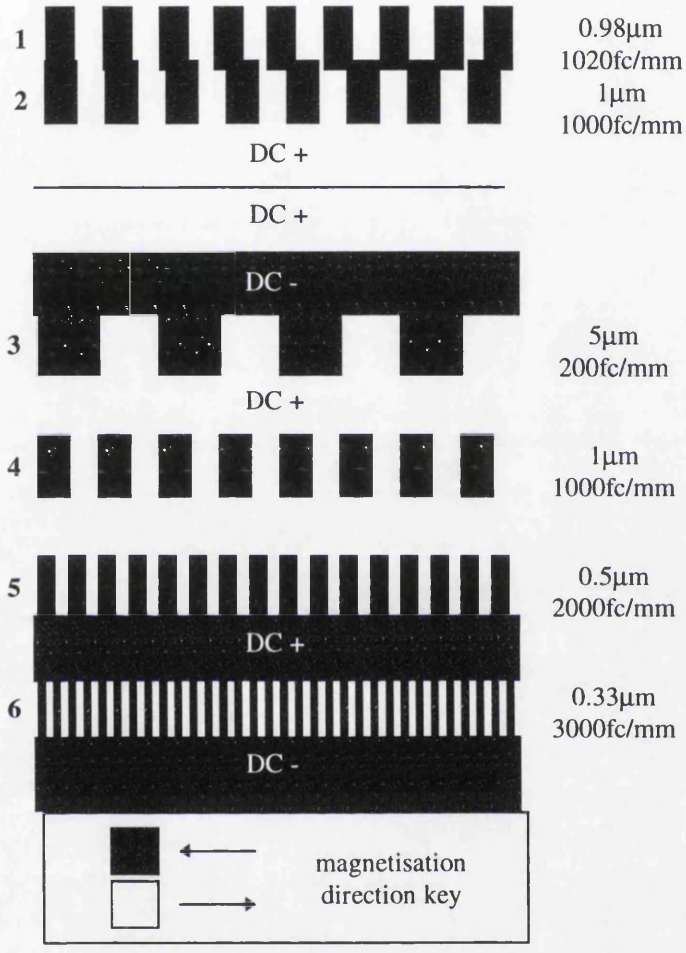

Fig.5.1 Binary representation of track map written across both disks.

3000fc/mm together with a DC banding structure alternating in direction of magnetisation between tracks; this proved useful in the MDPC setup and for a quantitative evaluation of the micromagnetic structure. An over-write experiment where one track is partially overwritten with the next was also included. These modifications are included in the track map shown in Fig.5.1. Each track is positioned such that its centre lies on the transition between the alternate DC erased regions as denoted in Fig.5.2.

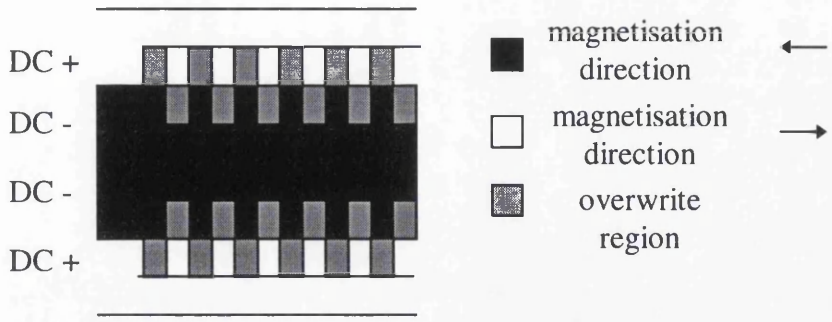

Fig.5.2 ***Binary representation of DC erasure and track positioning.***

Thus half of each written bit is written over the opposite DC erasure direction. The write head generally consists of two pole pieces in which the leading edge is wider across the track width than the other to allow for production tolerances, as in Fig.5.3. The flux leakage from the trailing pole of the head gives a specific form to the bits and allows the approximate write direction to be determined from the direction of the side write lobes as marked on Fig.5.3.

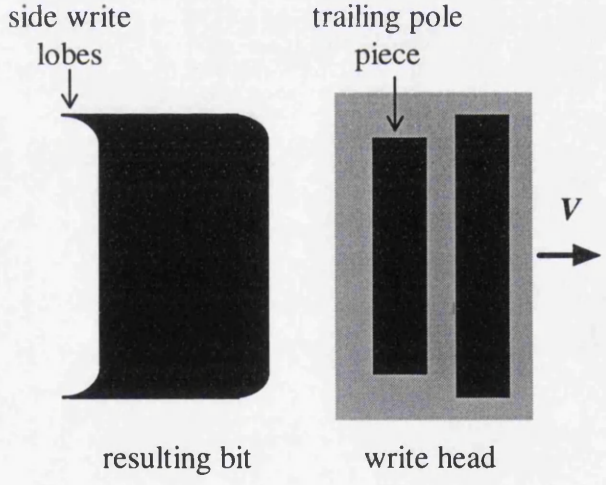

Fig.5.3 ***Schematic diagram showing the plan view of the write head and a written bit showing the side write lobes. The direction of the head velocity V with respect to the disk is defined as the write direction.***

5.3 CTEM Magnetic Bit Structure Analysis

As discussed in sections 2.3 and 2.4 the Lorentz interaction between the incident electron beam and the magnetic induction of the sample can be used to produce images containing information on the magnetic structure. In particular two TEM modes, the Fresnel mode and the Foucault mode, are useful here. The following sections present some results on the magnetic structure of the media using both TEM modes.

5.3.1 Scratch Suppression Through Sample Tilting

As stated in chapter 3, for TEM imaging the samples underwent a short sputtering in argon to remove the Cr seed layer. This reduces the sample thickness and any non-magnetic scattering contrast. If this was not performed the images would contain large amounts of contrast due to the texturing scratches which are the order of 100-200nm in width. Fig.5.4 shows a bright field image where the sample has been selectively sputter etched. The etched region contains less scratch contrast than the unetched as desired. Thus initial magnetic imaging sets were obtained with samples which had undergone a

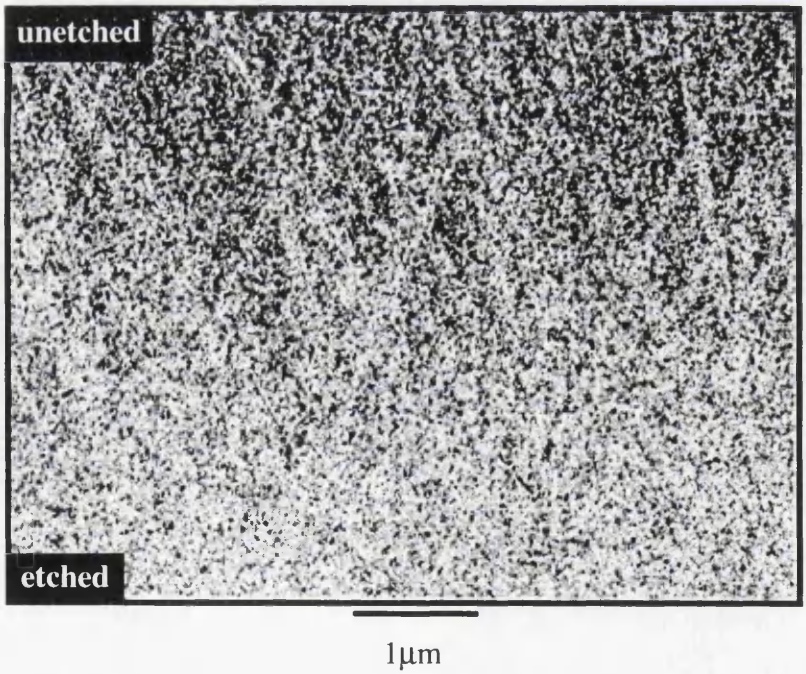

Fig.5.4 Bright field TEM image of a sample which has been etched selectively.

sputter etch. An alternative method of reducing scratch contrast which involves no further specimen preparation can also be used. Fig.5.5 displays a set of bright field images where the objective aperture is placed concentrically about the central bright spot of the diffraction pattern without obscuring any of it. The sample has undergone no sputter etching. Both images are of the same sample and essentially the same area. Fig.5.5a shows an image where the beam is incident normally on the specimen whereas in Fig.5.5b the sample has been tilted about the central axis of the rod by ~10° and the beam is now incident at an angle of ~80° to the plane of the sample. In Fig.5.5a the image is dominated by the texturing scratches across the whole sample as expected for

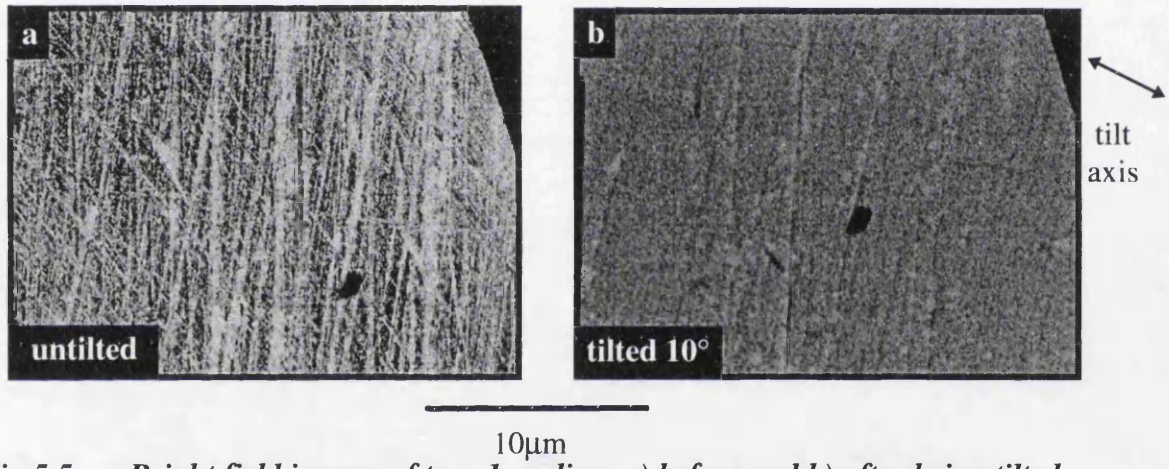

Fig.5.5 ***Bright field images of type 1 medium a) before and b) after being tilted ~10°.***

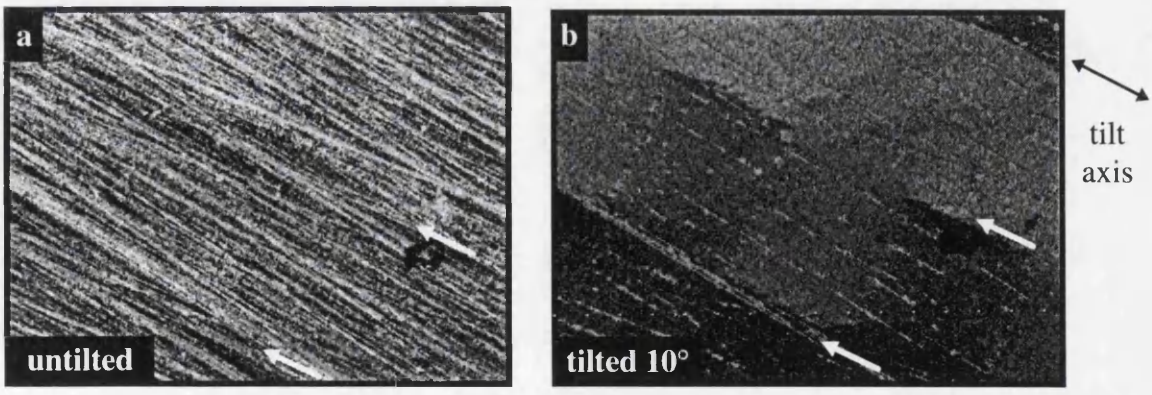

Fig.5.6 ***Foucault images of type 1 medium showing the same area a) before and b) after tilting.***

an unetched specimen. Whereas in Fig.5.5b of the same area, which has been tilted, the scratches have been almost completely suppressed. Contrast seen in the bright field image is due to scattering which is removed from the diffraction pattern formed in the back focal plane of the objective lens by either the aperture or the sides of the column. In the untilted case with no removed portion of the diffraction pattern in the bright field image the scratches are very prominent. This implies that following the 10° tilt, part of the diffraction pattern containing information regarding the structure of the scratches is reintroduced producing images with reduced scratch contrast. This effect is also very prominent in the TEM modes of Lorentz electron microscopy. Fig.5.6a shows a

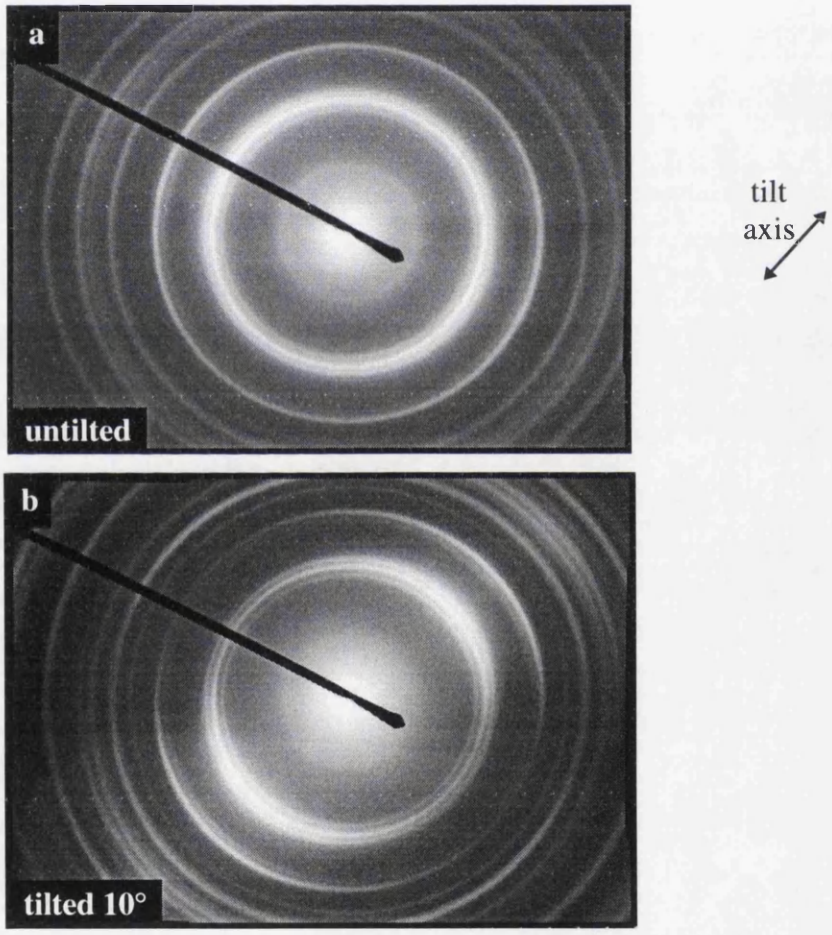

Fig.5.7 ***Diffraction patterns taken of the sample a) untilted and b) tilted by ~10° about the axis of the rod.***

Foucault image of a ferromagnetic sample with recorded tracks where the rod is tilted and the beam is incident normally on the sample. In this image the scratch contrast is extremely prominent and almost obscures completely the magnetic contrast; the track edges are marked by white arrows. In Fig.5.6b the sample has been tilted by ~10° about the axis of the rod which has reduced the scratch contrast to a minimum and the magnetic contrast can now be identified clearly. Further investigation is necessary to determine the changes that occur in diffraction pattern through the action of tilting. Fig.5.7 shows two typical diffraction patterns of the same sample untilted and tilted about the rod axis as above. Fig.5.7a of the untilted case shows a typical concentric ring diffraction pattern where the intensity is constant around each ring. In Fig.5.7b, where the sample is tilted the diffraction pattern is essentially unchanged with the main difference being that following the tilt the intensity of the rings has decreased in the direction orthogonal to the tilt.

Thus using this method, it is possible to extract images showing strong magnetic contrast from samples which have not undergone any sputter etch and reduce the specimen preparation period.

5.3.2 Fresnel Investigation

The first examination of the written media was performed using the Fresnel mode of TEM Lorentz electron microscopy. This mode produces image contrast in areas where the magnetisation direction changes in the sample. These can be localised as in a domain wall or extend across a whole area as in magnetisation ripple [Gillies 1993]. This mode is described fully in section 2.3.2.

Fresnel images of the four main frequencies written in medium 1 and medium 2 are shown in Fig.5.8 and Fig.5.9. The areas of note in Fig.5.8 are expanded approximately four times and are shown to the right of each figure. The first area of strong contrast occurs between the track and the oppositely magnetised DC erasure bands producing a domain boundary at the side of the written bit. This region is prominent in all the tracks in Figs.5.7 and 5.9 where it forms a ragged edge. Fig.5.8a shows an expanded area taken at the edge of the 5μm track denoted by white lines and

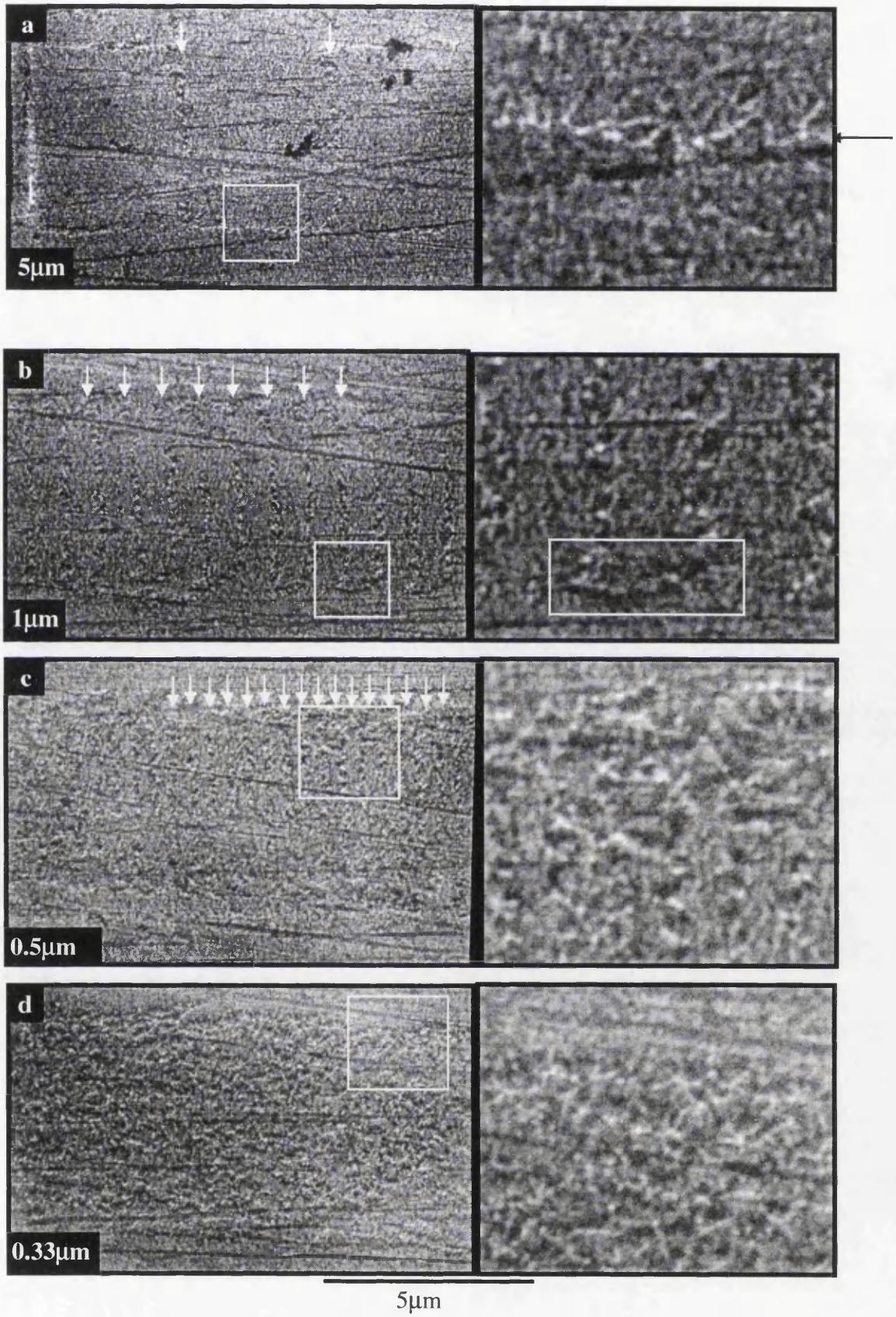

Fig.5.8 Fresnel images of medium 1 for each of the bit sizes.

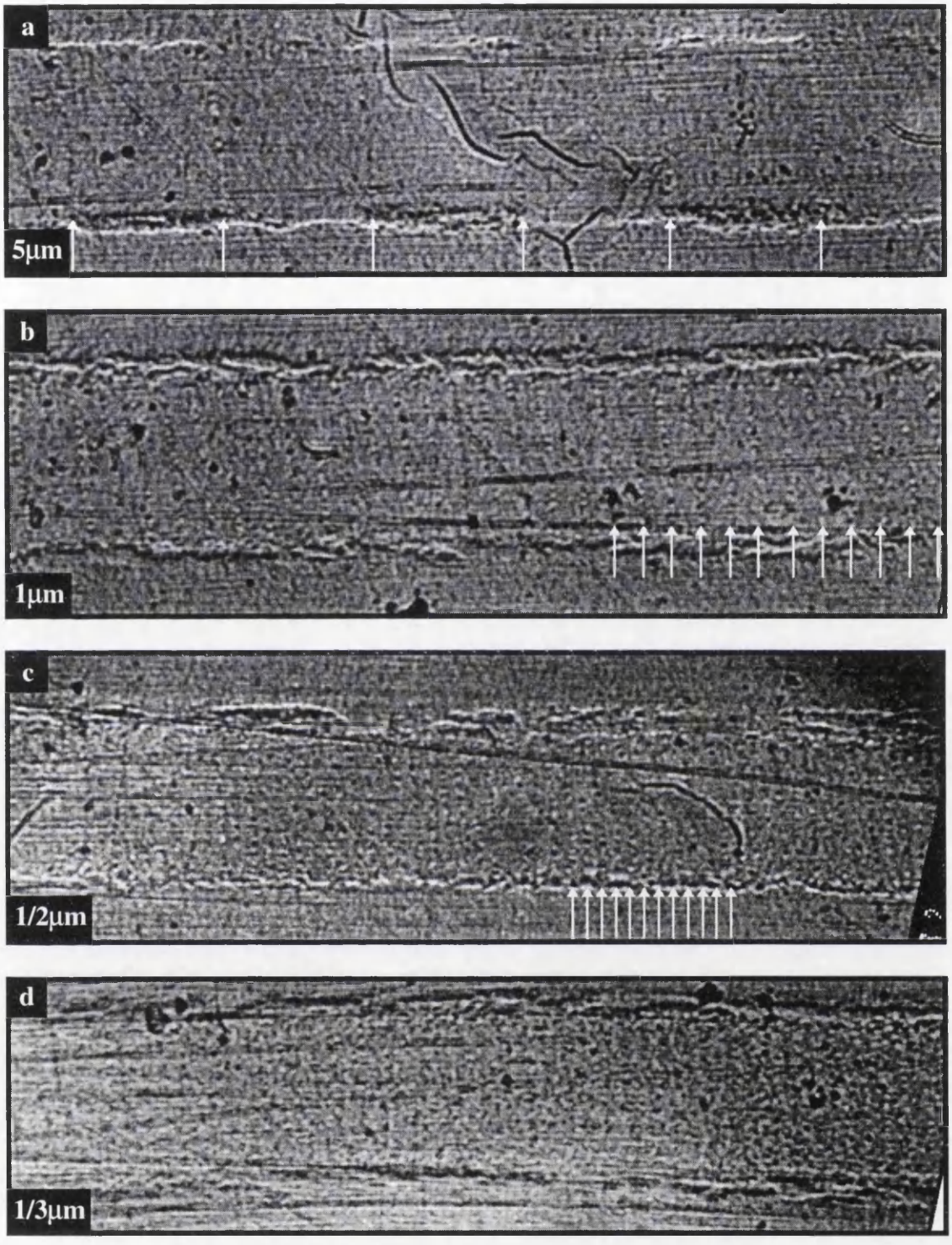

Fig.5.9 Fresnel images of medium 2 for each of the bit sizes.

indicated by the black arrow. This suggests that the magnetisation may not be rotating smoothly across the domain wall but in a manner referred to as a feathering structure

[Chen 1981]. The theory explaining this feathering pointed towards the formation of areas of several grains acting as single magnetic units known as clusters. The magnetisation in these clusters then rotates across the wall and their mutual interaction produces the discontinuities. The size of these clusters is difficult to estimate from these images and due to the nature of this method higher magnification images do not show any greater detail but this will be covered in later sections.

The second region of strong contrast occurs again at the region of the written bits called the side-write region. This region is formed by the flux leakage from the trailing pole of the write head when recording. The size and shape of the side write is strongly dependent on the write head dimensions and the write field at the edges of the pole pieces. The side write can be seen on each written bit as a lobe extending from one bit transition to the next adjacent, this can be seen in the expanded region of Fig.5.8b. As the bit length is reduced the lobes of the side write regions meet between alternate bits and the bit boundary between the bit and the DC erasure becomes dominated by the side write as can be seen in the structures at the edges of the bits in Figs.5.8c and d and in Figs.5.9b-d, as in the diagram of Fig.5.10.

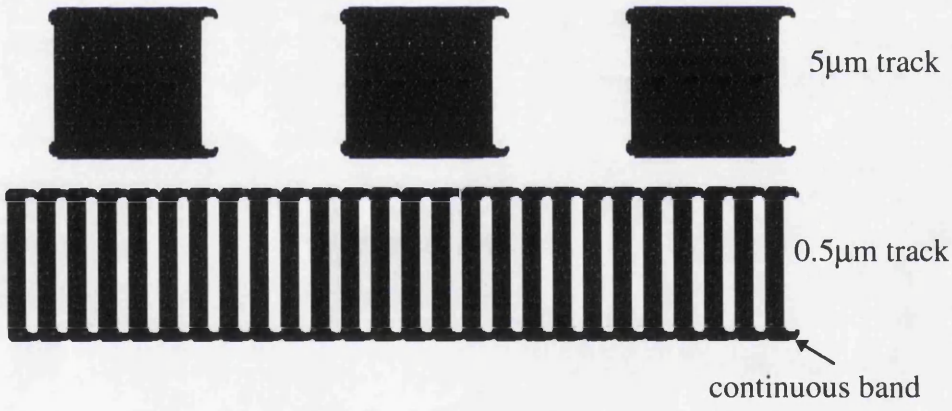

Fig.5.10 Binary diagram showing how the side write lobes can join as the bit size is reduced.

The third area of strong contrast is at the bit transition where the magnetisation in the written bits meet head on in the medium. As discussed in section 1.6.2 there is a large free pole density associated with the creation of head on transitions and as this is energetically unfavourable this is minimised through the formation of various

magnetisation configurations. In the images of Figs.5.8 and 5.9 the positions of the bit transitions are highlighted by necklaces of white and black spots as the electron beam converges and diverges across the track width. This observation suggests that the magnetisation in the bit transition is alternating in direction over the width of the track. From these images it is not possible to determine definitely the structure or the orientation of the magnetisation in the bit transition and this area will be closely studied using the other imaging modes available in the following sections of this chapter.

The images in Fig.5.9 show similar detail to that of Fig.5.8 but due to the reduced $M_r\delta$ of media of type 2, the Lorentz deflection is less and hence the corresponding contrast is also reduced. In Fig.5.9 a considerably larger defocus is used to produce the contrast seen and hence the actual magnification of the image decreases.

5.3.3 Foucault Investigation

Foucault is the final mode used to complete the TEM magnetic analysis of the bit structure. This mode generates domain contrast images by removing part of the central spot arising from the magnetic scattering contained in the central bright field spot using an aperture; this was fully discussed in section 2.2.3. This method has the advantage of allowing the approximate direction of the magnetic induction in the resulting images to be identified. This is done by noting the position of the aperture with respect to the central bright field spot and taking into account any rotation introduced by the lenses. Foucault images of medium 1 and medium 2 taken using this technique are shown in Figs.5.11 and 5.12 respectively with the corresponding low angle diffraction patterns, (LAD). There are again three main areas of interest in these images.

The first area of strong contrast is due to the DC erasure bands which appear in Figs.5.11 and 5.12 as dark and bright bands either side of the track. Lorentz deflections removed from the central spot by the aperture result in regions of dark contrast in the images and conversely Lorentz deflection allowed through by the aperture correspond to regions of bright contrast. The direction of the magnetic induction is perpendicular to the direction of the Lorentz deflection due to the nature of the Lorentz force. The edge of the aperture is positioned along the write direction to allow maximum sensitivity

along the write direction. The samples contain two DC erasure directions which give rise to two Lorentz spots about the central bright field spot as shown in the LAD pattern of Fig.5.11 and as seen in section 4.1.3. Thus if the position of the aperture is known with respect to the central spot and the track direction then the approximate direction of the magnetic induction giving rise to the contrast in the Foucault images can be determined. With the aperture positioned as shown in Fig.5.11, the bright contrast is due to the upper of the two Lorentz deflection spots. The positive magnetic induction direction is taken as being the write direction. Thus magnetic induction in the write direction produces the upper of the two Lorentz spots where the electron beam is incident into the plane of the page. Thus the bright contrast represents magnetic induction in the positive track direction and dark contrast represents magnetic induction

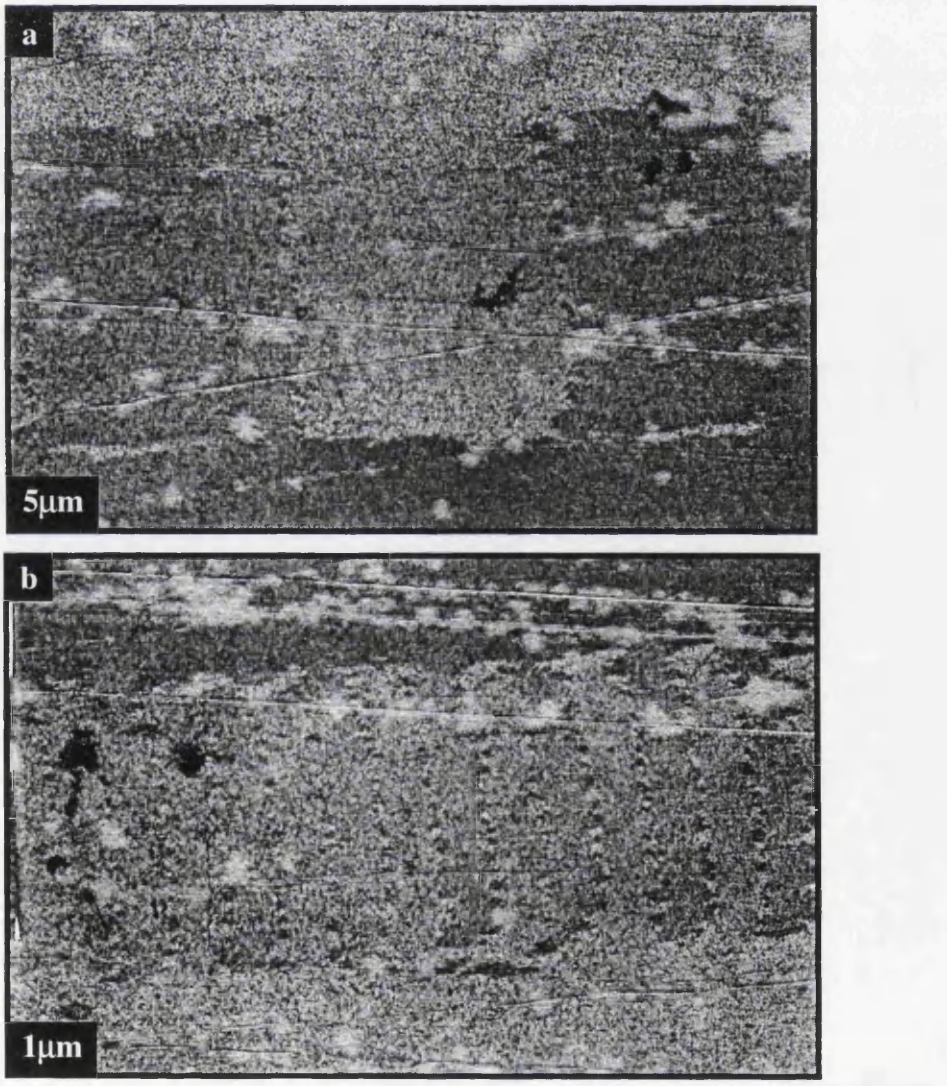

Fig.5.11 Foucault images of a) 5μm and b) 1μm tracks in medium 1.

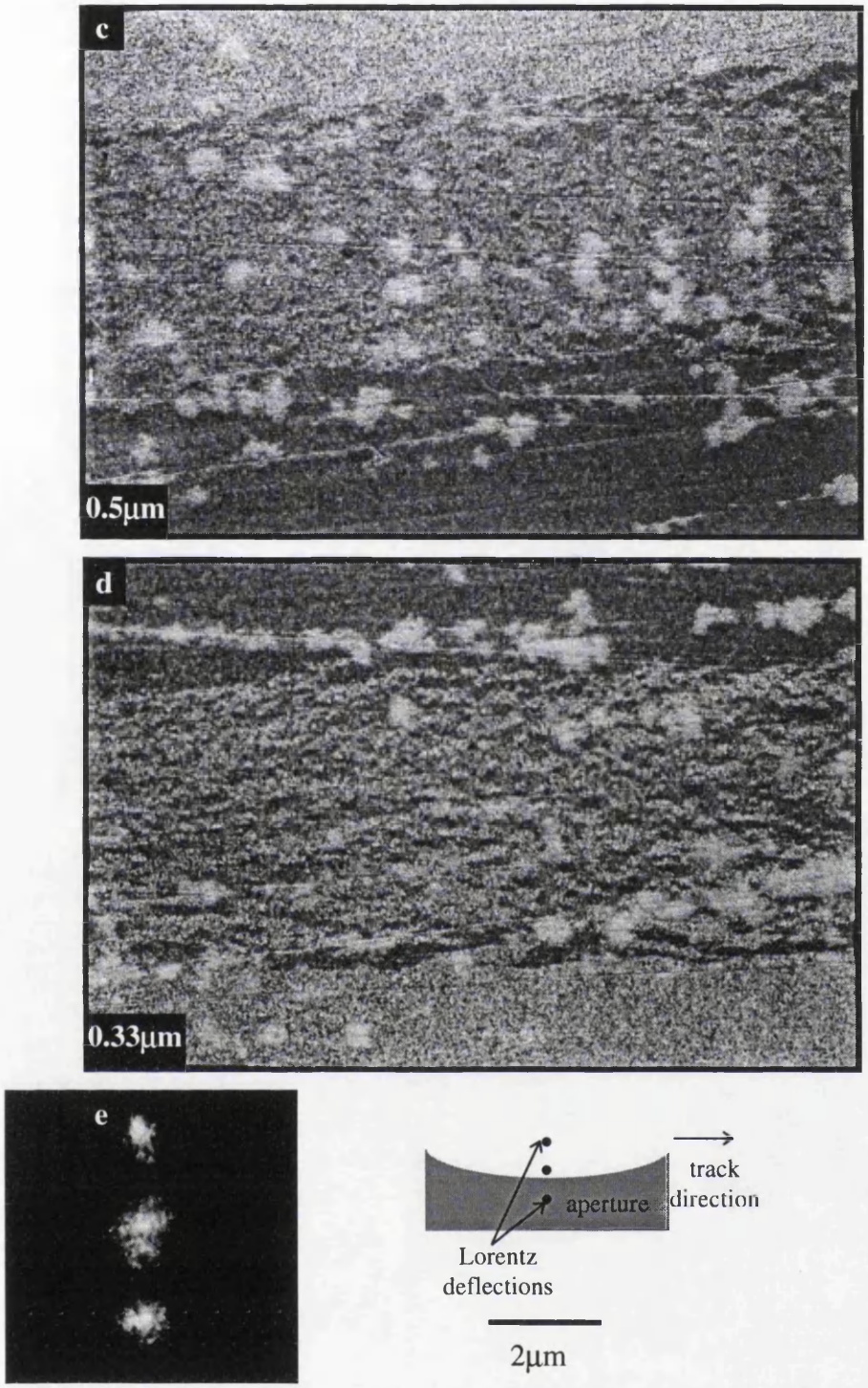

Fig.5.11 Foucault images of c) 0.5μm and d) 0.33μm tracks in type 1 medium with the LAD pattern generated by this medium from the 5μm track.

in the negative write direction. This applies to both sets of images in Figs.5.11 and 5.12.

The second area of interest is at the centre of the track where the expectation is to view dark and bright contrast in these images due to the alternating magnetisation of the

written bits. The total Lorentz deflection above the centre of the written bits is close to zero as a result of the space integral of the stray field induction above and below the film compensating for the deflection due to the magnetisation in the film. This gives grey contrast in the written bits in these regions. This effect also occurs in MDPC imaging and further discussion on this subject is given in section 5.4.1. In Fig.5.11d

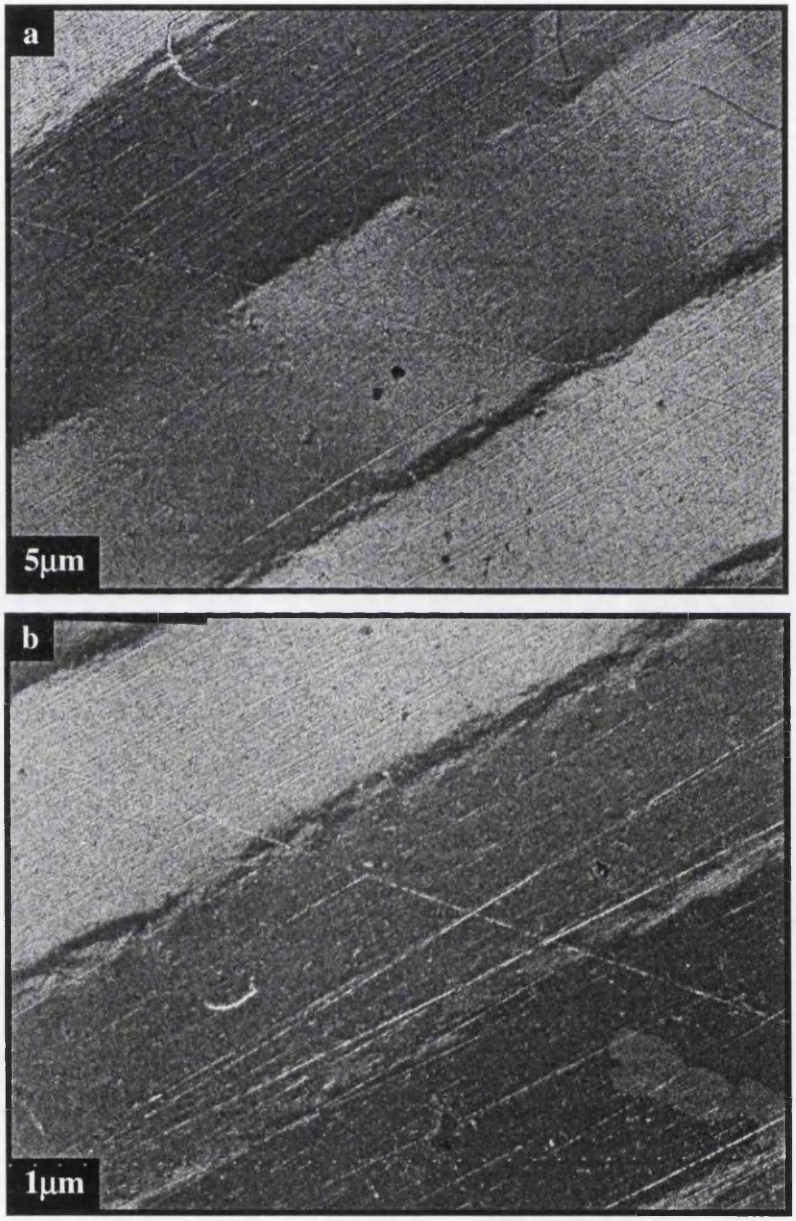

Fig.5.12 Foucault images of a) 5μm and b) 1μm tracks in medium 2.

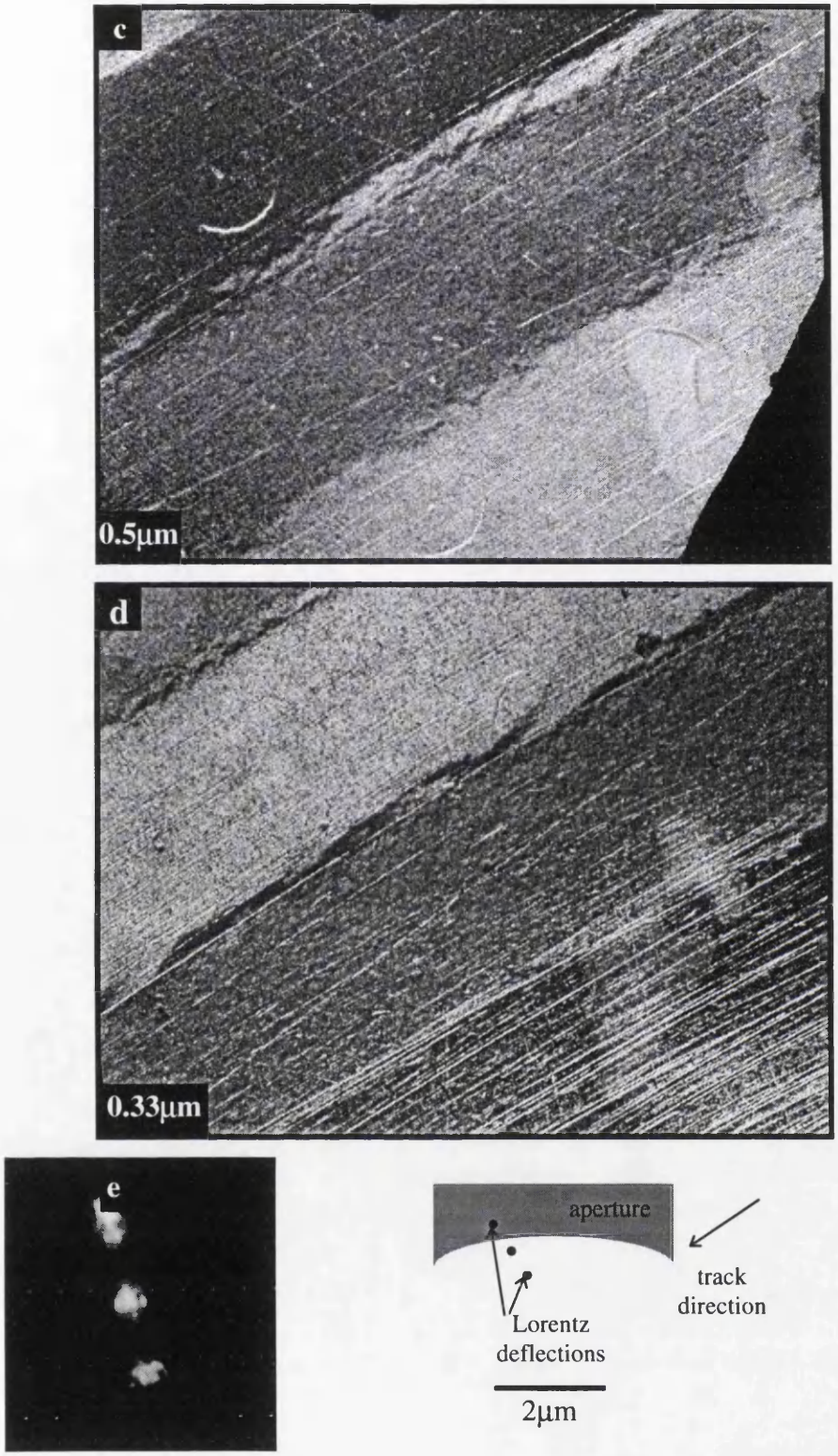

Fig.5.12 Foucault images of c) 0.5μm and d) 0.33μm tracks in type 2 medium with the LAD pattern generated by this medium from the 5μm track.

however, the centre of the track does not seem to be the same 'null' grey as in the previous images and the bit transitions are broken in form across the track suggesting

that small domains have formed which do not extend across the entire track width. This forms the grounds for a more detailed investigation of the 0.33μm track in section 5.4.2.

The final area of interest in these Foucault images is the bit transition which in Figs.5.11a-c and 5.12a can be seen as a line of alternate dark and bright contrast in a similar manner to the Fresnel images of Figs.5.8 and 5.9 reinforcing the view that the magnetic induction in these areas is also changing in direction along the bit transition. In the remaining images of medium 2 the bit transition is difficult to distinguish as a result of the reduced $M_R\delta$ product. The fine structure again cannot be determined using this mode as higher magnification images do not show any more contrast. This is due to the illumination area remaining constant as it is dictated by the beam convergence at the aperture plane and the Lorentz spot removal by the precision of the objective aperture position adjustment.

5.4 MDPC Magnetic Bit Structure Analysis

This section highlights the results from the application of the MDPC mode of Lorentz electron microscopy. In the MDPC mode the electron beam is scanned in a raster across the specimen which is then deflected by the in-plane components of magnetic induction integrated along the path of the electron beam. Images are then produced by taking difference signals from the opposite quadrants of a detector placed in the far field; this allows the in-plane components of magnetic induction to be mapped and displayed on a grey scale. The theories of DPC and MDPC were discussed in section 2.4. The following sections will cover the imaging characteristics for MDPC, how to interpret the images produced and the results and conclusions that can be drawn from the images.

5.4.1 MDPC Mapping Directions and Image Interpretation

Throughout the following sections optimised MDPC has been used for all imaging and analysis. The images are acquired on a highly modified Philips CM20 equipped with an annular quadrant detector as outlined in chapter 2. The data is collected using a

Macintosh Quadra 950 running Gatan's Digitalmicrograph software and with Gatan's hardware installed. The MDPC images produced are optimised to be sensitive to a particular direction of magnetic induction known as the mapping direction, this sensitivity reduces to zero for induction directed orthogonally to the chosen mapping direction. The signals from all four annular quadrants are collected and mixed electronically to create the desired difference signals and hence mapping directions. This allows several images of the same area with maximum sensitivity in different mapping directions to be acquired simultaneously. The bright field signal can also be obtained by addition of the signals from all four quadrants. The images are collected with an accuracy of either eight or sixteen bits running from 0 to 255 or 65535 respectively. The images in this thesis are all either acquired as 8 bit or converted to 8 bit images.

In MDPC the aim is to remove as much crystallite or non-magnetic contrast as possible from the magnetic images by setting the bright field cone to a size just larger than the inner quadrants. This is done by choosing a camera length with a spot larger than the inner detector and using the first projector lens to reduce the size of the spot to the desired value on the DPC detector. Changing the projector lens settings also introduces rotation into the beam which has to be compensated for in the MDPC setup. To investigate fully the magnetic induction due to the tracks, images which are ideally sensitive to magnetic induction parallel and perpendicular to the write direction are required. For this reason it is necessary to establish two orthogonal mapping directions. As an amount of rotation is introduced between the detector and the specimen due to the projector lens currents, a method is needed to verify the mapping direction sensitivity and if necessary to change the sensitivity direction with respect to the specimen as part of the MDPC setup.

The disks used here are all written with the same track map shown in Fig.5.1 containing alternate DC erasure banding and these provide a quick method of verifying the mapping directions. In this procedure a DC erasure transition between DC+ and DC- is selected. The sample is rotated about an axis perpendicular to the specimen plane, keeping the DC transition region in the field of view while two orthogonal mappings are visible on the CRT screens. The coarse rotation is complete when one mapping contains black and white contrast at the DC transition and the other shows little or no contrast variation in the same region. The image in Fig.5.13a is sensitive to induction orthogonal

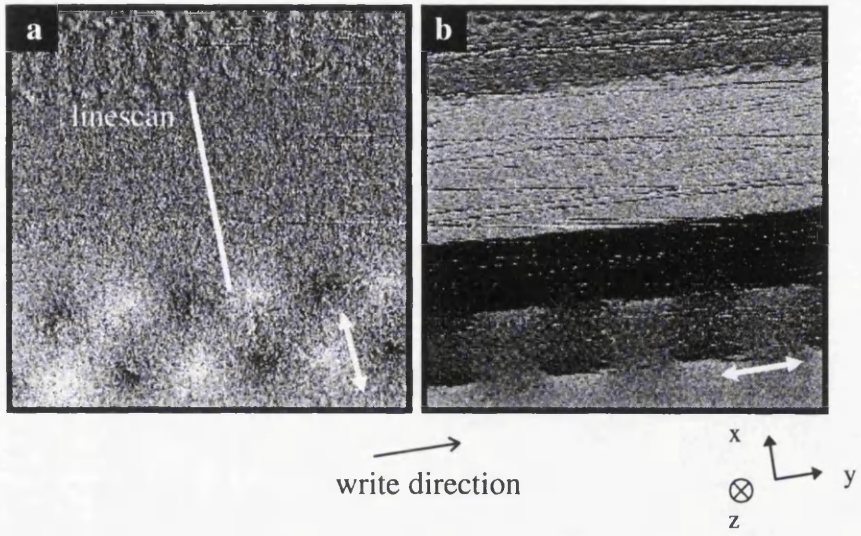

Fig.5.13 ***MDPC images of DC + and DC - erasure transition allowing the mapping direction to be checked.***

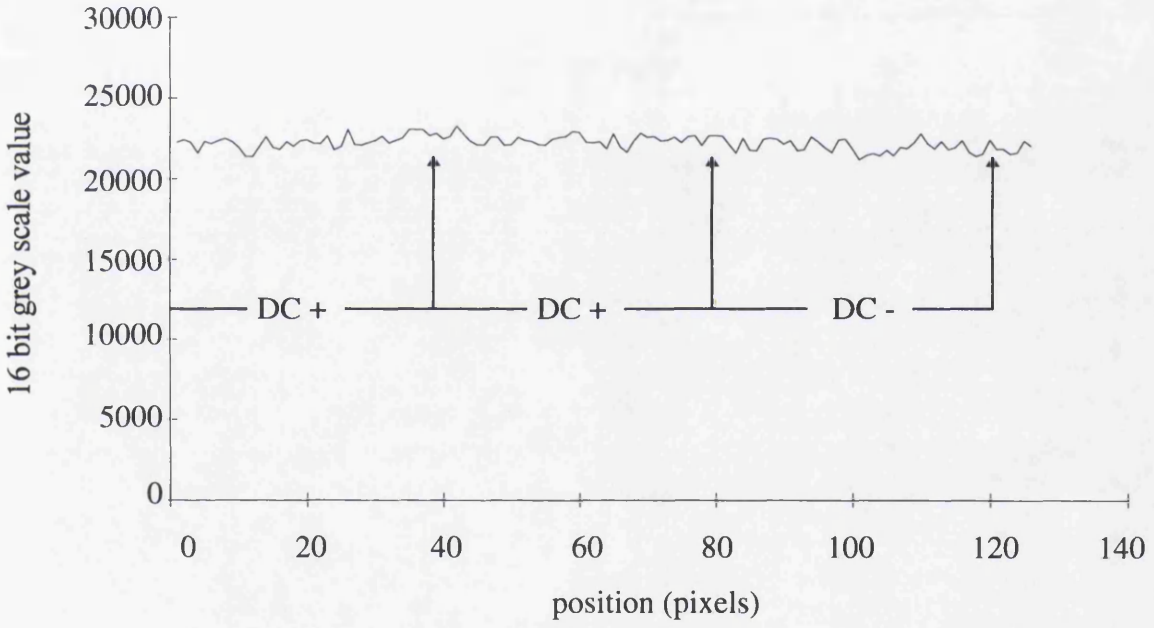

Fig.5.14 ***Graph of the linescan taken across Fig.5.13a mapped orthogonally to the write direction and averaged over the whole area.***

to the write direction and Fig.5.13b it is sensitive to induction in the write direction, as shown by the white arrows. Fig.5.13a shows very little contrast at the DC transition and Fig.5.13b shows maximum contrast in the same area. As a more precise check a linescan is taken across the mapping as in Fig.5.13a and is averaged over the entire DC

transition region resulting in the profile as in Fig.5.14. The linescan in Fig.5.14 confirms that there is negligible contrast difference at the DC+ to DC- transition region when mapping orthogonally to the write direction and that the detector mappings are now set to a known and correct orientation. This procedure was performed for each MDPC setup prior to DPC image acquisition as the strength of the projector lenses and hence the effective detector specimen rotation may be varied.

For consistency throughout the following discussions **mapping in the y direction** is equivalent to **mapping in the write** direction, **mapping in the x direction** is equivalent to mapping **transverse to the write direction** and the z direction is perpendicular to the plane of the tracks. This convention will be used from this point onwards.

When tracks are mapped along and orthogonal to the write direction, the y and x directions by the convention just stated, the MDPC images take a characteristic form. Two typical images of a 5μm track recorded in type 1 medium are shown in Fig.5.15. These images need to be explained fully before any other MDPC images can be considered.

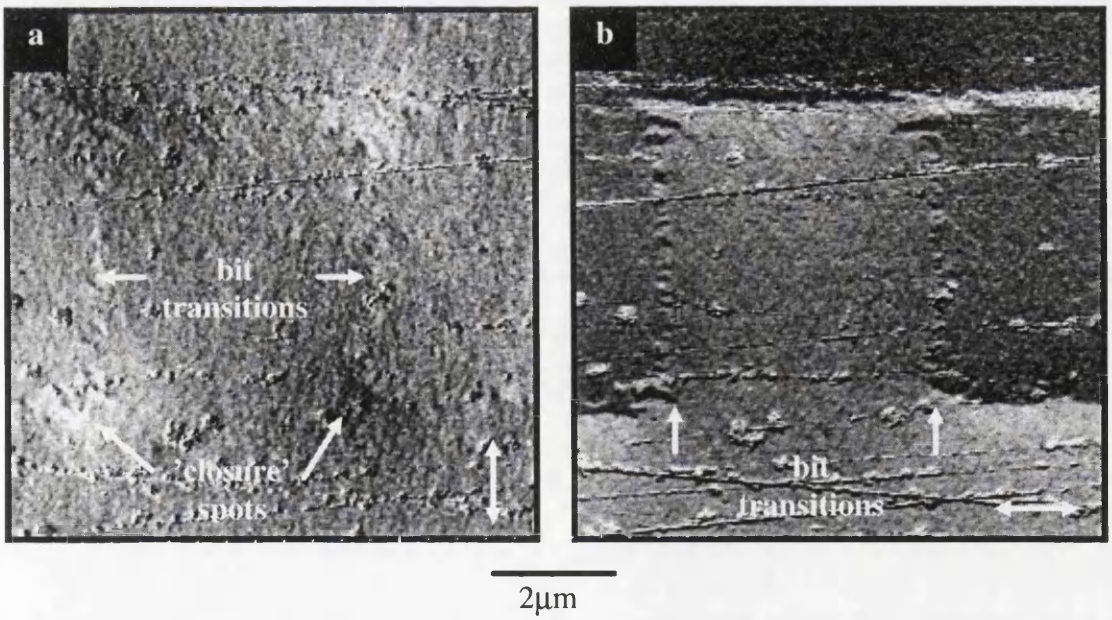

Fig.5.15 MDPC images of a) 5μm track mapped in the x direction and b) the y directions.

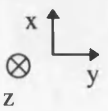

The first notable feature in Fig.5.15b is shown in the centre of the track which appears as grey contrast implying near null deflection in this area similar to the Foucault images in section 5.3.3. This is contrary to the magnetisation pattern recorded on the medium. The reason for this apparent paradox is that the MDPC images map the components of magnetic induction normal to and integrated along the electron path from source to detector. The written bits in these samples do not form magnetically closed structures rather free poles exist at the bit transitions, as discussed in section 1.6.1 giving rise to stray field which emanates above and below each written bit as shown in Fig.5.16. The deflection is due to the space integral of the two components of **B**; **H** outside the sample and **H+M** inside the sample. As the stray field, **H** forms in the opposite direction to the magnetic induction in the film it surrounds, the sum can be reduce to zero if the space integral of the two components are approximately equal in magnitude shown diagramatically in Fig.5.16. This produces near null deflection and grey contrast in the images.

The x mapping of Fig.5.15a also contains contrast that is not consistent with the expected magnetisation distribution. When mapped in the x direction, neglecting

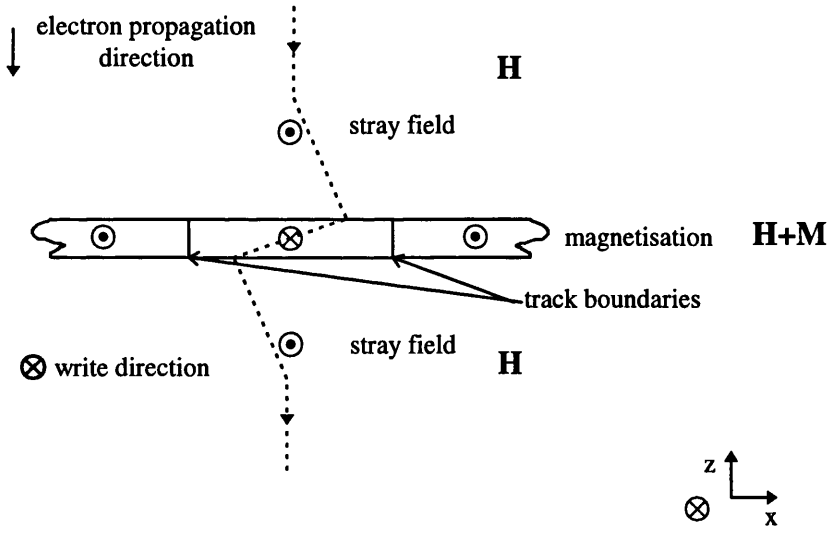

Fig.5.16 ***Schematic cross-section of a single track in a thin film medium showing the effect of the stray field on the electron trajectory. Only the y components of magnetic induction are shown. The sample thickness and deflections are exaggerated for clarity.***

dispersion there should be no component of magnetic induction in this direction. This is clearly not the case as in Fig.5.15a strong black and white spot contrast exists at the bit corners. This can again be explained through an understanding of the nature of the x and y components of the stray field [McVitie and Ferrier 1992]. The combined effect of the integral of the x components of the stray field produces closure effects at the edges of each bit as shown in Fig.5.17. In this diagram the stray field forms closed loops in the medium between adjacent bit transitions. The x component of the 'closure' is strongest at the corners of the bits and it alternates in sign along the track direction. This produces the spot contrast seen at the bit corners in Fig.5.15a. This occurs independently of the DC erasure outwith the track. There is also a y component of the stray field which can be seen in Fig.5.15b.

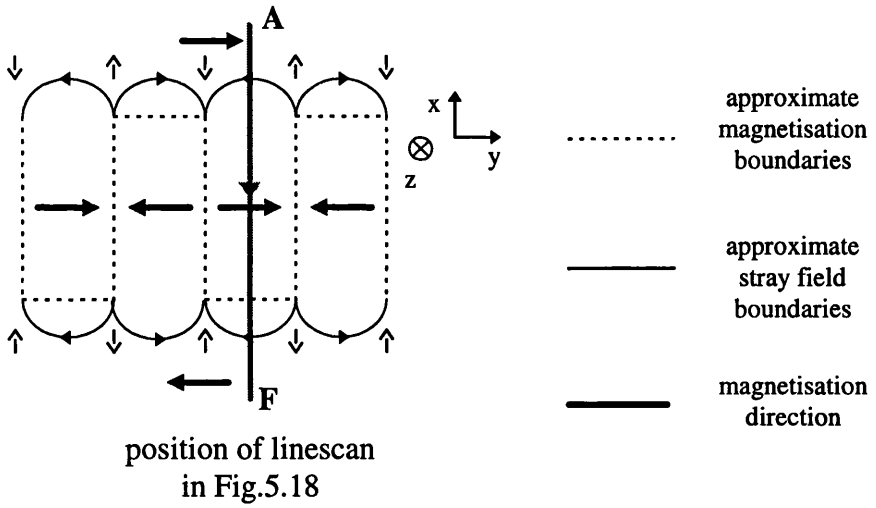

Fig.5.17 ***Plan view of written bits showing the in-plane stray field components. The x components are shown by the unfilled arrows.***

Fig.5.18 shows a simulated linescan taken across a DPC image at the position shown in Fig.5.17. The linescan maps the y components of integrated magnetic induction across the track width. At A the deflection is purely due to the DC erasure and is directly proportional to $M_R\delta$, at B the stray field from the written bit forms in the opposite direction to the erasure and reduces the total deflection. At position C the integral of the stray field and the magnetisation produces null deflection as before. At D

the stray field reduces as the edge of the track is reached; at this point the stray field is still in opposition to the magnetisation of the bit, but it is reducing in strength at the edges of the track. At E the stray field produced by the written bit is in the same direction as before but the DC erasure is now in the negative write direction allowing the two components to reinforce. At F the stray field has reduced and the deflection is now proportional to $-M_R\delta$.

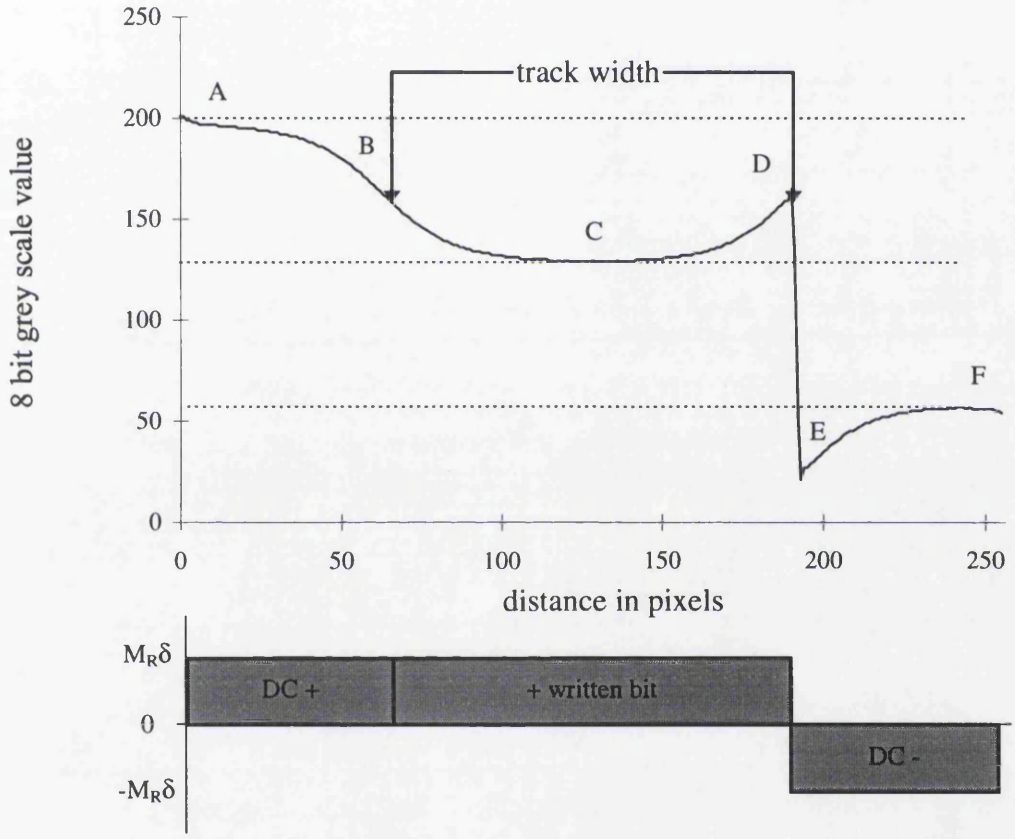

Fig.5.18 Simulated line scan taken across written bit in a typical MDPC image.

5.4.2 MDPC Images of Tracks Written Over a Range of Frequencies

This section presents images of tracks on both media types written over a range of bit lengths. The primary interest here is to determine the effects of reducing the bit length on the magnetic bit structure in these media. MDPC images of type 1 media are shown in Fig.5.19 and images of type 2 media are shown in Fig.5.20. The images generally follow the characteristic forms discussed in the previous section.

Considering the y mappings first, most of the images show grey contrast in the centre of the track, explained in the last section using stray field arguments. This supports the theory that the space integral of the stray field largely cancels the deflection due to the magnetisation for tracks written over the range of bit lengths in the media in this area. There are however two notable exceptions to this. Fig.5.19b shows a DPC image of the 5μm track mapped in the y direction. In this image there is a difference in the contrast levels between adjacent bits. The corresponding LAD pattern produced by this track is shown to the right of Fig.5.19b. The LAD pattern contains four spots; the two outer spots resulting from the deflection due to the positive and negative DC erasure bands either side of the track and two spots close to the centre of the pattern. For comparison the LAD pattern produced by the 1μm track where there is no contrast seen between adjacent bits, is shown to the right of Fig.5.19d. In the 1μm track LAD pattern there are only three spots; the two DC erasure spots and a single central spot as a result of the effect of stray field and magnetisation cancellation. Thus the central spot separation in the 5μm case confirms the magnetisation deflection is not fully compensated due to the large bit length of this track. The reason for this is that the larger bit length requires the stray field to cover a larger area but with approximately the same free pole density at the bit transition producing it. This results in a reduction in the stray field directly above the written bit and this produces the two central spots. Further the two central spots in LAD pattern of the 5μm track are rotated by an angle of ~20° to the axis of the outer spots suggesting that magnetic induction above the track supports an x component. This could have one of two sources the first being due to the closure at the edges of the bit which is discussed below or that the magnetic induction in the bits could support an uncompensated component of magnetic induction which is fully discussed in section 5.4.5.

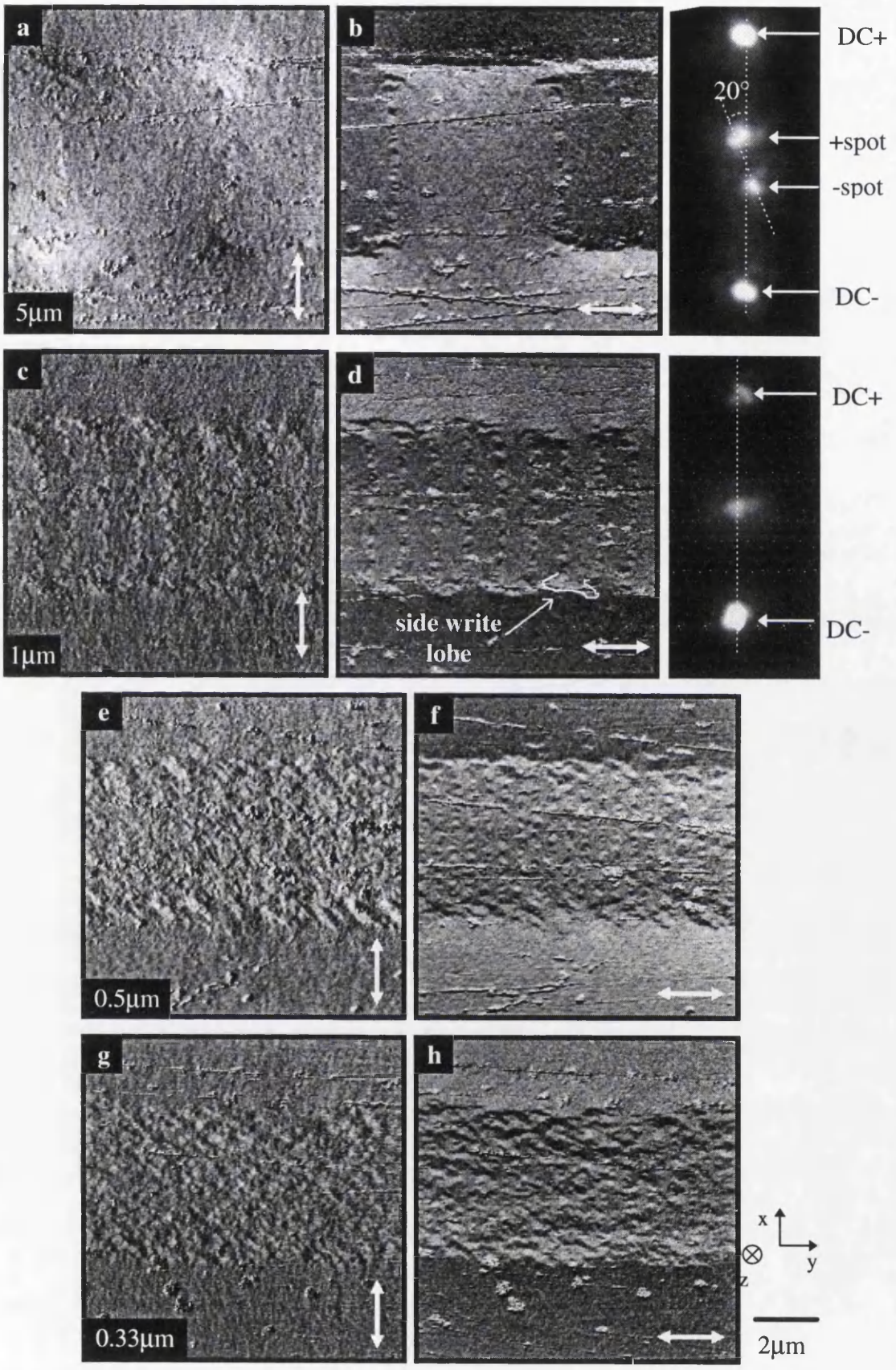

Fig.5.19 ***MDPC images of a range of track frequencies in type 1 medium with relevant LAD patterns .***

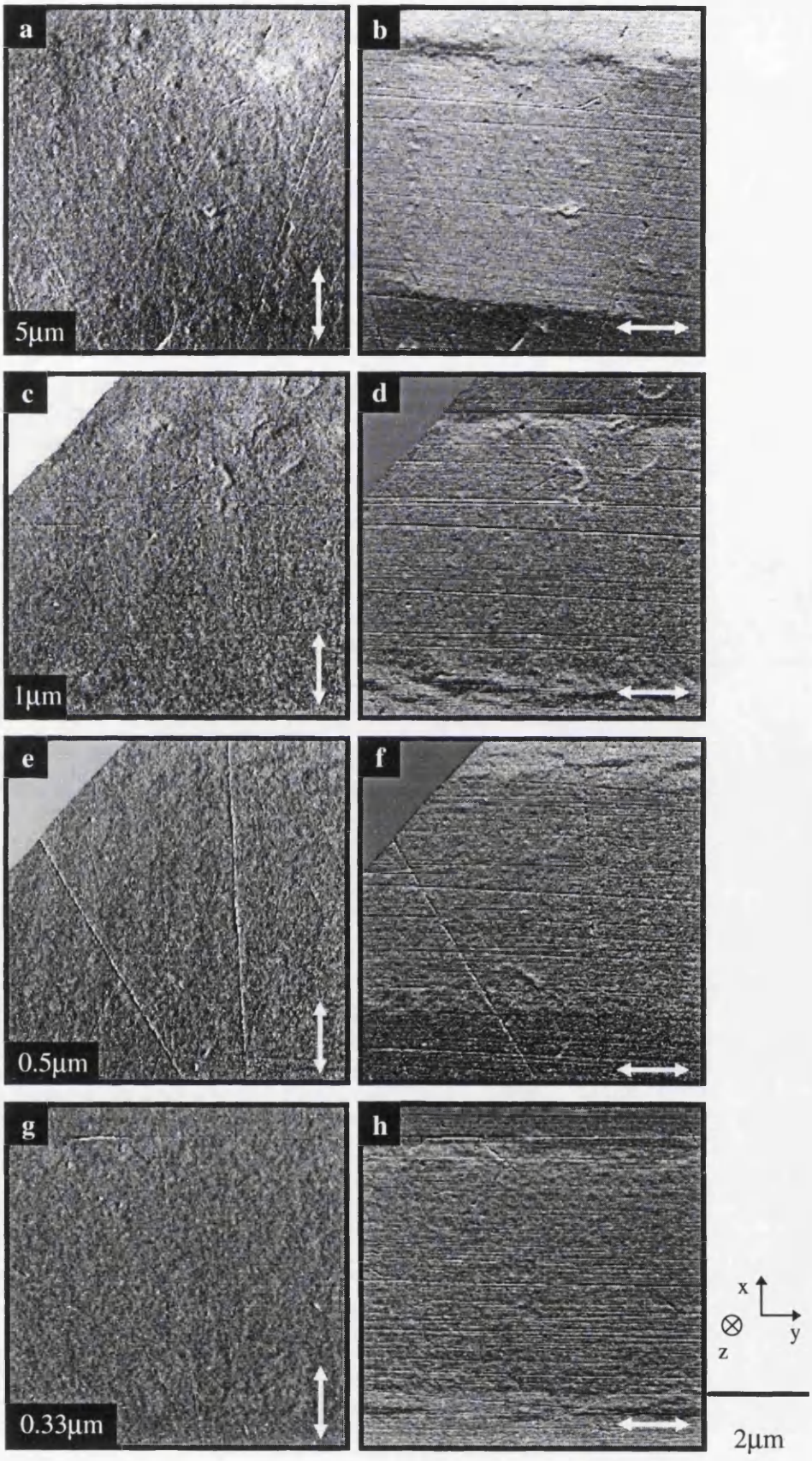

Fig.5.20 MDPC images of a range of track frequencies in type 2 medium.

Secondly Fig.5.19h of the 0.33μm track the image shows areas of either bright or dark contrast at the bit centre which are of approximately the same contrast level as the DC erasure bands on either side. It appears that the 0.33μm track is composed of small domain structures across the track width unlike the continuous structures of the longer bit lengths as seen in the Fresnel and Foucault images in section 5.3. The grey levels of these domains suggest less stray field is being produced above and below the media as a result of this small domain formation or the stray field and magnetisation are at least partially in different orientations. It is known that tracks of this frequency can be read back successfully, albeit with a lower signal, and hence must produce some amount of stray field. High magnification images of the 0.33μm track are shown in Fig.5.21. In the y mapping of Fig.5.21b the approximate bit transitions have been marked with arrows. This shows that the small domains tend to start and finish at the expected bit transitions for this bit length allowing any stray field to be in the correct position. Areas such as at A show a large concentration of small domains whereas areas such as at B show less smaller domains and closer to the grey contrast due to stray field cancellation. Thus the sample supports areas of both high and low stray field for this bit length. This interpretation of the results will be supported when MFM images are presented in section 5.5; these map only the stray field component at a distance above the sample. Secondly the contrast levels of these smaller domains suggest that they are either magnetised parallel or anti-parallel to the write direction. The side write region is the second prominent feature in the y mapped images. The images in Fig.5.19b and d show the side write lobe structure at the corners of the bits as in Fig.5.8b. As the bit length is reduced to 0.5μm as in Fig.5.19f, the edges of the side write between alternate bits join forming a near continuous band with the DC erasure shown diagramatically in Fig.5.10 which follows the binary conventions of Figs.5.1 and 5.2. This banding structure also occurs in the 0.33μm track in Fig.5.19h. In the MDPC images of type 2 medium of Fig.5.20 the side write region is increased and forms a band of ~0.5μm in width along side the track. This is consistent with the flux leakage from the write head in these regions being less than the coercive field, the domains then form orientated away from the track direction. This is consistent with the reduced write field used for this media type.

In the x mappings in Figs.5.19 and .5.20 the bit transition is seen as a thin line of black and white spots. This is a region that will be examined further using high magnification MDPC images in section 5.3.4. All that can be said about this region from these images is that the bit transition has both x and y components of magnetic induction as its structure is of the order of 0.1μm in width. As expected there is a significant amount of contrast in the x mapping of Fig.5.21a where the domains meet which implies that the small domains have not formed completely closed structures but produce free poles and stray field. It is considerably more complex to determine the position of the bit transition in Fig.5.21a due to the small domain formation.

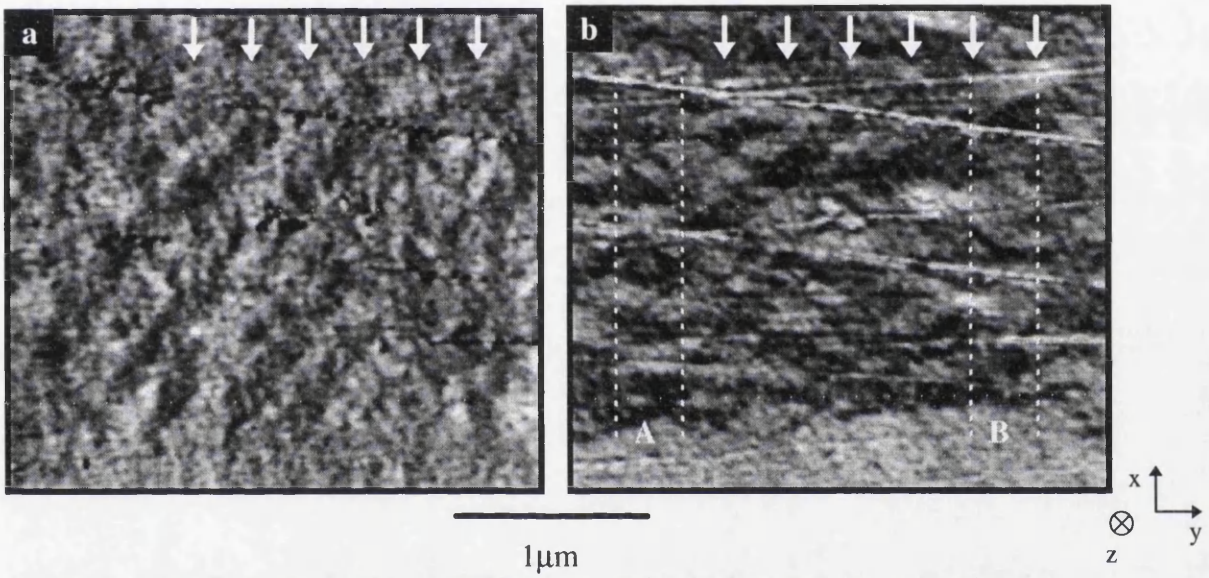

Fig.5.21 ***High magnification MDPC images of 0.33μm track showing the formation of small domains across the track width with the approximate bit transition positions marked with arrows.***

This effect is evident in the x mapped images of both Figs.5.19 and 5.20 where the spot contrast at the bit corners is diminished as the bit length is reduced.

The final tracks written in the map are the overwrite tracks where the edges of one track meet with the edges of the next. Fig.5.22 shows the over write between a 0.98μm track and a 1μm track in type 1 medium. The region between the tracks does not show the same closure spot structure as seen at the outer edges of both tracks implying reduced stray field components at the bit corners. The side write bands in this area have reinforced between similarly magnetised bits also there appears to be little or no stray

field above the side write which will be investigated in section 5.

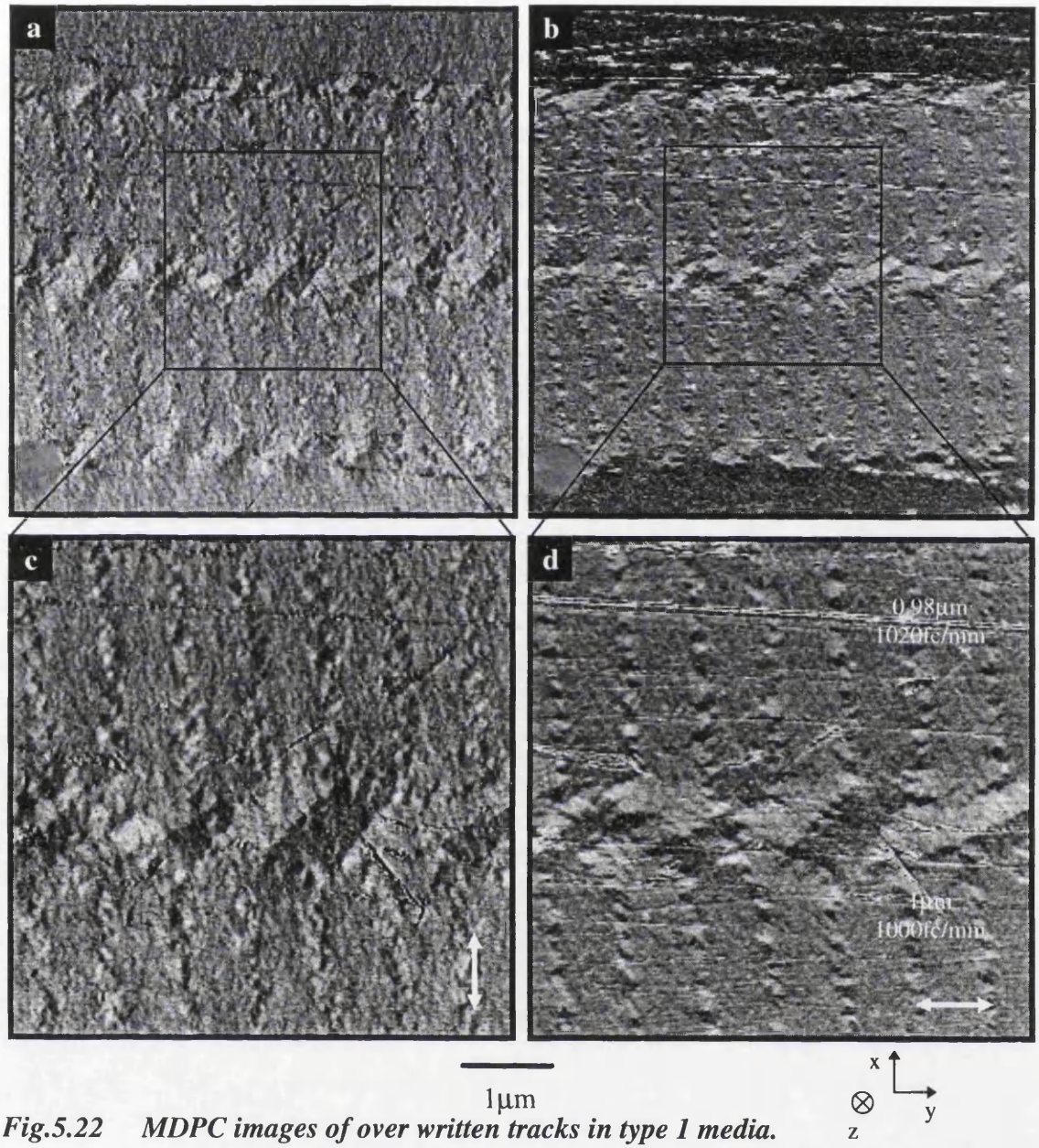

Fig.5.22 MDPC images of over written tracks in type 1 media.

5.3.4 Bit Transition Investigation.

As has already been discussed in chapter 1, one of the most important parameters of any recording medium is the width and nature of the bit transition between adjacent bits. These will determine the ultimate performance and the maximum areal density attainable in the medium. The bit transition in a typical MDPC set of images of these media are delineated by a necklace of black and white dots as in Fig.5.23 and in Figs.5.19 and 5.20. Strong contrast is seen in both mapping directions in the bit transition region in these images. When MDPC is used at the high magnifications required to view this region in detail, contrast from non magnetic sources becomes more prominent in the images. For the results of a high magnification MDPC bit transition investigation to be conclusive it is necessary to reduce the non magnetic contrast to a minimum through careful choice of the size of the spot on the detector.

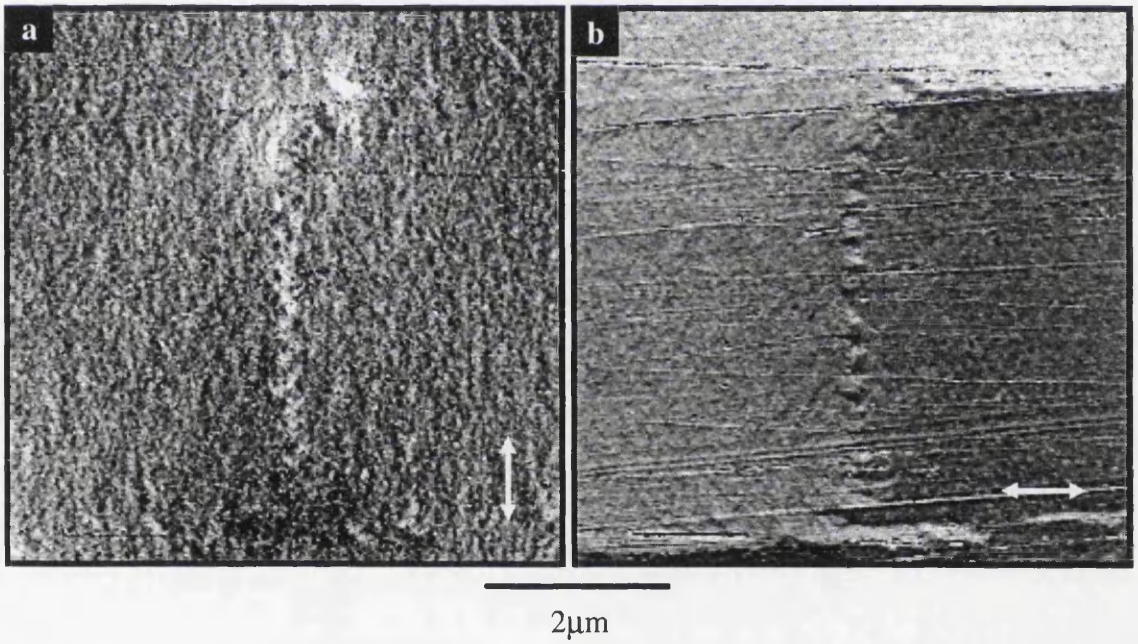

Fig.5.23 ***A typical set of MDPC images of the bit transition in a 5μm track written in medium of type 1.***

Fig.5.24 shows a set of high magnification MDPC images of a 1μm track written in type 1 medium. The bit transition varies in width from ~0.1μm-0.2μm across the track estimated from these images. Considering the y map of Fig.5.24b two areas have

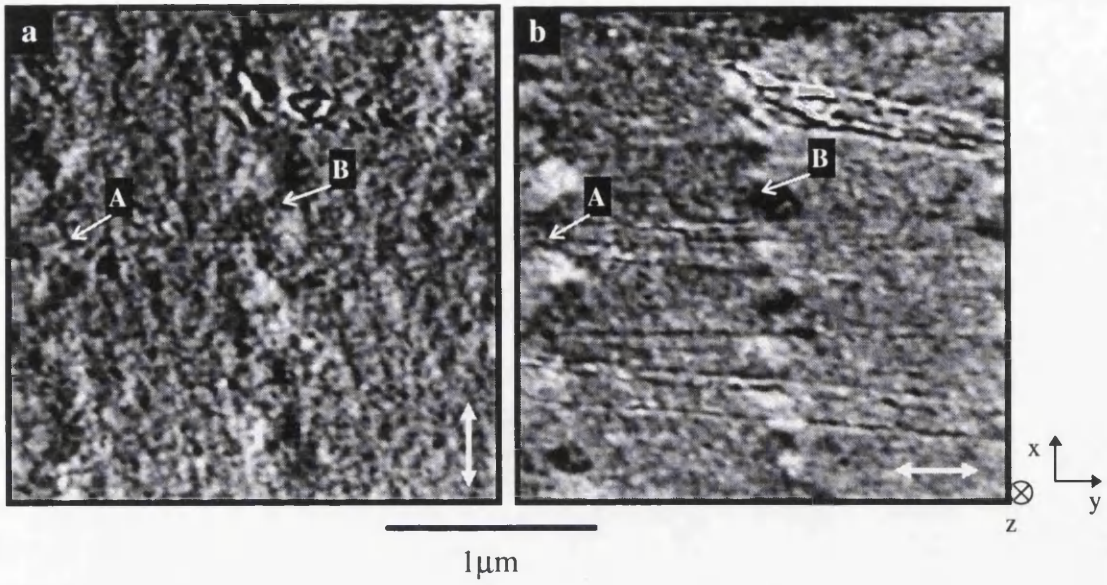

Fig.5.24 MDPC image of the bit transitions at high magnification in a 1μm track.

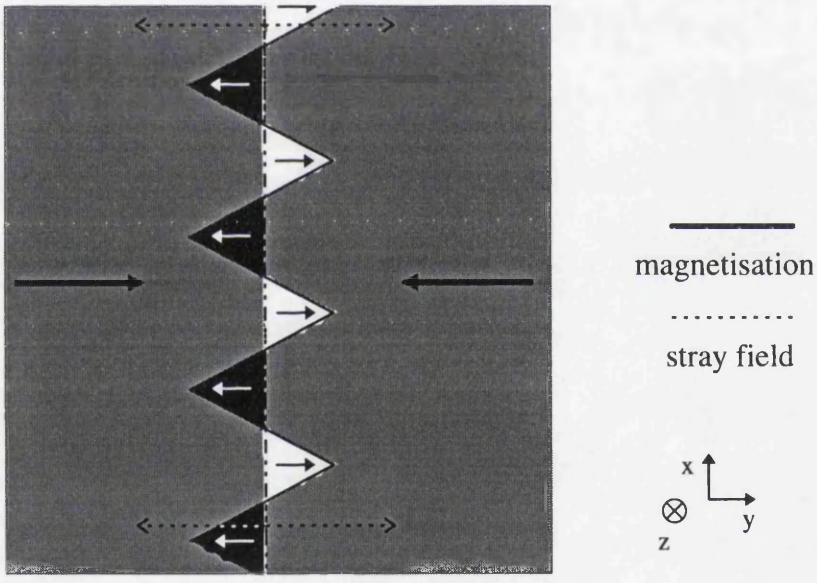

Fig.5.25 Diagram of the plan view of the y component of an MDPC image at a zig-zag bit transition in highly anisotropic media. Here the stray field can be reinforced by the zig-zag magnetisation.

been highlighted in these images. At area A the bit transition takes on the form of a zig-zag type structure. Fig.5.25 shows a schematic diagram of a zig-zag transition in a highly anisotropic medium. The approximate contrast levels are shown on a grey scale

with the magnetisation directions shown in each area using solid arrows. The dashed arrows represent the stray field direction above each of the two written bits, which are directed in the opposite sense to the magnetisation in each bit. The stray field forms an approximately straight boundary across the track width and along the centre of the zig-zag, as denoted by the double dashed line in Fig.5.25. As the zig-zag infringes over the stray field boundary, the magnetisation in the zig-zag is now in the same sense as the stray field above the bit. Thus instead of the sum of the space integral of the stray field and the magnetisation being null, the magnetisation now reinforces the deflection due to the stray field resulting in black or white contrast about the bit transition. It is important to notice that the contrast resulting from this type of structure forms black and white triangle contrast which is separated distinctly in the y direction by the stray field boundary. This magnetisation configuration has been seen in a highly anisotropic FeCoCr medium [M^{c}Vitie 1992] [Martin 1992]. In Fig.5.24b the zig-zag contrast at position A is very similar to that seen in these studies suggesting that this could be the structure seen there.

At position B the structure is significantly different and both mapping directions need to be considered to determine the magnetisation configuration. At position B the y mapping of Fig.5.24b shows black and white regions directly above each other centred on the same y coordinate, unlike the previous zig-zag case where the spots were separated by the stray field line. Similarly Fig.5.24a shows contrast centred about the same area but separated in the x direction. One possible magnetisation configuration that can produce this type of contrast is shown in Fig.5.26. The magnetisation configuration shown in Fig.5.26a is described as a vortex structure where the magnetisation circulates about a central point. Simulated MDPC images produced by this vortex are show in Figs.5.26b and c, the details of which will be covered in chapter 6. When mapped in the x direction, as in Fig.5.24b the MDPC image shows two black and white areas of contrast with different y coordinates, separated about the vortex centre. For the y mapping a similar spot configuration is seen but the spots have separate x coordinates.

Vortex structures have been observed by another researcher [Chen 1981 and 1988] considering isotropic CoRe films with $H_c \leq 450Oe$ and at bit lengths of ~10μm. Their results showed a large amount of dispersion within each bit which tend to form feather

like branches across the bit and vortices form where the branches meet from oppositely magnetised bits. The suggestion is that the vortex structure is favourable at the bit transition in these media because the gradual rotation of the magnetisation creates a domain wall with a lower energy density in comparison to the ~ 180° wall of a zig-zag structure. In Figs.5.23a and 5.24a there is some dispersion orthogonal to the write direction, as expected and there is also evidence of a cluster forming feathering

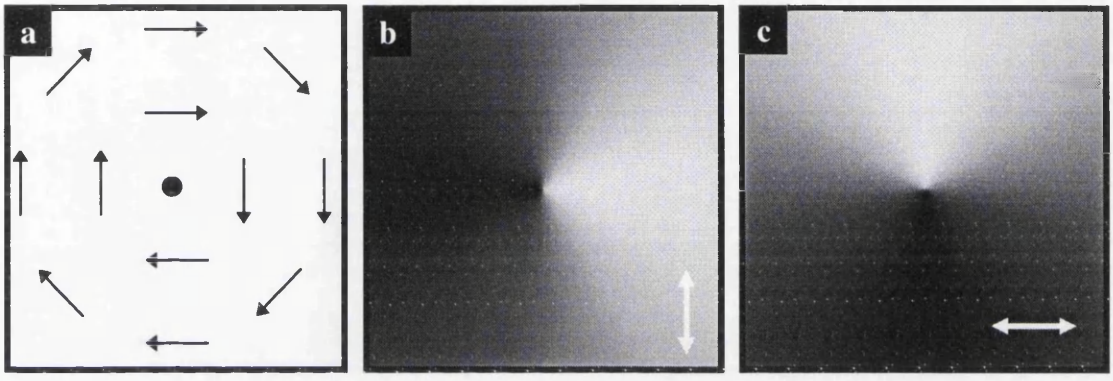

Fig.5.26 ***a) Schematic of vortex type structure with b) and c) MDPC contrast simulation images using a method which will be outlined in chapter 6.***

structure at the 180° boundary between the bits and the DC erasure, magnetised in the opposite direction, as discussed in section 5.3.1 and as seen in the Fresnel images in Figs.5.8 and 5.9. It has also been suggested [Miles 1995] that both bit transition structures can coexist in the same bit transition forming combinations of both zig-zag and vortex wall structures in an attempt to reduce the energy density of the bit transition. Fig.5.27 shows a set of images taken of the 5μm track written in medium 1 where the bit transition meets the side write region at the corner of a bit. At regions A and B in Fig.5.27b the characteristic vortex spots can be seen with the equivalent spots in Fig.5.27a. At position C the bit transition approximately meets the side write region of the track, with the white area at the bottom of Fig.5.27b signifying the edge of the track. At C the bit transition has formed the same structure as that expected from the zig-zag magnetisation configuration which continues along the bit transition in Fig.5.27b to

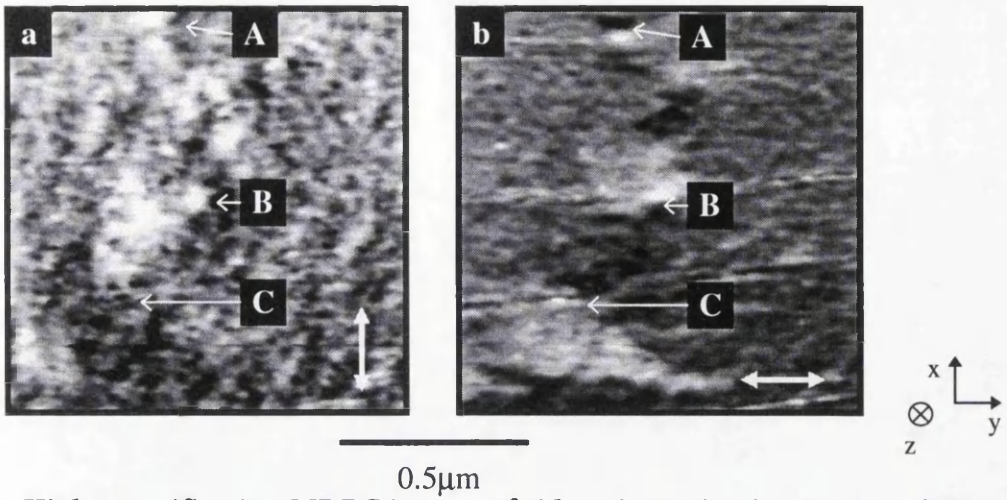

Fig.5.27 ***High magnification MDPC images of side write region in type 1 medium of the 5μm where vortex and zig-zag bit transition configurations exist in the same bit transition.***

position B where the vortex exists. Hence a combination structure must exist at the transition between region B and region C.

5.4.5 DC Erasure Linescan Analysis

The side write region of the written bits is an area at the edge of the track which is influenced by the flux leakage from the sides of the trailing pole of the write head. Its investigation is hampered by the inclusion of large stray field components in this region. To enable a precise mapping direction setup for MDPC both samples contain a plus to minus DC erasure transition region, as used in section 5.4.1. The DC erasure transition region will have similar magnetic characteristics to the side write magnetisation with the main difference that both DC erasure bands have virtually no stray field component

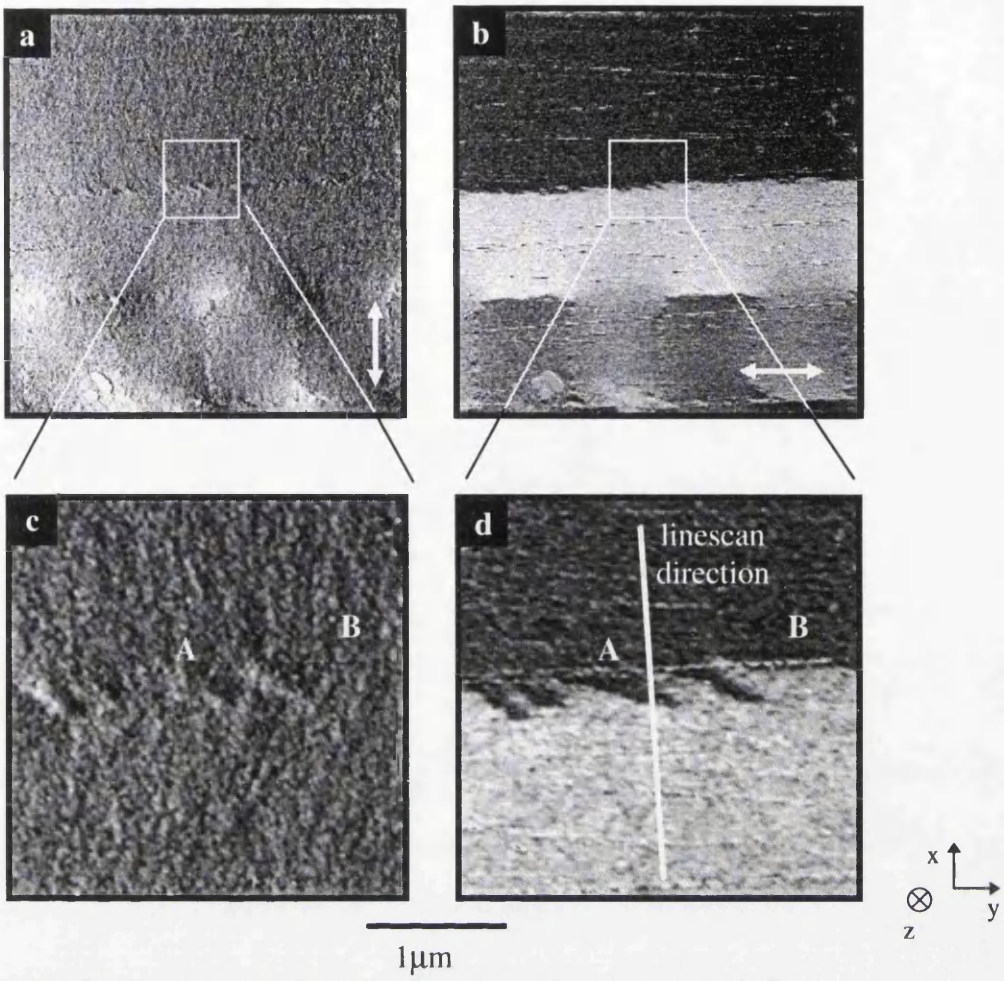

Fig.5.28 MDPC images of the DC erasure transition in type 1 media.

as the bit transition regions are effectively positioned at ± ∞. Fig.5.28 shows a set of MDPC images of the DC erasure transition region in type 1 medium. As commented in an earlier section in this chapter, the side write region takes a discontinuous ragged form at the transition with the DC erasure, as in Figs.5.19 and 5.20. When mapped in the y direction the DC erasure transition takes one of two forms, the first is a ragged transition shape as in region **A** and the second is an abrupt change with a flat transition as shown in region **B** in Figs.5.28c and d respectively. The x mapping in Figs.5.28a and c in the main part of the DC erasure bands contain grey or null contrast as expected but at the transition region again there is a significant difference between regions **A** and **B**. In Fig.5.28c mapping the x component of magnetic induction there is a component of magnetic induction at region **A** transverse to the wall a component corresponding with the position of the structure seen in the y mapping. This suggest that the magnetisation rotates towards the x direction as it gets closer to the wall producing free poles and

hence stray field in this region.

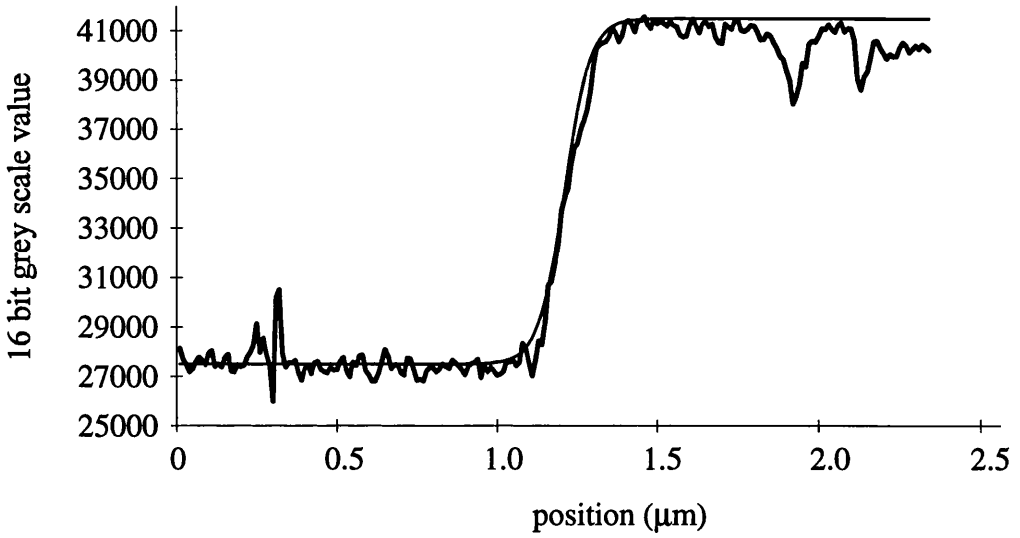

Fig.5.29 ***Graph of line scan along the x axis integrated across the whole y axis as shown in Fig.5.28d. The vertical scale is arbitrary and is highly dependent on the DC offset used.***

A linescan is used to investigate the long range magnetic order of the 180° DC erasure domain wall. Fig.5.29 above shows a linescan taken along the x axis of Fig.5.28d integrated over the whole y axis of the image shown as the thicker line, the thinner line is a fitting commonly used to determine wall thicknesses. The fitting function used here is a tanh(x/w) where w is the mean transition width and x is the position value. Here a value of w=80nm produced the above fit.

5.4.5 Alternate Bit Contrast Observation

The characteristic forms of two MDPC images mapped in the x and y directions were discussed in section 5.4.1. In particular the section highlighted that the only strong contrast in the y mapping comes from the closure loops of the in-plane stray field components. This section shows that a second and very important observation is also apparent in some of the images mapped in this direction.

Fig.5.30 shows a set of low magnification MDPC images of all the frequencies on a medium of type 1. Considering the x mapping of Fig.5.30a in which the

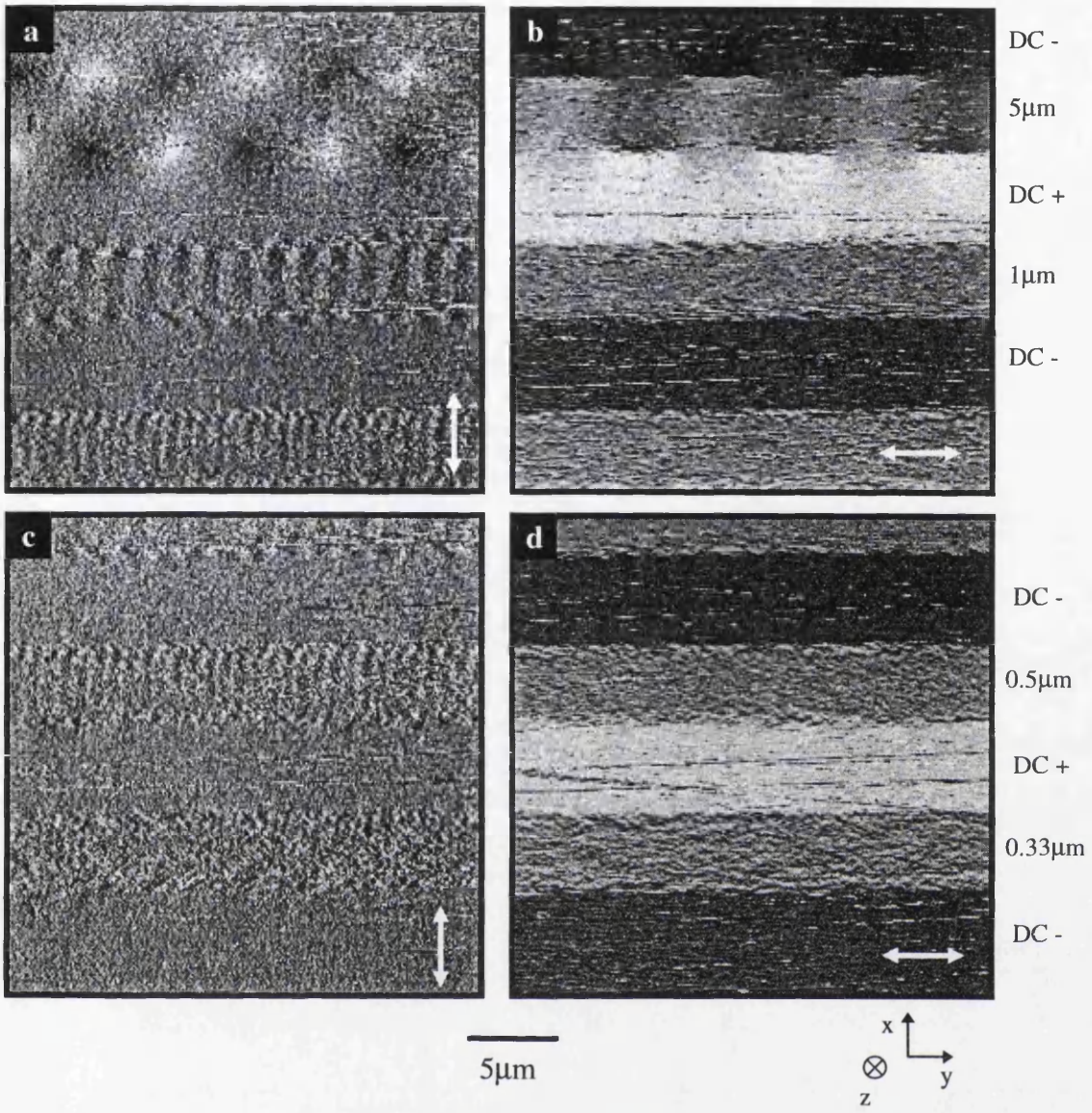

Fig.5.30 Low magnification MDPC images of tracks written in type 1 medium.

5μm, 1μm and 0.5μm tracks are visible. In the centre of the 5μm track the contrast is grey as expected and at the corners of each of the bits the same alternate closure spots as in Fig.5.15 are seen. When considering the 1μm track in Fig.5.30 the closure spots are still visible but in the centre of the track the contrast is no longer grey as before. Rather contrast bands exist which delineate the bits across the track width and which alternate in contrast along the track. Similarly in Fig.5.30c the 0.5μm and the 0.33μm tracks show the same alternating cross-track contrast. It was established in section 5.4.1 that the grey contrast near null deflection in the track centre was a result of compensation of the magnetisation deflection due to that of the space integral of the

stray magnetic induction above and below each bit. Thus this alternate cross-track bit contrast could arise if the stray field and the magnetisation in the bits were not aligned in the same direction. There are two possible ways that misalignment could occur.

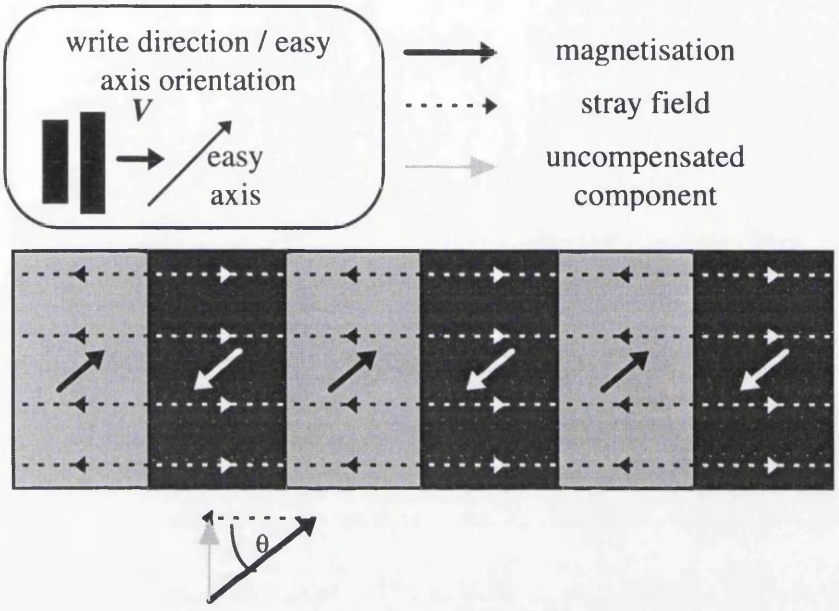

Fig.5.31 ***Plan view of written bits where the magnetisation and the stray field directions are no longer coincident arising in an uncompensated component of magnetic induction. The magnitude of θ has been expanded for clarity.***

The first explanation is shown diagramatically in Fig.5.31. In this diagram the sample supports an easy axis as shown by the arrow and the tracks are written in the direction defined by *V*, the head to medium velocity. The diagram also shows a set of tracks written at an angle to the easy axis. When the track is written the magnetisation is directed along the write direction. But on removal of the head field, the magnetisation relaxes to become directed along the easy axis of the medium. However the stray field direction is determined only by the free pole density at the bit transitions. This density would reduce if the situation depicted in Fig.5.31 arose as the density of free poles at the ends of the bits would increase. Essentially the stray field remains directed along the track direction, denoted by the dotted arrows in the diagram. There is now a misalignment between the stray field and the magnetisation

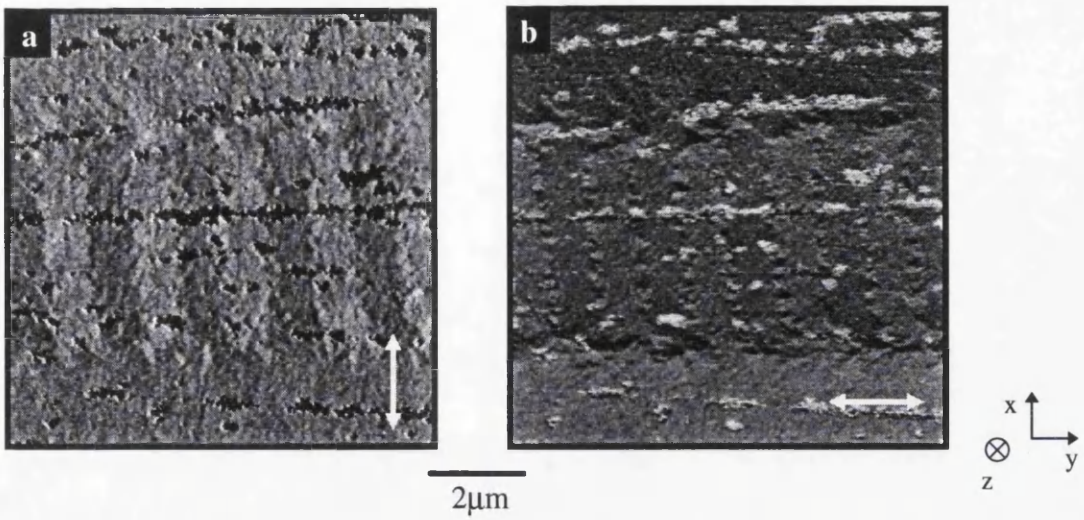

Fig.5.32 ***MDPC images of 1μm track which show alternate bit contrast when mapped in the x direction.***

in the bits denoted by the grey arrow. This misalignment gives rise to an uncompensated component of magnetic induction which is transverse to the write direction and which alternates along the track as has been seen in the Figs.5.27a and c. The same effect is shown at a higher magnification in Fig.5.32 which shows MDPC images of the 1μm track written in type 1 medium. An estimate can be made of the amount of skewing using the contrast level of Fig.5.32a which will be compared to

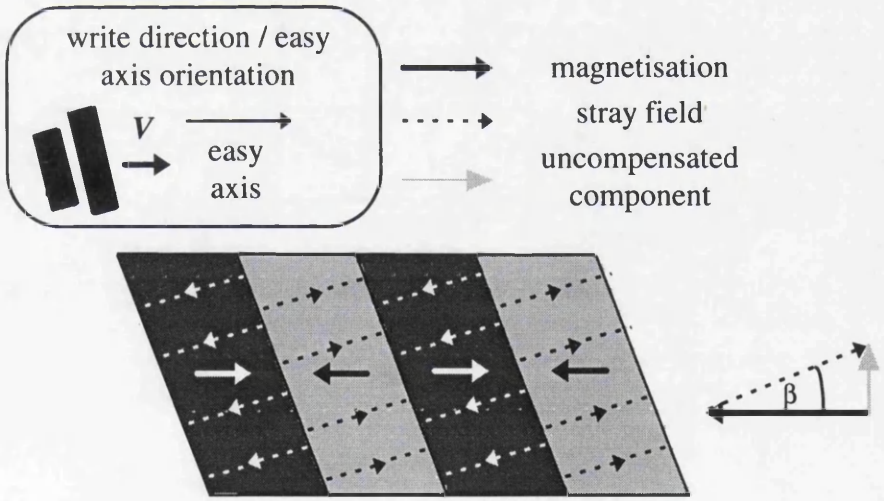

Fig.5.33 ***Diagram of magnetic induction pattern when the write head is skewed at an angle of β° to the x axis.***

skewing simulation covered in chapter 6.

A second possible configuration that could give rise to a misalignment between the magnetisation and the stray field occurs if the head is skewed at an angle during writing. A diagram of an example of head skewing is shown in Fig.5.33, in which the head is skewed at β° to the x axis. The skewed head writes a pattern of magnetisation as before but in this case the written bits are also skewed at the same angle to the x

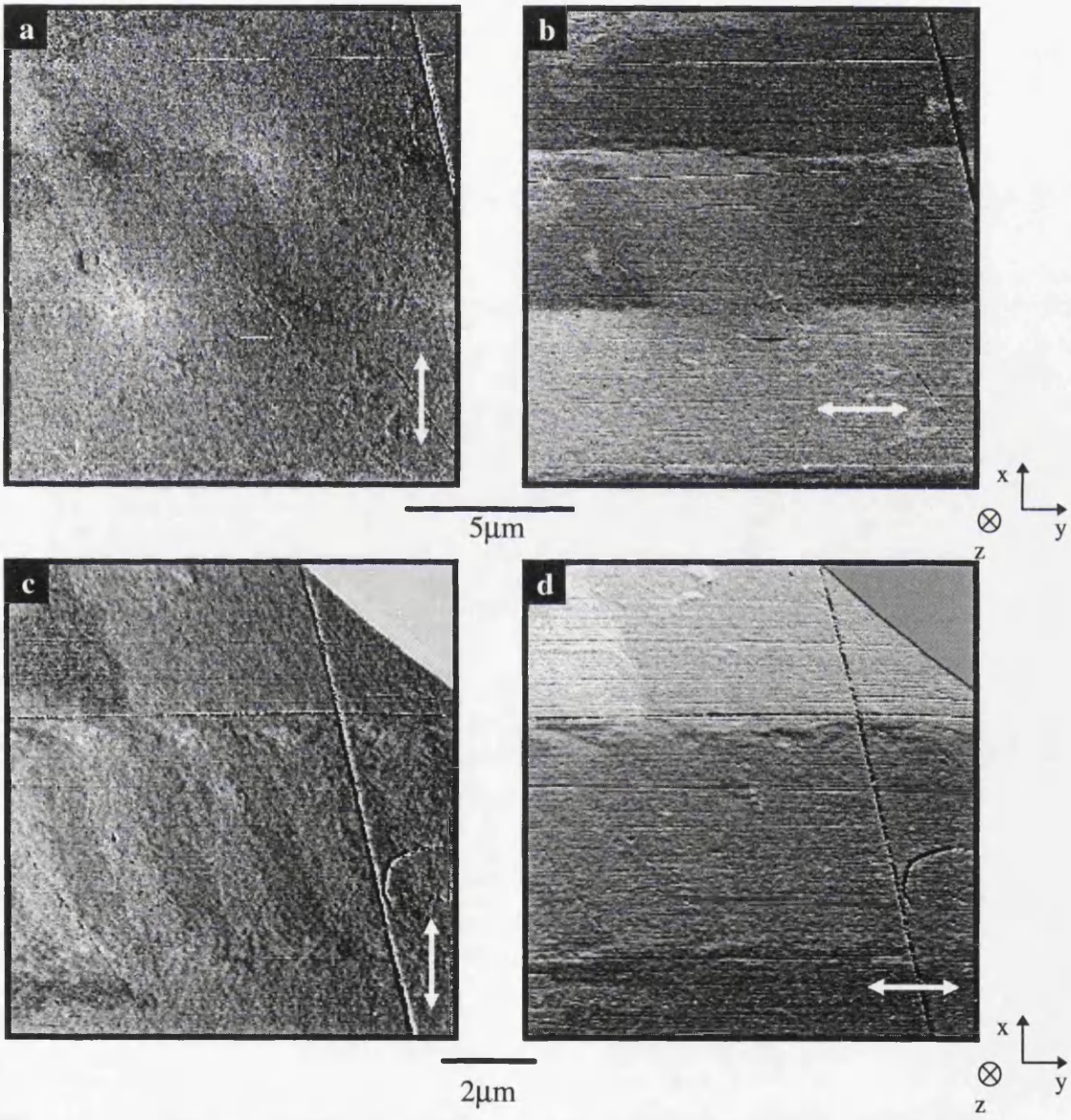

Fig.5.34 ***MDPC images of 5μm and 1μm tracks written in medium of type 2. the write head has been skewed at an angle of ~20° to the x axis producing bit contrast in the x mapped images.***

axis as the writing head. The bit transitions are also inclined forcing the stray field to lie at approximately β° to the write direction or y axis. However, the magnetisation relaxes back again to the easy axis, which for simplification lies in the y axis. Thus the magnetisation and stray field are again misaligned producing an alternate component of contrast along the track.

Examples of contrast arising from this configuration are clearly seen in Fig.5.34 of MDPC images taken of 5μm and 1μm track written type 2 medium. Here the bit transitions are skewed at an angle of ~20° to the x direction which is shown in the y mappings of Figs.5.34b and d. In the x mappings of Figs.5.34a and c the contrast in alternate bits varies periodically along the track, which is particularly prominent in 1μm track. This suggests that the write head may have moved with respect to its mounting arm during writing allowing the head to shift its position and angle the bit transitions. The effects seen in Figs.5.30, 5.32 and 5.34 imply that both media types support weak anisotropy despite the media being essentially isotropic.

5.5 Stray Field Analysis Through MFM Imaging

Section 5.4 has shown that the stray field plays an important role in Lorentz electron microscopy imaging of tracks recorded on magnetic media. Thus it would be useful if the stray field could be imaged directly. This information can be obtained using a magnetic force microscope (MFM), which forms images reflecting the interaction of the magnetic tip with the stray field above the sample surface.

Images in an MFM are formed by scanning a sharp ferromagnetic tip over the surface of a ferromagnetic sample as depicted in Fig.5.35. The stray field from the sample acts on the magnetisation of the tip through the magnetostatic dipole-dipole interaction [Grütter 1994]. The forces and force gradients caused by this interaction are sensed using mechanical resonance techniques and a map of the stray field above the sample is created. To first order the contrast obtained in these images can be interpreted as the response of the tip to the z components of the stray field from the sample [Schönenberger 1990]. Topographic contrast is reduced by first performing a 'tapping' procedure across the surface of the sample which allows the contours of the sample to be determined. This information is used to maintain a constant height above

the sample surface during the scan of the of the final magnetic image. MFM images in this thesis are displayed using an 8 bit grey scale as in the MDPC images in previous sections. In the images white contrast denotes maximum field along the positive z axis, grey denotes null deflection of the tip and black denotes maximum field in the negative z axis direction.

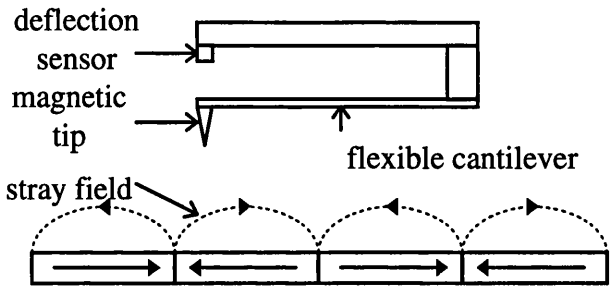

Fig.5.35 Diagram of the MFM instrument configuration.

Fig.5.36 shows a set of MFM images taken of a sample of type 1 media. This sample was taken from the same disk used in section 5.4 for MDPC. As expected for recorded tracks, the MFM images show strong black and white contrast bands at the bit transition. This is a result of the z component of the stray field emanating from the bit transitions which changes sign in the z direction as the magnetisation direction alternates between bits along the track direction. In all images the bit transition forms a band across the track which does not seem to show as much variation as the MDPC images. This confirms the view that the stray field should show much less variation than the magnetisation producing it. Images expanded to their full precision are shown of the 1, 0.5 and 0.33μm bit lengths as insets in Figs.5.36d, e and f. The higher magnification images show that the contrast varies across the bit transition and in some areas the band is discontinuous. These discontinuities are most prominent in the expanded 0.33μm image in agreement with the MDPC image where the magnetisation forms small domains which do not extend across the whole track width. The MFM images show that the stray field also supports the previous MDPC observation that the small domains tend to start and stop at the expected bit transition length for a 0.33μm track as the stray field bands have formed at the correct positions.

A further feature of these images is the contrast seen at the DC erasure transitions and at the side write region of the bits. In Fig.5.36a between the DC erasure bands lines of contrast exist which implies that there is a component of vertical stray field in these areas which must result from the formation of free poles. This is a result of the side write region having a small overlap region as the write head DC erases the disk. This is

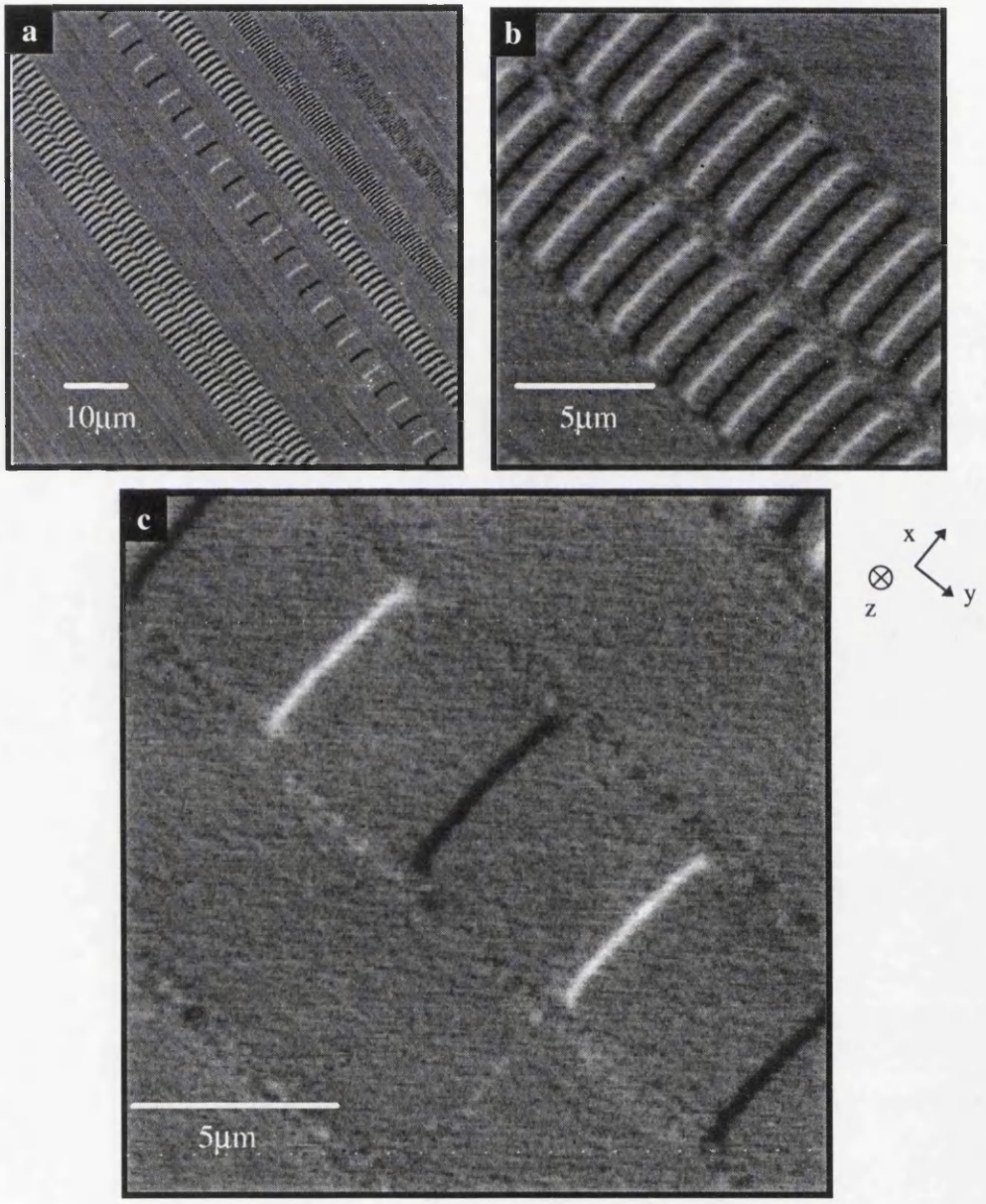

Fig.5.36 ***MFM images taken of medium of type 1 at a) of all tracks at a low magnification, b) the overwrite tracks and c) the 5m track.***

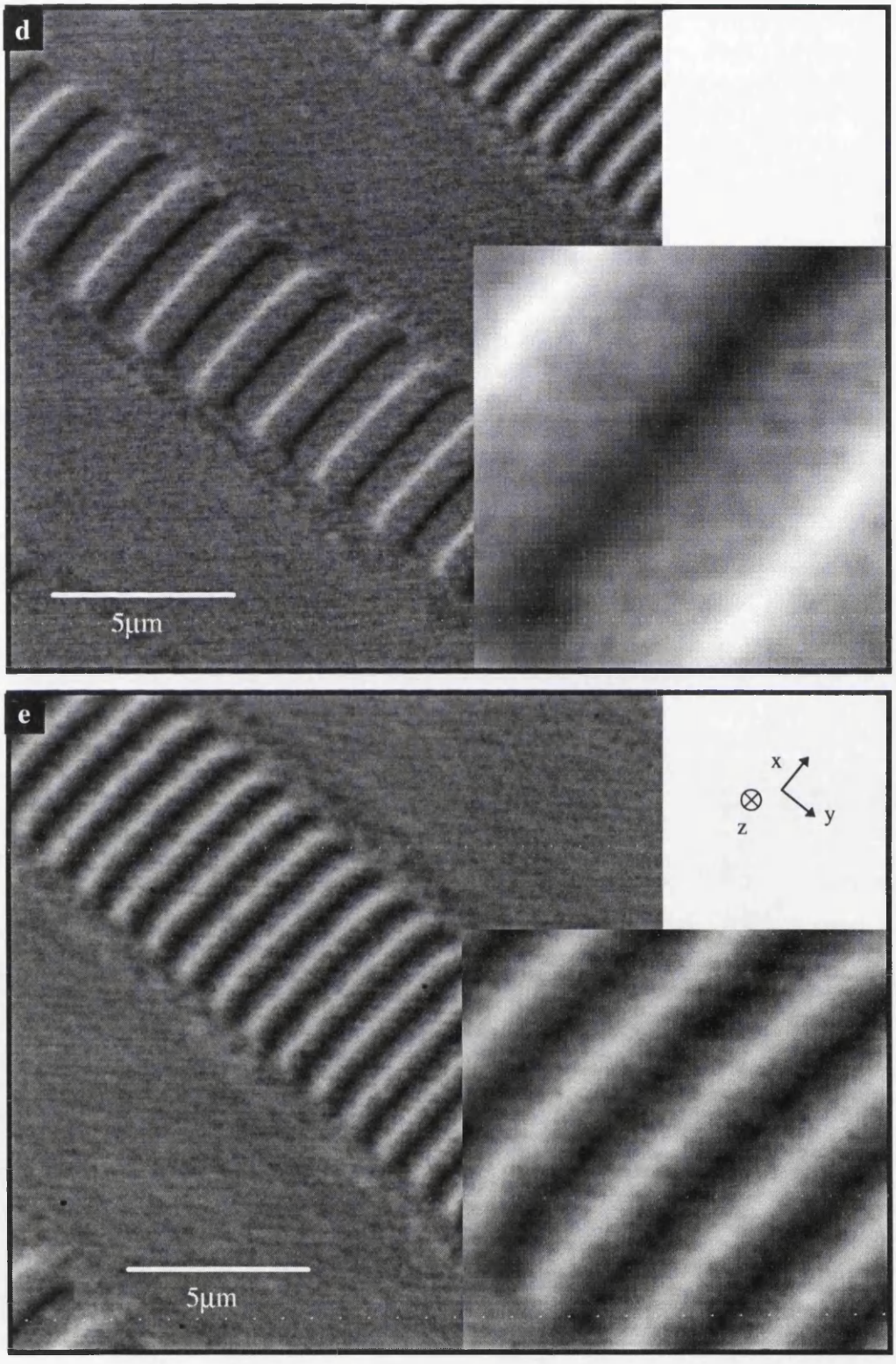

Fig.5.36 MFM images taken of medium of type 1 of d) the 1μm and e) the 0.5μm tracks.

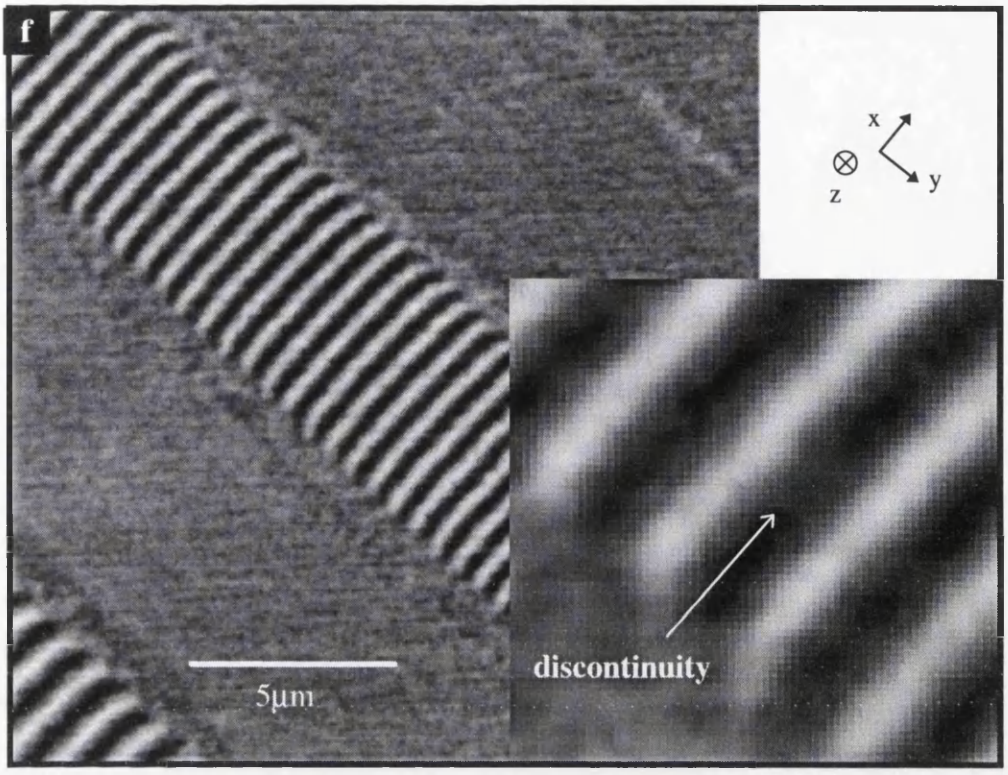

Fig.5.36 MFM images taken of medium of type 1 of e) the 0.33μm track.[courtesy of Drs T.C.Arnoldussen and T Chang of IBM corp., SSD, California].

prominent as a region of ~0.5μm in width at the side of all tracks in Figs.5.36b-f. This is seen at the edges of all the track and must therefore be independent of the bit length.

5.5 CONCLUSIONS

The aim of this chapter was to investigate the magnetic structure of two types of thin film magnetic recording media. A tilting method of reducing scratch contrast in TEM and STEM modes was discovered. This reduces considerably the time taken to produce TEM results from complete textured hard disk to specimen as the sputter etch of the Cr seed layer was not necessary. The reasons for this important observation have not yet been ascertained but we believe that the solution lies in the effect of the texturing on the diffraction pattern formed in the back focal plane of the objective lens. Fresnel and Foucault images were presented of both media types showing important features

such as the bit transition and the side write regions. The bit transition is estimated to be 0.15μm in width from these images. Evidence of clustering was also seen in the Fresnel images at the side write region.

MDPC imaging was then used to add to the information from the TEM modes. A simple but effective way of verifying the mapping directions using alternate DC erasure banding was outlined. The MDPC images of both media types take characteristic forms when mapped in and orthogonal to the write direction. The stray field above each bit tends to cancel the electron deflection due to the magnetisation of the written bits producing near null deflection in the centre of the tracks in the MDPC images. The stray field is also prominent when mapping orthogonal to the write direction and dark and bright spots are formed at the corners of the written bits. This applies to all tracks with the exception of the 0.33μm track. In 0.33μm track small domains form which do not extend across the whole track width. Further investigation using higher magnification MDPC images showed the small domains tended to start and stop to give the expected bit transition length for this track. This effect has occurred at almost exactly twice the bit transition width estimated from the other MDPC images and the TEM images. High magnification MDPC images were used to examine the magnetic structure of the bit transition. It was found that the media supports three main types of transition; a zig zag, a vortex and a combination of the two, with experimental images of each and simulated data for comparison. A linescan was then taken across the DC transition to estimate the mean transition wall width. This was found to be ~80nm in width using a tanh(x/w) fitting curve. The final MDPC observation was that of a component of magnetic induction orthogonal to the write direction which alternates with each written bit along the length of the track. If the stray field direction and the direction of the magnetisation in each bit were not parallel then an uncompensated component of magnetic induction is created. This could occur if the write direction was angled with respect to an easy axis in the sample. The magnetisation in each bit relaxes back to this easy axis following writing producing an uncompensated component of magnetic induction. Alternatively if the head is skewed at an angle to the write direction then after the magnetisation relaxation an uncompensated component of magnetic induction is produced as the majority of the stray field remains fixed by the bit transitions. Both these explanations require the sample to support at least weak anisotropy. This is

contrary to the isotropic nature of the sample. However the texturing scratches are strong in these sample suggesting that these could give rise to a preferred magnetisation orientation in the sample.

Finally MFM images were presented showing the stray field above the sample surface. The stray field from the bit transitions showed less structure than in the MDPC images as expected. The stray field of the 0.33μm track confirms that the small domains form stray field at the expected 0.33μm intervals. There is however some evidence of discontinuities

REFERENCES CHAPTER 5

T. U. Chen, "The Micromagnetic Properties of High-Coercivity Metallic Thin Films and their Effects on the Limit of Packing Density in Digital Recording", ***IEEE Trans. Magn.***, Vol. 17, No.2, pp 1181-1191, 1981.

T. U. Chen and T. Yamashita, "Physical Origin of Limits in the Performance of Thin Film Longitudinal Recording Media", ***IEEE Trans. Magn.***, Vol. 24, No.6, pp 2700-2705, 1988.

M. F. Gillies, J. N. Chapman and J. C. S. Kools, "Micromagnetic Characteristics of Single layer Permalloy Films in the Nanometer Range", ***J. Magn. Magn. Mat.,*** 140-144, pp. 721-722, 1995.

S. McVitie and R. P. Ferrier, "Model Stray Field Calculations of a Longitudinal Recording Medium", ***J. Magn. Magn. Mat.,*** 104-107, pp.963-964, 1992.

F. J. Martin, PhD Thesis, University of Glasgow, 1992.

J. J. Miles, Private Communication, University of Manchester, 1995.

P. Grütter, "An Introduction to Magnetic Force Microscopy", ***MSA Bulletin***, Vol. 24, No. 1, pp.416-425, 1994.

C. Schönenberger and S. F. Alvarado, "Understanding Magnetic Force Microscopy", ***Z. Phys. B 80***, pp. 373-383, 1990.

CHAPTER 6

MICROMAGNETIC MDPC SIMULATIONS

6.1 INTRODUCTION

The inherent properties of MDPC image production can cause difficulty when interpreting images of recorded tracks due to their magnetically open structures. The written bits produce stray field outwith the sample which result in div$\mathbf{M} \neq 0$ where **M** is the magnetisation vector as discussed in section 1.6. As a result of this the path integral of the magnetic flux density, **B** along the electron beam trajectory contains two components; **H** outside the sample and **M+H** inside the sample where **H** is the magnetic field vector. Thus due to this open flux configuration MDPC images are not direct mappings of **M** within the recorded tracks. This chapter presents two simulation techniques which allow the production of MDPC images from known and variable magnetisation vector distributions. The ability to simulate MDPC images from the starting point of a magnetisation vector distribution is an extremely useful tool in the analysis of experimental MDPC images.

The two methods of MDPC simulation utilise different physical perceptions of the interaction between the magnetic induction of the sample and the electron beam. The first method uses a current model of the moving electrons and an Amperian current representation of the magnetic induction of the sample; the second method uses a phase modulation approach, producing MDPC images following differentiation of the calculated phase. Both models are presented with a view to using this data as an aid to understanding the experimental results and to allow a magnetisation reconstruction method to be introduced in Chapter 7. Each method is discussed and following the theory, examples of the resulting images and comparisons between them are given in section 6.3. The latter sections of this chapter will show results of simulated off-axis writing and head skewing experiments performed using the phase modulation approach to MDPC. The simulation results are compared with experimental images from both CoPtCr media from section 5.4.5.

6.2 SIMULATION TECHNIQUES

6.2.1 Amperian Current Method

The first simulation method follows the theory developed by Mallinson and Rao [1993] which is based on the fundamental electromagnetic equations of Maxwell [Corson and Lorrain 1962]. In Maxwell's electromagnetic theory, he postulates that a current carrying conductor induces a circulating magnetic field in the space around the conductor. Conversely his theory implies that a magnetic field supports a circulating current. The relevant Maxwell's equations are :

$$\nabla \times \mathbf{H} = \mathbf{J} + \frac{\partial \mathbf{D}}{\partial t} \qquad (6.1)$$

$$\nabla \times \mathbf{E} = -\frac{\partial \mathbf{B}}{\partial t} \qquad (6.2)$$

where **J** is the current density, **D** is the electric flux density, **E** is the electric field strength and $\times$ represents the cross or vector product. All other parameters are as previously defined.

The initial assumption in this theory is that an electron travelling along the path of the beam is analogous to a current carrying wire as described by equation (6.1), where any time dependence is neglected. Following this theory a sample of magnetic material with magnetisation **M** therefore has a current density **J** associated with it expressed as:

$$\mathbf{J} = \nabla \times \mathbf{M} \qquad (6.3)$$

Thus **M** produces circulating Amperian currents over the surface of the magnetised material. To apply this theory to Lorentz electron microscopy, consideration must be given to the elements representing the magnetic structure of the electron beam and the written bits in the medium.

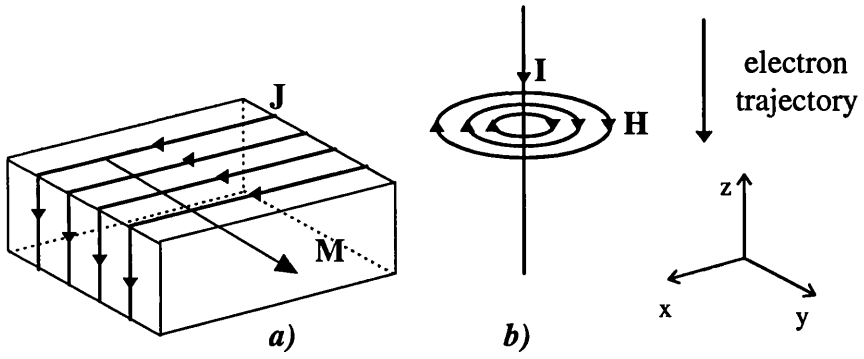

Fig.6.1 ***Diagrams of the two components in the Amperian current method a) a uniformly magnetised block and b) the electron beam / long straight conductor.***

The entire model system can be constructed using two components; a uniformly magnetised block and a single wire as depicted in Fig.6.1. A uniformly magnetised block has a surface current density which circulates around the magnetisation direction vector as described by equation (6.3). A recording track can then be 'built' from the addition of many uniformly magnetised blocks. From equation (6.3) the magnetic flux density surrounding the electron beam can be seen to be equivalent to that produced by a long straight current carrying conductor with a circulating **H** field. MDPC images are produced by addressing how the Amperian currents of the magnetised blocks interact with the current produced by the electron beam or a long straight conductor. Deflection of the electron beam due to a uniformly magnetised block can be viewed in this model as the action of the current density of a magnetised block on the current produced by the electron beam. For ease of calculation the problem can be reversed by applying Newton's law of equal and opposite reaction. Thus the deflection is the result of the action of the equivalent electron beam current on the Amperian currents of a magnetised block. It should be noted that this is only true where the currents are parallel [Mallinson and Rao 1993]. The magnetic flux density from the electron beam is then that of a long straight current carrying conductor which can be expressed as:

$$\mathbf{B} = \frac{\mu_o}{2\pi \mathbf{R}} \mathbf{I} \times \mathbf{r} \qquad (6.4)$$

where **I** is the effective current in the electron beam, **r** is a unit vector, **R** is the field point position vector and the other parameters are as previously defined. Before any calculation it is pertinent to study the interaction geometry of the Amperian currents. Through consideration of Fig.6.2 it can be seen that the x and y components of **J** produce $\mathbf{B}_\perp$ components which cancel and provide no net contribution to the force on the block. Effectively only the components of **J** parallel to the electron

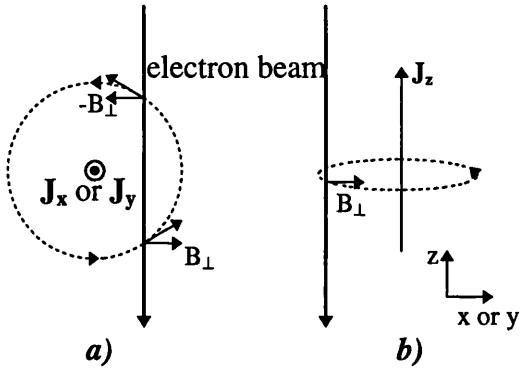

Fig.6.2 ***Interaction geometry of the B components (dashed lines) due to the Amperian currents J showing a) cancellation of the $B_\perp$ components due to J_x and J_y and b) the interaction of the z component of $B_\perp$ due to J_z.***

beam remain uncompensated and contribute to the deflection. Here these parallel components are the $\mathbf{J}_z$ Amperian currents. This creates significant simplification in the force calculation which reduces to the problem of considering the force experienced by a sheet of Amperian currents due to a single wire in a plane parallel to the sheet. Further, by considering a single Amperian current in the sheet the problem becomes the interaction between two parallel current carrying wires. Thus the force between an element of the sheet $M_r\delta dx$ and the electron beam can be expressed as:

$$d\mathbf{F} = \frac{0.2M_r\delta dx\mathbf{Ir}}{R} \qquad (6.5)$$

The Lorentz force on one electron beam integrated over the whole sheet of charge is then given by:

$$F_x = 0.2M_r\delta I \ln\left(\frac{S_2}{S_1}\right) \qquad (6.6a)$$

$$F_y = 0.2M_r\delta I(\theta_1 + \theta_2) \qquad (6.6b)$$

where the parameters are defined in Fig.6.3.

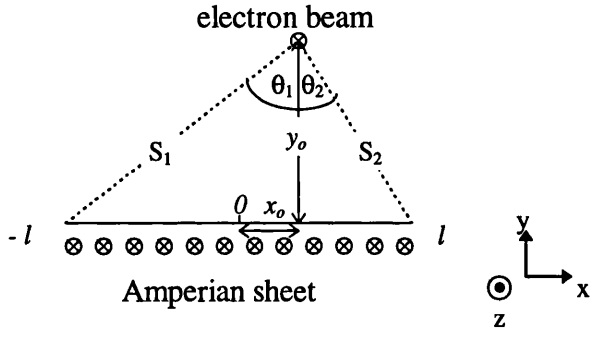

Fig.6.3 ***Plan view of a single sheet of Amperian current and a single electron beam defining the parameters used to calculate the Lorentz deflection of the electron beam due to a sheet of length 2l Amperian currents.***

The basis for modelling a track is a set of four Amperian current sheets representing the magnetisation distribution. Two oppositely magnetised written bits are represented by four Amperian current sheets with currents oriented along the z direction as in Fig.6.4a. Four further Amperian current sheets oriented in the z direction are added to represent the DC erasure bands either side of the track ~ 100μm in width, as in Fig.6.4b. Cancellation between Amperian currents occurs along the region where Amperian currents of opposing directions meet, as in regions B-C and D-E in Fig.6.4b. As a result of this no boundaries are generated in these regions. Conversely, at the regions A-B and E-F the Amperian currents are in the same direction and thus reinforce. A complete track is constructed by repeating the basis configuration of sheets as in Fig.6.4c. It is essential to use such a large array of basis elements to attempt a reduction in the

presence of any edge effects which would otherwise influence the MDPC images produced. The scanning area is then chosen to be at the centre of the tracks where edge effects would be expected to be a minimum, denoted by the shaded region in Fig.6.4c. The alternate DC erasure bands are required as an aid for use as a reference when scaling the images between simulation methods.

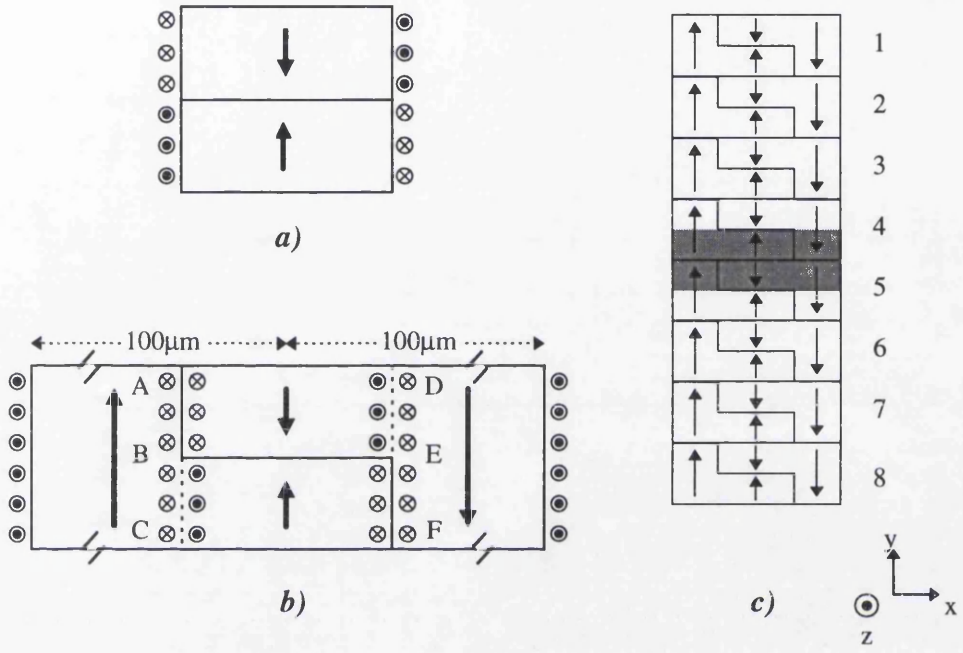

Fig.6.4 ***The Amperian current model elements are a) two magnetised bits, b) the repeating basis and c) a track built from the basis. The shaded area represents the area scanned to reduce the edge effects due to a finite track length.***

6.2.2 Phase Modulation Method

The second approach to MDPC image simulation interprets the interaction of the beam and sample as a phase modulation of the beam due to the sample. Chapter 2 discussed the Aharonov and Bohm effect [1959] which postulates that two electron beams originating from the same source, passing through a magnetic sample, undergo a phase change relative to one another when brought together after the sample. The phase change produced is proportional to the enclosed magnetic flux between the paths. Following this theory a magnetic sample can be viewed as a phase modulating object to the incoming electron beam.

The starting point of this theory development is the magnetic vector potential expressed in terms of the magnetisation of a general thin film. Through the use of Fourier analysis, the phase imparted by the magnetic thin film to the electron beam can be calculated [Mansuripur 1991]. The theory can be used to calculate the imparted phase function for a thin magnetic film with a defined array of magnetisation vectors which can be oriented in any direction with the proviso that the sample is magnetised uniformly in the z direction. The theory also incorporates electron beam incidence from any angle with respect to the sample. The results were used to produce Fresnel and Foucault contrast images. The theory has been extended further by differentiating the phase mapping produced to simulate MDPC images [Plöβl 1993].

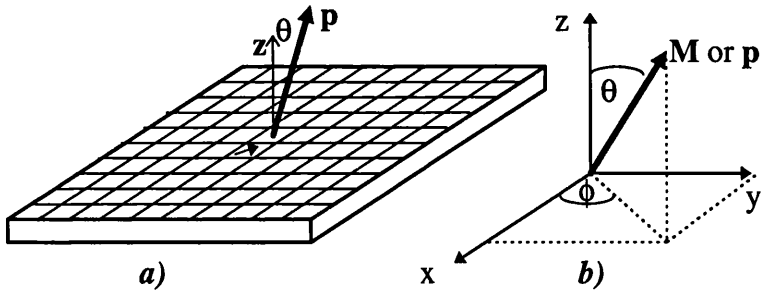

Fig.6.5 Diagram of a) the magnetisation array and the electron propagation vector **p** *and b) the magnetisation direction parameters.*

The formulae produced from this theory are lengthy and require in-depth

explanation which is suitably contained in either of the two texts referenced and will not be covered here. It is necessary however to define some parameters before any results from this theory can be interpreted. The initial magnetisation setup is defined over an array of 256 by 256 pixels. At each point in the array two angles defining the orientation of **M** are specified. The angles are denoted as θ and ϕ defined in Fig.6.5 as those angles made with respect to the z axis and the x axis respectively, this completely defines **M**. In the configuration necessary for the track setup **M** is only oriented in two directions either parallel or anti-parallel to the y axis as defined in Fig.6.6.

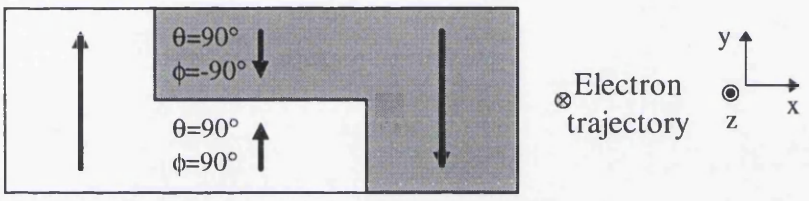

Fig.6.6 ***Diagram of written bit setup in the Phase modulation simulation defining the values of M.***

6.3 RESULTS

The MDPC images produced using the two simulation techniques described above are presented in this section. The images produced by both simulation methods are produced from an area of 10μm × 10μm with a scanning resolution, Δ = 39nm (each image is 256×256 pixels). The thin film used in each case has a track width of 5μm, a film thickness of 35nm and $M_R\delta = 2.5 \times 10^{-3}$ emu/cm^2 as defined by the experimental media of chapters 4 and 5. Bit lengths of 1μm and 5μm have been used in both methods to check agreement of effects seen at these bit lengths between the model and the experimental MDPC images. The images are correctly scaled using the alternate DC erasure bands to values of approximately 57 and 200 for the DC- and DC+ values on an 8 bit grey scale. This gives an expected 'null deflection' value of 128 and a maximum DC± shift of ±72 from null deflection.

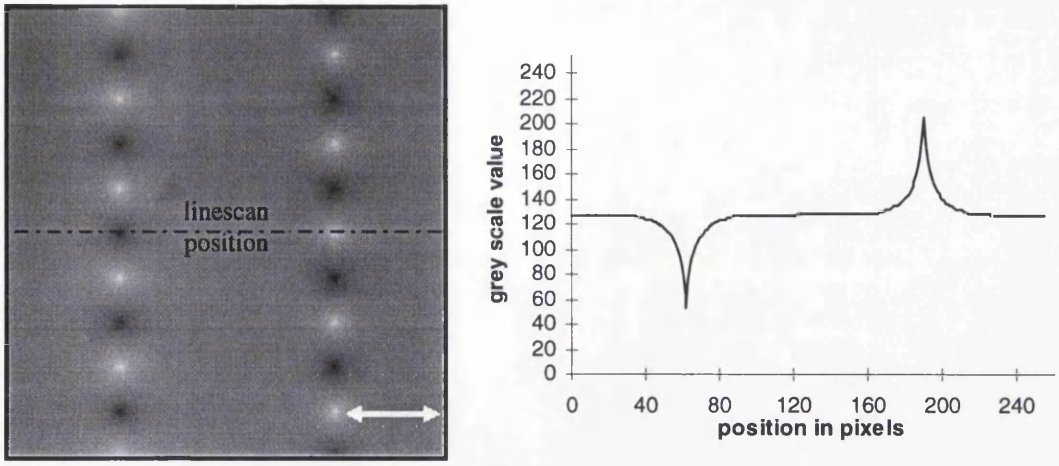

Fig.6.7 MDPC image mapped in the x direction of a 1μm bit length track produced using the Amperian Current simulation method with the associated linescan taken over the image at the marked position.

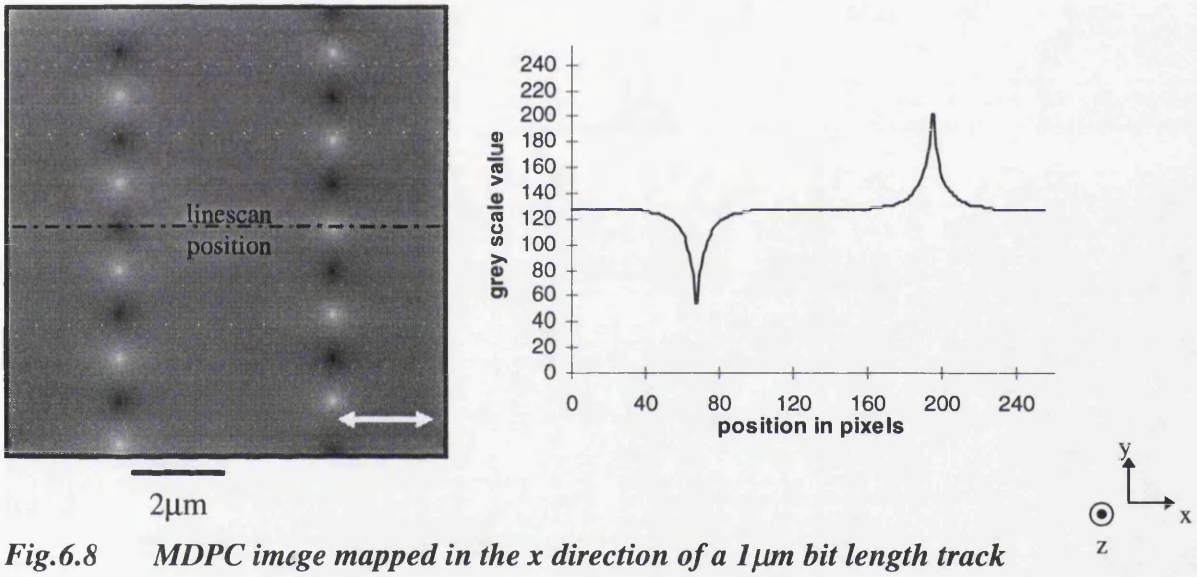

Fig.6.8 MDPC image mapped in the x direction of a 1μm bit length track produced using the Phase Modulation simulation method with the associated linescan taken over the image at the marked position .

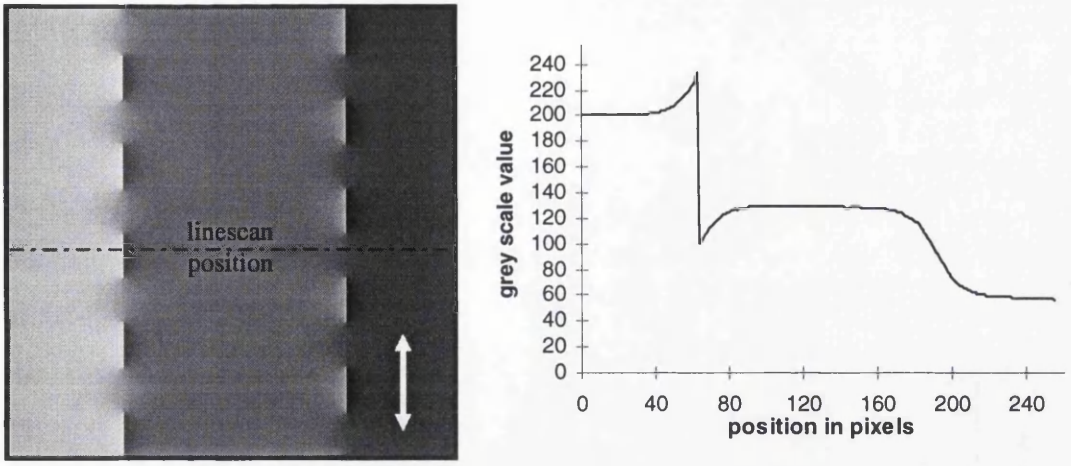

Fig.6.9 ***MDPC image mapped in the y direction of a 1μm bit length track produced using the Amperian Current simulation method with the associated linescan taken over the image at the marked position.***

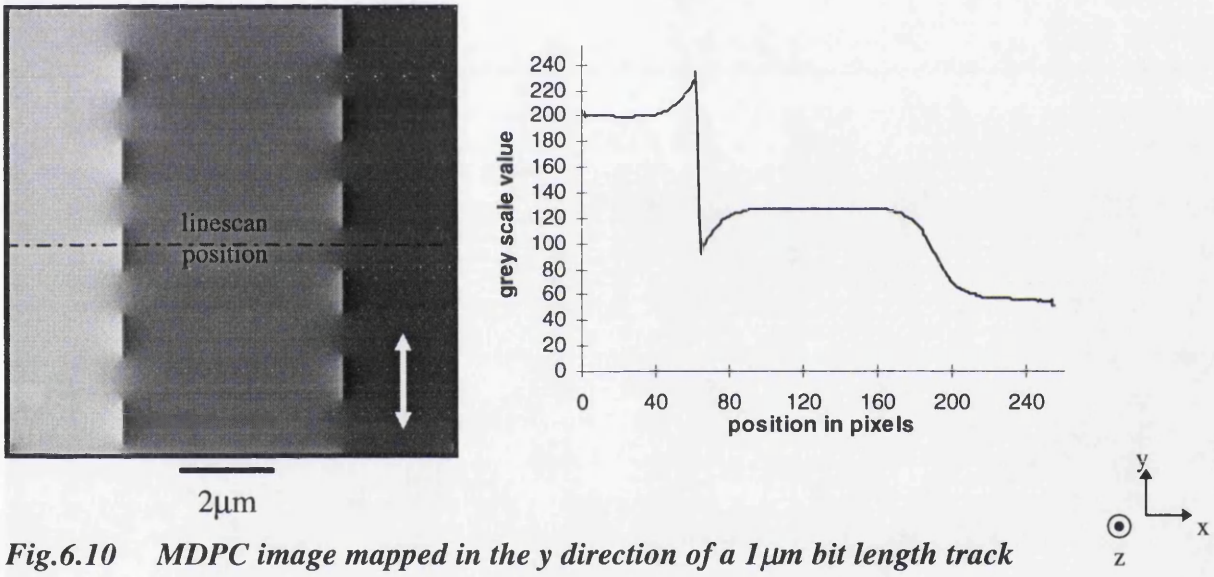

Fig.6.10 ***MDPC image mapped in the y direction of a 1μm bit length track produced using the Phase Modulation simulation method with the associated linescan taken over the image at the marked position .***

The simulated MDPC images of 1μm tracks are shown in Figs.6.7 - 6.10. Figs.6.7 and 6.8 show 1μm bit length x mapped MDPC images produced by the Amperian and Phase Modulation methods respectively. A linescan is shown to the right of each image which is scanned along the positive x axis of each of the images.

The simulated MDPC images in Figs.6.7 and 6.8 show similar contrast to the experimental MDPC images in Fig.6.11a and in chapter 5; the x mapped characteristic of alternate closure spots at the corners of the written bits and 'null deflection' over the remainder of the scanned area. Also comparing the linescans produced by each method both results are very similar starting at a null contrast level of ~128 as expected, peaking at the closure spots with a flat profile at ~128 in the centre of the linescans confirming the 'null deflection' expected in that area. Thus both simulations produce x mapped MDPC images which are consistent with the experimental x mapped MDPC images of chapter 5. In Fig.6.11a the closure spots are obscured by the side write configuration at the track edges.

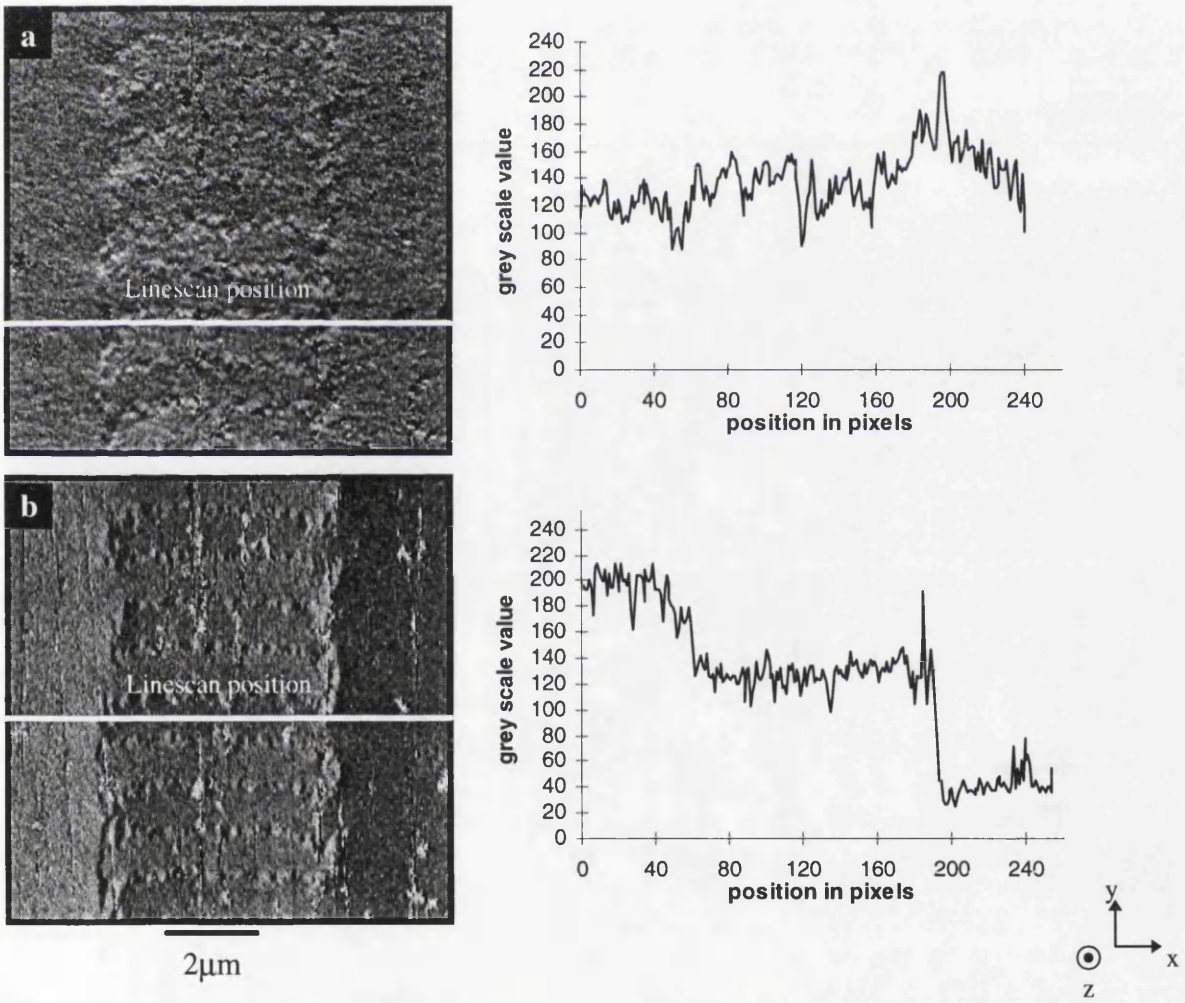

Fig.6.11 Experimental MDPC images mapped in a) the x and b) the y directions of a 1μm bit length track with the associated linescan taken over the image at the marked positions .

Figs.6.9 and 6.10 show y mapped MDPC images resulting from the Amperian current and Phase modulation methods respectively. As in the x mappings above, the images show very similar contrast to that seen in the experimental y mapped MDPC images in Fig.6.11b and in chapter 5. A linescan is shown to the right of each image which is scanned along the positive x axis of Figs.6.9 and 6.10. The DC + and DC- erasure bands can clearly be distinguished in the images of Figs.6.9 and 6.10 and in both linescans. The linescans start at the DC erasure value of 200 (DC+), pass through the stray field closure, the track edge where the magnetisation changes sign, null deflection in the centre of the track at 128 to a value of 57 (DC-) the edge of the scanned area. Thus the DC level adds or subtracts 72 to the null deflection in this set of images. Again this profile is consistent with the experimental y mapped MDPC results of Fig.6.11b chapter 5. The results of the simulation compare well with the experimental results of the set of MDPC images. In both experimental linescans in Fig.6.11, the experimental noise reduces the clarity of the linescans in comparison to the simulated data.

It was also noticed in the experimental MDPC results of section 5.4.2 that if the bit lengths were comparable in size to the track width, the stray field above and below each bit would not fully cancel the deflection due to the magnetisation leaving an alternate contrast level in the y mapping. This can also be investigated using the simulation techniques. Figs.6.12 to 6.15 show sets of images from both simulation methods using a 5μm bit length. Figs.6.12 and 6.13 are the x mapped MDPC images produced using the Amperian and the Phase modulation methods respectively. The contrast produced is again similar to the experimental images seen in Fig.6.16 and in chapter 5. Again there is close agreement between the two simulation methods. There is however a significant difference between the images produced at 5μm to those at 1μm bit lengths. In Figs.6.12 and 6.13 the closure spots cover an area of ~5μm; null deflection does occur at the centre of the track but over a very small area of only a few pixels in width where each pixel represents 39nm.

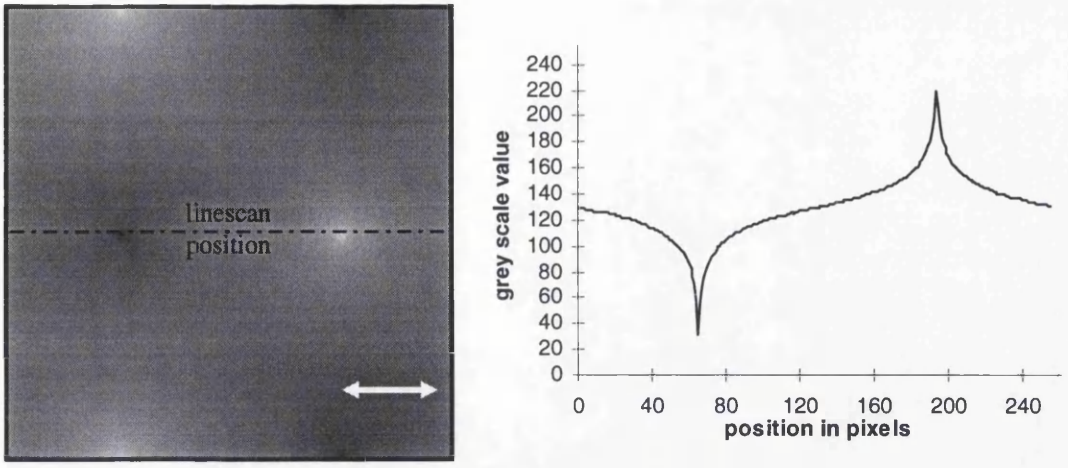

Fig.6.12 ***MDPC image mapped in the x direction of a 5μm bit length track produced using the Amperian Current simulation method with the associated linescan taken over the image at the marked position.***

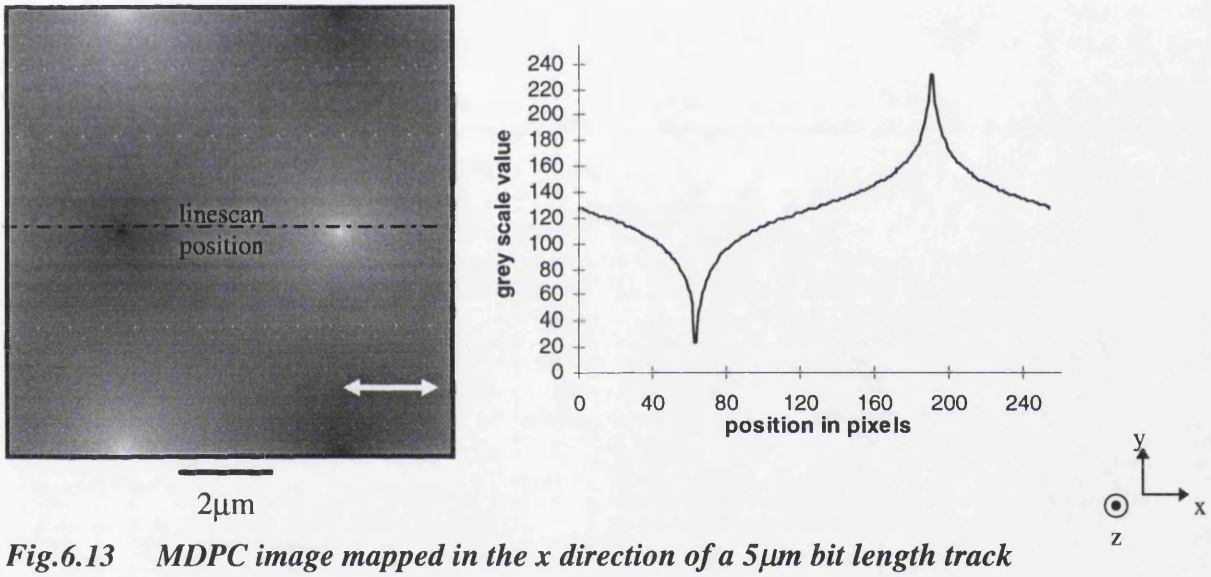

Fig.6.13 ***MDPC image mapped in the x direction of a 5μm bit length track produced using the Phase Modulation simulation method with the associated linescan taken over the image at the marked position.***

Similarly Figs.6.14 and 6.15 show y mapped MDPC images simulated using the Amperian and Phase methods respectively with their associated linescans shown to the right of each image scanned left to right. The images are again very similar between the two methods which is verified by the linescans. Again the linescans suggest a larger spreading of the stray field in comparison to that of the 1μm tracks. From the linescans taken at position 1, it is apparent that the DC bands contain a large amount of stray field

as the DC+ grey level is 220 and the DC- level is 68 which is an increase of approximately 25% of the maximum DC deflection obtained from the 1μm images. Taking the phase simulation and scanning across the other track at linescan position 2 left to right as before, a similar difference is seen and the DC levels are now

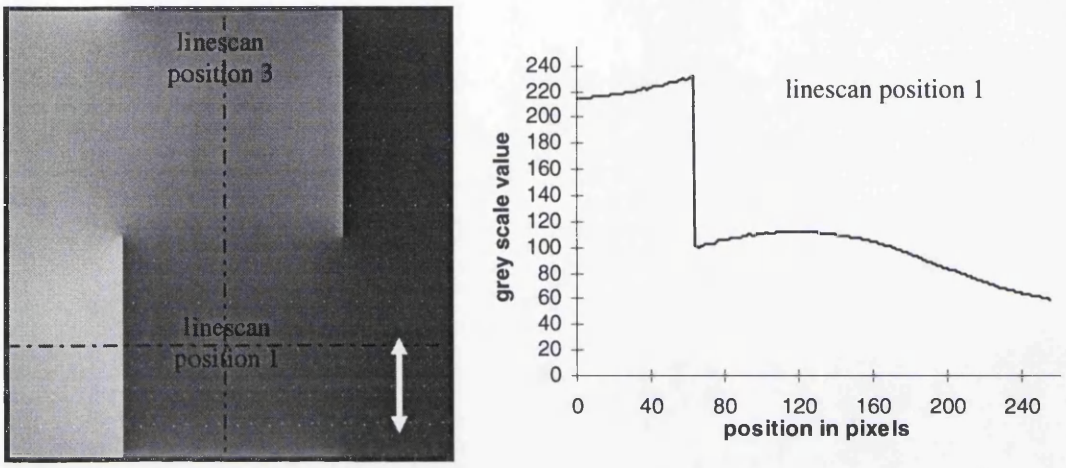

Fig.6.14 ***MDPC image mapped in the y direction of a 5μm bit length track produced using the Amperian Current simulation method with the associated linescan taken over the image at the marked position.***

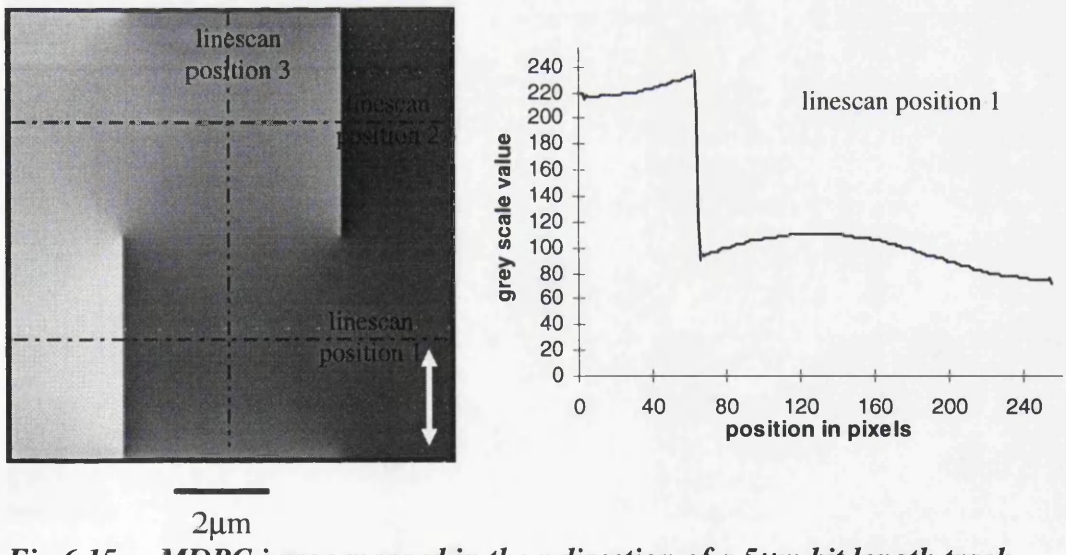

Fig.6.15a ***MDPC image mapped in the y direction of a 5μm bit length track produced using the Phase Modulation simulation method with the associated linescan taken over the image at position 1.***

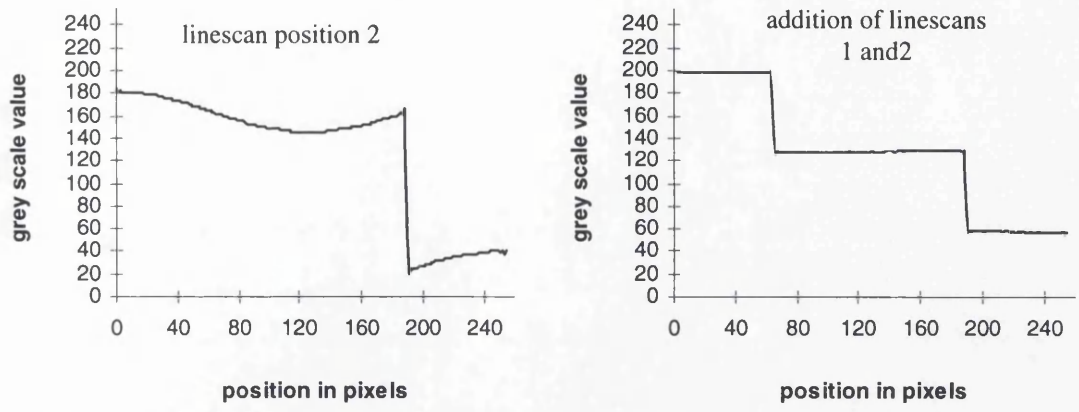

Fig.6.15b The associated linescans taken over the image at the position 2. The final linescan is the addition of the linescans taken at positions 1 and 2.

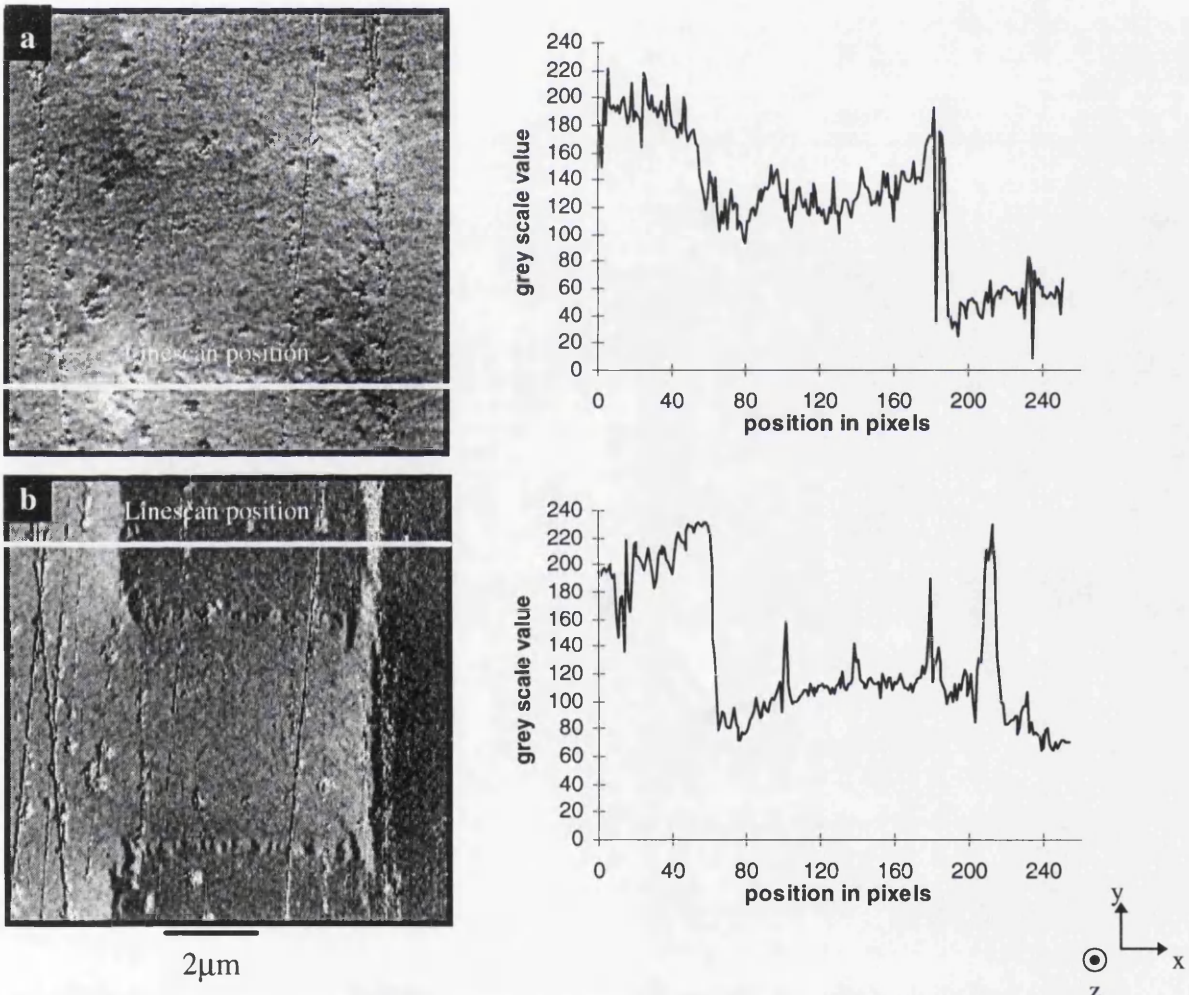

Fig.6.16 Experimental MDPC images mapped in a) the x and b) the y directions of a 5μm bit length track with the associated linescan taken over the image at the marked positions .

180 and 41, approximately a 25% decrease in the grey level with respect to the 1μm images. Adding the two linescans produces a composite linescan with grey levels of 200 and 57 at the positions of the DC erasure. The cancellation occurs due to the change in the sign of the expected stray field components between linescans at positions 1 and 2 due to the alternate magnetisation in the written bits. This also confirms that the images are correctly scaled with respect to the 1μm images as the levels are very similar.

Again comparisons can be drawn between the simulated and experimental MDPC results. Fig.6.16 shows a set of MPDC images of a 5μm track. The linescans produced are shown to the right of each image as before. The linescans are very similar to the results seen in Figs.6.12-14 further confirming the validity of the results.

A third set of simulation linescans taken at position 3 along the negative y axis of Figs.6.14 and 6.15, are shown in Figs.6.17 and 6.18. There is significant difference in the grey levels between the bits the maximum grey level of ~146 and minimum of ~109 on the eight bit scale which is ~24% of the maximum DC offset. The maximum grey level in Fig.6.17 corresponds to the y position of linescan 2 which has a minimum contrast level in the track centre. Similarly the position of minimum contrast corresponds to the position of linescan 1. Thus an increase in the stray field outwith the bits is compensated by an equivalent decrease in the stray field above the track. The 1μm simulated MDPC images scanned over the same area in the y direction produce a constant grey level of 128.

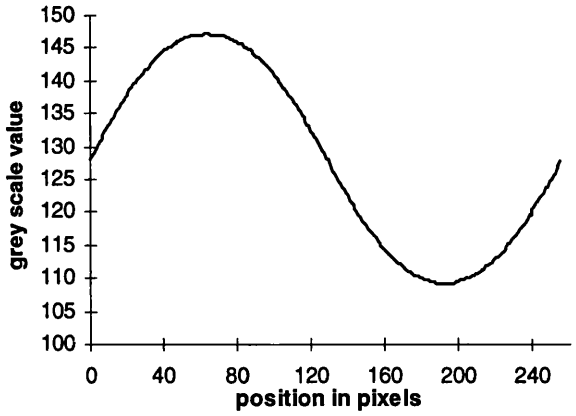

Fig.6.17 Linescan of Fig.6.14 at position 3

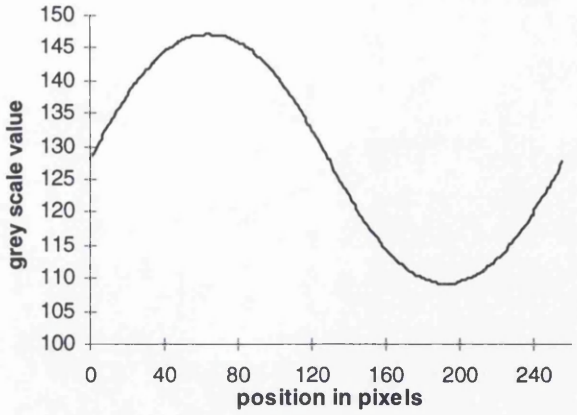

Fig.6.18 Linescan of Fig.6.15 at position 3

These results can be compared directly with the experimental results of Fig.6.19. Fig.6.19a shows a y mapped MDPC image of a 5μm bit length and 5μm width track in medium of type 1 ($M_r\delta = 2.5 \times 10^{-3}$ emu/cm^2). The image is scaled using the linescan taken at the DC+ and DC- bands on either side of the track, also shown in Fig.6.19c and d. There is close agreement between the experimental linescan in Fig.6.19b and the simulated linescans of Figs. 6.17 and 6.18 further confirming the validity of the method and the results. A simulated linescan is overlaid on Fig.6.19b.

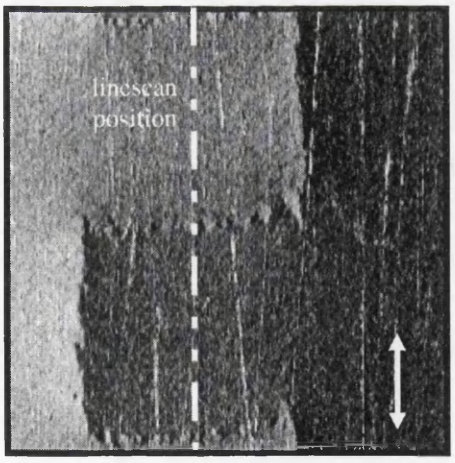

a)

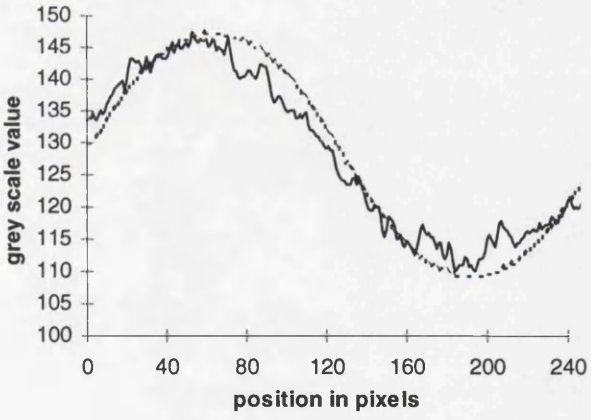

b)

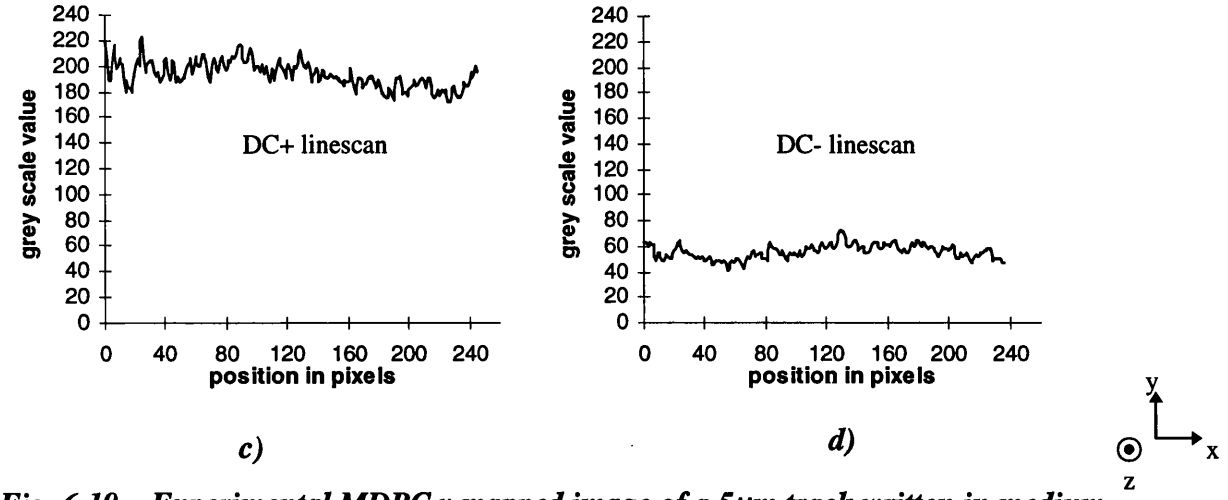

Fig. 6.19 Experimental MDPC y mapped image of a 5μm track written in medium of type 1 with a track width of 5μm with the linescan scanned over the centre of the track (the simulated data is shown by the dotted cuvre). The scaling DC+ and DC- linescan averaged over the DC band are also shown.

6.4 ALTERNATE BIT CONTRAST SIMULATION

6.4.1 Introduction

In the preceding chapter MDPC images were presented which displayed significant contrast level difference between alternate bits when mapped in the x direction. It was suggested that the depth of contrast seen was the result of one of two possible mechanisms; either off-axis writing or head skewing. The explanations proposed that these mechanisms introduced a misalignment between the stray field above and below the film and the magnetisation within the film creating an uncompensated component of magnetic induction in the cross-track direction. Using the above techniques these mechanisms can be simulated and the resulting MDPC images can be compared with experimental images.

The remainder of this chapter can be divided into three sections; off-axis writing, head skewing and a combination of both effects. MDPC images are presented for each of the mechanisms.

6.4.2 Off-axis Writing

The first mechanism resulting in the introduction of misalignment between the stray field and the magnetisation is that due to off-axis writing as discussed in section 5.4.5. The results of chapter 5 postulate the existence of a slight easy axis in the isotropic media to explain the cross-track contrast seen in the experimental MDPC images. In this case the write direction is inclined in-plane at an angle with respect to the direction of the assumed easy axis of the medium. Following removal of the write head field, the magnetisation vector can relax from the write direction to the easy axis direction of the medium. This produces uncompensated components of magnetic induction in the x direction which can give rise to the alternate contrast seen in the x mapped MDPC images.

The easiest and quickest of the simulation methods is the phase modulation technique. A typical input magnetisation vector distribution which produces off-axis writing is shown in Fig.6.20. Here the direction of the easy axis is varied whilst the write direction is kept constant for ease of calculation. The off-axis angle, $\alpha°$ is defined as the angle between the easy axis and the write direction of the head. This simulation method uses a matrix of magnetisation vectors which sum to form the total magnetisation of the medium. As a result of the relaxation of the magnetisation, the free poles previously concentrated at the bit transitions can redistribute within the film allowing free poles to exist at the boundaries with the DC erasure, in regions such as shown in Fig.6.20 along A-B and C-D.

The MDPC results from running the Phase Modulation method simulation using off-axis write input magnetisation distributions of the type described above are shown in Fig. 6.22.

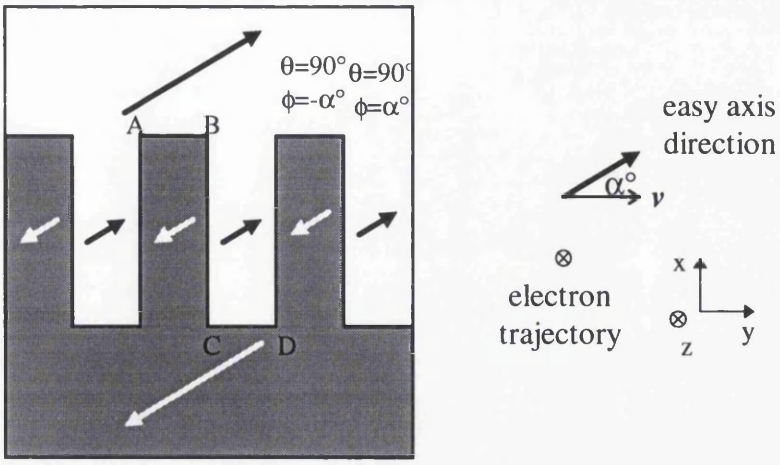

Fig.6.20 Schematic diagram of the magnetisation setup for off-axis writing used in the phase simulation method.

The images in Fig.6.22 are mapped in the x direction and form a series where the off-axis angle, $\alpha°$ varies from 0° to 25° in steps of 5°. Continuous contrast bands are produced across each bit due to the uncompensated components of magnetic induction adding to or subtracting from the grey level along the track direction. Before comparisons can be made between the images produced by this simulation, the grey scale levels must be adjusted. The alternate DC erasure bands allow the images to be rescaled. The maximum grey scale value expected from the DC erasure bands can be obtained from the y mapped MDPC image with $\alpha° = 0°$, this is denoted DC(0°). Using a simple coherent rotation model of the magnetisation as in Fig.6.21, the value of DC(α) is calculated using equation (6.7). Thus the expected DC band values in both the x and y mappings at any value of $\alpha°$ can be calculated and the images can then be set to these values.

$$DC(\alpha°) = |DC(0°)| * \cos\alpha° \qquad (6.7)$$

Equation 6.7 is used to set the contrast levels in the of the images in Fig.6.22.

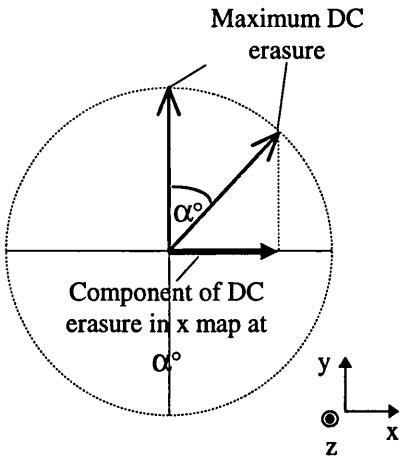

Fig.6.21 ***A coherent rotation model approach to the evaluation of the DC erasure level in an x mapped image with an off axis write angle of α°.***

These simulated x mappings contain very similar contrast effects to those seen in the experimental MDPC images of Figs.5.30a, c and 5.32a in section 5.4.5. There is a linescan shown to the right of each MDPC image in Fig.6.22 taken along the y direction. This allows a closer examination and comparison of the grey levels between each image. The linescans are integrated over an area of 80 pixels in the x direction for each mapping; this is the maximum extent in the x direction possible before being influenced by the closure spots. The integration smooths out any local variations in the contrast providing a mean result. The linescans show that as the off-axis angle is increased, the difference in the grey contrast levels in the bits also increases, as expected. Fig.6.23 shows a plot of α° against the difference in the grey levels between alternate bits taken from the linescans of Fig.6.22. From this plot it can be seen that there is a linear relationship between the off-axis angle and the difference in contrast levels. Thus

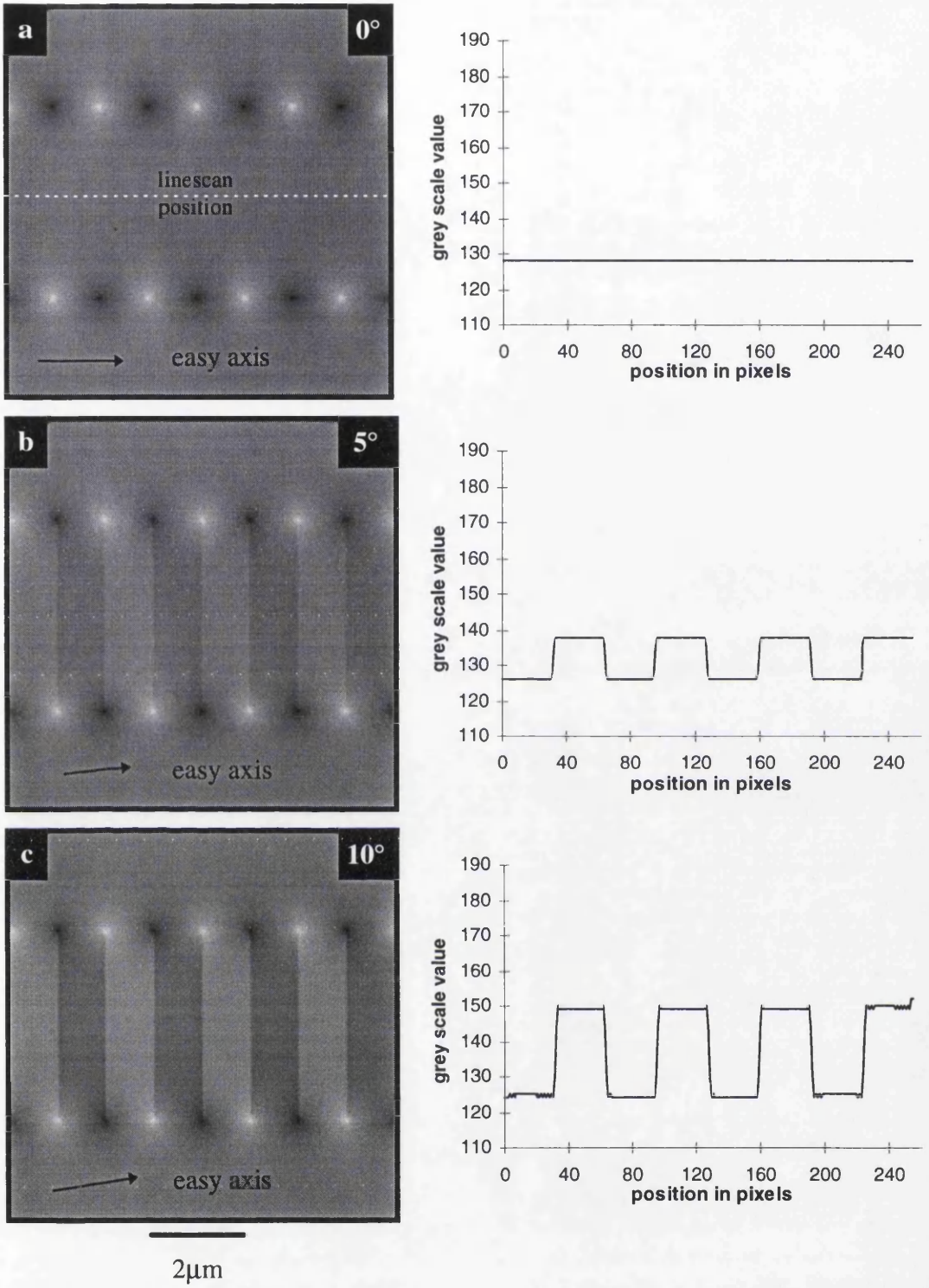

Fig.6.22 (a) - (c) Simulated MDPC off-axis writing images mapped in the x direction with their associated linescans in the x direction.

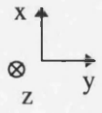

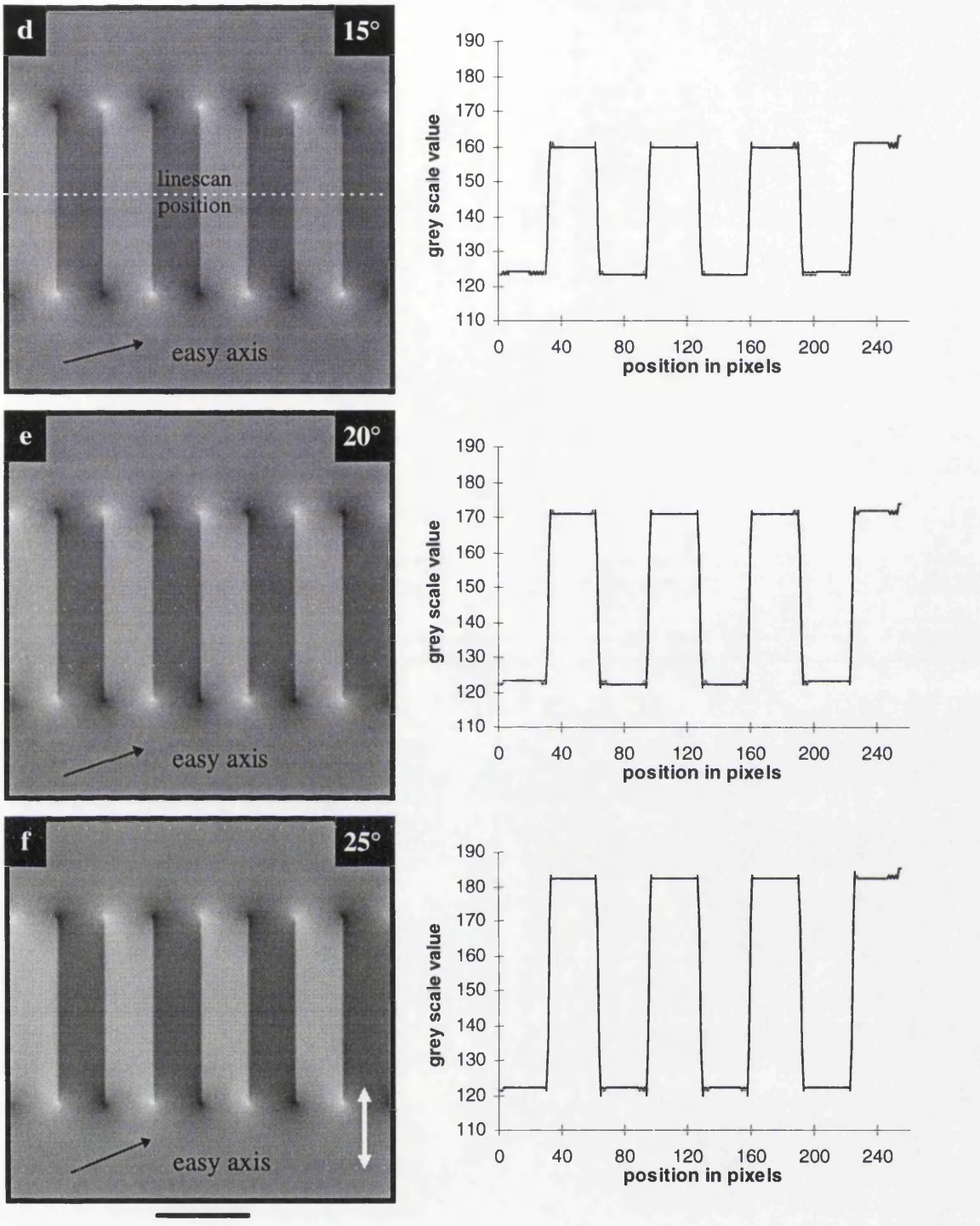

Fig.6.22 ***(d) - (f) Simulated MDPC off-axis writing images mapped in the x direction with their associated linescans in the x direction.***

the approximate off-axis angle in the experimental MDPC images mapped in the x direction can be estimated using the difference in the grey level of the alternate bits and

the plot of Fig.6.23. The experimental data is scaled to the simulated data using the DC erasure bands and the grey level of both mapping directions.

Fig.6.24 shows an experimental MDPC image displaying alternate bit contrast as described above. The bit transitions are not angled with respect to the y axis thus it is more likely that the contrast seen in this image is due to off-axis writing. Each bit in Fig.6.24 is ~26 pixels in length, the difference in the grey levels of the bits is estimated from this image by averaging over each bit as above. The linescan taken across image is also shown in Fig.6.25. The grey level difference between alternate bits is defined by the

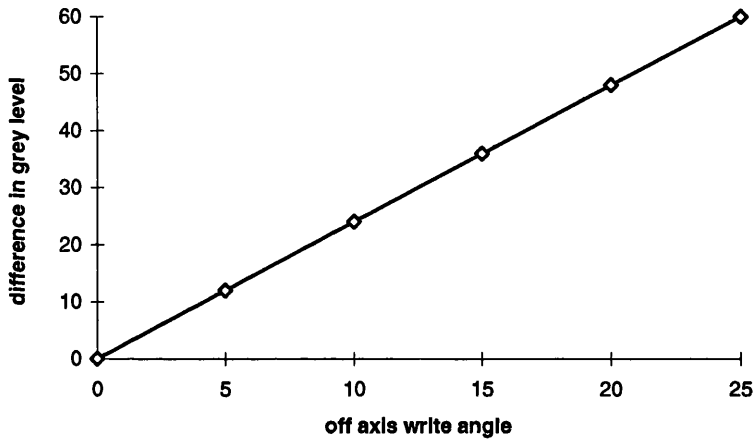

Fig.6.23 ***Plot of difference in grey levels in Fig.6.12 against off-axis writing angle, α°.***

image in Fig.6.24 to be 56 on an 8 bit scale. Using the plot of Fig.6.23, this gives an estimate of the off-axis writing angle to be $\alpha^{\circ} \sim 23^{\circ}$ from the easy axis

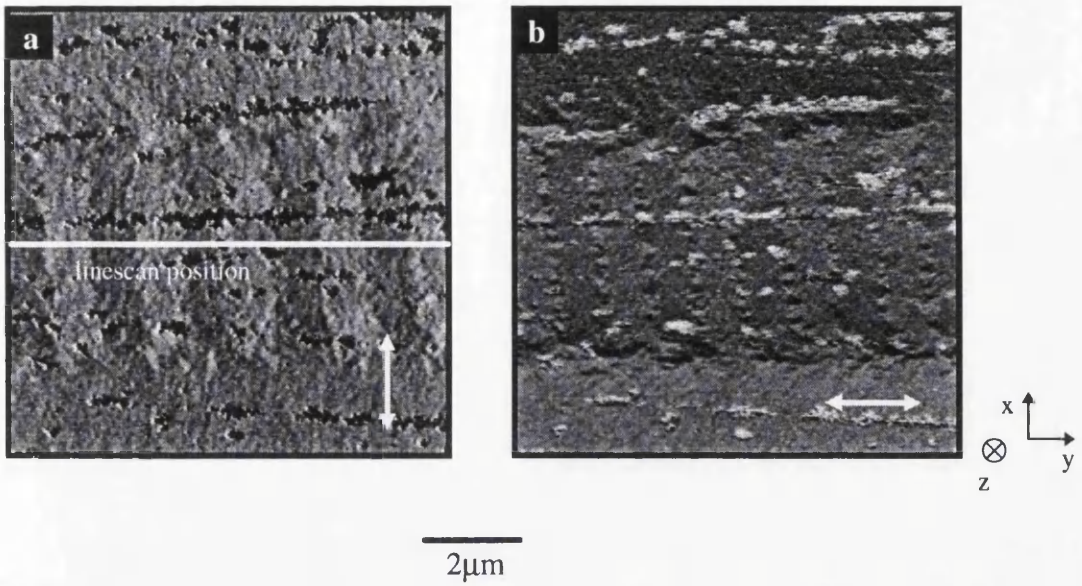

Fig.6.24 ***MDPC images of 1μm track which show alternate bit contrast when mapped in the x direction.***

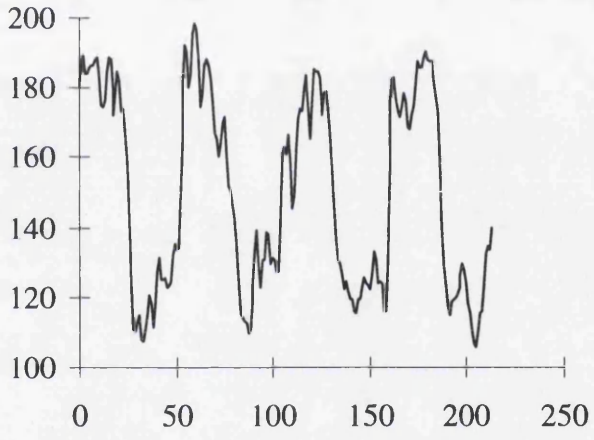

Fig.6.25 ***Experimental MDPC image of 1μm track written in type 1 medium mapped in the x direction showing alternate bit contrast with the associated linescan taken over the area marked.***

6.4.3 Head Skewing

There is a second mechanism which could be responsible for the production of alternate contrast across a track; this mechanism is head skewing. As discussed in

chapter 5, head skewing occurs when the pole gap of the write head is not orthogonal to the write direction. This is shown diagrammatically in Fig.6.26, where the written bits are inclined at an angle β°, to the normal to the write direction. Head skewing is a common effect due to the increasing use of rotational drive arm geometries to reduce the overall space occupied by the complete drive. In Fig.6.26 the write direction, the easy axis and the y axis are all collinear. Thus on removal of the write head field the magnetisation remains along the easy axis. However the stray field remains orthogonal to the bit transitions and introduces the uncompensated components of magnetic induction in the x direction.

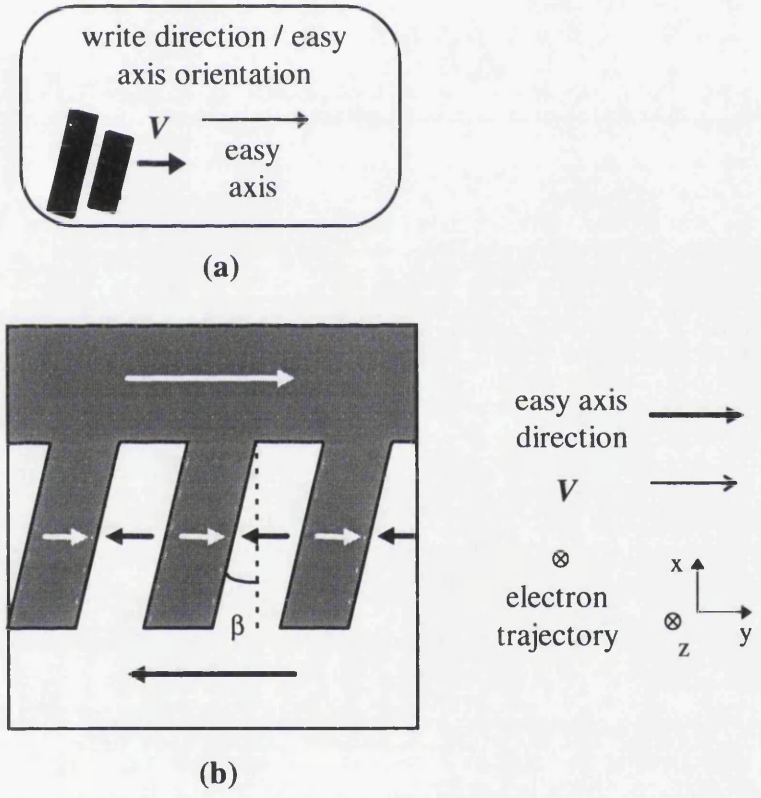

Fig.6.26 ***Schematic diagram of a) the head skewing and b) the magnetisation configuration produced. This is used as the input magnetisation distribution in the phase simulation method.***

Throughout this examination the pole pieces are assumed parallel and it is the entire

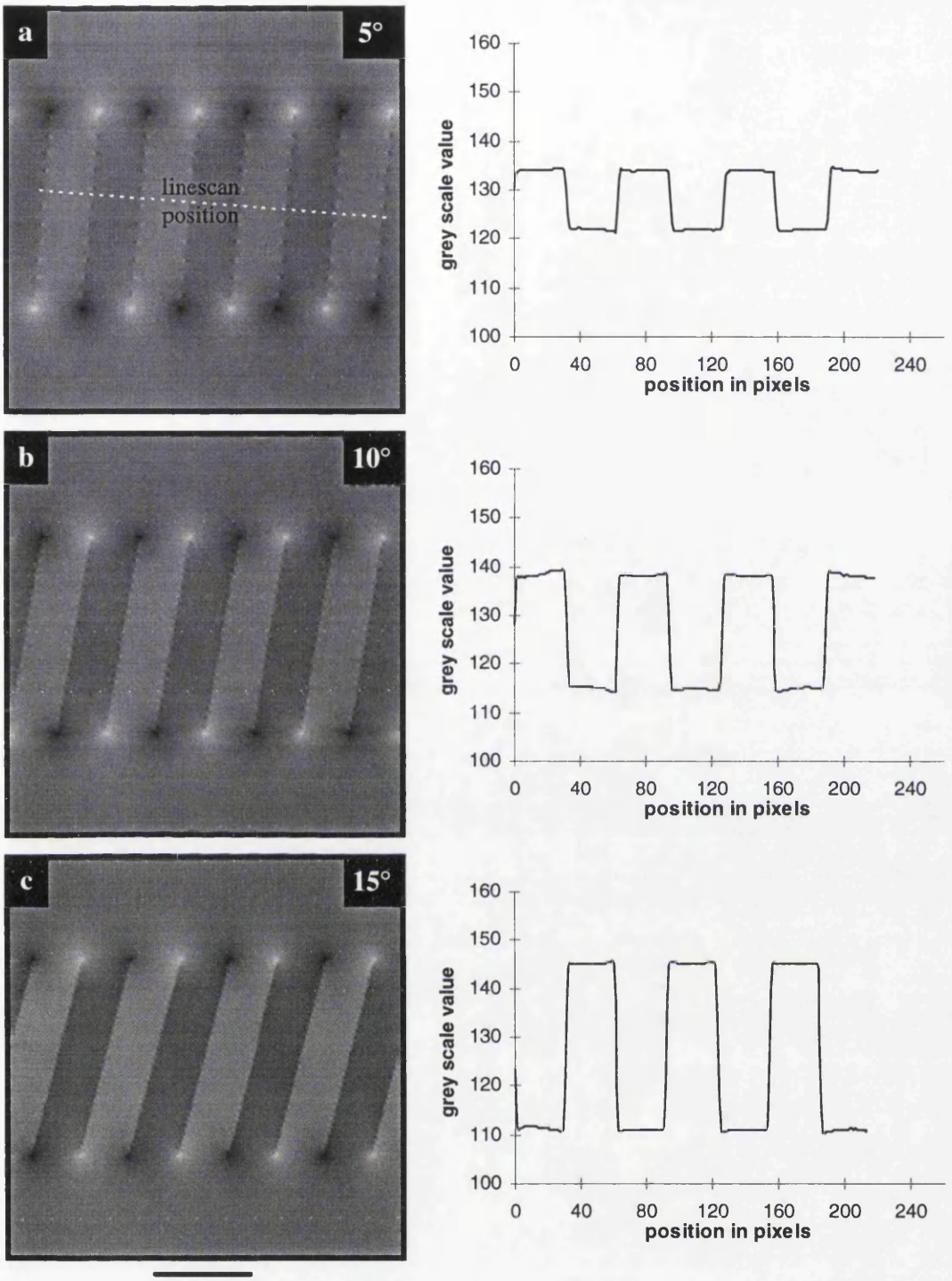

Fig.6.27 ***Simulated MDPC images of head skewing where the head is skewed at angle to the write direction. To the right of each image the associated linescan taken over the area marked is shown .***

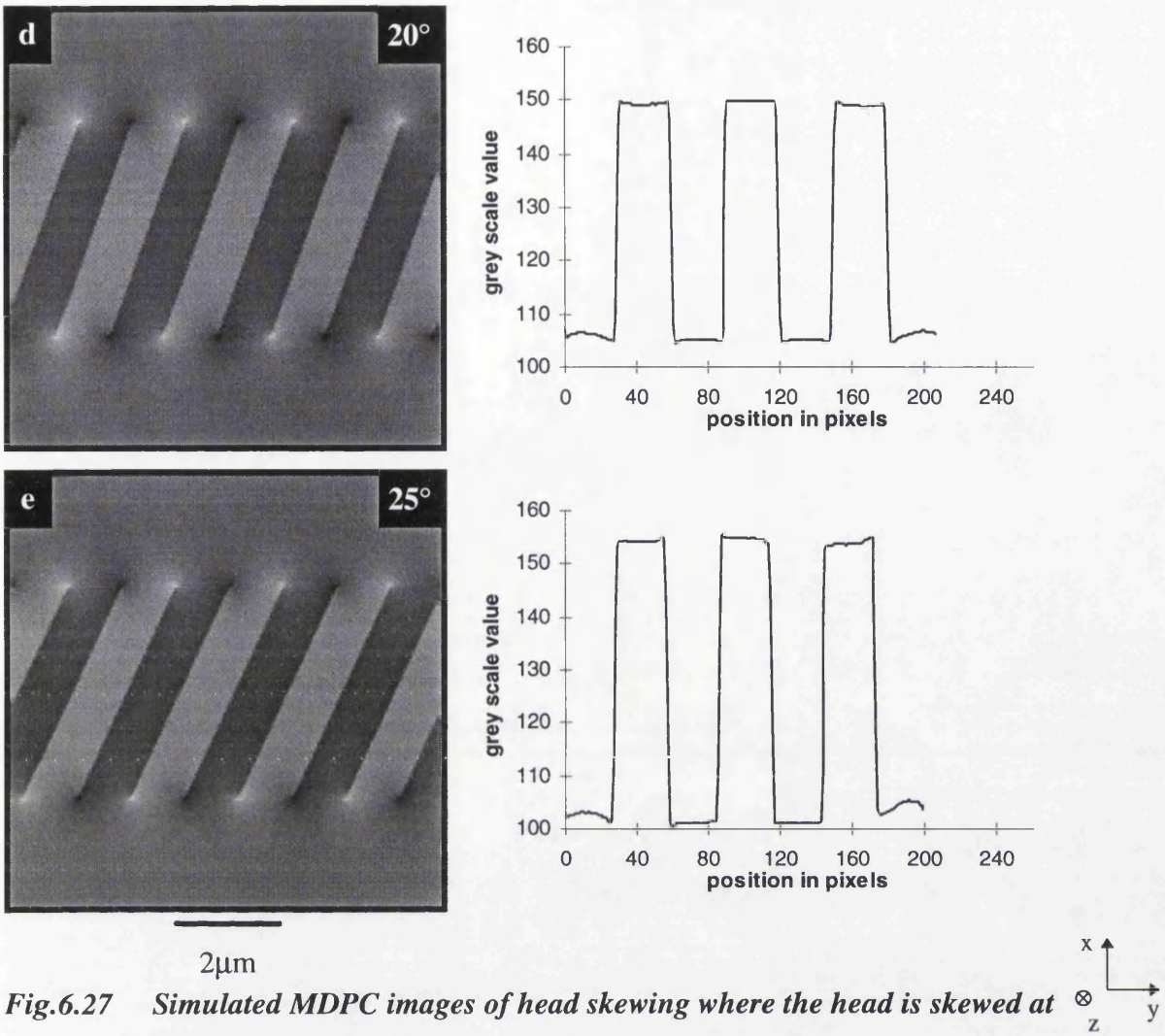

Fig.6.27 ***Simulated MDPC images of head skewing where the head is skewed at angle to the write direction. To the right of each image the associated linescan taken over the area marked is shown .***

write head which is skewed with respect to the write direction.

Fig.6.27 shows a complete set of head skewing simulated MDPC images using the magnetisation input configuration shown in Fig.6.26 mapped in the x direction. The skewing angle β° is varied from 0° to 25° in increments of 5° (The 0° image is not shown as the standard MDPC track image is produced). Fig.6.27 shows the alternate contrast due to the uncompensated component of magnetic induction as expected. As before, to allow a numerical examination of the results, linescans are taken over each of the images. No scaling is necessary as the magnetisation in the DC erasure bands remains essentially unchanged by this effect. To maintain orthogonality with the bit

transitions the linescan is inclined at an angle of β°to the write direction. The linescans are averaged over an area which has been restricted to 40 pixels in width due to the possible influence of the closure spots and to gain a maximum linescan length. As in the previous section, the results of the linescans can be compared numerically by averaging the difference in contrast along each scan. The results are plotted in Fig.6.28 to provide a relationship between the skew angle β°, and the contrast variation produced. The relationship is approximately linear as in the previous off-axis writing case with the contrast variation produced by this simulation being very similar.

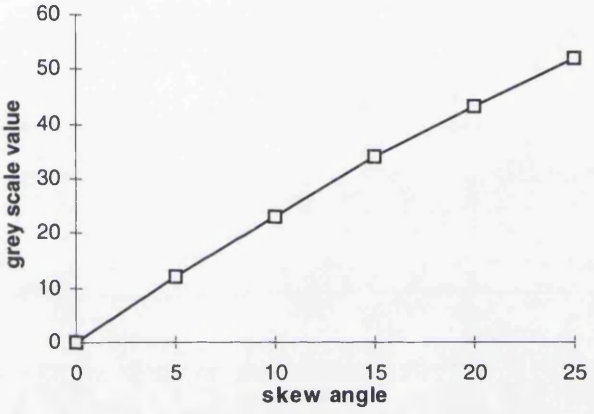

Fig.6.28 Plot of the difference in the grey levels for varying head skewing angles β°.

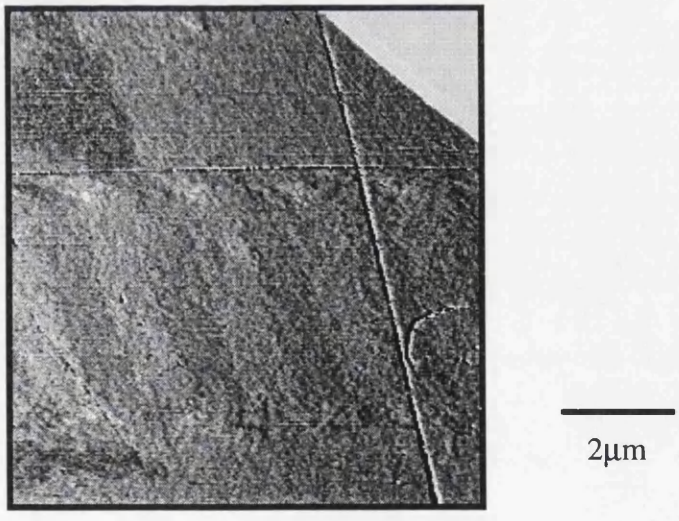

Fig.6.29 MDPC image of head skew of the 1μm track in type 2 medium.

There is a slight decrease in the contrast level difference when the head is skewed in comparison to the difference when writing off-axis. This could be due to redistribution of the free poles at the bit transitions increasing the x component of the stray field in the off-axis case.

An example of experimental imaging of head skewing is shown in Fig.6.29. The image shows a 1μm track written in type 2 medium where the head has been skewed at an angle of ~20° to the write direction. The contrast is very similar to that seen in Fig.6.29 but with a reduction in the difference of the grey levels due to the reduced $M_r\delta$ of medium 2.

6.4.4 Combination Writing

To complete the simulation analysis of the off-axis writing and head skewing effects a set of images are shown in Fig.6.30 where both effects are present. The images shown are simulated with a constant head skew angle β =20° and off-axis angles α varying from

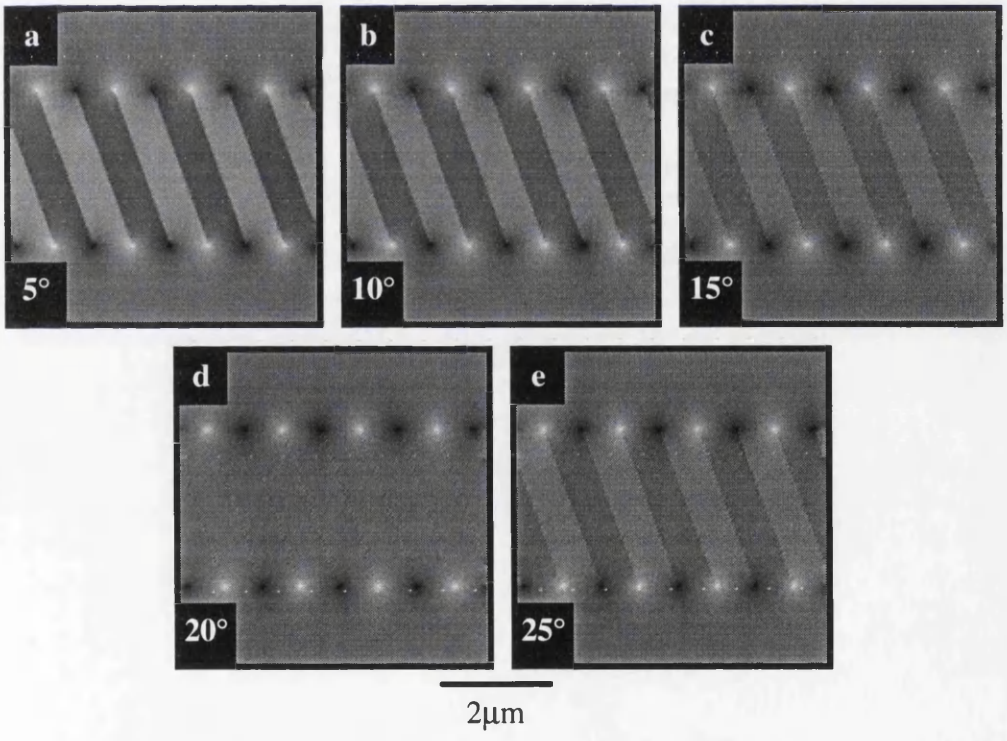

Fig.6.31 Simulated MDPC images with a constant head skewing angle of 20° with stated easy axis directions.

0°to 25° in Figs.6.31a to e respectively. From these images it is immediately obvious that at α = 20° the alternate contrast is reduced to zero. Thus both effects cancel out producing null deflection. This is as expected and merely reinforces the theory that the contrast is due to an uncompensated component of magnetic induction. Alternatively if the easy axis were to be rotated from $\alpha°$ = 0° to -25° with the same head skewing angle, no cancellation would be seen in the x mapping as a result of the rotation.

Fig.6.32 shows a plot of the difference in the grey levels between alternate bits as a function of the skewing angle. The plot shows a linear relationship as expected from the contrast which falls to zero at $\alpha°$= 20°.

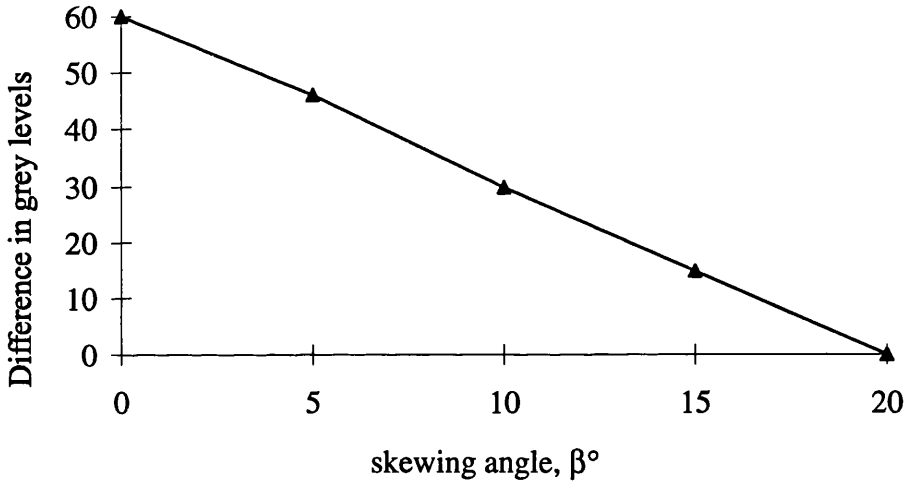

Fig.6.32 Plot of the difference in the grey levels for varying head skewing angles β° at a constant off axis angle of 20°.

6.5 CONCLUSIONS

Two methods of MDPC image simulation have been presented and compared in this chapter. Images from both the Amperian Current and Phase Modulation methods show very similar contrast levels and compare well with the experimental MDPC images. There are restrictions to the use of either method. Both methods can be applied to general magnetisation distributions however the theory produced for the Amperian method is required to be specific to blocks of magnetic material which form open flux

configurations. Further, the implementation of the Amperian current method is specific to recorded tracks making the use of different magnetisation configurations more time consuming. The Phase Modulation method is not specific to open flux configurations however due to the use of FFT's to reduced the CPU time the magnetisation distribution is effectively infinitely wrapped around during processing. This requires the magnetisation distribution to be congruent if artefacts such as saw tooth shading are to be avoided.

The simulated images show the characteristic contrast expected from x and y mappings of tracks. The experimental MDPC images showed that at a bit length to track width ratio of ~1 alternate contrast is produced, this too has been observed with in both simulation methods further agreeing with the experimental MDPC results.

As an application of the phase simulation method of section 6.4, off-axis writing and head skewing MDPC images can be created from known magnetisation distributions. These were compared with experimental MDPC images thought to display these effects. Thus the simulations have shown off-axis writing and head skewing produces MDPC images with very similar contrast characteristics to those seen experimentally. Further that when both effects are present cancellation and null deflection can occur in the centre of an x mapped track again. This simulation method will be used as input data in the following chapter as reconstruction methods are discussed.

REFERENCES CHAPTER 6

D. Corson and P. Lorrain, "Introduction to Electromagnetic Fields and Waves", ***W. H. Freeman and Co.***, first Edition, pp. 304 - 311, 1962.

G. R. Fowles, "Analytical Mechanics", ***HRW International Editions***, fourth edition, pp. 15-17, 1986.

S. McVitie, PhD Thesis, University of Glasgow, 1988.

S. McVitie and R. P. Ferrier, "Model Stray Field Calculations of a Longitudinal Recording Medium", ***J. Magn. Magn. Mat.,***104-107, pp. 963-964, 1992.

S. McVitie and R. P. Ferrier, " Stray Field and Lorentz Image Calculation of a

Longitudinal Recording Medium", ***IEEE Trans. Magn.***,Vol. 29, 1993

J. C. Mallinson and K. V. Rao, "On Electron-Beam Lorentz Microscopy", Royal Institute of Technology, Stockholm, Sweden, 1993.

M. Mansuripur, "Computation of Electron Diffraction Patterns in Lorentz Electron Microscopy of Thin Films", ***J. Appl. Phys.***, Vol. 69 (4), pp. 2455-2464, 1991.

R. Plöβl, PhD thesis, University of Regensberg and University of Glasgow, 1993.

CHAPTER 7

MAGNETISATION RECONSTRUCTION

7.1 INTRODUCTION

The subject of this chapter is to present and discuss the theory and results obtained from a magnetisation reconstruction method. Chapters 5 and 6 have shown that a large amount of both qualitative and quantitative data can be obtained from MDPC images of recorded tracks. However, the MDPC mappings do not form a direct representation of the magnetisation within the film; this is the problem that this chapter addresses.

The following sections discuss a method which aims to extract a magnetisation map from MDPC images of written tracks. The reconstruction method discussed and implemented is the curl / divergent technique [Arnoldussen 1993] which attempts to separate the vector components of the magnetisation through vector based image processing. The method is then applied to a set of simulated MDPC images.

7.2 CURL / DIVERGENT METHOD

7.2.1 Introduction

MDPC images are the result of the combined deflection due to the magnetisation within the film and the stray field above and below the film, as discussed in previous chapters. Thus to obtain a magnetisation mapping from a set of MDPC images a reconstruction method must separate the stray field components from magnetisation components. In this method the basic assumption is that the magnetic induction produced by the thin film can be divided into two types of vector components: curl and divergent components [Cohen 1970]. The divergent contributions to the MDPC images are comprised of both magnetisation and stray field components. The curl component of the MDPC images is produced solely by the magnetisation. Thus there is a separation between the stray field and the magnetisation

when considering their vector components which forms the basis of this reconstruction theory.

It should be noted that the curl of a divergent component is zero; conversely the divergence of a curl component is also zero. These mathematical relations form a critical part of this reconstruction procedure.

7.2.2 Curl / Divergent Reconstruction Method

As discussed above, the Curl / Divergent reconstruction method uses the separation of the curl and divergent vector components of the MDPC images to attempt a magnetisation reconstruction. The theory of the Curl / Divergent reconstruction method is as follows. The magnetisation in a thin film is assumed to contain both curl and divergent components as expressed in equation (7.4).

$$\mathbf{m}_{total}(x,y) = \mathbf{m}_{curl}(x,y) + \mathbf{m}_{divergent}(x,y) \qquad (7.4)$$

The stray field produced by the thin film is assumed to be a completely divergent

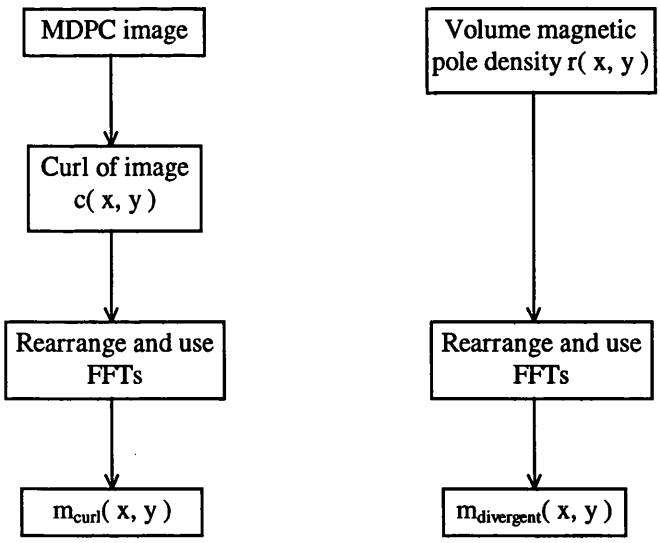

Fig.7.1 Flow chart showing the progression from MDPC images to magnetisation reconstruction.

component. The MDPC images contain deflections due to both the magnetisation within the film and the stray field surrounding the film. Thus the MDPC images consist of curl and divergent components from the magnetisation and a further divergent component from the stray field, as expressed in (7.5).

$$\mathbf{B}_{\text{MDPC image}}(x,y) = \left[\mathbf{B}_{\text{curl}}(x,y) + \mathbf{B}_{\text{divergent}}(x,y)\right]_{\text{magnetisation}} + \left[\mathbf{B}_{\text{divergent}}(x,y)\right]_{\text{stray field}} \quad (7.5)$$

Taking the curl of the MDPC images removes all the divergent components as its curl is zero. Thus the stray field contribution to the MDPC images is removed leaving an image of $[\nabla\times\mathbf{m}_{\text{curl}}(x,y)]_{\text{magnetisation}}$. However, the divergence of the magnetisation $\mathbf{m}_{\text{divergent}}(x,y)$ is also removed through the curl operation and needs to be reintroduced to provide $\mathbf{m}_{\text{total}}(x,y)$. The method to perform this is outlined in Fig.7.1 and discussed below. Only the x and y components are considered in this discussion as the z components of the magnetic induction due to the sample are collinear with the propagation direction and have no effect on the x-y deflection of the beam as in the MDPC images.

The first step in the theory is to remove all the divergent components by taking the curl of the MDPC images. The curl is performed using a composite image created from both mappings, each point in the image to be 'curl'ed contains an x and y component from the x and y mapped MDPC images respectively. The curl of the MDPC image produces the curl image $\mathbf{c}(x,y)$ (= $\nabla\times\mathbf{m}_{\text{curl}}(x,y)$) as expressed in equation 7.6a. However this is not the curl component of the magnetisation. A method must be used which can return from the 'curl' image to the original curl component of the magnetisation, $\mathbf{m}_{\text{curl}}(x,y)$. It should also be noted that the divergence of $\mathbf{m}_{\text{curl}}(x,y)$ is equal to zero as expected, expressed in equation 7.6b. A similar set of equations can be written for the $\mathbf{m}_{\text{divergent}}(x,y)$ components as in equations 7.6c and 7.6d, where $\mathbf{r}(x,y)$ is the divergent of $\mathbf{m}_{\text{divergent}}(x,y)$ and the curl of $\mathbf{m}_{\text{divergent}}(x,y)$ is zero. An initial guess of the divergent component can be made from a basic model which will be discussed in greater detail later in this section.

$$\nabla\times(\text{MDPC image}) = \nabla\times(\mathbf{m}_{\text{curl}} + \mathbf{m}_{\text{divergent}}) = \nabla\times\mathbf{m}_{\text{curl}}(x,y) = \mathbf{c}(x,y) \quad (7.6a)$$

$$\nabla \cdot \mathbf{m}_{curl}(x,y) = 0 \qquad (7.6b)$$

$$\nabla \times \mathbf{m}_{divergent}(x,y) = 0 \qquad (7.6c)$$

$$\nabla \cdot \mathbf{m}_{divergent}(x,y) = \mathbf{r}(x,y) \qquad (7.6d)$$

The stray field has now been removed from the MPDC images. The next step in the process is to extract the initial $\mathbf{m}_{curl}(x,y)$ and $\mathbf{m}_{divergent}(x,y)$ components of the magnetisation from the $\mathbf{c}(x,y)$ and the $\mathbf{r}(x,y)$ components. The technique of Fast Fourier Transforms, FFT [Brigham 1974] offer such a solution. Taking FFT's of equations 7.6a-d, rearranging the equations in transformation or k space and then inverse transforming back to real space expressions removes the spatial differential. This leaves the $\mathbf{m}_{curl}(x,y)$ and $\mathbf{m}_{divergent}(x,y)$ components of the initial magnetisation. Equations 7.7a-d describe the rearrangement relations which extract the original magnetisation from the results of equations 7.6a-d.

$$\left|\mathbf{m}_{curl}(x,y)\right|_{y\ component} = FFT^{-1}\left\{-\frac{ik_x \mathbf{C}(k_x,k_y)}{(k_x^2+k_y^2)}\right\} \qquad (7.7a)$$

$$\left|\mathbf{m}_{curl}(x,y)\right|_{x\ component} = FFT^{-1}\left\{\frac{ik_y \mathbf{C}(k_x,k_y)}{(k_x^2+k_y^2)}\right\} \qquad (7.7b)$$

$$\left|\mathbf{m}_{divergent}(x,y)\right|_{y\ component} = FFT^{-1}\left\{\frac{ik_y \mathbf{R}(k_x,k_y)}{(k_x^2+k_y^2)}\right\} \qquad (7.7c)$$

$$\left|\mathbf{m}_{divergent}(x,y)\right|_{x\ component} = FFT^{-1}\left\{\frac{ik_x \mathbf{R}(k_x,k_y)}{(k_x^2+k_y^2)}\right\} \qquad (7.7d)$$

Where $\mathbf{C}(k_x,k_y)$ and $\mathbf{R}(k_x,k_y)$ are the FFT's of the $\mathbf{c}(x,y)$ and the $\mathbf{r}(x,y)$ components respectively. Thus through equations 7.7a-d the original magnetisation $\mathbf{m}_{total}(x,y)$ can be obtained.

As mentioned above the divergent component $\mathbf{m}_{divergent}(x,y)$ of the magnetisation in the MDPC image is removed by the curl operator and thus must be

added back into the system. From fundamental electromagnetic theory [Lorrain and Corson 1969] the divergent of the magnetisation can be expressed as:

$$\nabla \cdot \mathbf{m}(x,y) = -\rho(x,y) \qquad (7.8)$$

where $\mathbf{m}(x,y)$ is a general magnetisation distribution and $\rho(x,y)$ is the free magnetic pole density associated with such a distribution. It can be seen that equations 7.6d and 7.8 are essentially the same. The magnetic free pole density in a set of recorded bits is shown diagramatically in Fig.7.2.

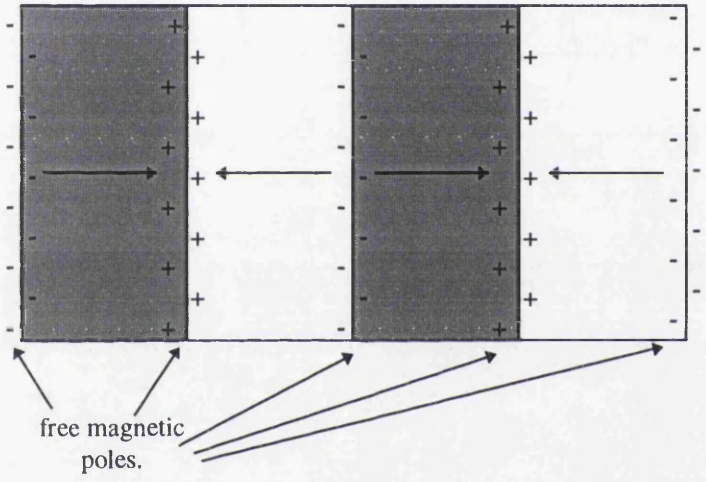

Fig.7.2 ***The model used as the expect free magnetic pole density of an ideal recorded track.***

Thus a value of $\mathbf{m}_{total}(x,y)$ can be obtained if the estimate of the free magnetic pole density is correct.

7.2.3 Results

This section presents and discusses the results obtained using the above reconstruction technique. The results which are discussed were produced by applying the reconstruction technique to a set of simulated MDPC images generated using the phase modulation method of chapter 6. Images are presented from each stage in the process showing the progression to the completed magnetisation reconstruction image set.

The starting point for the reconstruction is a set of x and y mapped MDPC images. In this reconstruction a set of simulated MDPC images are used as shown in Fig.7.3 where all the dimensions and parameters are as defined in chapter 6. The first step in the analysis is to take the curl of the composite image created by combining the x and y mapped MDPC images of Fig.7.3. The curl image produced is shown in Fig.7.4a. The positions where there is significant contrast correspond to the positions where the magnetisation in a bit meets an oppositely magnetised DC band at the track edge. The curl of the composite image can be represented as in equation 7.9 where **A** is a general vector in the x-y plane of the composite image. The resulting expression shows that the curl measures the rate of change of a vector orthogonally to the

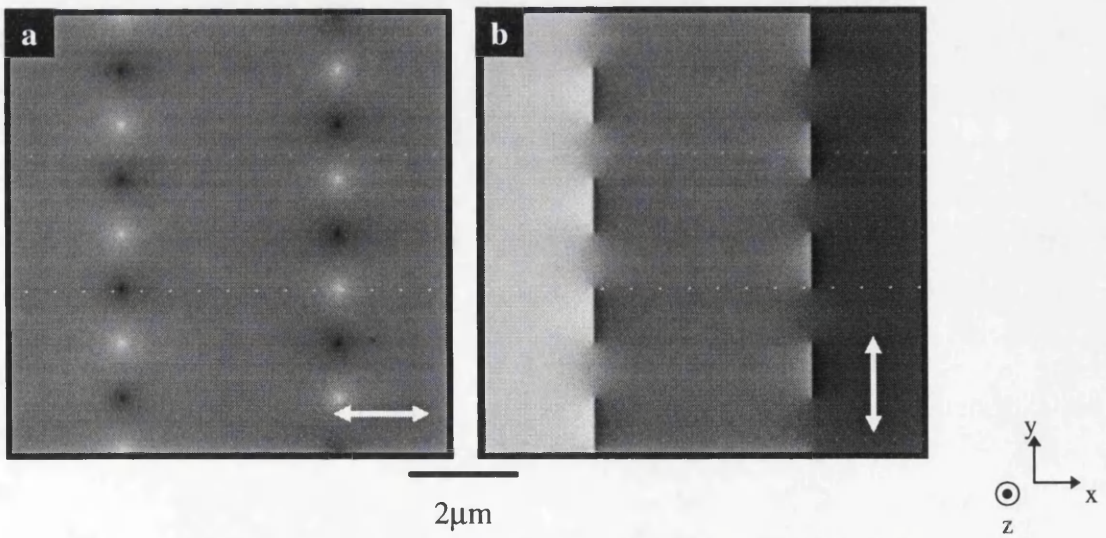

Fig.7.3 The input MDPC images simulated using the Phase Modulation technique described in chapter 6 mapped in the a) x and b) y directions.

direction of interest. Considering Fig.7.5a the curl as defined in equation 7.9 can be seen to be at a maximum at the boundary where $\nabla \times \mathbf{A} \propto 2 * M_s \delta$.

$$\nabla \times \mathbf{A}(a_x, a_y, 0) = \left[\frac{\partial a_y}{\partial x} - \frac{\partial a_x}{\partial y} \right] \mathbf{k} \qquad (7.9)$$

The curl process removes the divergent components of the images leaving only the curl components as expected. Following the double FFT and rearrangement in k space through equations 7.7 a and b, the images in Fig.7.6a and b are produced which show the $|m_{curl}(x,y)|_x$ and $|m_{curl}(x,y)|_y$ components of the final magnetisation reconstruction. Fig.7.6a shows some spreading of the spot contrast in the y direction. This is possibly a wrap around artefact from the use of the FFT's. Further comment is postponed until the magnetisation reconstruction is completed.

The second component to the final reconstruction is obtained from the $m_{divergent}$ components. These components are removed from the composite image by the curl procedure. Under normal circumstances an estimate must be made of the magnetic free pole distribution to represent the divergent component of the MDPC images. As this reconstruction uses simulated MDPC image input the exact magnetic free pole density can be used, as shown in Fig.7.4b. This can be explained using Fig.7.5b and equation 7.10. The divergence measures the rate of change of a vector along the direction of consideration and thus the head on magnetisation configuration at the bit transitions gives a maximum value.

$$\nabla . \mathbf{A}(a_x, a_y, 0) = \frac{\partial a_x}{\partial x} + \frac{\partial a_y}{\partial y} + 0 \qquad (7.10)$$

Following equations 7.7c and d the FFT is taken of the image, the components are then rearranged in k space and the inverse FFT taken of the result. This generates the images in Figs.7.7a and b. The curl and the divergent reconstruction images of Figs.7.6 and 7.7 are then added to produce the final magnetisation x and y mappings from the input MDPC images as shown in Figs.7.8a and b respectively.

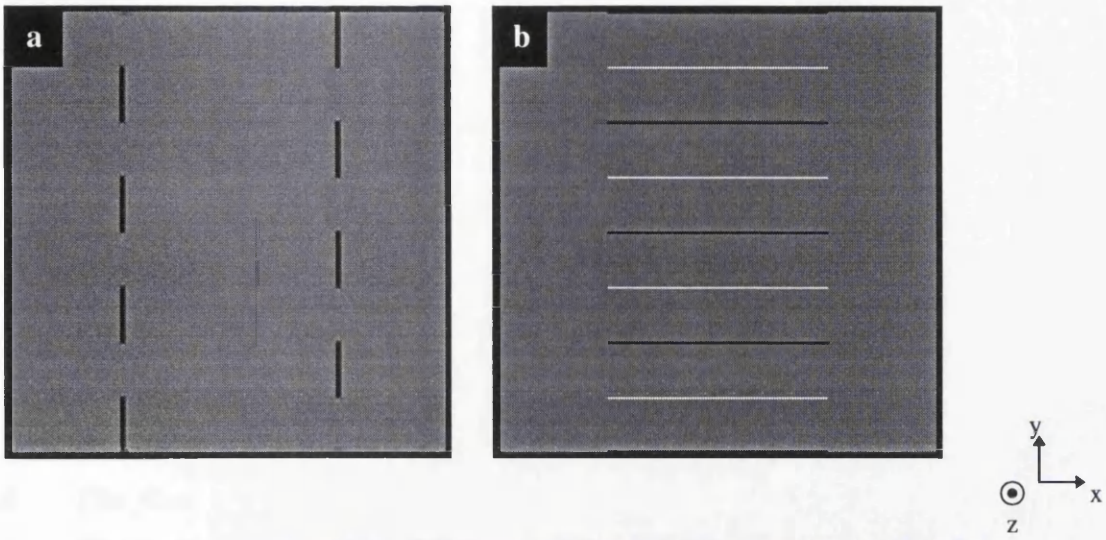

Fig.7.4 ***The images produced by a) the curl of the MDPC image set of Fig.7.3 and b) the divergent contribution from the free pole distribution of Fig.7.2.***

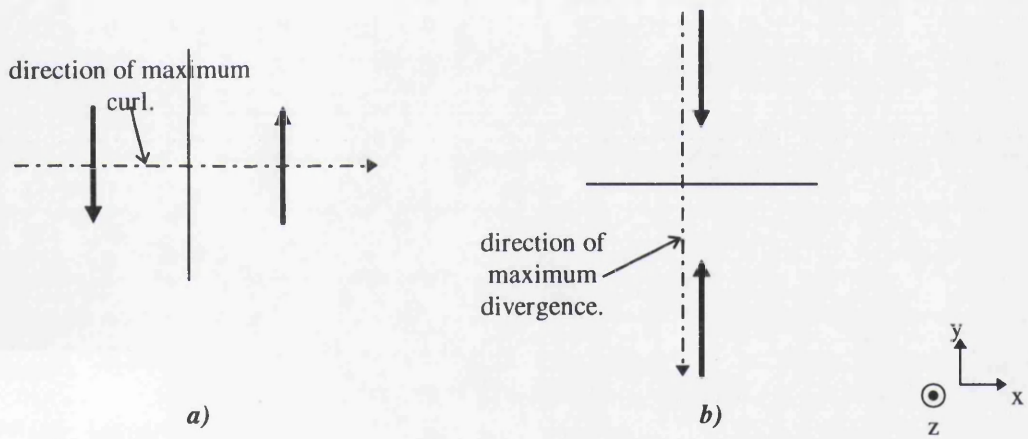

Fig.7.5 ***Representation of the magnetic induction configuration expected to produce the maximum a) curl and b) divergent in Fig.7.4 a) and b) respectively.***

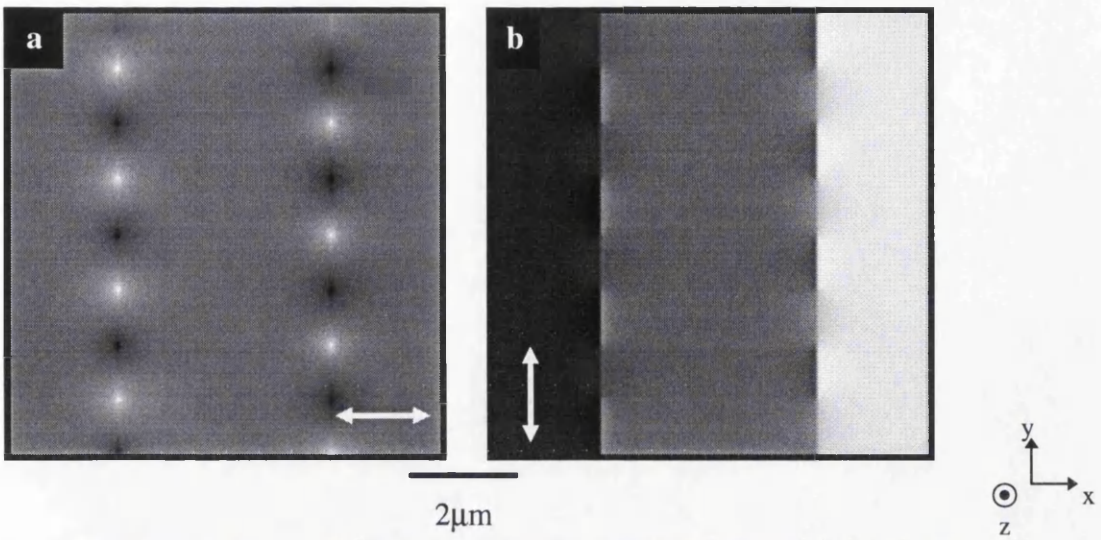

Fig.7.6 *The final a) $m_{curl\ x}$ and b) $m_{curl\ y}$ images following the curl processes outlined in Fig.7.1.*

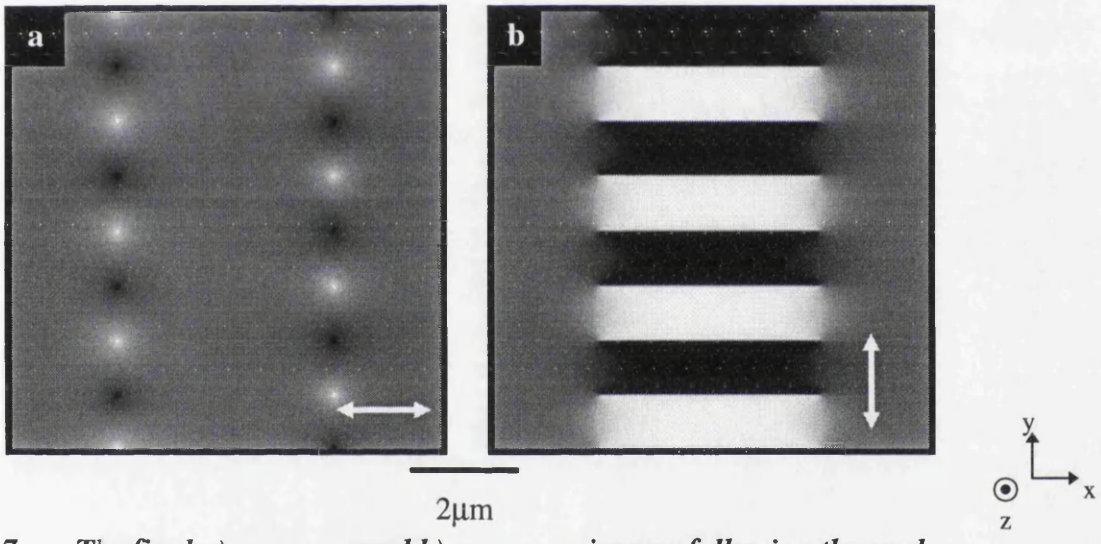

Fig.7.7 *The final a) $m_{divergent\ x}$ and b) $m_{divergent\ y}$ images following the curl processes outlined in Fig.7.1*

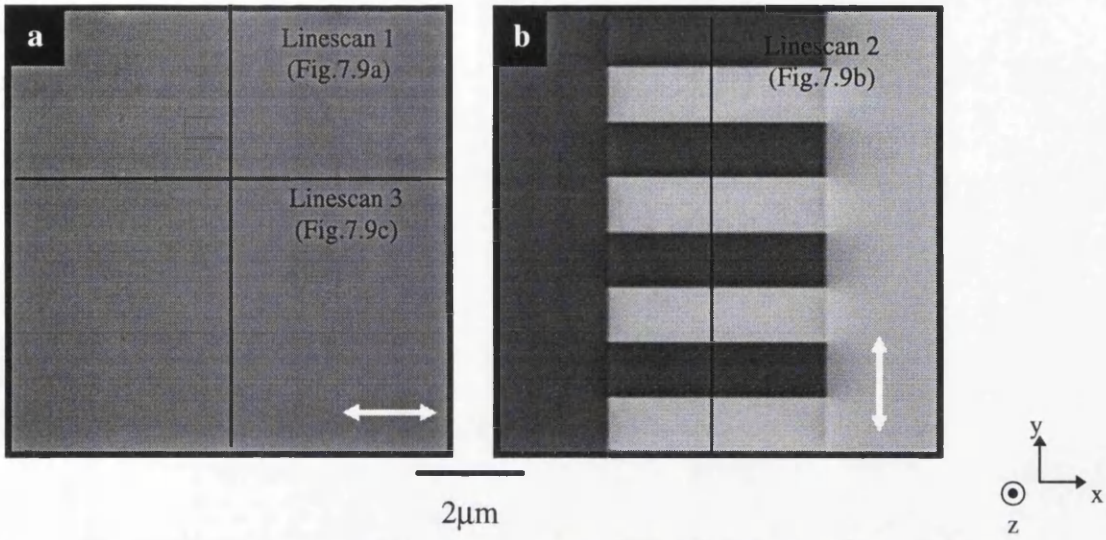

Fig.7.8 ***The final a) $m_{total\ x}$ and b) $m_{total\ y}$. images following the curl processes outlined in Fig.7.1***

The contrast in the x mapping of Fig.7.8a is almost constant over the whole area verified by the linescan in Fig.7.10a: a constant value of 127 corresponding to zero magnetisation as expected. The contrast in Fig.7.8b shows the alternate written bit as and the DC erasure bands with two constant levels of ~200 and ~50 as in the simulated MPDC images. There is a slight deviation from the expected magnetisation which occurs at the positions of the bit corners in the x mapping of Fig.7.8a. The linescan in Fig.7.9c shows the area of interest scanned along the x direction with the grey scale expanded by a factor of 2 to increase the contrast of the desired feature. The linescan shows that there is not complete cancellation in these areas. One possible explanation for this anomaly is that this is due to an FFT wrap around effect which can be seen as a spreading of the closure spots as in Fig.7.6a. Attempts were made to reduce this effect by using a Hanning function to envelope the images and by introducing symmetry to the bits to make the images cyclic. The Hanning function produced no noticeable improvement in the images. However by maintaining symmetry in both the x and y directions reductions were made in the wrap around effect. The number of tracks is kept even for symmetry in the y direction. In the x direction the image is reflected about its right hand edge effectively producing a second track and then reflected about is bottom edge. This creates two tracks in the image and a DC+ erasure band at each side which allow the image to be added

congruently and wrap around. (The final reconstructed image is then taken from only one quarter of the image after the FFTs.)

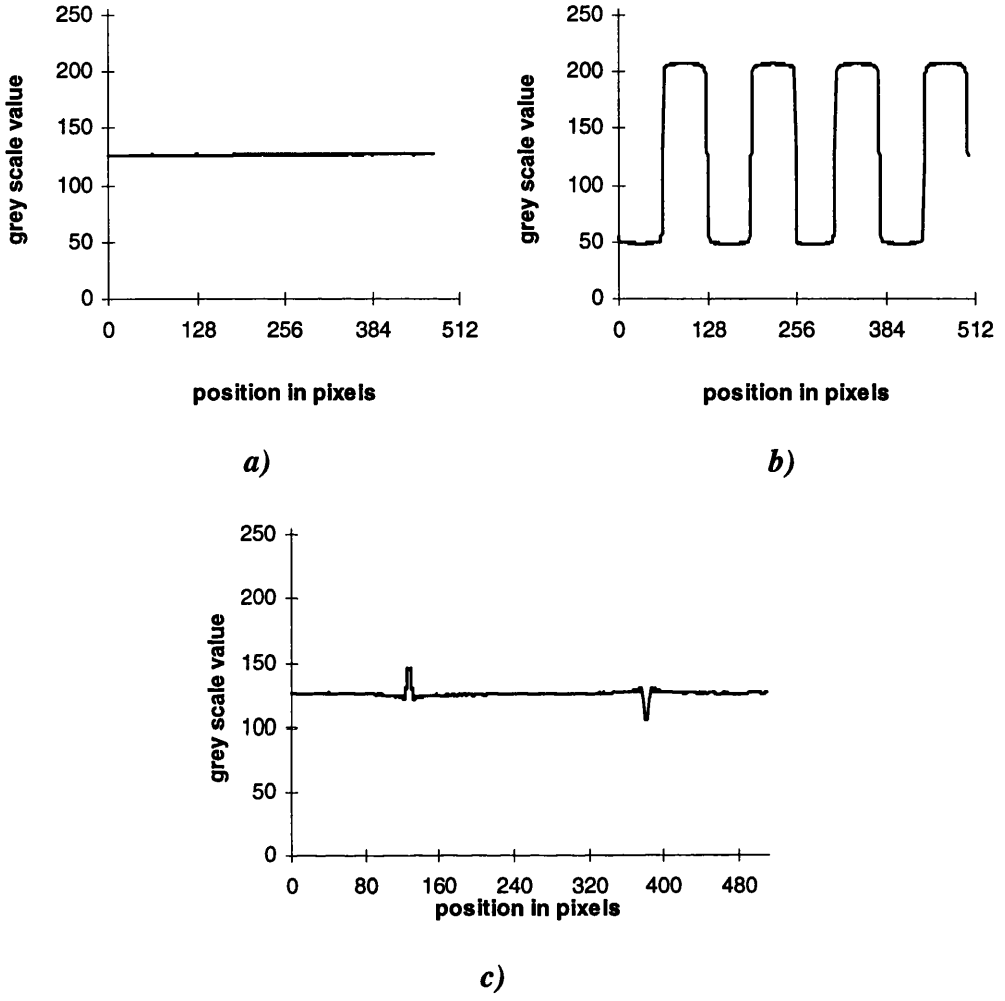

Fig.7.9 ***Linescans of a) Fig.7.8a at position 1, b) Fig.7.8b at position 2 and c) Fig.7.8a at position 3.***

7.3 CONCLUSIONS

This chapter has presented a method of obtaining a possible magnetisation distribution from a set of MDPC images mapped along and orthogonally to the write direction. The method was successfully implemented for a simulated set of MDPC images where the original magnetisation distribution was known. There is close agreement between the original and the reconstructed magnetisation distributions with the exception of a spreading effect in the x mapping.

It was hoped to apply the method to experimental images but due to the time constraints for submission of this thesis this was not possible. The method would expect to increase the noise present in the experimental MDPC images due to the differentials required in the curl of the composite image. In addition the divergent component for an experimental image would be considerably more complex than that of Figs.7.2 and 7.4b due to the nature of the bit transition as discussed in chapter 7 and the inclusion of a side write component at the track edge. To help overcome this an iteration method might be feasible to improve the divergent component guess at each loop around the process.

REFERENCES CHAPTER 7

T. C. Arnoldussen, SSD San Jose, IBM corporation, private communication, 1993.

E. O. Brigham, "The Fast Fourier Transform", Prentice-Hall, 1974.

M. Cohen, "Handbook of Thin Film Technology", Editors L. I. Maissel and R Glang, Chapter 17, McGraw Hill, 1970.

CHAPTER 8

CONCLUSIONS AND FUTURE WORK

8.1 INTRODUCTION

The subject of this thesis is the investigation of the micromagnetic structure of longitudinal recording media. This chapter highlights and summarises the results and conclusions which have been presented through the course of this thesis. Future directions for this work are discussed in the final part of this chapter.

8.2 CONCLUSIONS

To perform Lorentz electron microscopical studies on hard disk media, a reliable process for creating good quality usable specimens was required. Chapter 3 discussed the methods developed and used in this thesis for fabricating planar and cross-sectional samples. During the planar sample preparation an oxide layer was observed to form on the exposed chrome seed layer thought to be the order of 10nm in thickness. This layer could be removed by sputter etching in Argon for 15-20 minutes. The planar sample method was refined allowing microscope specimens to be produced with 2-3 days preparation. Chapter 3 also outlined a method of EDX analysis which allows the verification of the composition of a sample. The method is based on the ratio technique presented by Cliff and Lorimer and it results in an experimental estimate of the sample composition through comparisons of the background corrected peaks of an EDX spectrum. The EDX method of analysis was applied successfully to verify the composition of both media types in chapter 4; values of 72.7:10.4:17.0 and 71.6:6.1:22.3 for the Co:Pt:Cr compositions in atomic percent for media of type 1 and type 2 respectively. Using the cross sectional sample the deposited layer thicknesses of each media were found to be 125:550:350 and 85:255:255 for the C:CoPtCr:Cr layers measured in Å. The $M_r\delta$ were verified using measurements taken of the deflection of the electron beam resulting from the DC erasure bands giving values of 17.8 and 5.87 μmrads for deflections from media of

type 1 and 2 respectively compared with the calculated values of 18.8 and 8.3 μmrads respectively.

The experimental Lorentz electron microscopy results were presented and discussed in Chapter 5. Preliminary results suggested that the clarity of the Lorentz electron microscope images of the hard disk specimens could be greatly enhanced through tilting the specimen by approximately 5° with respect to the incident electron beam. The tilting of the specimen served to enhance the magnetic contrast and suppress the scratch contrast in the images. The diffraction patterns produced by the specimen show differences before and after the tilt; but the effect requires more detailed investigation for a complete explanation. Images were presented from Fresnel and Foucault investigations of both media types. The images from both techniques showed very little ripple contrast and large areas of constant magnetisation within the bits in all but the 1/3μm tracks. Feathering structures suggested by others workers to be an indication of clustering of grains were also distinguished at the side write regions over the range of bit lengths. MDPC images were then presented which displayed the magnetic features of the media. The first MDPC image sets offered a clear view of the bit transitions and the side write lobes and their variation over a range of bit lengths from 5 to 1/3 μm; the bit transition width was found to be ~ 0.15μm over the range of bit lengths. In addition to this the stray field produced above and below the written bits was seen to have a significant effect on the MDPC image contrast ; cancellation above the written bits and closure spots at the corners of the written bits where only a small component of magnetisation is expected. High magnification MPDC images of the 1/3μm track revealed the formation of small domains where alternate bit transitions meet and interfere across the bits. Further MDPC imaging of the bit transitions at high magnification suggested three types of bit transition: zig zag, vortex and a combination of both. An estimate of the mean transition width between alternate DC bands producing a value of ~80nm. An alternate contrast effects were observed which are consistent with off axis writing and head skewing. These effects suggested the existence of a slight anisotropy in the media along the track direction creating uncompensated cross track components of magnetic induction. The final part of chapter 5 presented MFM images which map the vertical components of the stray field. The results produced compare favourably with

the MDPC results over the bit transition regions. The bit transitions show some of the structure seen in the MDPC images; in particular the 1/3μm track show discontinuities in the stray field.

Chapter 6 discussed both the Amperian Current and Phase Modulation simulation methods which were used to produce two sets of simulated MDPC images. The results were very similar when the two methods were compared. Simulated results were also compared with experimental MDPC images confirming that both simulation methods show the standard image characteristics; stray field cancellation which varies with bit length in the y mappings and closure spots in the x mappings. The Phase Modulation method was also extended to include off axis writing and head skewing producing images which could quantitatively compare with the experimental MDPC images.

A method of magnetisation reconstruction which starts from a set of MDPC images of written tracks was introduced in chapter 7. The method uses the curl and divergent components of the MDPC image sets to produce the final magnetisation mapping. A mathematical treatment of the method was presented and the results of the method applied to a set of simulated MDPC images generated using the Phase Modulation technique. The reconstructed magnetisation was consistent with the input magnetisation which produced the simulated MDPC image. The reconstruction method could be extended to use experimental MDPC images as an input but this was not possible due to time constraints.

8.3 FUTURE WORK

The work of this thesis could be extended in one of several directions. This thesis has discussed at length the interpretation of MDPC images in terms of both the stray field and the magnetisation and a magnetisation reconstruction technique was discussed and implemented on simulated images. An alternative approach to magnetisation reconstruction which could be used is the ART Algebraic Reconstruction Technique [Gordon 1994].

The ART technique is a general method which attempts to reproduce an N dimensional object or field from a series of (N-1) dimensional projections taken from

various directions with respect to the object, as in Fig.8.1. In this case the objects to be reconstructed are the **B** vectors produced by the recorded tracks in the thin film and the result of each projection is an MDPC image pair. Each projection can be thought of as being a slice through the reconstruction volume with a value of magnetic induction contained in each reconstruction cell. The deflection experienced by the electron beam is the sum of the contributions from the magnetic induction of each cell entered by the electron beam. The reconstruction field area is represented by a 3 dimensional grid with the thin film at its centre. Each MDPC image is a projection taken through that grid as in Fig. 8.2. The contribution from each cell to the overall deflection or the pixels of an MDPC image is proportional to the path length of the electron beam within that cell. By varying the angle of the beam to the reconstruction area the path length through each cell is varied between projections and as a result the contribution from that cell is varied. Through an iterative procedure and using weight factors which are proportional to the varying path lengths through each cell, a value of the magnetic induction in a cell can be calculated. Taking MDPC images at various angles with respect to the thin film provides the required projection series.

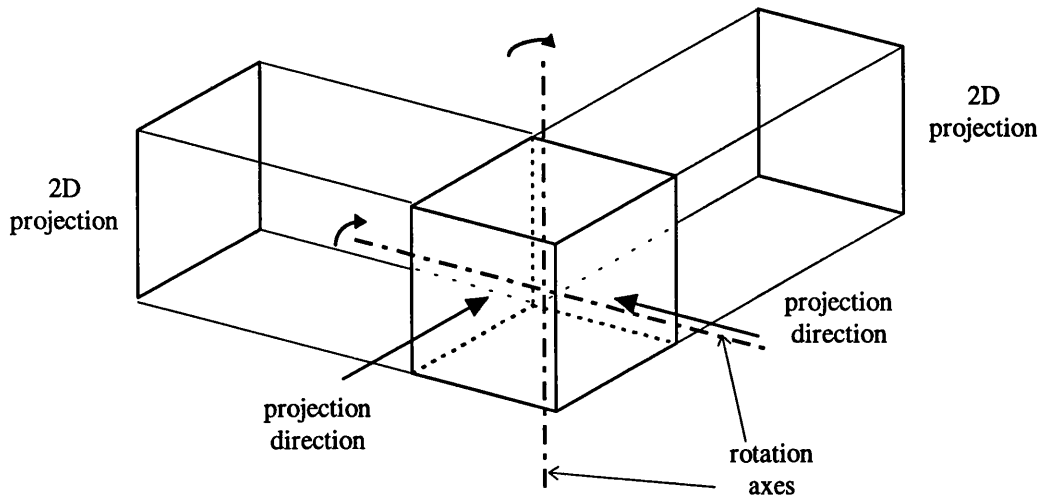

Fig.8.1 Diagram showing the production of 2D projections from a 3D object.

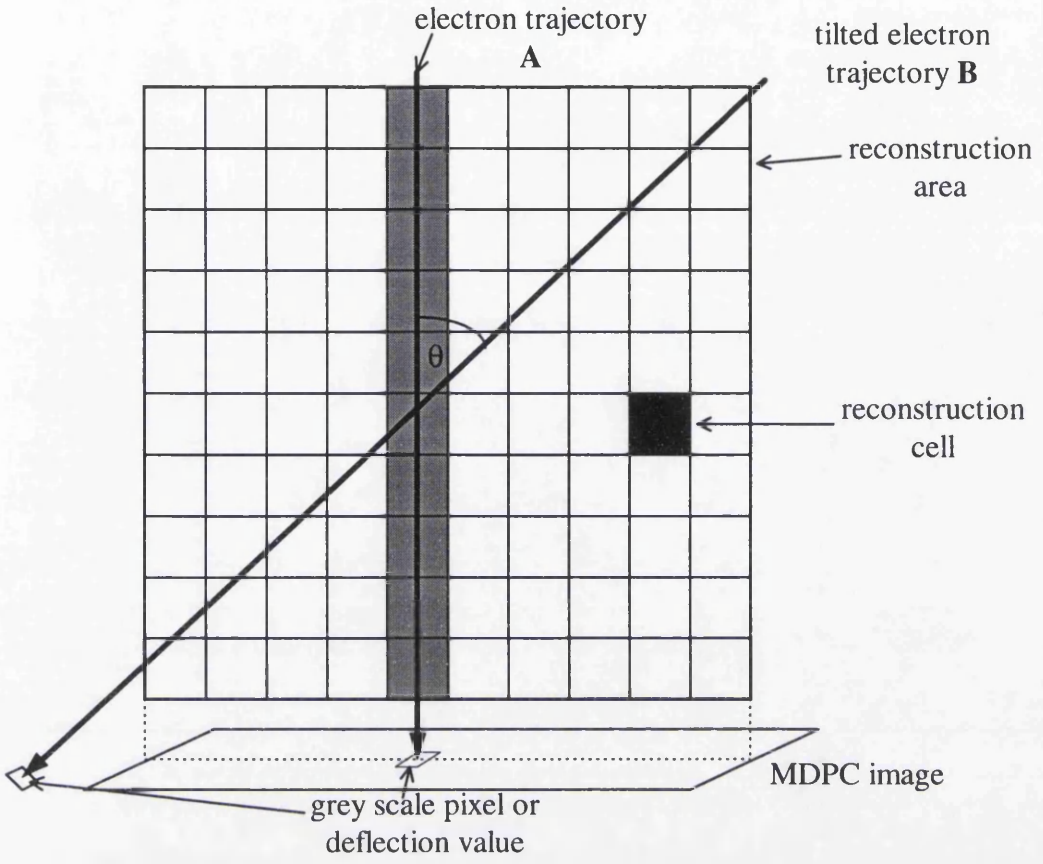

Fig.8.2 ***Diagram of a slice through the reconstruction volume showing the path of single electron beam.***

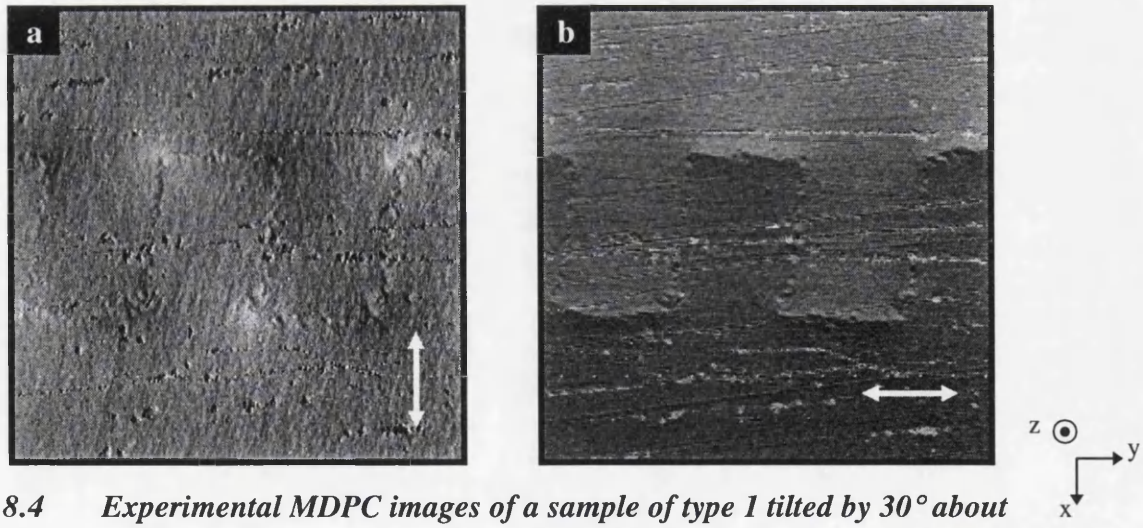

Fig.8.4 ***Experimental MDPC images of a sample of type 1 tilted by 30° about the x axis mapped in the a) x and b) y directions.***

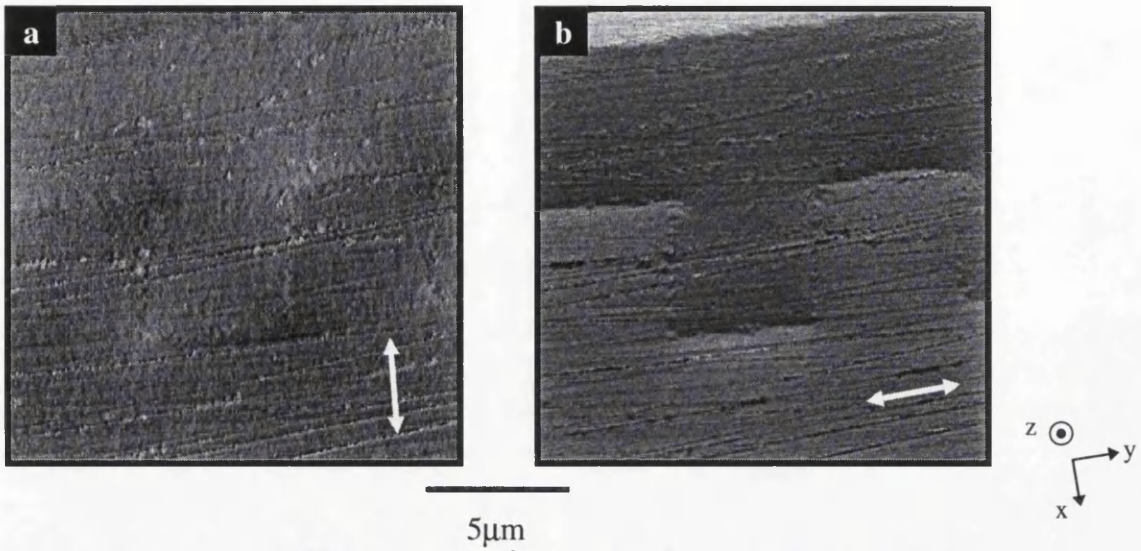

Fig.8.5 ***Experimental MDPC images of a sample of type 1 tilted by 30° about the y axis mapped in the a) x and b) y directions.***

A set of preliminary tilted experimental MDPC images are shown in Figs.8.4 and 8.5 at a tilt of 30° about the x and y axis respectively; the zero tilt images are shown in Fig.8.3. In each case the sample was positioned with the relevant axis directed along the axis of the specimen rod in the electron microscope. The post specimen lenses are then excited to produce rotation to maintain the correct orthogonal mapping directions with respect to the tracks in the sample. In each case the expectation is to introduce a z component of magnetic

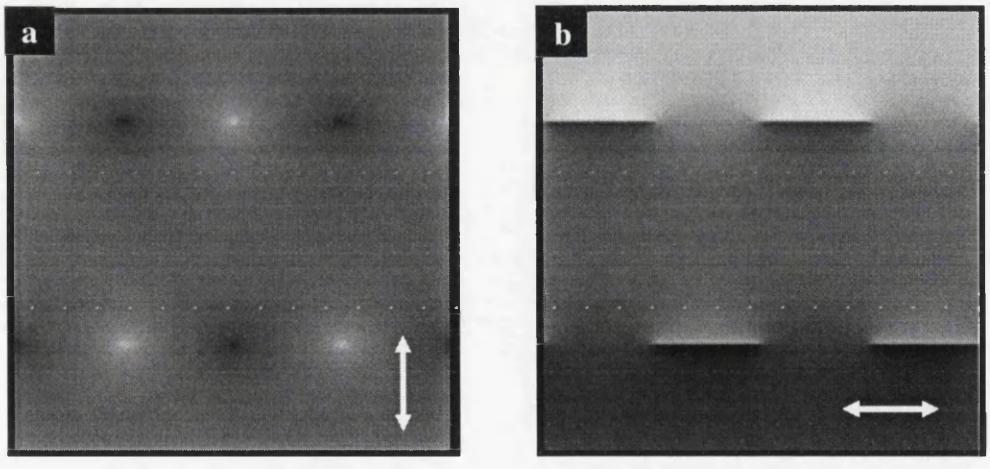

Fig.8.6 ***Simulated MDPC images of a sample of type 1 medium with no tilt mapped in the a) x and b) y directions.***

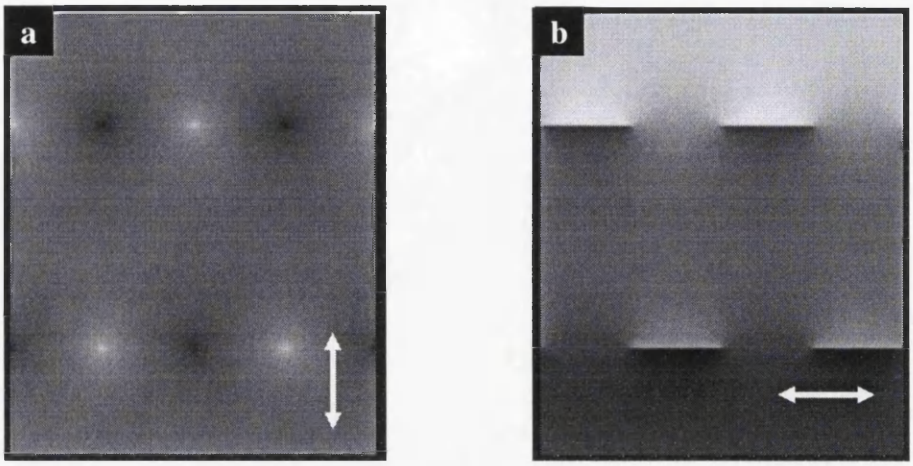

Fig.8.7 ***Simulated MDPC images of a sample of type 1 tilted by 30° about the x axis mapped in the a) x and b) y directions.***

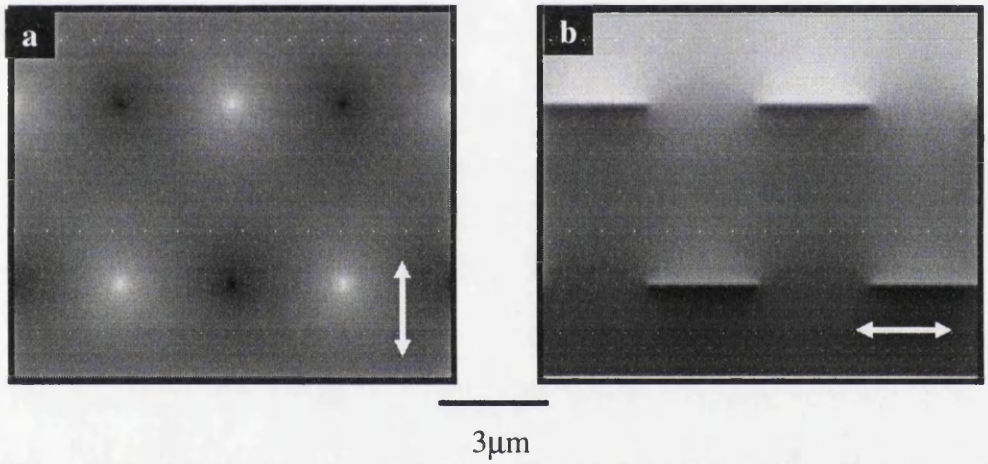

Fig.8.8 ***Simulated MDPC images of a sample of type 1 tilted by 30° about the y axis mapped in the a) x and b) y directions.***

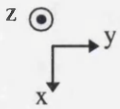

induction into the y and x mappings respectively. The contrast is reduced as a result of the increased path length through the thin film. A set of tilted MDPC images which are simulated using the Phase Modulation method of chapter 6 are shown in Figs.8.7 and 8.8 titled about the x and y axis respectively, with untilted images shown in Fig.8.6. There is still a large amount of stray field cancellation following either tilt. There is however a reduction in the contrast in the x mapping of the x tilted samples and some increase in the stray field spreading at the track edges in the y mappings of the y titled images which may be exploited by the ART investigation.

An alternative method would be to combine MFM imaging with the ART reconstruction to give initial values of the stray field above the sample to give a more accurate calculation. The MFM images could be taken over a sample at various heights to create mappings of the z component of the stray field. This could then be used as the first guess in the iteration procedure of the ART of the MDPC images. This would require very accurate positioning in both microscopes possibly requiring a position marker on the sample which was visible in both microscopes i.e. deliberate contamination due to beam damage in three positions for triangulation. The sample would also be required to be durable enough to be use in both STEM and MFM systems; the tapping procedure to form the topographic image in the MFM causes stresses on the sample which may result in irreparable damage to the specimen.

REFERENCES

R. Gordon, "A Tutorial on ART", ***IEEE Trans. Nuc. Sci.,*** Vol. NS 21, pp. 78-93, 1974.

Y. Liu and R. P. Ferrier, "Quantitative evaluation of a thin film recording head field using the DPC mode of Lorentz electron microscopy", ***IEEE Trans. Magn.,*** Vol. 31, No. 6, pp. 3373-3375, 1995.